Synthesis and Characterization of Verdazyl Containing Molecules and Metal-Verdazyl Complexes

by

Bryan Douglas Koivisto
B.Sc., University of Waterloo, 2000

A Dissertation Submitted in Partial Fulfillment of the
Requirements for the Degree of

DOCTOR OF PHILOSOPHY

in the Department of Chemistry

University of Victoria

Supervisor: Dr. Robin G. Hicks

ABSTRACT

This work presents three new classes of 6-oxoverdazyl radicals. Each of these classes of radicals bears a different substituent in the 3-position of the verdazyl ring. These classes include *N*-heteroaromatic monoverdazyls, oligopyridine diradicals, and ferrocenyl-based verdazyl radicals and diradicals. With the exception of the ferrocenyl-based radicals, these verdazyl radicals have been designed to serve as ligands and the direct metal-radical interactions have been explored. The ferrocenyl verdazyls have been designed to investigate the indirect interactions between iron(II) and the covalently linked verdazyl radical. All verdazyl radicals and precursors were fully characterized and the metal-radical magnetic interactions were investigated where structural characterization was available.

A series of bidentate verdazyl radical ligands were prepared and the metal-radical magnetic interactions have been investigated. The magnetic susceptibility data for the octahedral complexes indicates that cobalt(II) couples ferromagnetically ($J_{\text{Co-vd}}$ = +95 cm^{-1}) and iron(II) antiferromagnetically ($J_{\text{Fe-vd}}$ = -66 cm^{-1}) to the verdazyl radical. The nature of these interactions appears to be dictated by orbital symmetry and is consistent with previously reported nickel and manganese verdazyl complexes. This work also demonstrates that imidizole-based verdazyl radicals are effective ligands in tetrahedral copper(I) complexes.

Oligopyridine-based diradicals have been designed as ligands, but decompose in solution preventing metal complexation. An attempt was made to construct grids as a higher order molecular structure. To this end, a diradical ligand with the topology necessary to form discrete grid architectures was synthesized, but has not yet demonstrated the ability to coordinate to metal ions. Other monoverdazyl radicals that are symmetrically substituted in the N1 and N5 positions were also investigated as potential grid forming ligands.

A series of ferrocenyl verdazyl and methylated ferrocenyl verdazyls were prepared to investigate the electronic and magnetic interactions between the ferrocene and verdazyl electrophores. As evidenced by UV-Vis and electrochemical solution measurements, the two electrophores exhibit mutual electronic perturbations. In the case of the methylated ferrocene derivatives the degree and pattern of methylation appears to have a regiospecific influence on the verdazyl electrochemistry. In the solid state Mössbauer data is consistent with a Fe^{2+} ground state and there is no evidence of Fe^{3+} at or below room temperature. Weak antiferromagnetic behaviour ($|J| < -13$ cm^{-1}) was observed within and between pairs of ferrocenyl monoverdazyls in the solid state.

In order to investigate the interactions between radicals separated by an organometallic spacer, a ferrocenyl verdazyl diradical was prepared. The ferrocene diradical demonstrated significant differences between the solid state and solution phase. While the ferrocene diradical and ferrocene monoverdazyl exhibited similar solution electronic properties, the magnetic properties were vastly different. In solution the spins associated with the diradical appeared to be weakly coupled, but in the solid state the diradical has been characterized as a strongly coupled antiferromagnetic π-dimer. This is the first example of a verdazyl π-dimer. The π-dimer appears to be diamagnetic with the lower limit of exchange estimated at $J_{inter} \approx -2000$ cm^{-1}.

TABLE OF CONTENTS

PRELIMINARY PAGES

LIST OF FIGURES

LIST OF SCHEMES

LIST OF TABLES

LIST OF NUMBERED COMPOUNDS

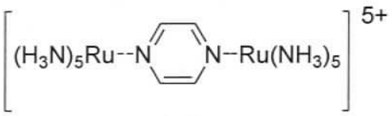

1.1

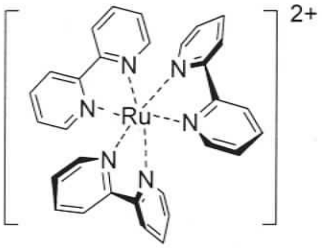

1.2

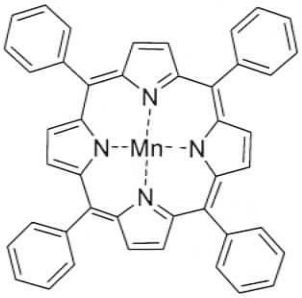

1.3

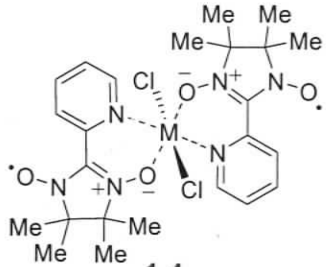

1.4

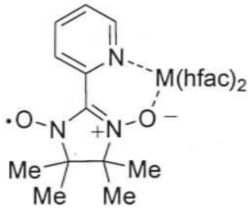

1.5

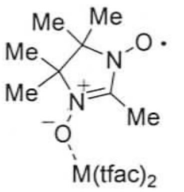

1.6

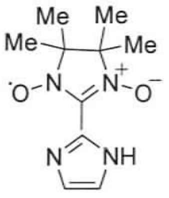

1.7

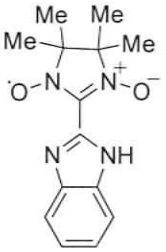

1.8

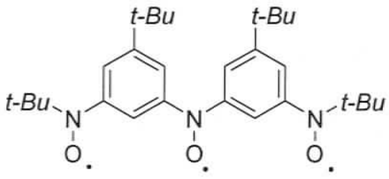

1.9

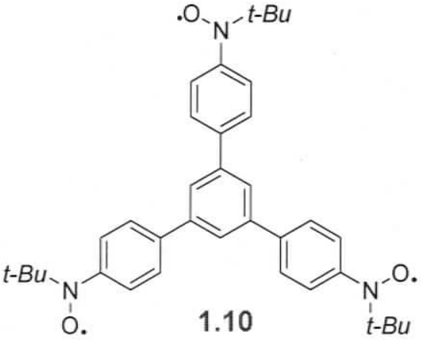

1.10

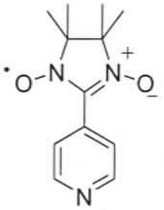

1.11

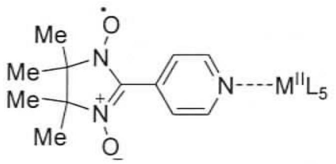

1.12

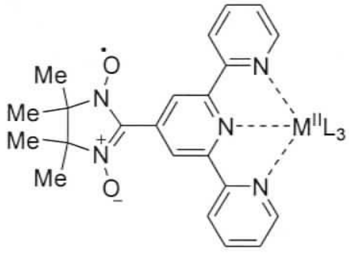

1.13

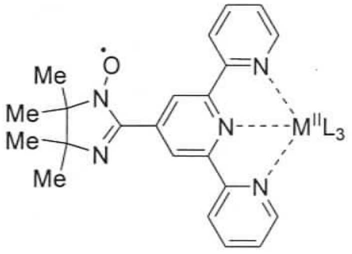

1.14

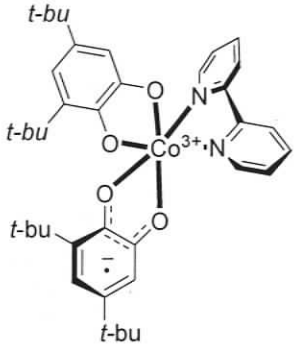

1.15

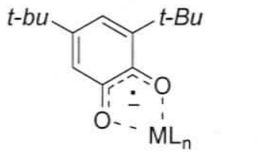

1.16a; M = Cu(II)
1.16b; M = Ni(II)

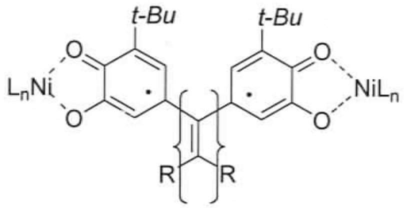

1.17

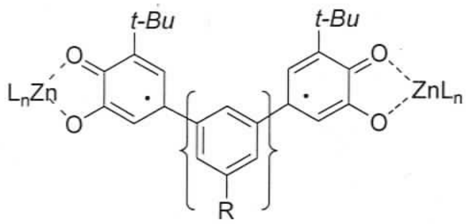

1.18

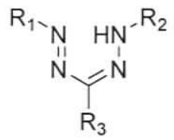
2.1

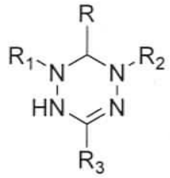
2.2

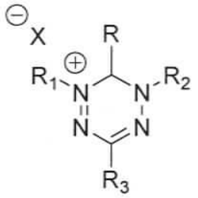
2.3

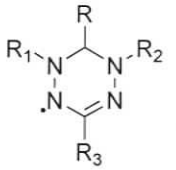
2.4

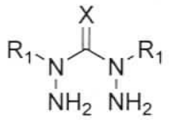
X = S, O

2.5

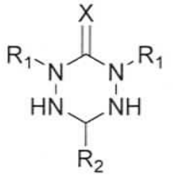
X = S, O

2.6

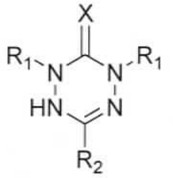
X = S, O

2.7

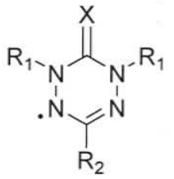
X = S, O

2.8

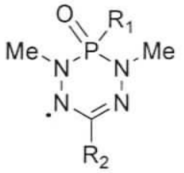
2.9

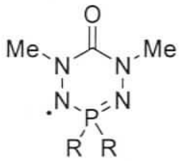
2.10

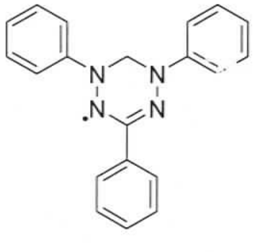
2.11

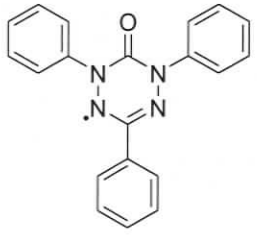
2.12

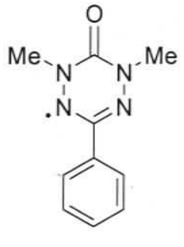
2.13

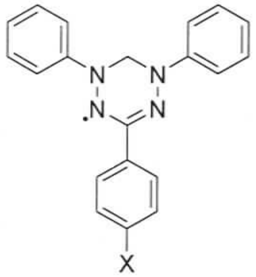
2.14

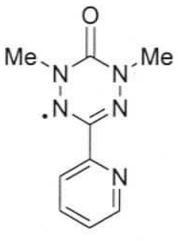
2.15

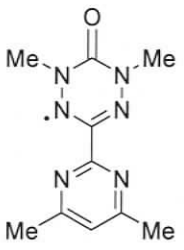
2.16

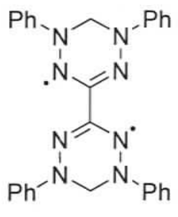
2.17

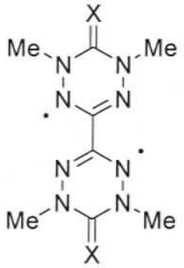
X=O, **2.18a**
X=S, **2.18b**

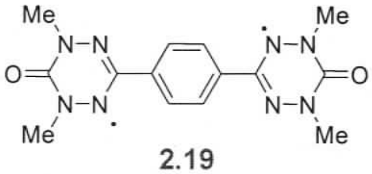
2.19

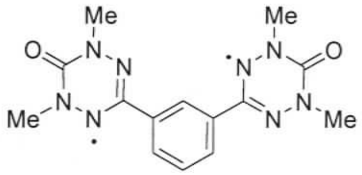
2.20

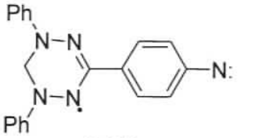

2.21

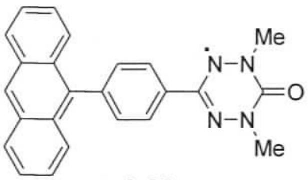

2.22

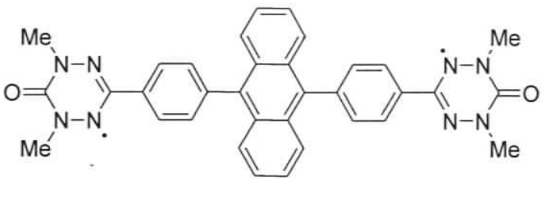

2.23

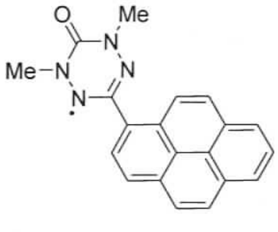

2.24

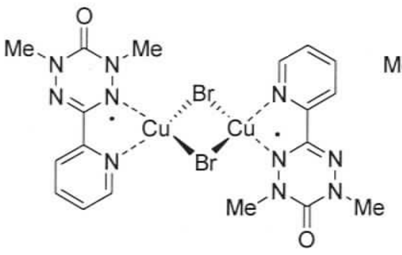

2.25

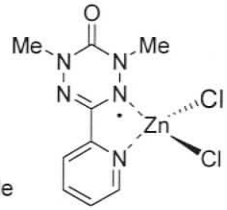

2.26

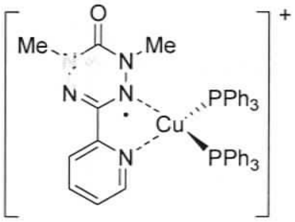

2.27

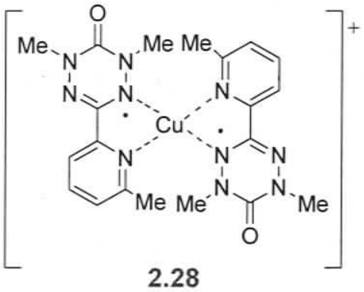

2.28

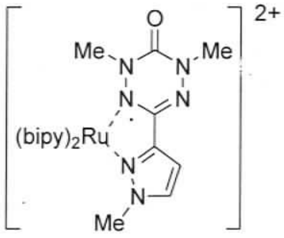

2.29

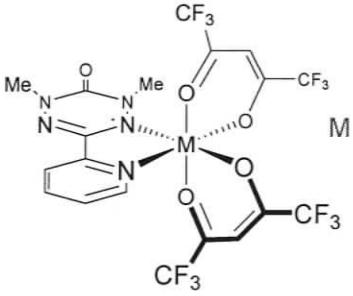

M = Mn **(2.30)**
Ni **(2.31)**

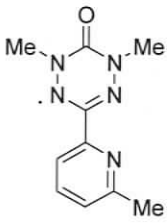

2.32

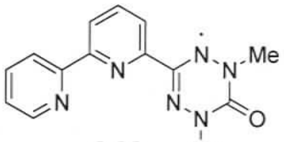

2.33

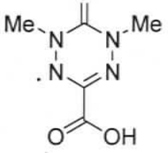

2.34

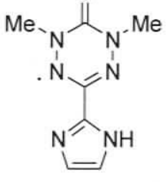

2.35

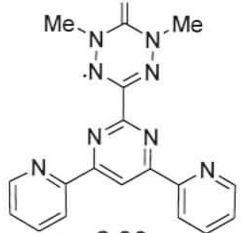

2.36

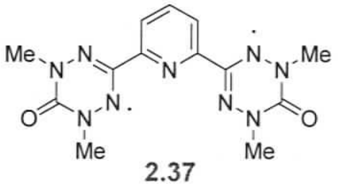

2.37

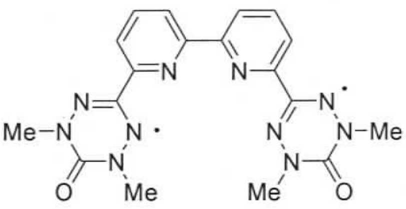

2.38

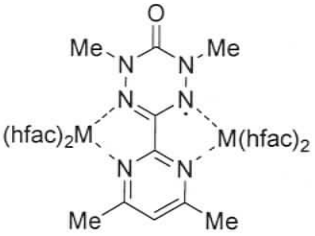

M = Ni, **2.39a**
M = Mn, **2.39b**

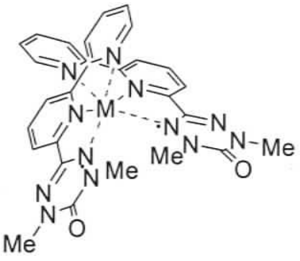

M = Ni, **2.40a**
M = Mn, **2.40b**

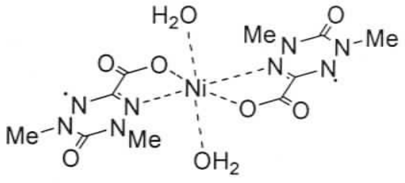

2.41

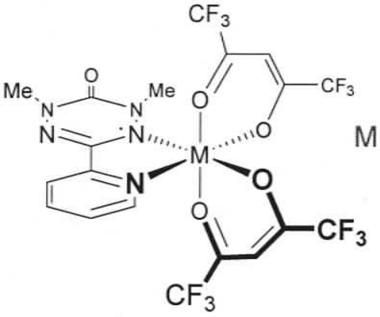

M = Fe (**2.42**)
Co (**2.43**)

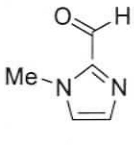

2.44

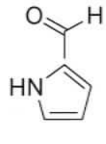

2.45

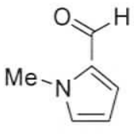

2.46

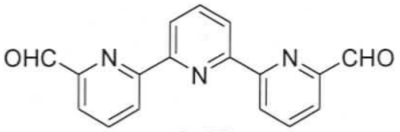

2.47

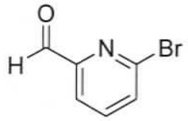

2.48

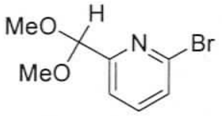

2.49

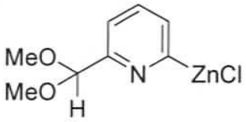

2.50

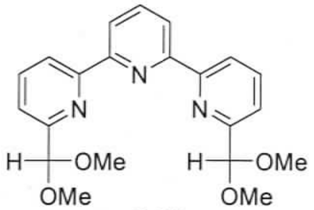

2.51

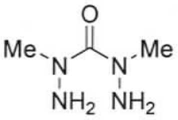

2.52

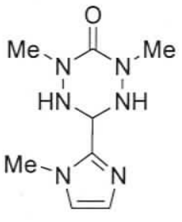

2.53

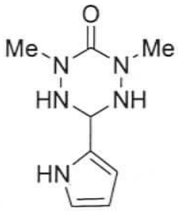

2.54

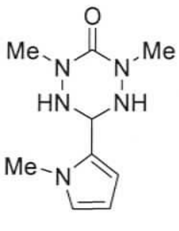

2.55

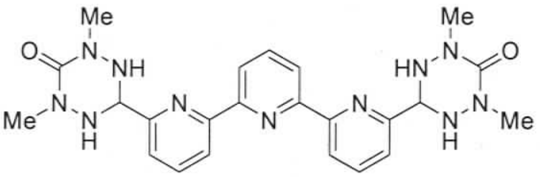

2.56

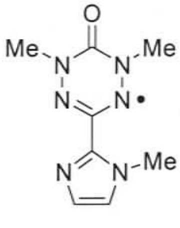

2.57

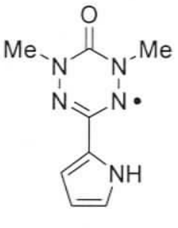

2.58

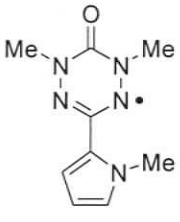

2.59

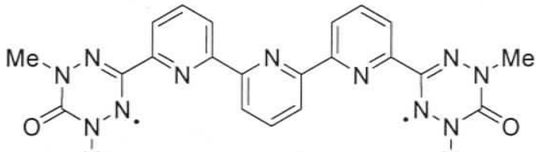

2.60

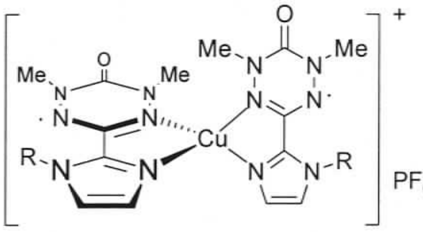

R = H **2.61**
R = Me **2.62**

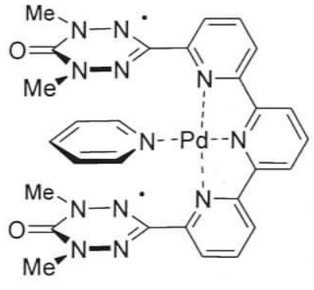

b) **2.63**

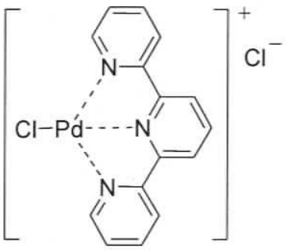

2.64

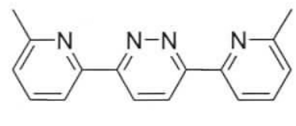

3.1

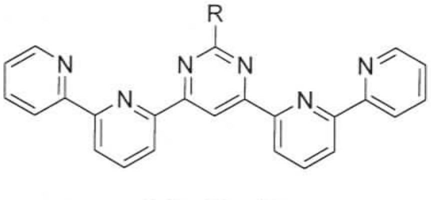

3.2 - R = H

3.3 - R = CH_3

3.4 - R = Ph

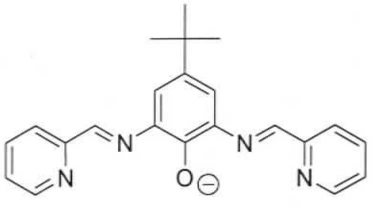

3.5

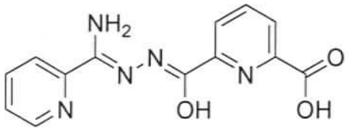

3.6

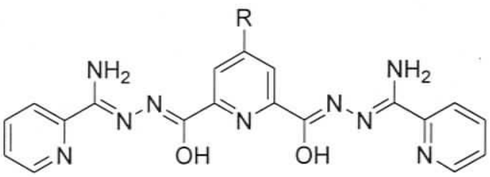

3.7

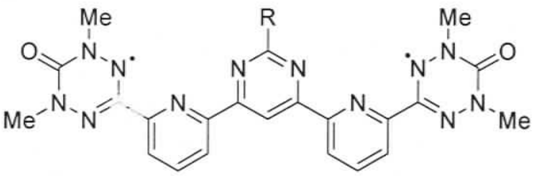

3.8

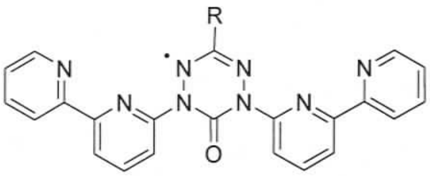

3.9

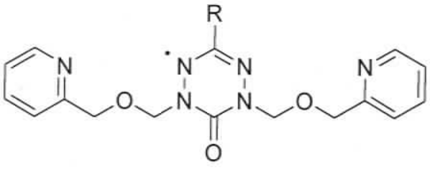

3.10

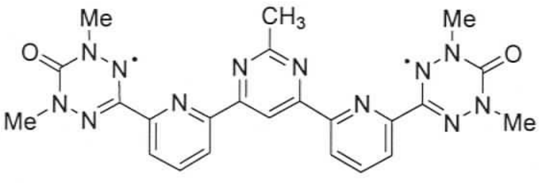

3.11

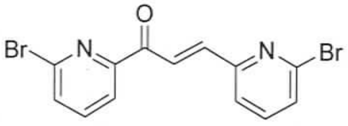

3.12

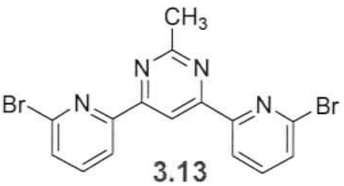

3.13

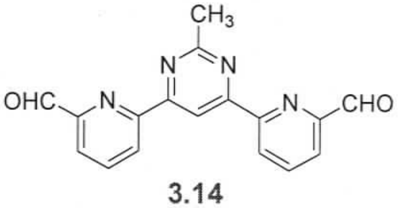

3.14

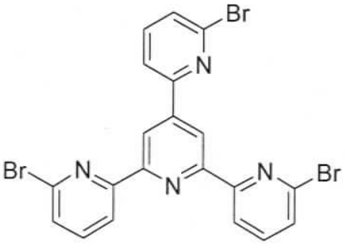

3.15

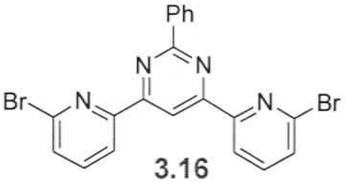
3.16

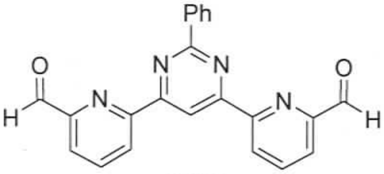
3.17

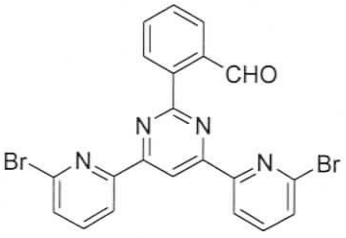
3.18

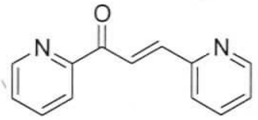
3.19

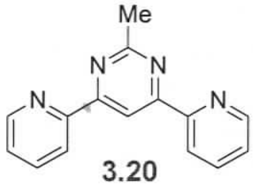
3.20

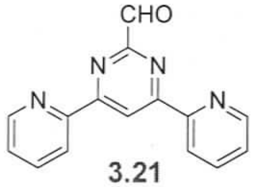
3.21

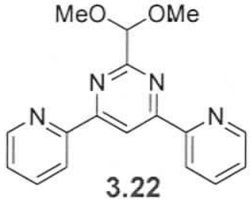
3.22

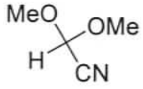
3.23

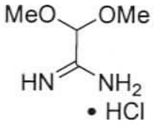
3.24

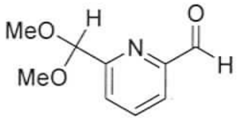
3.25

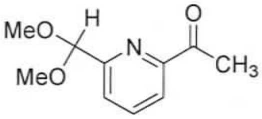
3.26

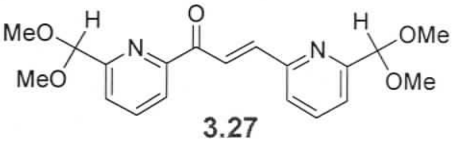
3.27

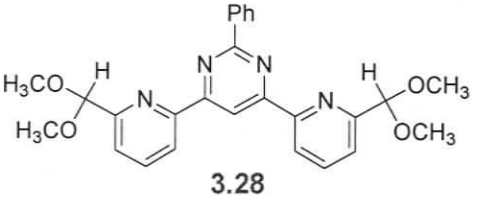
3.28

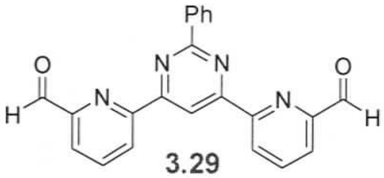
3.29

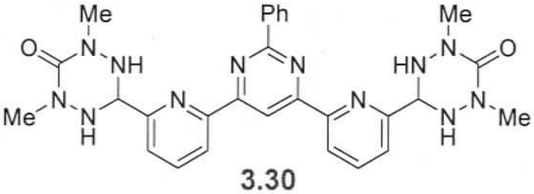
3.30

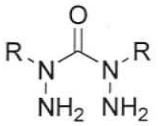

R = 2-pyridyl **3.31**

R = 2-bipyridyl **3.32**

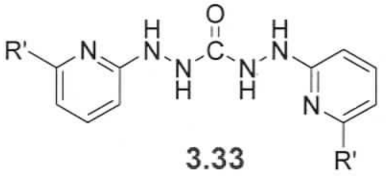

3.33

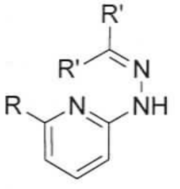

3.34

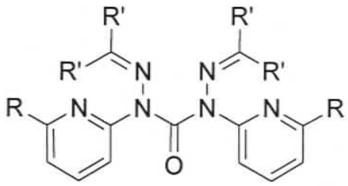

3.35

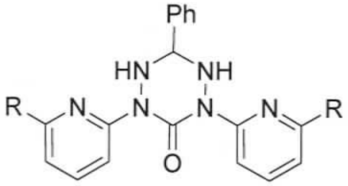

3.36

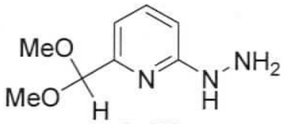

3.37

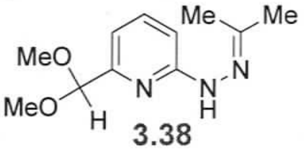

3.38

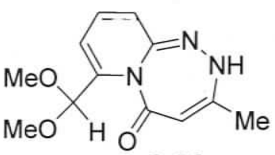

3.39

3.40

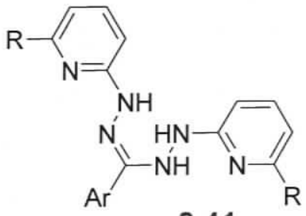

3.41

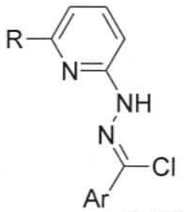

3.42

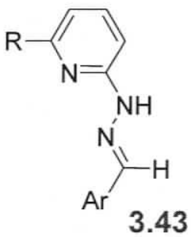

3.43

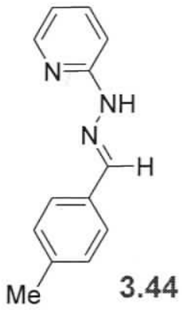

3.44

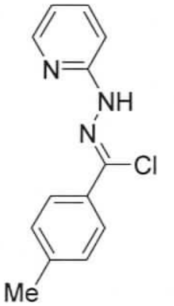

3.45

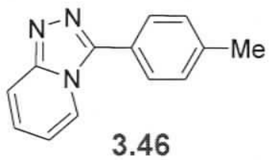

3.46

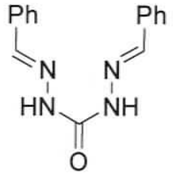

3.47

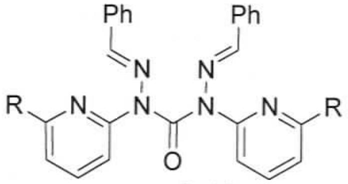

3.48

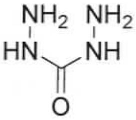

3.49

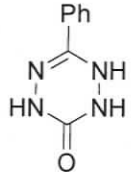

3.50

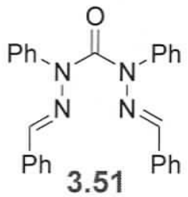

3.51

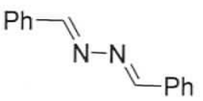

3.52

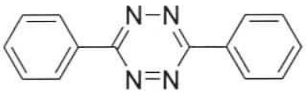

3.53

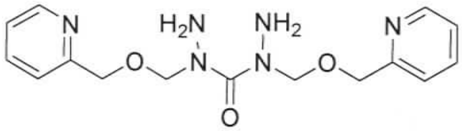

3.54

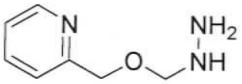

3.55

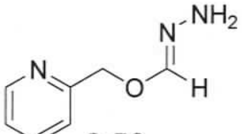

3.56

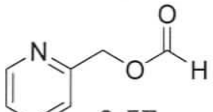

3.57

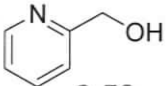

3.58

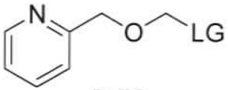

3.59

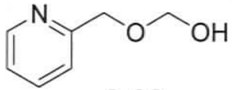

3.60

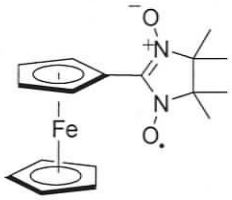
4.1

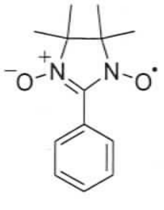
4.2

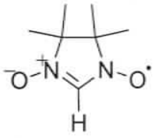
4.3

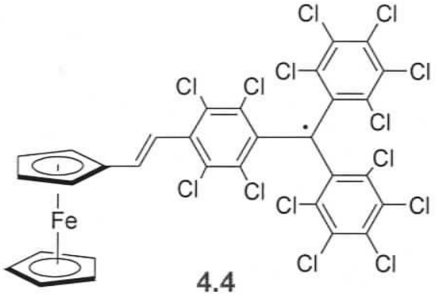
4.4

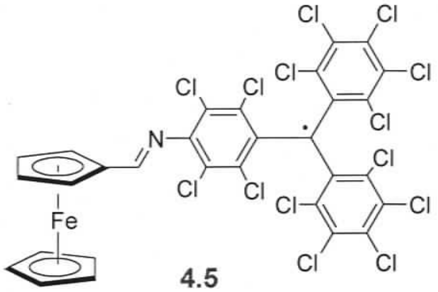
4.5

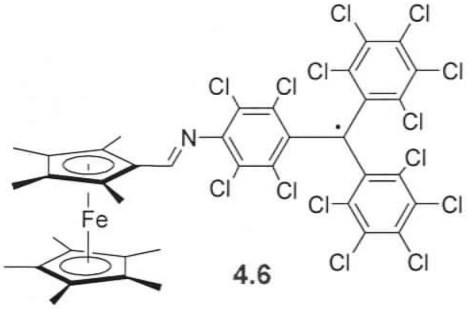
4.6

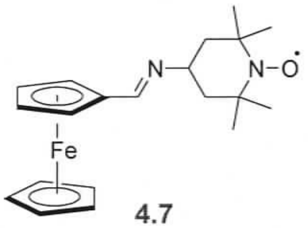
4.7

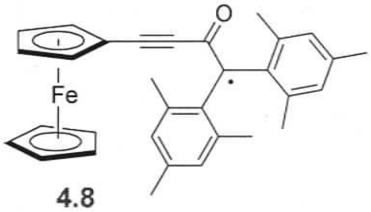
4.8

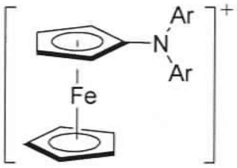
4.9

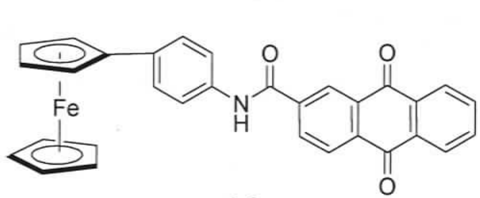
4.9

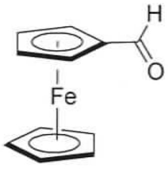
4.11

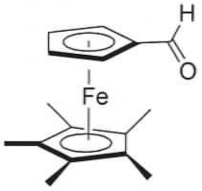
4.12

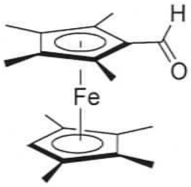
4.13

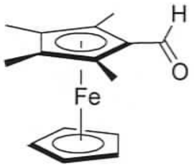
4.14

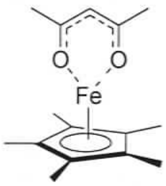
4.15

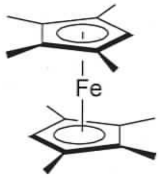
4.16

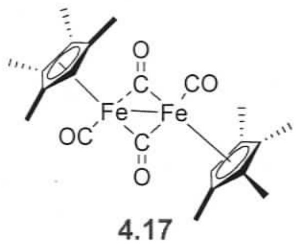

4.17

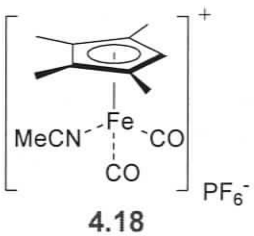

4.18

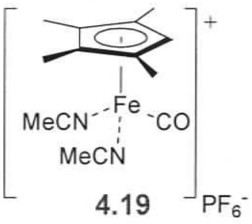

4.19

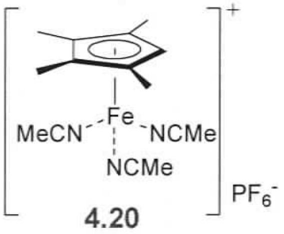

4.20

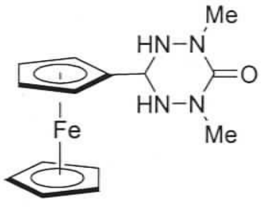

4.21

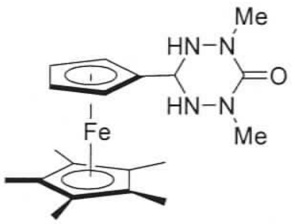

4.22

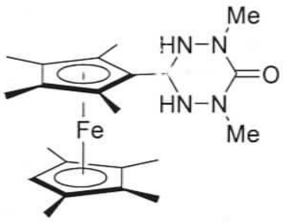

4.23

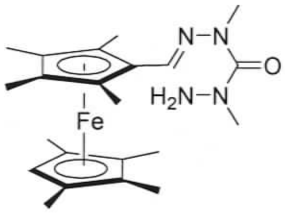

4.24

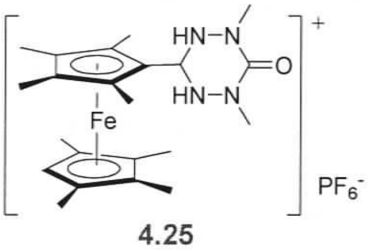

4.25

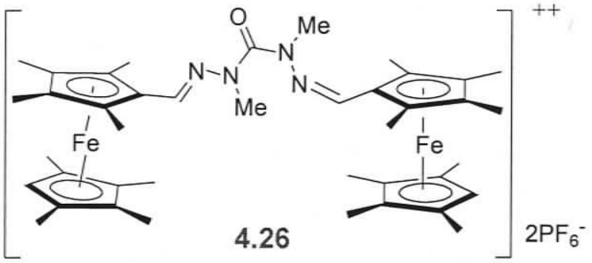

4.26

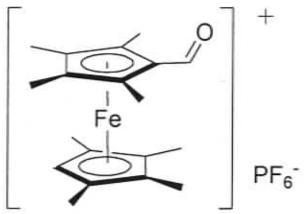

4.27

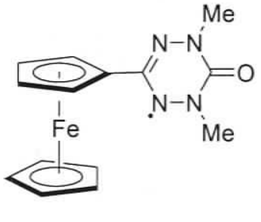

4.28

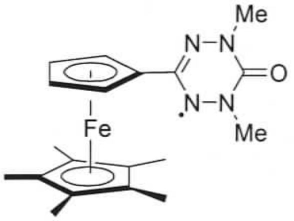

4.29

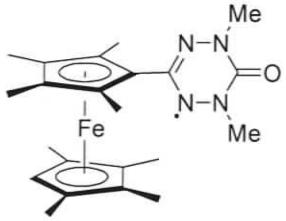

4.30

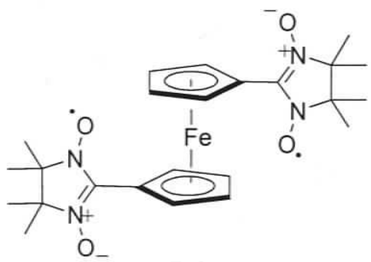

5.1

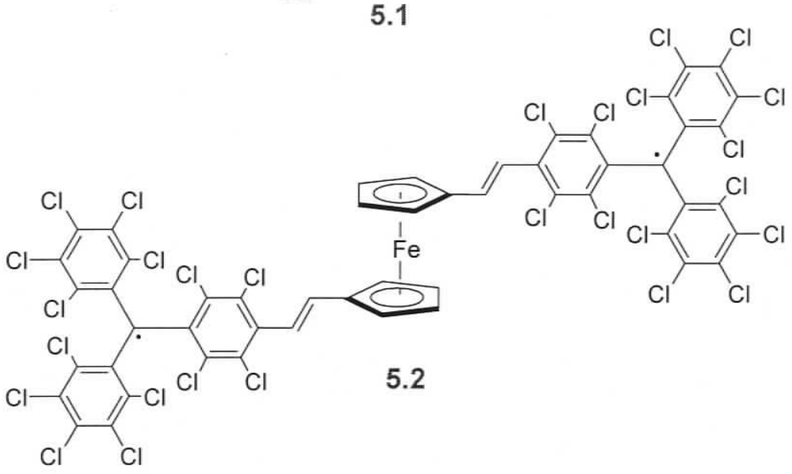

5.2

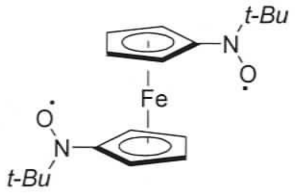

5.3

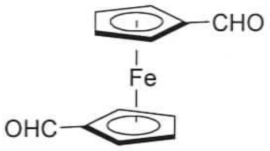

5.4

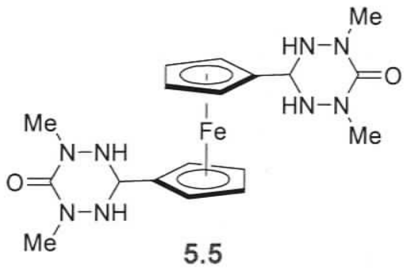

5.5

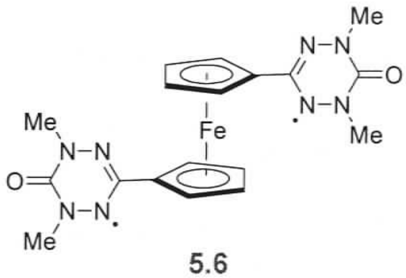

5.6

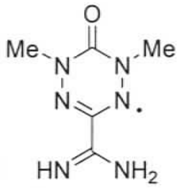

6.1

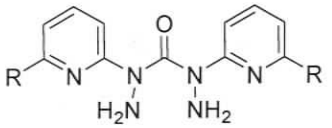

6.2

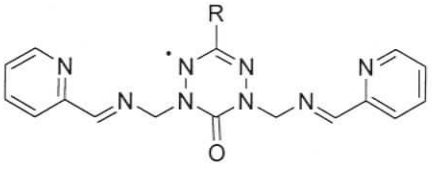

6.3

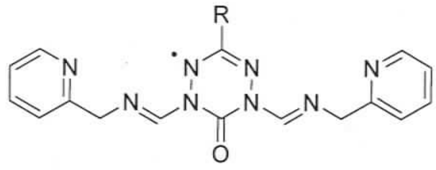

6.4

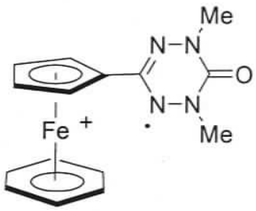

6.5

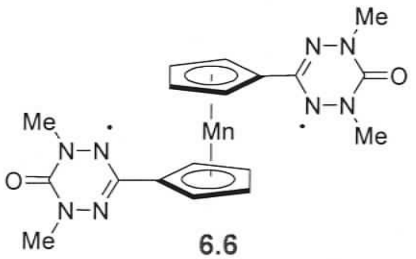

6.6

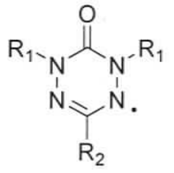

6.7

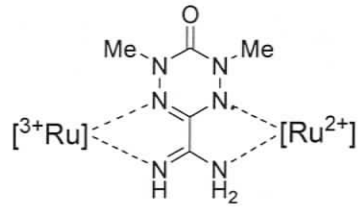

6.8

LIST OF ABBREVIATIONS

1D	one-dimensional
2D	two-dimensional
3D	three-dimensional
a	hyperfine coupling constant
A	absorbance
Å	angstrom (10^{-10} m)
acac	acetylacetonate
AF, or AFM	antiferromagnetic
Ag/AgCl	silver/silver chloride reference electrode
Ar	aryl substituent
B	magnetic induction
B.	basic
bipy	2,2′-bipyridine
br	broad (IR and NMR peak descriptor)
$B_s(y)$	Brillouin function
Bu	butyl
Bu_4NBF_4	tetrabutylammonium tetrafluoroborate
Bz	benzo
C	Curie constant
CaH_2	calcium hydride
C_{60}	buckminsterfullerene
°C	degree(s) Celsius
CI	chemical ionization
cm	centimeter
CN	cyanide
Cp_2*	decamethyldicyclopentadienyl
CT	charge transfer
CTH	5,7,7,12,14,14-hexamethyl-1,4,8,11-tetraazacyclotetradecane
CuBr	copper(I) bromide
CV	cyclic voltammetry

d	doublet (NMR peak descriptor)
dd	doublet of doublets (NMR peak descriptor)
dec	decompose
DCM	dichloromethane
DDQ	dichloro-dicyanon-*para*-quinone
DFT	density functional theory
DMA	dimethylacetamide
DMF	dimethylformamide
d_6-DMSO	deuterated dimethylsulfoxide
DMSO	dimethylsulfoxide
DNP	dynamic nuclear polarization
DTBSQ	3,5-di-*tert*-butylsemiquinone
E	energy
EI	electron impact
emu	electromagnetic units (cm^3)
en	ethylenediamine
ELDOR	electron-electron double resonance
ENDOR	electron nuclear double resonance
E_{ox}	oxidation potential
EPR	electron paramagnetic resonance
E_{red}	reduction potential
ESI	electrospray ionization
Et	ethyl
eV	electron volt
Fc	ferrocene, or ferrocenyl
FM	ferromagnetic
FT-IR	Fourier transform infrared
fs	femtosecond(s) (10^{-15} s)
g	g-factor
G	gauss
GHz	gigahertz

h	hour(s)
H	magnetic field
H	spin Hamiltonian
HCl	hydrochloric acid
hfac	1,1,1,5,5,5-hexafluoroacetylacetonate
HMO	Hückel molecular orbital
HOMO	highest occupied molecular orbital
hq	hydroquinone
Hz	hertz
I	intensity
J	coupling constant (nmr), or magnetic exchange coupling constant
k	Boltzmann constant (1.3806580 × 10^{-23} J K^{-1} or 0.695 $cm^{-1}K^{-1}$)
K	exchange integral, degree Kelvin
kJ/mol	kilojoules per mole (83.5934612 cm^{-1})
L	litre
LG	leaving group
L_n	ancillary ligand
LMCT	ligand-to-metal charge transfer
LSIMS	liquid secondary ion mass spectrometry
LUMO	lowest unoccupied molecular orbital
m	multiplet or medium (NMR or IR peak descriptor)
M	magnetization
M	molarity
$M^{+\bullet}$	molecular ion
M^{-1}	inverse molarity
MCU	magnetic coupling unit
Me	methyl
mg	milligram
MHz	megahertz
min	minute(s)
mL	millilitre

MLCT	metal-to-ligand charge transfer
mmol	millimole
mNBA	*meta*-nitrobenzylalcohol
Mp	melting point
MS	mass spectrometry
$mV\ s^{-1}$	millivolt per second
m/z	mass/charge ratio
N	Avogadro's number ($6.0221367 \times 10^{23}\ mol^{-1}$)
N.	neutral
NIT	nitronyl nitroxide
nm	nanometer (10^{-9} m)
NMR	nuclear magnetic resonance
Oac	acetate
ORTEP	Oakridge thermal ellipsoid program
ox	oxalate
Ox	oxidizing agent
p	para
*p*BQ	para-benzoquinone
Ph	phenyl
ppm	parts per million
py	pyridine
q	quartet (NMR peak descriptor)
R	generic functional group
R	agreement factor
R_f	Retention coefficient (chromatography)
rbf	round-bottomed flask
RT	room temperature
s	singlet, strong, (NMR, IR peak descriptor) or standard
S	overlap integral
S	spin multiplicity
sh	shoulder

SCE	saturated calomel electrode
SOMO	singly occupied molecular orbital
SQUID	superconducting quantum interference device
t	triplet (NMR peak descriptor)
T	temperature, or Tesla
t-Bu	tertiary butyl
T_c	critical temperature
TCNE	tetracyanoethylene
TCNQ	7,7,8,8-tetracyano-*p*-quinodimethane
terpy	2,2′:6′,2″-terpyridine
tfac	1,1,1-trifluoroacetylacetonate
TIP	temperature-independent paramagnetism
THF	tetrahydrofuran
TLC	thin layer chromatography
T_{max}	temperature at the maximum of χ
TPP	*meso*-tetraphenylporphinato
TPV	triphenylverdazyl
UV	ultraviolet
V	volt
vs	very strong (IR peak descriptor), or versus
$V\ s^{-1}$	volt per second
vw	very weak (IR peak descriptor)
w	weak (IR peak descriptor)
β	Bohr magneton ($9.27401549 \times 10^{-24}$ J T^{-1}), or resonance integral
δ	parts per million
Δ	heat
ε	molar absorptivity (M^{-1} cm^{-1})
λ_{max}	wavelength of lowest energy electronic absorption
μ_{eff}	effective magnetic moment
θ	Weiss constant, or interligand dihedral angle
ρ	paramagnetic impurity factor

χ_g	gram magnetic susceptibility
χ_m	molar magnetic susceptibility
χT	product of the molar magnetic susceptibility with temperature

ACKNOWLEDGEMENTS

Learning how to become a research scientist is one of the reasons that I decided to pursue graduate studies. My belief at the time was that pursuing graduate studies at UVic would provide me the opportunity to improve as a researcher, teacher and student of chemistry. To this end, the faculty, staff and students have been either economically or intellectually encouraging throughout my tenure at UVic. In particular, I would like to thank Dave Berry for his enormous teaching support, and his countless altruistic hours spent providing graduate students with the opportunities to learn about chemical education. Furthermore, the faculty has provided me with numerous opportunities to get involved, and represent the department at various levels and functions. This endorsement from the faculty is very much appreciated. I have also learned a great deal from my fellow group members and grad students over the years but I would especially like to thank Mhamed, Joe, Christine, Manian, Steve, Dan, Horace, Kevin, Sharon, Bandy, Raj, Marty, Greg, Todd, Craig, Matt, Tamara, Dave, Kabir, Peter, Athena and Tyler for their intellectual support and friendship over the years.

Several collaborations were employed to obtain information about the structural, magnetic and electronic properties of the molecules presented in this thesis. X-ray structural determinations were performed by Dr. Michael Ferguson and Dr. Robert McDonald at the University of Alberta. Magnetic measurements were carried out by Prof. Laurence K. Thompson and his colleagues at the Memorial University of Newfoundland. Mössbauer spectroscopy and a limited number of magnetic measurements were carried out by Prof. William Reiff at Northeastern University. Some EPR investigations were carried out by Prof. Andrew Ichimura at San Francisco State University and Dr. Rob Reid at the University of Waterloo. I would like to acknowledge each of these collaborators, in particular Laurie Thompson for his valuable discussions relating to this work.

Lastly, I wish to acknowledge the efforts and support of my Ph.D. supervisor Prof. Robin Hicks. Robin's mentorship has provided me with nearly every opportunity to learn about interpreting, carrying out, and communicating science. Robin's patience and insight have truly been an inspiration. Thank you!

For those who have helped me get this far.
Especially, Ken, Brenda, Jason and Christine.
Thanks for everything!

Chapter 1: Introduction

1.1 Towards molecule-based magnets

The development of materials that exhibit new and unusual properties has become one of the premier goals of modern science. From the chemists perspective, design of novel materials is inspired by the physical properties exhibited at both the macroscopic and molecular level. Of the properties exhibited by matter, magnetism is one of the most fascinating.

At the macroscopic level, magnets are ubiquitous in our daily lives. Traditionally, most bulk permanent magnets have been made of metals, metal alloys, or metal oxides. Conversely, the field of molecular magnetism offers some possible advantages. The possibility exists to create new materials where the magnetic, chemical, and electronic properties could be tuned via external stimuli or by simply modifying the molecular subunits involved. This may lead to magnetic materials that are lightweight, transparent, more processable, or exhibit a hybrid array of magnetic, optical, or electronic properties. With such possible materials applications, there has been an explosion of interest in molecular magnetism over the past two decades.[1-5] These studies have led to an improved understanding of molecular magnetism and have improved strategies to assemble molecular magnets.

With vast advances in the field of molecular magnetism, there are still some challenges that must be overcome in order for these novel magnetic materials to be utilized in real-world devices. Most of the existing molecule-based magnets exhibit their magnetic properties at very low temperatures (<<100 K). For modern applications it will be essential to raise this magnetic ordering temperature (T_c) closer to room temperature. Theoretically there is no restriction preventing formation of room temperature magnetic materials. Therefore, the judicious choice of molecular subunit and assembly strategy is critical.

The current pursuit of new magnetic materials can be described as the science of finding new magnetic building blocks and/or ways of assembling them. A building block is a spin-bearing entity, such as a paramagnetic metal ion or organic-based radical.

'Assembly' refers to a method of piecing together molecular building blocks in order to have multidimensional control over the magnetic interactions between the adjacent spin-bearing units.

The field of molecular magnetism is multidisciplinary with its unique combination of synthetic and physical chemistry.[6] With advances in synthetic chemistry, molecular magnetism has expanded its repertoire of building blocks and assembly strategies. In the assembly of molecular-based magnets there are three major strategies; (i) paramagnetic metal ions bridged by diamagnetic ligands, (ii) crystal engineering of organic radicals, and (iii) paramagnetic metal ions bridged by organic radicals. Although each approach has been explored in some detail, it would appear that neither the use of diamagnetic ligands, nor the crystal engineering of organic radicals represents a viable pathway to molecular magnetism.

Cyanometallates[7-14] are the only example of coordination networks with diamagnetic ligands that have overcome[15] the room temperature barrier (T_c). Cyanometallates are extended structures based on Prussian blue[14, 16-18] that use cyanide as the diamagnetic bridging ligand. Although these cyanometallates are assembled using molecular components and synthetic chemistry techniques, the products are by no means molecular. Recent efforts to improve the tunability of these materials has led to photoinduced magnetic cyanometallates.[19]

At the other extreme, crystal engineering of organic radicals is tunable via the building block selection, but through-space exchange is generally weak and the approach lacks the multidimensional topological control needed to extend the magnetic interactions into multiple dimensions.

Perhaps the most promising route to molecular magnetism is to explore the utility of bridging paramagnetic metal ions with organic radicals. This approach may lead to enhanced magnetic exchange or novel electronic interactions between the spin bearing units. The remainder of this chapter will focus on the magnetic and electronic features of metal-radical assemblies and outline some of the more popular radical families that have been used in the study of molecular magnetism.

1.2 Magnetic exchange between spin bearing units

When Michael Faraday discovered electromagnetic induction in 1831, he revolutionized scientific understanding by providing a conceptual link between electricity and magnetism. Since Faraday's discovery, and the emergence and understanding of molecular magnetism, it is difficult to separate the notion of electronic versus magnetic communication. For the purpose of our discussions electronic interactions will refer to electronic redistribution, while magnetic interactions will be considered as the magnetic exchange between adjacent paramagnetic centres.

An important parameter used to evaluate magnetic communication between paramagnetic species is magnetic exchange (*J*). Although *J* is not the only quantity to be considered in the development of bulk magnetic materials, it is a very important value when developing molecular subunits because *J* quantitatively describes the nature and strength of the magnetic coupling between paramagnetic building blocks. This value quantifies the utility of combining various building blocks. Unlike the directly determinable T_c, the value of *J* is obtained from a fit to a mathematical model for the temperature-dependant magnetic susceptibility.

1.2.1 Magnetic exchange: The *J*-value

In order to realize utility as a magnetic material, a sample must possess the ability to generate a magnetic dipole when placed in an external magnetic or electric field. This implies that the sample will show a degree of magnetic susceptibility where the molar quantity is defined as;

$$\chi = \frac{M}{H} \tag{1.1}$$

Molar magnetic susceptibility, χ, is a function of the induced magnetic moment *M* of a sample when placed in a weak external magnetic field *H*. This susceptibility often has temperature dependence (*T*) that is shown in equation 1.2.

$$\chi = \frac{Ng^2\beta^2}{3kT}S(S+1) \tag{1.2}$$

N is Avogadro's number, g is the Landé g-factor for a free electron, β is the Bohr magneton, S is the total spin quantum number, and k is the Boltzmann constant. Equation 1.2 is also known as the Curie law and is generally written as shown in equation 1.3.

$$\chi = \frac{C}{T} \tag{1.3}$$

C is the Curie constant and assumes the constants of equation 1.2. The Curie law is one of the simplest of the expressions relating temperature to magnetic susceptibility.

The Curie-Law does not consider intermolecular interactions within the solid state of the material, and therefore a modification of this law is given in equation 1.4.

$$\chi = \frac{C}{T-\theta} = \frac{Ng^2\beta^2 S(S+1)}{3k\left(T - \frac{zJS(S+1)}{3k}\right)} \tag{1.4}$$

Equation 1.4, known as the Curie-Weiss Law, introduces a correction factor θ. Equation 1.4 presents two analogous forms of the Curie-Weiss Law which can use θ or zJ to describe the deviations from the Curie Law. θ is a semi-quantitative correction factor that is not based on structural information, but is a function of the interaction parameter, J, between z neighboring molecules. If J (or θ) is positive or negative the intermolecular interaction is said to be ferromagnetic or antiferromagnetic, respectively.

These intermolecular interactions, depending on the magnitude of J, manifest as strong differences in the low temperature regime of a χ vs T plot; however, as the temperature increases and overcomes the weak interactions depicted in Figure 1.1 all three sample curves go to similar high temperature limits, obeying the Curie law. The example where J (or θ) = 0 represents the Curie law of equation 1.3.

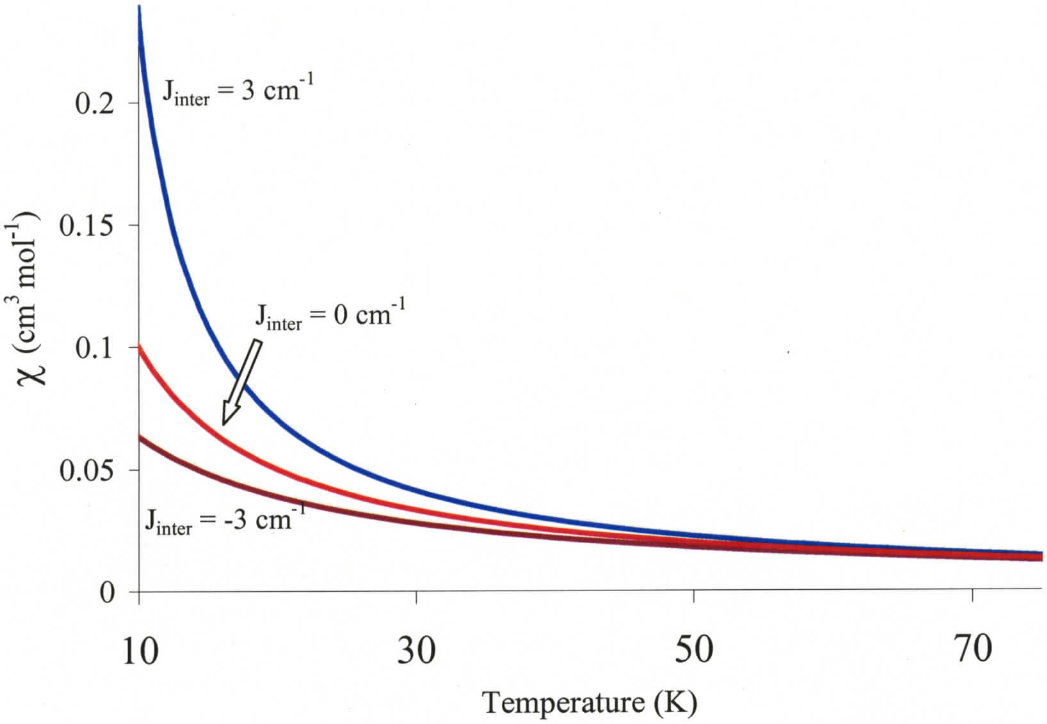

Figure 1.1 - χ vs T plot for systems that obey the Curie-Weiss Law (Equation 1.4) (C= 0.375 cm^{3}Kmol^{-1}; $g = 2.00$; $S = 1$; $z = 2$)

A more dominant contribution to temperature-dependant susceptibility occurs when the molecule under study possesses multiple paramagnetic centres and intramolecular interactions need to be considered. Due to their proximity within the molecule, intramolecular interactions are often much stronger than intermolecular interactions.

Consider the case of a two spin model with two possible ground states (Figure 1.2). A triplet ground state (a) suggests that the ground state of the molecule has two spins that are ferromagnetically aligned. The energy required to reach the singlet excited state is J_{intra}. Similarly a triplet excited state could be populated if energy, J_{intra}, is provided to the system possessing a singlet ground state (b). The sign of J_{intra}, whether it is negative or positive, implies that the ground state is either antiferromagnetically or ferromagnetically coupled, respectively.

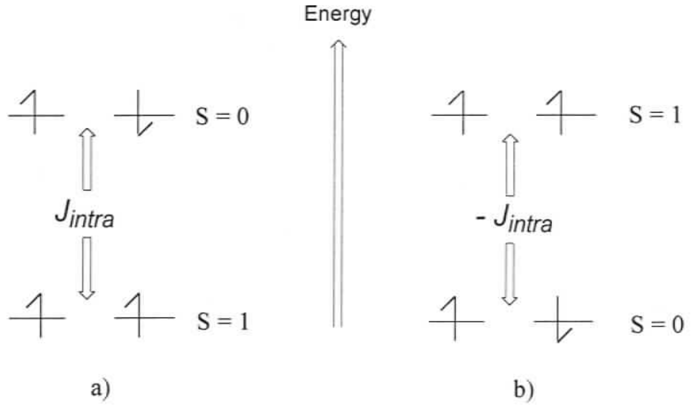

Figure 1.2 - Frontier Molecular orbitals in diradicals. a) triplet ground state, b) singlet ground state

This relationship between intramolecular exchange interactions and magnetic susceptibility for diradicals is given by the Bleaney-Bowers[3] equation, which is given in equation 1.4.

$$\chi = \frac{2Ng^2\beta^2}{(3kT + kTe^{(-J/kT)})} \tag{1.4}$$

Here J is referred to as a magnetic exchange parameter, and is a scalar constant that is inherent to the Heisenberg-Dirac-Van Vleck (HDVV) Hamiltonian (H) of the form;

$$H = -JS_A \cdot S_B \tag{1.5}$$

where S_A and S_B are local spin operators (in the case describe above, $S_A = S_B = ½$). This Hamiltonian yields eigenvalues that also contain J, representing the energy separation between spin states as depicted in Figure 1.2. Conceptually there is no difference between metal-radical exchange and radical-radical exchange.[20]

There are more complex models for susceptibility utilized for more complicated combinations of *inter-* and/or *intra*molecular interactions between paramagnetic components of a crystalline lattice. These models are specific and will be explained in future sections as required. Fitting magnetic data (χ vs T) to various models helps to determine the magnitude and sign (*ferro-* or *anti*ferromagnetic) of the magnetic exchange parameters.

1.3 Metal-radical complexes

1.3.1 General considerations

Of the approaches to molecular magnetism, the combination of organic radicals with transition metal ions is a very attractive methodology. From a basic research perspective, the coordination of paramagnetic metals with organic radicals is relatively new and little is known about the nature of these metal-radical interactions. From a materials perspective, the potential of using a wide range of organic building blocks and metal centres provides a high degree of diversity, which may lead to materials that are more easily tuned or perturbed chemically, electronically, photochemically, and/or magnetically.

From a synthetic point of view, another benefit of using paramagnetic transition metals as building blocks is that they possess a wide range of coordination geometries that are not available to exclusively organic structures. In addition they have a variable (depending on choice of metal used) number of unpaired electrons that can be aligned with the organic radicals to realize high spin molecules. Furthermore, the metal-radical approach to molecular magnetism can be systematically investigated using molecular species. Metals and radicals may be combined together resulting in a variety of lower dimensional structures, before the generation of 3D networks (Figure 1.3). For example, ancillary ligands can be added to make a 1D molecule or bimetallic species, or 2D grids and squares. This approach is extremely attractive, as it allows the researcher to study the properties of these materials in the solid state as well as in solution.

In order for the metal-radical approach[21] to yield molecular magnets with high critical temperatures, it requires that the organic paramagnet used; (i) be an effective ligand for transition or lanthanide metals, (ii) possess the ability to engage in strong magnetic exchange between the radical ligand and the metal, and (iii) be synthetically versatile so that it can serve as a building block with a variety of topologies. To this end, the preparation of metal-radical assemblies utilizes two common approaches. Either the radical can be connected indirectly to the metal centre using a diamagnetic spacer or the radical can be linked directly to the metal centre via a coordinative bond. Stronger magnetic interactions are typically observed when the radical is coordinated directly to the adjacent metal ion, thus the direct approach generally has stronger interactions than those observed when using the indirect approach.

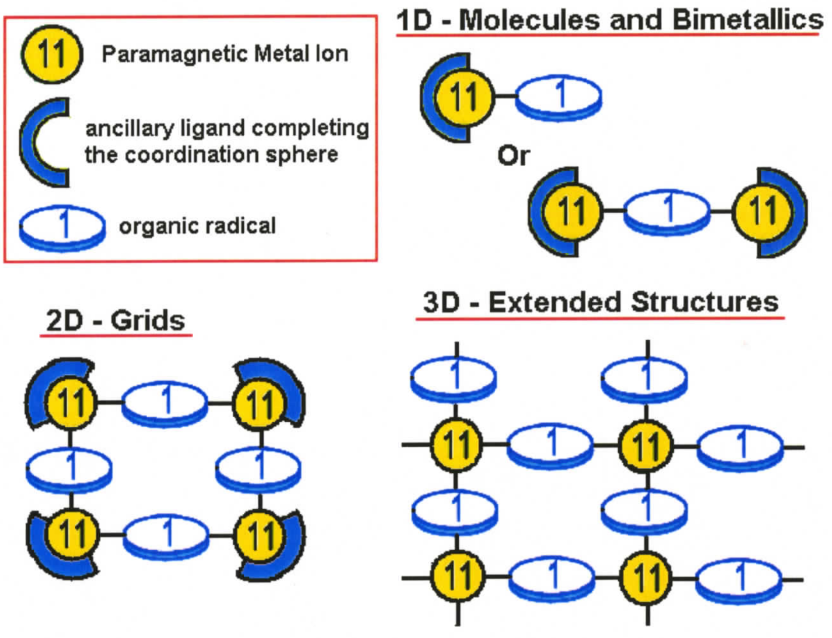

Figure 1.3 - Metal-Ligand strategies in the creation of higher order structures

1.3.2 Electronic interactions between metals and electroactive ligands

Radical ligands are electroactive and they exhibit some rather interesting electronic interactions in metal-ligand coordination complexes and assemblies. Although metal-radical assemblies have been extensively explored for their magnetic interactions, there are also several modes of ground state electronic communication that have been observed between transition metals and their corresponding electroactive ligands.

1.3.2.1 Classes of mixed-valence metal complexes

In the late 1960's a classification system was employed to organize the electronic communication observed in bimetallic mixed valent metal complexes. This electronic communication was classified into three categories based on the strength of the interaction between the redox centres.[22, 23] Class I mixed-valent systems have interactions that are extremely weak, or non-existent and therefore the two metals behave as isolated redox centres. Class III mixed valence species have electronic interactions that are so strong that the electron is completely delocalized over the entire molecule.

The final class of electron communication is the Class II mixed-valence systems, where the barrier to intermolecular electron transfer is small enough to be overcome by external thermal or optical stimuli.[24] The first type of class II metal complexes investigated were the bimetallic Creutz-Taube ions based on ruthenium metal ions bridged by pyrazine (**1.1**). Since the observation by Creutz and Taube[25-28] that there can be strong electron communication between metal centres via an aromatic spacer, a variety of homo- and heteronuclear species have been prepared. Most of these species are based on ruthenium or ferrocene complexes because they are stable and readily oxidized.[29, 30]

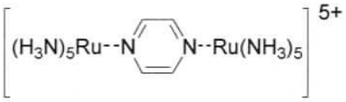

1.1

1.3.2.2 Non-innocent ligands

Although the above classification system was originally designed to describe bimetallic mixed valent species, it can also be applied to any set of two redox centres. Electroactive or non-innocent ligands can also be considered as redox active centres. Non-innocence is observed when metal-based and ligand-based redox orbitals are similar in energy, resulting in a variety of possible ground state electronic configurations.

An example of a redox-active metal-ligand complex that demonstrates isolated redox centres is $Ru(bpy)_3^{2+}$ (**1.2**). Although **1.2** contains metal and ligand components that can be reversibly oxidized and reduced, respectively, the energy barrier for electron transfer between the HOMO on the metal and the LUMO of the ligand is too large to overcome. Therefore, bipyridine would be considered as an innocent ligand in this complex.

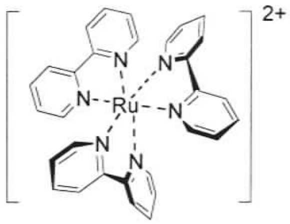

1.2

An example of a non-innocent ligand can be seen in the dithiolene series. In the early 1960s a series of planar dithiolene complexes of the noble metals[22] was prepared, and it was extremely difficult to assign formal oxidation states to the metal and ligand components. In Figure 1.4 the three possible resonance structures for these metal complexes are given. The notion that there were three possible resonance structures suggested that the ligand was engaged in what is now referred to as non-innocent behaviour.[31-34]

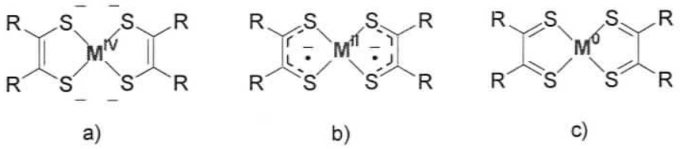

Figure 1.4 - Three possible resonance structures for diamagnetic dithiolene complexes; where the two radical mono-anions are aligned antiferromagnetically in b)

1.3.2.3 Valence Tautomerism

When non-innocent ligands are combined with transition metals possessing multiple accessible oxidation states, it is possible to observe a subclass of metal-ligand electronic interactions known as valence tautomerism.

Valence tautomerism requires that the coordination complexes have two (or more) distinct and nearly degenerate electronic structures. As the word tautomerism suggests, the distribution between these electronic isomers is an equilibrium process that can be perturbed using a variety of stimuli including light, temperature, or pressure. Although valence tautomerism has been primarily studied using the dioxolene series of electroactive ligands, it can conceptually take place using any electroactive ligand as depicted in Figure 1.5.

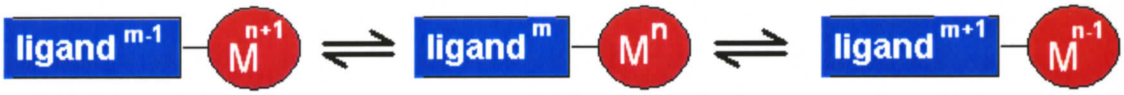

Figure 1.5 - Valence tautomerism using electroactive ligands

Valence tautomerism has received a great deal of attention because of its possible application in molecular switching.[35] The ability of these molecules to serve as switches, using the aforementioned equilibrium shifting stimuli, has resulted in molecules that can thermally interconvert between low and high spin molecules. Although there are several other electroactive ligands that can undergo valence tautomerism,[23] the dioxolene complexes (discussed further in section 1.4.3) have been most successfully utilized because they satisfy three basic requirements. In order for an electroactive ligand to be involved in valence tautomerism, 1) the ligand must exhibit a high degree of stability in its various oxidation states, 2) the covalent nature between the metal and ligand must be low enough to allow electron redistribution, and 3) the energy difference between the frontier orbitals of metal ion and ligand must be low.

1.3.3 Stable radical families

In order to create materials based on organic radicals the radicals must be stable. The radical must be stable enough to be prepared, isolated, characterized and thermally stable for the desired application. Unfortunately there are very few radical systems that possess suitable thermal stability, and even fewer with the ability to coordinate to a metal ion.

Since Gomberg's discovery of the triphenylmethyl radical,[36] several stable families of stable radicals have been discovered. The list of radicals presented in Figure 1.6 is by no means exhaustive, but it does present a sample of the organic radicals that have been explored for potential applications in molecular magnetism.

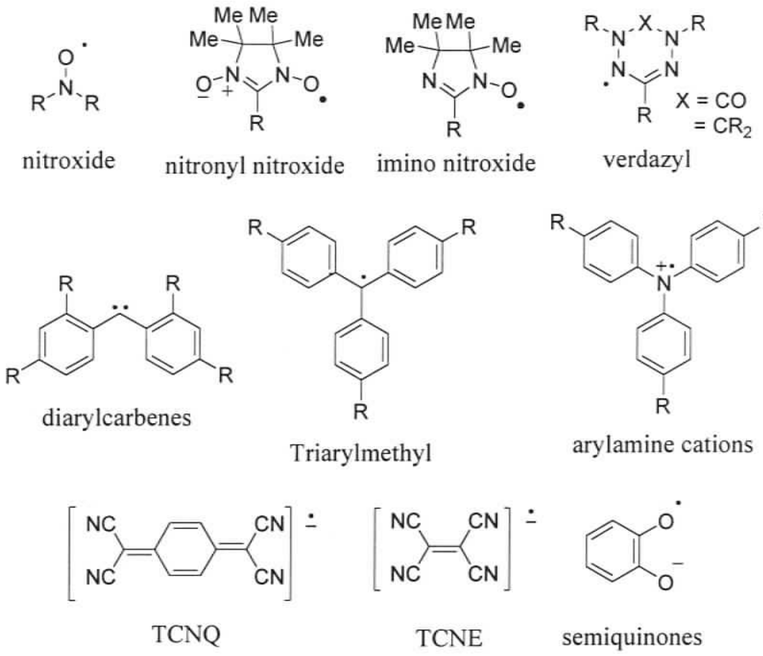

nitroxide nitronyl nitroxide imino nitroxide verdazyl

diarylcarbenes Triarylmethyl arylamine cations

TCNQ TCNE semiquinones

Figure 1.6 - Organic radical families explored as molecular magnet building blocks

Radicals can be either charged or neutral. The arylamine cation, TCNQ, TCNE, and semiquinone anion are examples of charged species and the remainder are neutral radicals. Of the families of radicals that have been explored for their metal-radical interactions, the polynitriles (TCNQ and TCNE), quinones, and nitroxides have received the most attention. These popular magnetic building blocks are discussed in more detail in section 1.4.

1.4 Radicals as Ligands

1.4.1 Polynitrile radical anions

Fundamental studies on the coordination chemistry of polynitriles has been reviewed by Kaim,[37] but the majority of the magnetic investigations have been carried out by Miller and coworkers.

In the 1980's, Miller and coworkers[38-41] observed low temperature magnetic ordering[42, 43] in a series of ferrocenium-polynitrile charge transfer complexes. In these original polynitrile complexes, the polynitrile radical anion ligand was not coordinated to the metal. However, this work was extended to include a variety of metallocenes which serendipitously led to the discovery that polynitriles could be chelated to metal ions in order to achieve room temperature metal-radical based magnets. In 1991 Miller and coworkers reported the first room temperature molecule-based magnet with an ordering temperature above the decomposition temperature of the material (T_c>350 K)[44]. The magnet is a complex of vanadium(II) with TCNE and has the empirical formula of $V(TCNE)_x \cdot yCH_2Cl_2$ where x ~ 1 and y ~ 0.5. The vanadium TCNE complex was formed at room temperature by combining $V(C_6H_6)_2$ and TCNE. Unfortunately, the magnetic material is pyrophoric, and its amorphous nature has prevented the solid state structural determination. Without the structural information a complete understanding of the magnetic behaviour is not possible. Miller has suggested that the vanadium TCNE complex is a three-dimensional network, with each vanadium(II) centre surrounded by up to six ligands, and the TCNE binding up to four different vanadium(II) ions.[45]

Miller and coworkers have also extended their own investigations by combining TCNE with a variety of other transition metals resulting in the general formula $[M^{II}(TCNE)_2]\cdot 0.5CH_2Cl_2$, where M^{II} = Mn, Fe, Co, and Ni. In general these complexes display very complex and poorly understood magnetic behaviour, but many do magnetically order, albeit at much lower temperatures (T_c<125 K). Since Miller's initial discovery similar complexes using other polynitrile acceptors, such as TCNQ, have also been investigated.[46, 47]

With a poor understanding of the magnetic interactions within the TCNE-based materials, Miller and coworkers prepared and structurally characterized a 1D coordination polymer by combining a metalloporphyrin unit (**1.3**) and TCNE.[45] By thoroughly studying the 1D interactions the authors hoped to develop a structure–function relationship that could be used to rationalize the 3D interactions in the other TCNE magnetic materials. This 1D coordination polymer (Figure 1.7) bearing the formula $[Mn^{III}TPP]^{+}[TCNE]^{\cdot -}$ (TPP = *meso*-tetraphenylporphinato) was determined to be a ferrimagnet with T_c of 14 K. A number of derivatives with the same 1D magnetic behaviour have been prepared,[48-50] and in each case the interchain interactions are only significant at low temperatures.

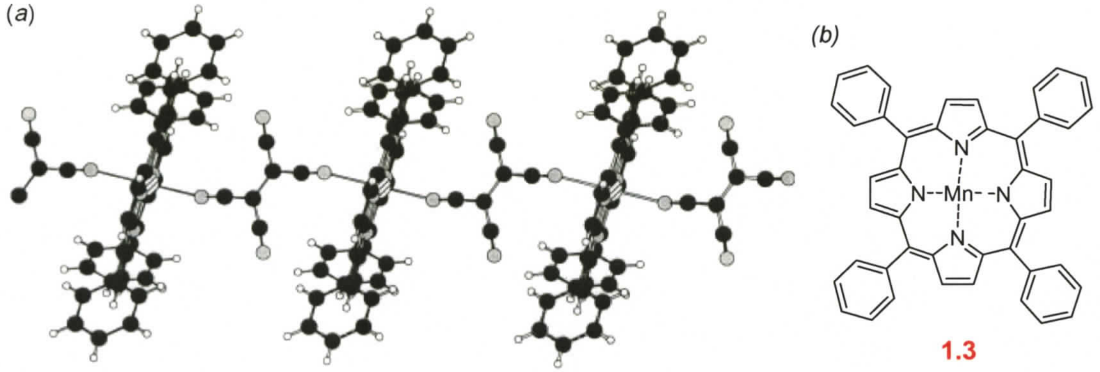

1.3

Figure 1.7 – (a) 1D coordination polymer of [Mn^{III}TPP]$^+$[TCNE]$^{-\cdot}$, and (b) the Mn(TPP) subunit. Crystal structure reproduced with permission from *Chem. Comm.* **1998,** 1319-1325. Copyright 1998 Royal Society of Chemistry.

Although many studies have shown the utility of polynitrile radical anion complexes, the interactions between the metal and radical anions are generally weak, and poorly understood. In the cases of the polynitrile anions that demonstrate high temperature magnetic ordering, the structures are not known, and little is understood about the intermolecular magnetic interactions. This lack of understanding has led to the study of other metal-radical complexes to investigate the nature of metal-radical interactions.

1.4.2 Nitronyl Nitroxides

Although the coordination chemistry of anionic radicals has been well established,[51] the study of metal-radical interactions involving neutral radicals has been less studied. Of the neutral stable radicals, nitroxides and their related nitronyl nitroxides are perhaps the most studied class of spin-bearing ligands. Both the direct and indirect metal-radical interactions have been investigated using the nitroxide family of ligands

1.4.2.1 Direct magnetic interactions

The first nitronyl nitroxide coordination complexes were described in 1977[52]. Since then much of the work in the field of the metal-radical approach using nitronyl nitroxides has been pioneered by Gatteschi and coworkers.[21] A large series of nitronyl nitroxide ligands has been prepared (Figure 1.8), and their metal-radical interactions explored.[53, 54] The first observation in these systems is that the metal-radical exchange is generally quite strong, and in the case of the octahedral complexes **1.4** and **1.5** antiferromagnetic. The strength of the interaction is consistent with the notion that these spins have good molecular orbital overlap with the metal owing to their close contact.

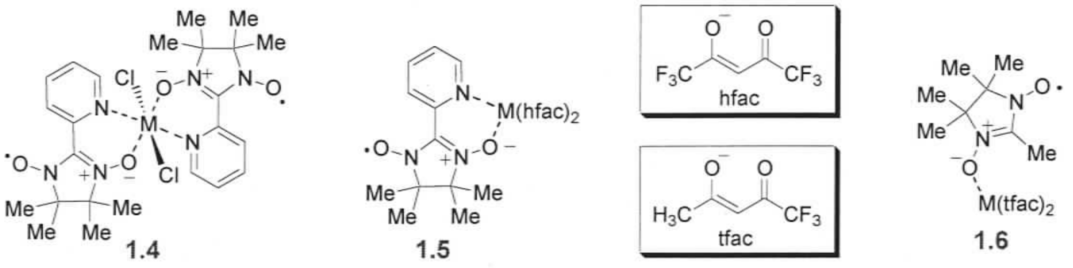

1.4 **1.5** **1.6**

M = Mn(II); J = -158 cm^{-1}
M = Ni(II); J = -220 cm^{-1}

M = Mn(II); J = -130 cm^{-1}
M = Ni(II); J = -334 cm^{-1}

M = Cu(II); J = 65 cm^{-1}

Figure 1.8 - Direct exchange in nitroxide metal complexes

To a first approximation, the $d_{x^2-y^2}$ and d_{z^2} orbitals are degenerate in octahedral complexes. Both Mn(II) and Ni(II) have unpaired electrons in these orbitals. The bidentate nitroxide ligand has two points of contact with the metal centre in **1.4** and **1.5.** There exists a d-σ overlap with the 2-pyridyl nitrogen and a d-π overlap between the metal and the nitronyl nitroxide oxygen. It can be safely assumed that the predominant spin density is localized on the nitroxide oxygen. As such, there is a mechanism for direct orbital overlap between the nitroxide oxygen and metal unpaired electrons.

The tenets of orbital orthogonality predict that the magnetic exchange will be ferromagnetic if there is no overlap between the metal orbitals possessing the unpaired electrons and SOMO of the ligand; this is essentially an extension of Hunds rule. If there is orbital overlap between singly occupied metal orbitals and the radical SOMO, then the exchange will be antiferromagnetic. The $d_{x^2-y^2}$-π orbital overlap provides a mechanism for molecular orbital overlap, and hence antiferromagnetic exchange is observed ($J<0$).

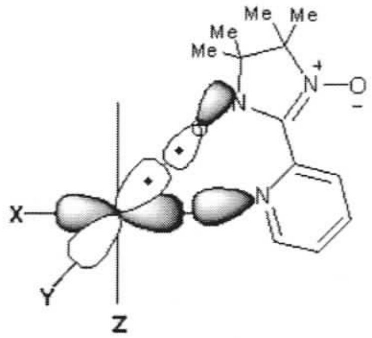

Figure 1.9 - Metal – radical orbital overlap that is responsible for antiferromagnetic exchange in octahedral complexes (**1.4** and **1.5**)

While the nature of the interaction is explained using the tenets of orbital orthogonality, the magnitude of *J* represents the degree of orbital overlap between the metal and radical. Therefore the bond lengths and angles about the metal centre are very important. In both **1.4** and **1.5**, the Ni-O (nitroxide) bond (2.06Å and 2.03Å, respectively) is shorter than the Mn-O (nitroxide) bond (2.16Å and 2.14Å, respectively), which suggests that there is a greater degree of metal-nitroxide overlap in the Ni(II) analogues resulting in a significant difference between the respective exchange values. Generally speaking, nitronyl nitroxides are not particularly strong ligands, and as such there are several steric and electronic influences that affect the strength of the metal-radical magnetic exchange. Sterics of an ancillary ligand may cause conformational changes in the radical, and hence the degree of orbital overlap may be altered. Furthermore, the interaction with the metal centre depends strongly on the nature of the ancillary ligand used. This may result in an increase or decrease in bond length, resulting in reduced or increased orbital overlap, altering the magnitude of *J*.

The copper nitroxide complex **1.6** (Figure 1.8) shows a weaker, but ferromagnetic metal-radical interaction. The ligand field about the metal centre is best described as square pyramidal. To a first approximation the $d_{x^2-y^2}$ metal orbital is the highest energy frontier orbital in square pyramidal systems, and Cu(II) with a d^9 electron configuration has one unpaired electron residing in the $d_{x^2-y^2}$ orbital. This nitronyl nitroxide is no longer bidentate, and as a result has only one point of contact with the metal centre involving d-π orbital overlap. The tfac ancillary ligands occupy the xy plane of the metal and the nitroxide-metal dative bond involves the metal d_{z^2} orbital. Although geometric distortion may lead to a slight projection of orbital overlap on the xy plane, the unpaired electron on the metal and radical are essentially orthogonal and this favours ferromagnetic alignment between spins. The weaker strength of the interaction may be due to an elongated (2.30 Å) Cu-O (nitroxide) bond. Figure 1.10 depicts the bonding axis in this copper-nitroxide complex.

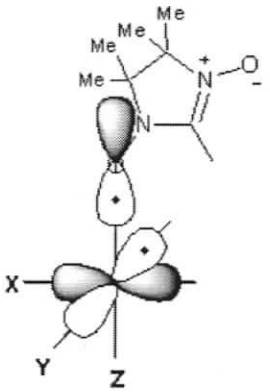

Figure 1.10 - Metal – radical orbital overlap that is responsible for ferromagnetic exchange in **1.6**.

Nitronyl nitroxides **1.7** and **1.8** have also been prepared.[55] These imidazole based radicals have the potential to form anionic bis-bidentate ligands upon deprotonation of the imidazole hydrogen. Although imidazoles are not as common as pyridyl substituents in coordination chemistry, Rey and coworkers have been able to successfully coordinate the neutral ligand to create monometallic coordination complexes using a variety of transition metal (Mn, Cu, Co, Ni, and Zn)[56] and lanthanide (Eu, Gd, and La)[57-59] ions. With the exception of Cu(II), all monometallic imidazole nitronyl nitroxide complexes have antiferromagnetic ($-111\text{cm}^{-1} < J < -53\text{cm}^{-1}$) metal-radical interactions. These antiferromagnetic interactions are a result of direct orbital overlap between the SOMO and metal d-orbitals, similar to the previously discussed pyridyl substituted analogues. Cu(II), on the other hand, is octahedral, but Jahn-Teller distorted resulting in the orthogonality between the π-SOMO of the radical and the metal $d_{x^2-y^2}$ orbital. The result is a metal-nitroxide ferromagnetic interaction of $J = 75\text{cm}^{-1}$.[55]

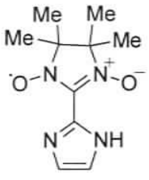

1.7

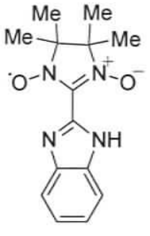

1.8

More recently investigations have focused on using ligands **1.7** and **1.8** to generate coordination polymers. Upon coordination of the anionic ligand to a Mn (II) metal centre, Rey and co-workers have been able to prepare one-dimensional coordination polymers[60] and two-dimensional honeycomb-like extended structures.[61] Despite antiferromagnetic interactions between metal and radical fragments, this coordination polymer strategy results in the extended structure having metal-nitroxide moments that are non-compensating, resulting in weak ferrimagnetic behaviour.

The highest T_c metal-nitroxide complexes have been prepared and studied by Iwamura and co-workers.[62-64] Iwamura investigated two multitopic polynitroxide ligands, **1.9** and **1.10**, where both ligands possess the desired topology to form 3D coordination polymers. It was found that both **1.9** and **1.10** formed 3D networks when coordinated to $Mn(hfac)_2$, but owing to the weak intramolecular exchange coupling ($J_{intra} = +4.7\ cm^{-1}$) in triradical **1.10** the T_c was merely 3.4 K. However, the 3D network formed with ligand **1.9** had a T_c = 46 K, owing largely to a much stronger intramolecular exchange coupling ($J_{intra} = +167\ cm^{-1}$) in triradical **1.9**.

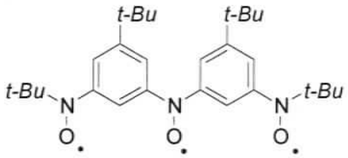

1.9

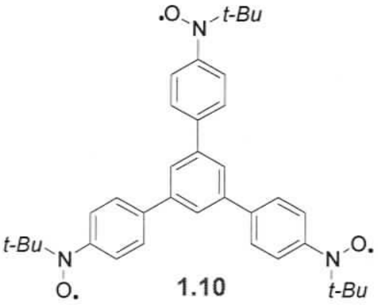

1.10

1.4.2.2 Indirect magnetic interactions

Another possible approach to realizing magnetic molecules is the indirect combination of metals and radicals through a conjugated spacer (Figure 1.11). Unlike direct metal-radical magnetic interactions, indirect magnetic interactions are a result of delocalization of the spin density onto the conjugated spacer. This π-spacer then serves as a magnetic bridge between the metal and radical. The effect that rationalizes spin density redistribution onto the diamagnetic spacer is known as spin polarization.

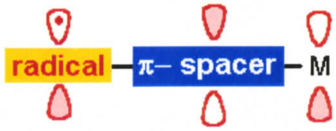

Figure 1.11 - Indirect magnetic interaction through a conjugated spacer

At the Hückel level the π-SOMO of the nitronyl nitroxide radical has a nodal plane running through the radical that prevents spin density from 'leaking' out onto the substituents (Figure 1.12). However, spin polarization leads to a small, yet significant, negative spin density on the substituent atoms. Spin polarization results from mixing of the SOMO with the next highest occupied molecular orbital, or with the next-lowest unoccupied molecular orbital resulting in new electronic configurations. This mixing of molecular orbitals results in a spin density distributed on the π-spacer in an alternating fashion. The 4-pyridyl substituted nitronyl nitroxide radical has a spin polarized electronic structure that is shown in Figure 1.12. The 4-pyridyl substituent is one of the simplest ligating moieties, but it has a slightly larger spin density on the pyridyl nitrogen due to the electronegativity of this heteroatom.

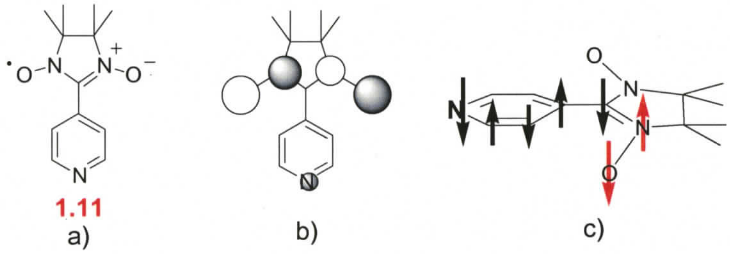

1.11
a) b) c)

Figure 1.12 – Effects of spin polarization on the electronic character of substituted nitroxides; a) phenyl-substituted nitronyl nitroxide, b) nodal plane through the nitroxide π-SOMO, c) electron delocalization via spin polarization.

Although indirect interactions allow for greater radical and topological diversity, generally speaking, it is expected that ligating a radical indirectly will result in weaker interactions than the direct interactions because there is significantly less spin density on the coordinating atom. Gatteschi and coworkers prepared a variety of metal-radical complexes based on **1.12**,[65, 66] and the metal-radical interactions were significantly weaker than the directly coordinated nitroxides. Antiferromagnetic coupling is observed for the octahedral copper(II) and nickel(II) ions which possess unpaired electrons in orbitals of σ-symmetry ($d_{x^2-y^2}$ and d_{z^2}), while ferromagnetic interactions were observed for manganese(II) which has unpaired electrons in orbitals of both σ- and π-symmetry.

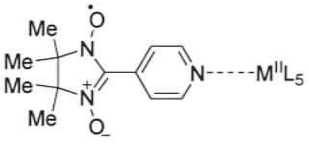

M = Mn, J = 1 cm^{-1}
M = Ni, J = -10 cm^{-1}
M = Cu, J = -20 cm^{-1}

1.12

Gatteschi and coworkers surmised that there are two possible mechanisms that help to rationalize the antiferromagnetic behaviour observed in the Ni(II) and Cu(II) complexes. By looking at the symmetry of the frontier orbitals (Figure 1.13) it is possible to rationalize these mechanisms further.[66] The spin on the pyridyl nitrogen has a small component of σ-symmetry and therefore has a non-orthogonal overlap with the unpaired electrons on the metal centres. If this is recast in the superexchange formalism, it can be shown that the HOMO has significant σ-symmetry and provides an alternative mechanism for antiferromagnetic alignment.

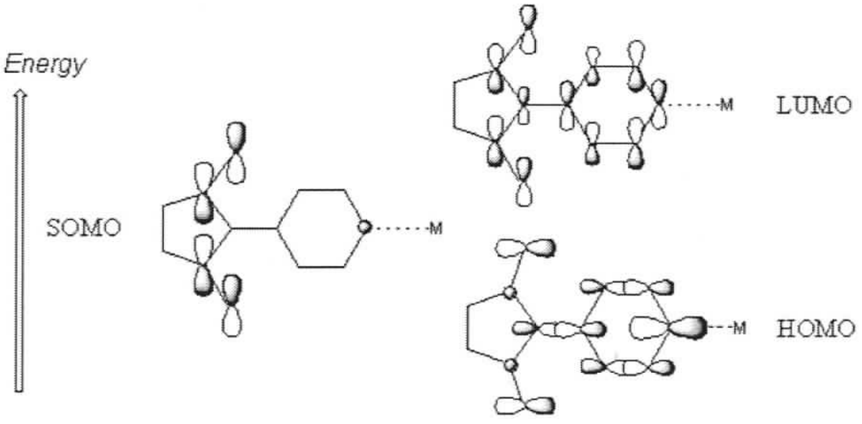

Figure 1.13 - Calculated frontier molecular orbitals of 4-pyridyl nitroxides.[66]

The one exception to this antiferromagnetic exchange is the manganese complex where there exist three orthogonal interactions to coincide with two non-orthogonal interactions, where each of the metal frontier orbitals possess one unpaired electron. It is possible to attribute the weak ferromagnetic interaction in Mn(II) to 3 ferromagnetic exchange pathways that overcome the two antiferromagnetic components.

More recently terpyridine analogues of the 4-pyridyl nitroxides have been prepared.[67] In this case, the addition of two ligating pyridyl groups should not have large effects on the spin distribution on the pyridyl ring adjacent to the nitroxide. The magnitude and directionality of J suggests that there are no significant differences between these terpyridyl analogues and their predecessors. The small differences in magnitude of the interaction could be rationalized by modest variations in bond lengths and angles between the metal centre and the ligating nitrogen.

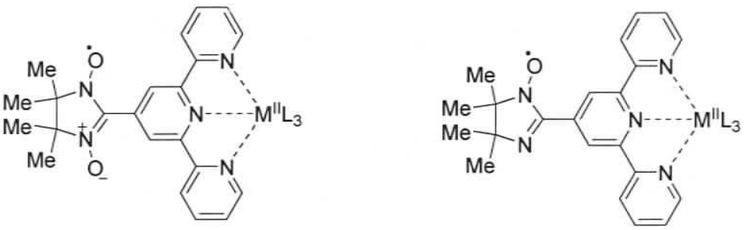

1.13

M = Ni, J = -13.7 cm^{-1}
M = Cu, J = -16 cm^{-1}

1.14

M = Ni, J = -4 cm^{-1}

Figure 1.14 - Terpyridyl nitroxide radical-metal complexes

1.4.3 Semiquinone radical anions

1.4.3.1 Electroactive considerations

Similar to the dithiolene ligands, the dioxolene-based ligands are electroactive and participate in non-innocent coordination behaviour. The dioxolene series (X=Y=O, Scheme 1.1) can exist in three oxidation states, the quinone (a), semiquinonate (or semiquinone, b) and catecholate (c). Wieghardt and coworkers[31-34, 68-73] have thoroughly studied the X=NR, Y=O imino-benzoquinonato-metal complexes to find that many factors (bond lengths, counterions, and ancillary ligands) can affect the communication between ligand and metal centre.

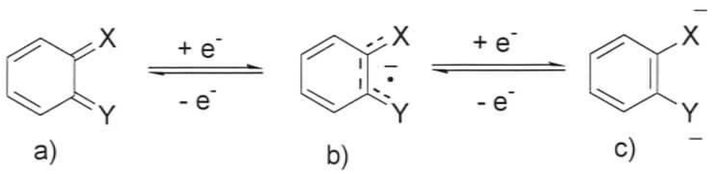

Scheme 1.1 – The electroactive dioxolene redox series

Fundamental studies on the coordination chemistry of the semiquinones has been reviewed by Pierpont[74, 75] and Kaim.[51] Due to the small energy difference between the LUMO of the catecholate ligand and the HOMO of transition metal ions, this system undergoes non-innocent behaviour in the form of valence tautomerism. The cobalt semiquinone complex **1.15** is an example of valence tautomerism where an anionic radical ligand is generated from a diamagnetic catechol ligand upon electron transfer.

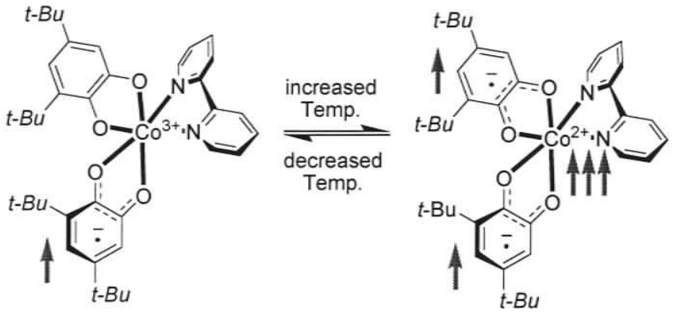

1.15a

1.15b

Scheme 1.2 – Valence tautomerism observed in a cobalt semiquinone complex. **1.15a** is low spin Co complex where S = ½ and **1.15b** is a high spin Co complex where S = 2.

As the temperature is raised, **1.15b** becomes a more dominant component of the equilibrium mixture. The change in the cobalt oxidation state is also coupled to a spin crossover phenomenon. The interconversion observed in Scheme 1.2 is entropy driven, where large gains in entropy arise from a gain in electronic entropy as a result of generating a degenerate high spin state on the cobalt ion. Furthermore, increased metal-ligand bond lengths increase the vibrational entropy of the molecule.[23]

1.4.3.2 Magnetic Considerations

In the late 1980's two semiquinone-based metal complexes were prepared that demonstrated quinones could be used effectively in the metal-radical approach. In both cases, DTBSQ (3,5-di-*tert*-butyl-o-semiquinonato-) was the quinone under investigation with polyamines used as ancillary ligands. Kahn and coworkers reported a four-coordinate Cu(II) DTBSQ complex (**1.16a**) that exhibited strong ferromagnetic coupling with J = 200 cm^{-1}.[76] Following this result Gatteschi and Dei reported very large intramolecular metal-radical exchange coupling in an octahedral Ni(II) DTBSQ complex (**1.16b**).[77] The observed exchange coupling between the metal and radical was so strong that the ferromagnetic quartet state was the only state thermally populated at room temperature. A lower limit of the magnetic exchange parameter was estimated as J = 400 cm^{-1}.

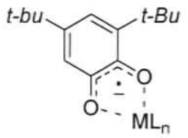

1.16a; M = Cu(II)
1.16b; M = Ni(II)

Similar to the nature of the magnetic interactions observed in the metal-nitronyl nitroxide complexes, the sign and magnitude of the exchange coupling of this direct exchange interaction can be easily rationalized on the basis of orbital symmetry. The unpaired electron of the semiquinone radical anion is located in an orbital having π-symmetry. The octahedral nickel complex **1.16b**, the metal centre has two unpaired spins in d-orbitals (d_{z^2} and $d_{x^2-y^2}$) of σ-symmetry. Therefore ferromagnetic exchange results, because there is no quantum mechanical overlap between the SOMO π* orbital of the radical and the metal orbitals possessing the unpaired electrons. In the distorted square planar copper case **1.16a**, the metal centre has one unpaired electron in a d-orbital of σ-symmetry, thus orbital orthogonality dictates that the interaction is ferromagnetic. The magnitude of both interactions is related to the direct nature of the exchange, where the ligating oxygen atoms have a large degree of spin density resulting in strong interactions between the radical and metal ion. The smaller magnitude of the copper-radical exchange is most likely due to either the poorer metal-semiquinone overlap or to the fact that the orthogonality between the molecular orbitals of the paramagnetic centres is less rigorously maintained.

Although semiquinones ligated to paramagnetic metal ions show strong ferromagnetic exchange, semiquinones capable of bridging two or more metal ions have received considerably less attention. Current semiquinone research involves the creation of multidentate semiquinone polyradical ligands. To this end, Shultz and coworkers have prepared several ligands[78, 79] that are capable of chemically and magnetically bridging two or more transition metal centres. These ligands have been designed such that the intraligand and metal-radical interactions are both ferromagnetic (Figure 1.15).

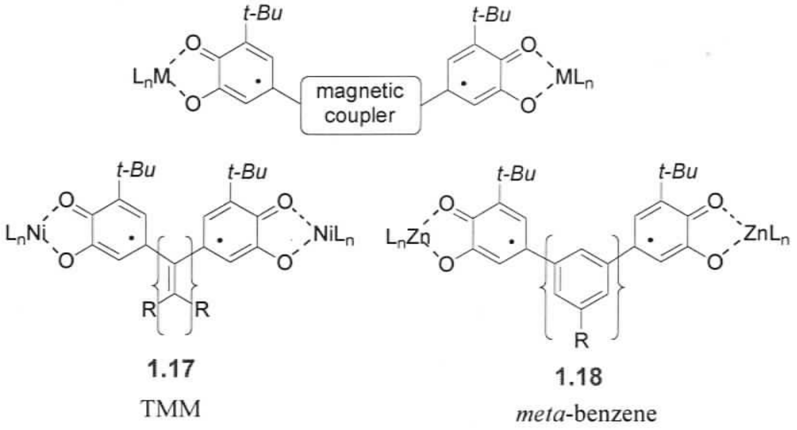

1.17
TMM

1.18
meta-benzene

Figure 1.15 - Magnetic coupling units used in bridging semiquinone diradical ligands

Using *meta*-benzene as a magnetic coupling unit (MCU), a diradical ligand coordination complex has been prepared using octahedral Ni (II) (**1.17**, with polyamine ancillary ligands). This system has very strong ferromagnetic metal-radical coupling ($J_{met-rad} > +400$ cm^{-1}) and ferromagnetic coupling between the two spins on the bridging ligand ($J_{intra} = +27$ cm^{-1}). Although *meta*-benzene is a common ferromagnetic coupling unit, the intraligand exchange that it mediates is relatively weak in comparison to the metal-radical exchange. To improve this intraligand exchange Shultz and coworkers[80] have extended their studies to include trimethylenemethane (TMM) as a MCU (**1.18**). Through selective modification of the R-groups in the TMM spacer, Shultz has been able to increase the magnitude of the intraligand exchange to $J_{intra} = +210$ cm^{-1}.

Semiquinone ligands are promising candidates for magnetic materials, owing to their strong metal-ligand and intraligand magnetic interactions and the ability to modify and improve the strength of intraligand interactions. While these kinds of complexes are useful as models for elucidating the magnetic coupling between metal and radical fragments, one should bear in mind that both the nitroxide and semiquinone series of metal-radical complexes are only paramagnetic molecules and not molecular magnets. In order for these systems to exhibit molecular-based magnetism the strength and dimensionality of the exchange between molecules must increase. This will certainly be a result of more elaborate ligand architectures that are capable of forming higher order structures.

1.5 Objectives

Existing investigations studying the radical-radical and metal-radical interactions involving the nitronyl nitroxide and semiquinone families of spin-bearing ligands have demonstrated that it is possible to control the strength and nature of the magnetic interactions between paramagnetic building blocks. The semiquinones are limited in that there are very few examples where they can magnetically bridge two or more metal ions. Although the nitronyl nitroxide family can be readily functionalized and is a neutral stable radical, it is limited by the fact that it is not a particularly good ligand. The nitronyl nitroxide radical typically overlaps weakly with metal orbitals of σ-symmetry leading to antiferromagnetic, or at best very weak ferromagnetic interactions. In addition, the nitronyl nitroxide ring system is sterically demanding, thus limiting the interaction between spins in the solid state. One possible stable radical family that is capable of overcoming these electronic and magnetic limitations is the verdazyl.

The 6-oxoverdazyls are a class of stable radicals whose general structure is depicted in Figure 1.16. The 6-oxoverdazyls are planar and possess two donor atoms for potential metal coordination. The structural features of this ring make it a paramagnetic analogue of pyrimidine. Previous studies[81] have shown that through judicious substitution at the R_2 position, the verdazyl framework is well suited for coordination to metal centres, and can partake in direct magnetic exchange. Unlike the nitroxide family, the metal-verdazyl exchange is similar to the magnitude and nature of the semiquinone ligands. Verdazyl chemistry, including metal radical complexes, will be discussed in more detail in chapter 2.

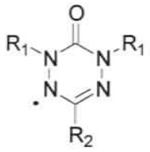

Figure 1.16 - General structure of the 6-oxoverdazyl radical

Preliminary investigations suggest that verdazyls are an attractive organic radical building block for molecular magnetism, and this thesis looks to extend the study of metal-verdazyl interactions. Both electronic and magnetic interactions will be explored, where the specific goals of this thesis are to provide answers to the following queries:

1. Can verdazyl radical ligands be used to generate extended or higher order discrete coordination structures?
2. What are the electronic and magnetic interactions between compounds possessing two verdazyl radical substituents?
3. Can verdazyls be used to generate complexes that effectively demonstrate electronic interactions or indirect magnetic exchange?

The chapters that follow represent primarily a synthetic endeavor to make new verdazyl-based molecules. Chapter two serves as an introduction to the verdazyl radical ligands. The synthesis, characterization, and various properties of new verdazyl ligands, as well as monometallic-verdazyl complexes, are discussed. Chapter three investigates the utility of verdazyls to be incorporated into oligopyridyl backbones for use in synthesizing metallosupramolecular structures. Chapter four and five investigate the metal-radical and radical-radical interactions through an organometallic scaffold.

Chapter 2: Design and Synthesis of *N*-Heterocyclic Verdazyl Radical Ligands

2.1 Verdazyl radicals

Polynitrile radical anions, semiquinones, and nitroxides represent radical families that have demonstrated the utility of the metal-radical approach to molecular magnetism. Furthermore, these metal-radical assemblies have also been shown to exhibit unique electronic properties, such as valence tautomerism. Investigating other radical families could lead to new materials that exhibit room temperature magnetic behaviour or possess novel electronic properties owing to their electroactive nature. As an alternative to the previously explored radical families, the verdazyl radical family has not been well studied. Despite the early verdazyl research focusing on using this radical family exclusively for organic-based magnets,[82] very little is known about how this radical interacts with paramagnetic metal ions. It was not until 1997 that the first metal-verdazyl radical complex appeared in the literature.[83]

Verdazyls (3,4-dihydro-*s*-tetrazin-1-(*2H*)-yl) have the structure shown in Figure 2.1, where atoms in the 3- and 6-positions are primarily carbon, but may also include heteroatoms. The verdazyl can be considered as a paramagnetic, partially π-conjugated sub-class of 1,2,4,5-tetrazines.[84] The verdazyls structure and reactivity,[85,86] coordination chemistry,[81,87] and magnetic properties[82] have all been investigated.

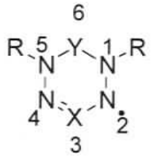

Figure 2.1 - Generic structure of verdazyl ring

As verdazyl research has expanded rapidly in recent years, this chapter frames the synthetic strategies used in the preparation of verdazyl radicals, as well as their electronic and magnetic properties. Later in this chapter the understanding of verdazyl properties is extended with the presentation of a new series of potential verdazyl ligands and metal-verdazyl complexes.

2.1.1 Synthesis of verdazyl radicals

The verdazyl was first discovered serendipitously (as is often the case with new stable radicals) by Kuhn *et al.* in the early 1960s upon attempts to alkylate formazans.[88] Alkylating formazan **2.1** generated the verdazyls structurally-related[89] diamagnetic precursor, the leuco verdazyl (1,2,3,4-tetrahydro-*s*-tetrazine, **2.2**). This leuco verdazyl then underwent auto-oxidation in air to generate the verdazyl (**2.4**) (Scheme 2.1).

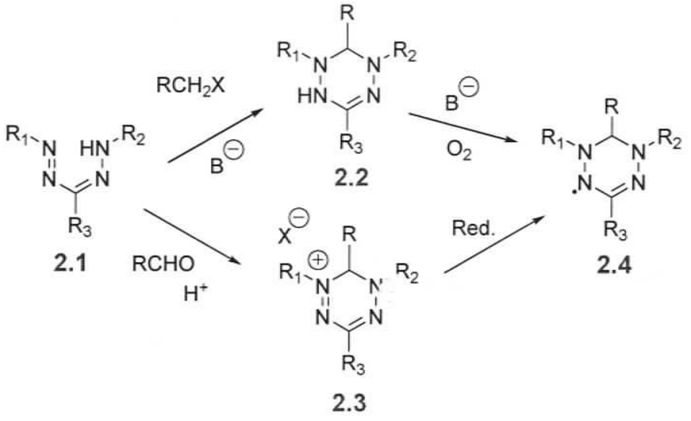

Scheme 2.1 - Routes to verdazyl radicals from formazans

Alkylation of formazans with aldehydes is another technique for generating verdazyls. In this route a verdazylium cation (**2.3**) is generated, which is subsequently reduced in the presence of base to yield the verdazyl radical **2.4** (Scheme 2.1). Until the early 1980s, alkylation of formazans was the only approach to generating verdazyls.

A different method for the creation of verdazyls was developed by Neugebauer[90, 91] (Scheme 2.2). The condensation of a bis(hydrazide) (**2.5**) with an aldehyde generates a tetrazane (**2.6**), which may be oxidized to a leuco verdazyl (**2.7**), or directly to the verdazyl (**2.8**), depending on the stoichiometry of the oxidant. This method can generate verdazyls having a carbonyl or thiocarbonyl group at the C6 position.[90, 91] Both routes are versatile and dozens of derivatives have been prepared using this method.

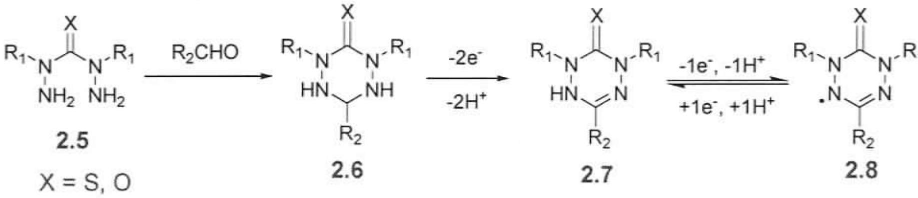

Scheme 2.2 - bis(hydrazide) routes to thio- and oxo-verdazyls

The stability of the leuco verdazyl **2.7** is dependant on several factors (solvent, C3 substituent, etc.), but will eventually oxidize to the verdazyl in an oxygen atmosphere. The verdazyl can be reversibly reduced to the leucoverdazyl[89] with a wide range of reductants, including reducing sugars.[92] While both methods permit some variation in substituents at C3, N1, and N5, the formazan approach also allows for more varied substitution at the C6 position.

The third type of verdazyl is the phosphaverdazyls.[93-97] Typically the phosphorus is located in the 6- or 3-position (Figure 2.2; **2.9** and **2.10** respectively). Theoretically there are many combinations of phosphaverdazyls that can be made, however due to synthetic limitations, only dimethylcarbohydrazide strategies have been explored

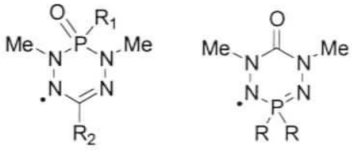

2.9 **2.10**

Figure 2.2 - Phosphaverdazyls

Owing largely to the verdazyl stability and synthetic ease by which they are made, polyverdazyls have also been constructed using formazan and bishydrazide strategies. Bi[98-104]-, tri[105, 106]- and tetra[107]- verdazyls have seen considerable interest and show remarkable stability. Polystyrene[108-110] and polyurea[111] containing verdazyls have also been prepared.

Verdazyls generally show remarkable stability[85, 86] in the solid state as well as in solution. Verdazyls can be stable for years as a pure crystalline solid and weeks in solution. However, not all verdazyls show the same stability as their stability is very much dependant on the substitution at the C3 and C6 positions. By substituting the verdazyl at these positions with bulky or electron-withdrawing or donating groups the stability can be altered.

2.1.2 Structure of verdazyl radicals

The introduction of an sp^2 carbon (i.e. carbonyl) in the C6 position results in a planar ring system (Figure 2.3, Type II), as seen with the 6-oxoverdazyls.[104, 112] This planarity presumably results from the conjugation of the amide-type resonance with the adjacent nitrogens (N1 and N5). When an sp^3 atom is substituted in the verdazyl C6 position (Figure 2.3, Type I), the ring system lacks such conjugative possibilities and consequently, the C6 and the C3 positions are raised above (42.9°, and 9.5°, respectively)[113] the ring plane resulting in a pseudo-boat conformation.[114]

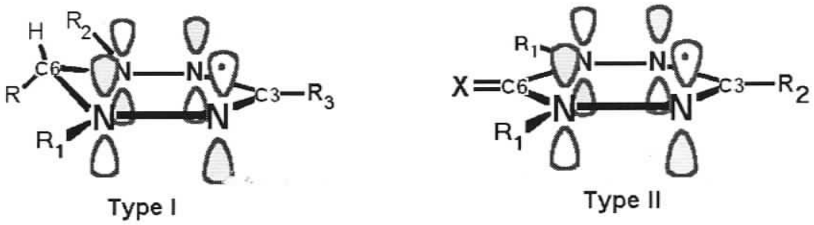

Figure 2.3 - Structure of verdazyl radicals

2.1.3 Electronic structure of verdazyls

Electronic differences between Type I and Type II verdazyls can be observed in the electronic absorption spectra. Non-planar verdazyls are green (hence the name verdazyl, *Latin vert* = green), and the planar verdazyls are red/orange in colour. This phenomenon is easily understood as a result of extending the π-conjugation within the verdazyl ring. Traditionally, non-planar Type I verdazyls have been derived from formazan precursors possessing N-aryl substituents resulting in the verdazyl possessing N-aryl substituents. This aromatic substitution at the N1 and N5 positions extends the conjugation, resulting in a large bathochromic shift versus the planar structures. Conversely, in the construction of bishydrazide-derived planar structures N1 and N5 substituents tend to be alkyl, which has been a limitation of this synthetic approach. Substitution in the C3 position also extends conjugation, but has a more modest role in the electronic absorption spectrum.

The first attempt to calculate the diverse properties of verdazyls such as; spin density distribution, charge density, bond orders, bond lengths, and optical transitions was done using Hückel LCAO-MO theory.[115] Verdazyls are π-radicals in which the semioccupied molecular orbital (SOMO) spans the four nitrogen atoms (Figure 2.4). This distribution over the four nitrogens constitutes the bulk of overall spin density (~80%). The remaining spin density is primarily located on the N1 and N5 substituents. At the Hückel level of approximation there is a SOMO nodal plane perpendicular to the plane of the molecule which bisects C6 (Figure 2.4, X) and C3 (Figure 2.4, Y). In the McLachlan approximation there is some spin leakage in the form of spin polarization at C3 (Y), but the extent of spin distribution is small.

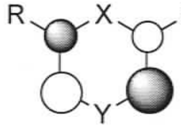

Figure 2.4 - π-SOMO of the verdazyl radical

2.1.3.1 Electronic structure studied by EPR

Verdazyl spin distributions can be readily observed using electron paramagnetic resonance (EPR) spectroscopy[116-121] although other methods have been employed including; electron nuclear double resonance (ENDOR)[122], electron-electron double resonance (ELDOR)[123], dynamic nuclear polarization (DNP)[124], and ^{1}H- or ^{2}H-NMR.[125-129] Generally speaking, the EPR spectra are dominated by hyperfine coupling (hfc) to four nearly equivalent N atoms (Table 2.1). In addition, hyperfine coupling to the N1- and N5-substituents is also observed leading to complex multi-line spectra.

Table 2.1 - Hyperfine coupling constants for various verdazyl radicals as determined by EPR

Verdazyl	a(N)/G	a(H){R_1}/G	a(H){R_5}/G	g-value	Reference
2.11	5.79 ($N_{2,4}$) 5.79 ($N_{1,5}$)			2.0034	86, 122
2.12	6.45 ($N_{2,4}$) 4.50 ($N_{1,5}$)			2.0037	112
2.13	6.45 ($N_{2,4}$) 5.3 ($N_{1,5}$)	5.3 (H_{CH3})	5.3 (H_{CH3})	2.0036	90

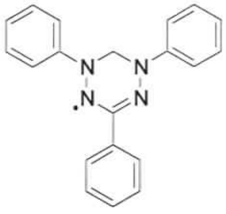

2.11

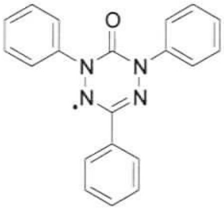

2.12

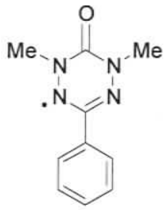

2.13

Derivatives of triphenylverdazyl **2.11** show a dominant nine-line EPR splitting pattern that results from coupling to four nearly-equivalent nitrogen atoms. It has been very difficult to deduce the aryl hyperfine coupling of 1,3,5-triphenylverdazyls (TPV) from EPR alone due to line broadening. The electronic structure of 6-oxo- and 6-thioxo-verdazyls is similar to **2.11** in that they too possess a π-SOMO that has spin density confined to the nitrogens of the verdazyl ring. 1,3,5-triphenyl-6-oxoverdazyl (**2.12**) has some spin delocalization into the N-phenyl groups, but it is reduced when compared to its TPV equivalent, owing largely to the torsion angle about the N-C(phenyl) bond.[112] Both of the 6-oxo-verdazyls (**2.12** and **2.13**) have much larger hyperfine coupling to the N2 and N4 substituents, generating a more complex EPR pattern. The g-values of verdazyls are typical for organic radicals being around 2.0034.

The introduction of heteroatoms can also have a large effect on the spin distribution of the verdazyl radicals. In the phosphaverdazyls there are substantial differences in the phosphorus hyperfine coupling, despite each of the heteroatoms being located on the SOMO nodal plane. The non-planar geometry permits mixing of the σ and π systems, allowing for spin leakage onto the heteroatom.[94] Phosphaverdazyls provide an example of this spin leakage onto the heteroatom through spiroconjugation mechanisms.[95]

2.1.3.2 Electrochemical properties

There have only been a small number of reports on the electrochemical properties of verdazyls.[85, 130-136] Electrochemical oxidation of verdazyls to their corresponding cation, or reduction of verdazyls to their corresponding anion generates very reactive species and occasionally reversibility is not observed. Table 2.2 shows the oxidation and reduction potentials of a series of verdazyls. Generally speaking, voltammetry studies indicate that there is a large potential window of stability which makes verdazyls versatile for a wide range of applications. Although it is difficult to make conclusions on such a small subset of data, Table 2.2 shows that substitution (electron withdrawing or donating groups) in the C3 position can alter the oxidation and reduction potentials. Furthermore, the 6-oxo-verdazyls seem to exhibit a larger oxidation-reduction window, which could reflect differences in the frontier molecular orbital energies of these compounds.

Table 2.2 - Redox Potentials of selected verdazyl radicals (in V vs. SCE)

Compound	E_{ox}	E_{red}	Reference
2.14 (X=H)	0.20	-0.73	85
2.14 (X=NO_2)	0.31	-0.68	
2.14 (X=OCH_3)	0.17	-0.76	
2.15	0.60^a	-1.25^b	131
2.16	0.60^a	-1.25^b	

^{a} Quasi-reversible. ^{b} Irreversible.

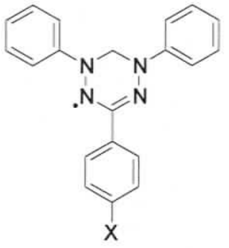

2.14

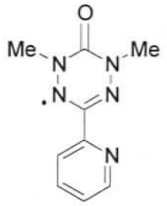

2.15

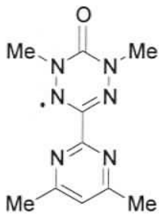

2.16

2.1.4 Polyverdazyls

Verdazyl moieties can be linked together using a variety of strategies. The formazan derived verdazyls are typically connected through the N1, C3, N5, or C6 positions, while the bishydrazide derived verdazyls are bridged through the C3 position. These differences, and the fact that multi-verdazyl linkages tend to be highly symmetric (i.e.C6-C6'), are primarily due to synthetic limitations. The absorption spectra for multi-verdazyls linked through the nodal planes tend to be identical to that of the component verdazyl moieties, with a nearly *n*-fold increase in the molar extinction coefficient, where *n* represents the number of radical substituents.

2.1.4.1 Electronic structure of type II verdazyl polyradical

The simplest of the bisverdazyls based on the 1,3,5-triphenylverdazyl has been prepared[101] (**2.17**), but at room temperature this compound decomposes quantitatively within a few days. This instability has made it difficult to characterize the spin distributions and interactions. Conversely, the bis-(6-oxo-verdazyl) (**2.18a**) has been prepared[90] and fully characterized by x-ray crystallography and EPR.[104]

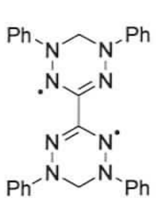

2.17

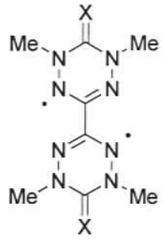

X=O, **2.18a**
X=S, **2.18b**

X-ray crystallography shows that bisverdazyl **2.18a** is a planar structure in the solid state, but due to lone pair repulsion it is unlikely to exist as such in solution. In a frozen solution, **2.18a** behaves as a ground state singlet with $J = -758\ \mathrm{cm}^{-1}$.[104] Similarly, **2.18b** behaves also as a ground state singlet with $J = -560\ \mathrm{cm}^{-1}$.[102] Theoretical calculations on **2.18b** are in good agreement with this experimental data.[137, 138]

A series of bis(6-oxoverdazyls) has been studied electrochemically and the results of this study suggest that aromatic spacers linking verdazyl moieties together through the C3 position decrease the magnitude of coupling between the two unpaired electrons. This is consistent with what is observed in the absorption spectrum, EPR, and cyclic voltammetry.

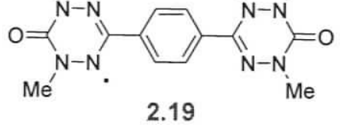

2.19

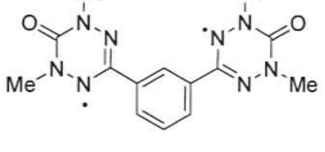

2.20

When contrasting **2.18a** with the phenyl spaced **2.19** and **2.20**, significant red shifts occur indicating that there is a structural perturbation by these aromatic linkers.

Based on the MO calculations described earlier, perturbation in the SOMO level is not expected because the aromatic spacer is connected on the nodal plane and C3 position. However, the LUMO of the 6-oxoverdazyl does not possess a nodal plane at C3, and conjugation with a phenyl ring lowers the energy of the LUMO, hence red shifting occurs. The bands in the visible region have been assigned to Φ_h (SOMO) → Φ_l (LUMO) and Φ_{h-1} (SOMO) → Φ_h (SOMO) transitions.

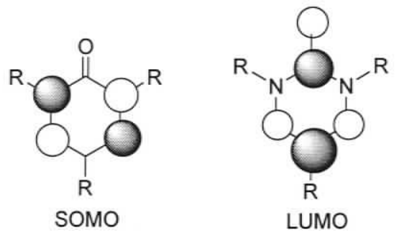

Figure 2.5 – Symmetry of frontier orbitals in 6-oxo-verdazyls

The aromatic spacing unit also affects the extent of electronic communication between the two radicals, as evidenced by electrochemical studies. With the addition of the π-conjugated spacer there is no longer any coupling between these radical systems, hence the verdazyl exists as a ground state triplet or has nearly degenerate singlet/triplet states, which is confirmed by linear Curie plots. The redox values for **2.18a** indicate that the antiferromagnetic coupling results in the molecule having two different oxidation values. **2.18b** (although being highly air sensitive), when compared to **2.18a**, has a smaller singlet-triplet energy gap, and this is reflected in the smaller difference between the oxidation potentials. **2.18b** exists as an unstable dication, and is not reversible. Both **2.19** and **2.20** also exhibit similar oxidation potentials as would be expected for non interacting spins.

2.1.5 Verdazyl – radical hybrids

Other multi-spin verdazyl systems have been designed to investigate intramolecular exchange. Hetero-spin systems are of considerable interest due to their potential for understanding molecular structure and magnetic exchange. A hetero-spin nitrene-verdazyl radical system[139] separated by a phenyl group (**2.21**) has been prepared.

In this particular system the authors have simulated the data to be consistent with the arylnitrene and radical units giving rise to a quartet ground state.

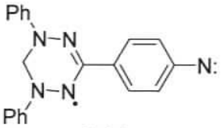

2.21

Another system designed to investigate intramolecular exchange is a photoinduced spin system. Photoinduced spin alignment through π-conjugation is a new strategy for the photoinduced/switching, which could potentially lead to photo-control of magnetism behaviour. Verdazyls combined with a chromophore, should allow for excitation of the chromophore leading to a triplet state. Photoinduced alignment would then be realized when the exited state triplet ferromagnetically couples to the radical moieties. Such systems have been explored in molecules **2.22**[140], **2.23**[141], and **2.24**[142].

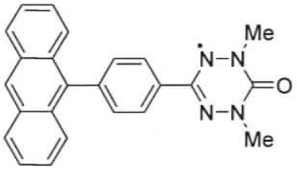

2.22

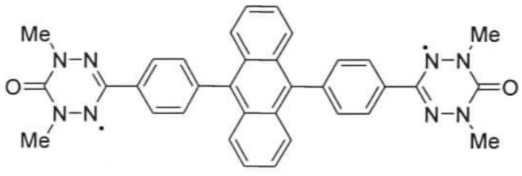

2.23

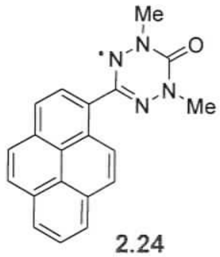

2.24

2.1.6 Verdazyls as ligands

2.1.6.1 Verdazyls coordinated to diamagnetic metal ions

Since the discovery of the 6-oxoverdazyls in 1980, verdazyl research has expanded to include molecules with a wide range of substituents in the C3 position. With its planar ring system and sp^2 nitrogens in the 2- and 4-positions, the verdazyl ring has structural similarities that resemble the pyrimidine ring. With judicious substitution in the C3 position of the 6-oxoverdazyl it is also possible to create bipyridine and bipyrimidine mimics (Figure 2.6).

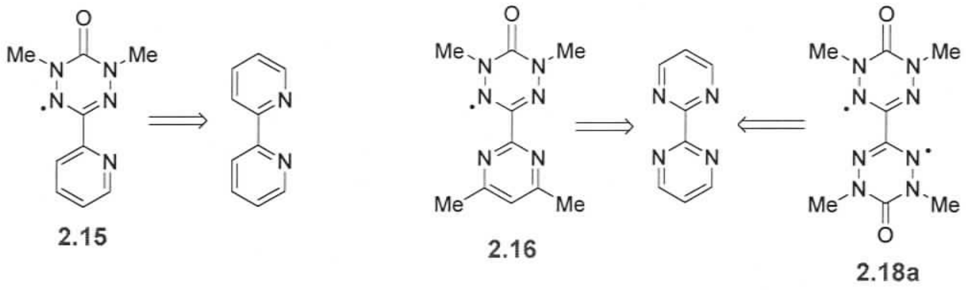

Figure 2.6 - Verdazyls as oligopyridine mimics

The first demonstration of verdazyls as ligands was in 1997.[83] Using **2.18a** as a bridging ligand, it was shown that verdazyls could coordinate to copper(I) metal centres, resulting in 1D chains. Brook and coworkers prepared a series of chloride, bromide, and iodide bridged copper (I) coordination polymers containing **2.18a** (Figure 2.7). Using a diamagnetic metal centre allowed them to determine the effect of altering the halide bridge on the magnetic properties of the material. Changing the halide in the copper bridge altered the interchain magnetic exchange between adjacent coordination polymer chains; J_{inter}= -116 cm^{-1} for the CuCl complex, J_{inter} = -110 cm^{-1} for the CuBr complex, and J_{inter}= -200 cm^{-1} for the CuI complex.

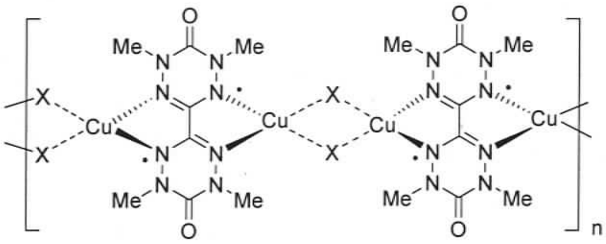

Figure 2.7 - Copper (I) halide bridged metal verdazyl complexes of **2.18a**

In 2000 Brook and coworkers[143, 144] extended their work of verdazyl coordination by preparing several metal–radical complexes based on **2.15**. A bromide-bridged copper(I) dimer **2.25** shows a very weak radical-radical exchange of J_{intra}= -5 cm^{-1}. Similarly Hicks and co-workers[145] prepared a 2:1 homoleptic, mononuclear Cu(I) complex (**2.28**) and it was found that the intramolecular radical–radical exchange in this cationic species was similarly weak (J_{intra} = -2 cm^{-1}). Other verdazyl complexes of diamagnetic metal ions have also been reported such as **2.26**, **2.27**,[146] and **2.29**.[147]

Although these complexes could be characterized in solution, no structural or solid state magnetic data was obtained.

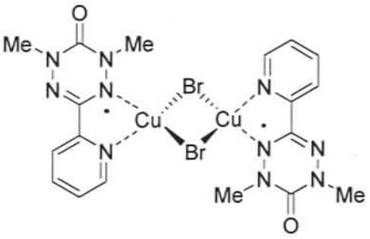

2.25

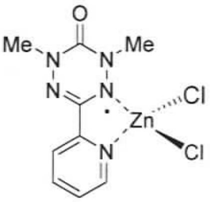

2.26

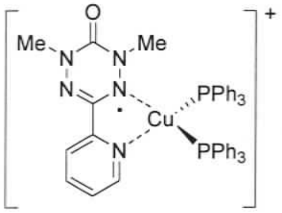

2.27

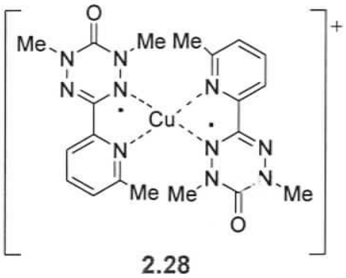

2.28

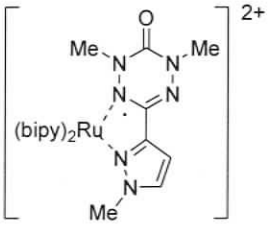

2.29

2.1.6.2 Verdazyls coordinated to paramagnetic metal ions

The diamagnetic metal complexes demonstrated that it was possible to make metal-verdazyl coordination complexes; however, until 2000 there were no verdazyl coordination complexes involving paramagnetic metal ions. Hicks and coworkers[148, 149] prepared two coordination complexes of **2.15** with hexafluoroacetylacetonate (hfac) as ancillary ligands. A solid state structural investigation of the two M(hfac)$_2$(**2.15**) complexes (where M = Ni, and Mn) showed that the complex formed was the expected monometallic species with a pseudooctahedral geometry about the metal centre (**2.30** and **2.31**). The verdazyl behaves as a fully planar chelating ligand where the bond lengths within the verdazyl ring are affected little upon metal coordination and, generally, the stability of verdazyl radicals increases upon metal coordination.[149]

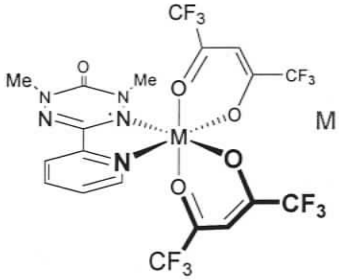

M = Mn (**2.30**)
Ni (**2.31**)

Three conclusions were made regarding the nature of the metal-radical interaction based on magnetic studies: 1) The ligand binds to the metal principally as a σ-donor, 2) high spin density at the ligating verdazyl nitrogen atom ensures strong coupling to the metal centre, and 3) electron occupancy of the metal orbitals dictates the type of magnetic interaction.

In the metal-verdazyl direct exchange the rules of orbital orthogonality apply. Magnetic exchange will be ferromagnetic if there is no overlap between the metal orbitals possessing the unpaired electrons and the π-SOMO of the ligand. If there is orbital overlap between singly occupied metal orbitals and radical SOMO, then the exchange will be antiferromagnetic. In the case of octahedral M(hfac)$_2$(**2.15**) complexes where the unpaired electrons are confined to exclusively the d_{z^2} or $d_{x^2-y^2}$ metal orbitals, then this favours ferromagnetic exchange. If unpaired electrons are located in the d_{yz}, d_{xy} or d_{xz} orbitals, overlap favours antiferromagnetic coupling. Figure 2.8 depicts these two exchange modes: (a) d_{z^2} – SOMO with no orbital overlap, (b) d_{xz}-SOMO direct orbital overlap.

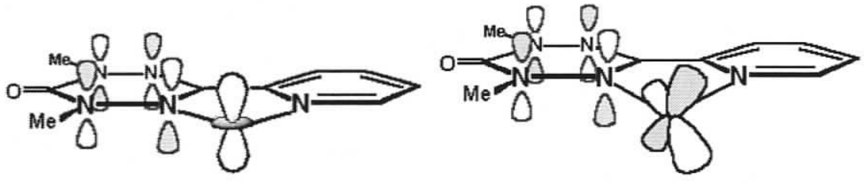

(a) (b)

Figure 2.8 - Orbital orthogonality in magnetic exchange of M(hfac)$_2$(**2.15**); (a) d_{z^2}-SOMO orthogonality and (b) d_{xz} orbital with orbital overlap.

Nickel (**2.30**) and manganese (**2.31**) complexes based on the formula M(hfac)$_2$(**2.15**) have metal-radical exchange values of $J_{Ni\text{-}rad} = 240$ cm^{-1} and $J_{Mn\text{-}rad} = -45$ cm^{-1}, respectively. The positive sign for the nickel compound suggests a ferromagnetic interaction and this is consistent with nickel having its unpaired electrons confined to the

d_{z^2} and $d_{x^2-y^2}$ metal orbitals. The Mn^{2+} derivative has a negative exchange value, which is consistent with the antiferromagnetic exchange predicted as Mn^{2+} has three unpaired electrons in the d-orbitals with non-zero metal-radical overlap.

Hicks and coworkers[149] have made a number of other verdazyl containing ligands including mono- and bis- verdazyls with a variety of binding topologies as can bee seen in Figure 2.9. This small library of verdazyl radical ligands demonstrates the versatility of verdazyl ligands, and may be used to design more complex radical ligands that would lead to other unique property directed structures.

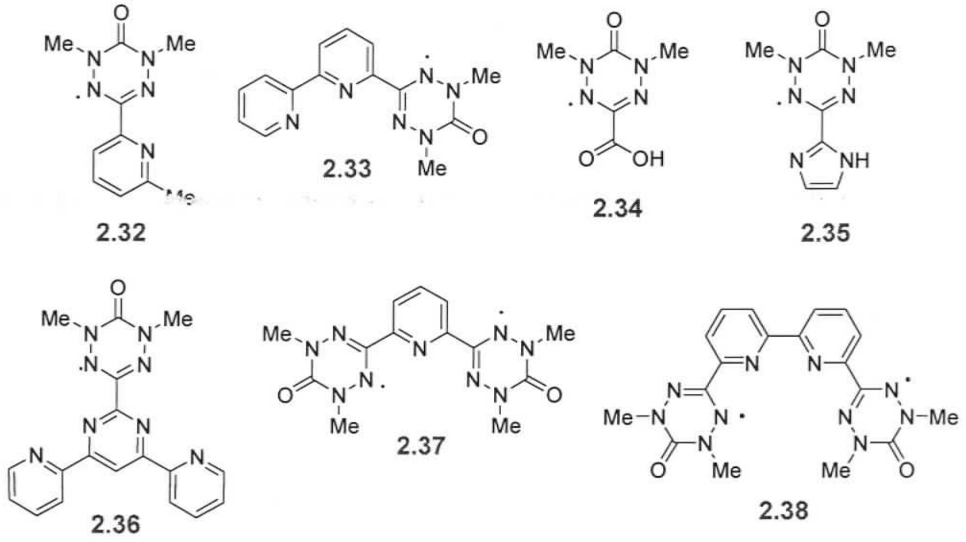

Figure 2.9 - Other verdazyl radical ligands

Of particular interest magnetically are the coordination complexes involving verdazyl ligands **2.16**, **2.33**, and **2.34**. Pyrimidine substituted verdazyl **2.16** has a bis-bidentate topology and was shown to magnetically bridge two M(hfac)$_2$ metal ions (**2.39**). Again Mn(II) and Ni(II) were the metal ions explored and it was found that the Mn- and Ni–verdazyl exchange parameters in the binuclear systems are nearly identical to those found in their mononuclear counterparts (**2.30** and **2.31**). This implies that in both cases the radical is successful at bridging the two metals so that they align ferromagnetically.

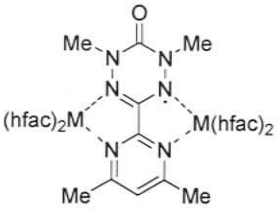

M = Ni, **2.39a**
M = Mn, **2.39b**

Bis-verdazyl metal complexes were prepared using terpyridine analogue **2.33** and carboxylate derivative **2.34**. In the octahedral $M^{II}(\mathbf{2.33})_2$ structure (**2.40**) the Ni(II)–verdazyl exchange remains strongly ferromagnetic ($J_{Ni\text{-}vd}$ = +240 cm^{-1}) and the Mn(II)–verdazyl exchange is uniformly antiferromagnetic ($J_{Mn\text{-}vd}$ = -93 cm^{-1}).[150, 151] There is some variation in the magnitude of exchange in these bis-verdazyl octahedral complexes as compared to **2.30** and **2.31**, which suggests that the metal-verdazyl magnetic interactions are influenced by the ancillary ligands and subtle geometry changes. Generally speaking, in complexes where the radicals are not coplanar the radical–radical interaction tends to be very weak ($-10\text{cm}^{-1} < J_{vd\text{-}vd} < +2\text{cm}^{-1}$).

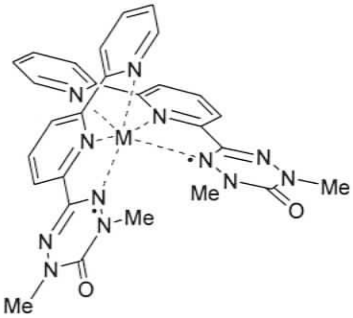

M = Ni, **2.40a**
M = Mn, **2.40b**

Ligand **2.34** is another example of a potentially *bis*-bidentate ligand, yet it has only generated *mono*-metallic complexes to date. In the nickel-radical Ni(**2.34**)$(H_2O)_2$ complex (**2.41**) the magnetic exchange interaction is $J_{Ni\text{-}vd}$ = +94 cm^{-1}. Unlike the octahedral complexes of **2.33**, this pseudo-octahedral complex has the two radicals lying in the same plane and this results in an enhanced radical–radical exchange interaction of $J_{vd\text{-}vd}$ = -21 cm^{-1}.

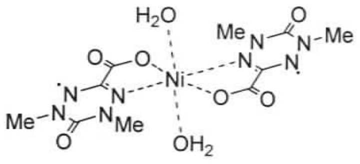

2.41

Overall, the coordination chemistry of verdazyl radicals demonstrates that this family of radicals is amenable for use in the metal-radical approach towards molecular magnetism. The structural resemblance of the verdazyl moiety to that of the pyrimidine group offers much potential in the arena of metallosupramolecular chemistry. To this end, a new series of heteroaromatic substituted verdazyls has been prepared in hope of better understanding the verdazyls place in molecular magnetism.

2.2 Syntheses of (hfac)$_2$M^{II}(2.15) complexes (M = Co and Fe)

In order to confirm that the metal-verdazyl magnetic exchange interaction obeys orbital orthogonality arguments, more octahedral verdazyl metal complexes need to be made to complement the existing Mn- and Ni-verdazyl complexes. Continuing with the series that includes **2.30** and **2.31,** corresponding cobalt and iron complexes were prepared in order to investigate their metal-radical exchange interactions.

Complexes of the form (hfac)$_2$M^{II}(**2.15**) (M= Fe and Co) were prepared as outlined in Scheme 2.3. The combination of **2.15** (either free of hydroquinone or as the molecular adduct) with one equivalent of the hydrated (hfac)$_2$M^{II} salt afforded air- and moisture-stable complexes in moderate to high yield. Both complexes were recrystallized by slow cooling of saturated hexane solutions. There was no success in isolating X-ray quality crystals, but based on other characterization methods the atomic connectivity of **2.42** and **2.43** is analogous to **2.30** and **2.31**.[148, 149]

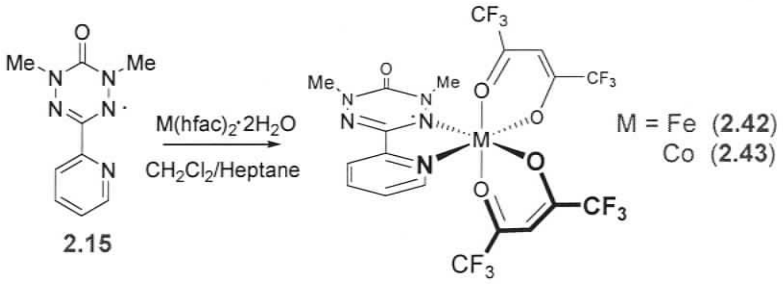

Scheme 2.3. Preparation of (hfac)$_2$M(**2.15**) complexes (M = Co, Fe).

The structural relationships between complexes **2.42**, **2.43**, and previously explored complexes with the formula M(hfac)$_2$(**2.15**) are supported by FT-IR spectroscopy, LR-MS, and UV-Vis. The complexes have virtually identical IR spectra and upon coordination each possesses a diagnostic carbonyl stretching shift that is observed upon coordination of virtually all verdazyl radical ligands. This verdazyl carbonyl frequency shifts to higher energy compared to the free verdazyl **2.15**. Further evidence of structure came from low resolution mass spectrometry, where each of the complexes had nearly identical fragmentation patterns. UV-visible spectroscopy also support the fact that metal-radical complexation had occurred. The UV-Vis spectrum of verdazyl radical ligand **2.15** shows a maximum at 409 nm, with an extinction coefficient of 1600 $M^{-1}cm^{-1}$. Upon coordination this absorption maximum shifts to lower energy (426 nm and 427 nm for **2.42** and **2.43**, respectively) and there is a three-fold enhancement in the molar extinction coefficient (Figure 2.10). The nature of this enhancement is not clear, but it could be due to efficient energy transfer from the metal chromophore in the excited state or enhanced absorption due to the planarity of the complexed radical ligand. Nearly identical shifts and verdazyl absorptivity enhancements have been observed in **2.30** and **2.31**. In addition, **2.42** also exhibits a strong absorption around 500 nm that could be assigned to charge transfer.

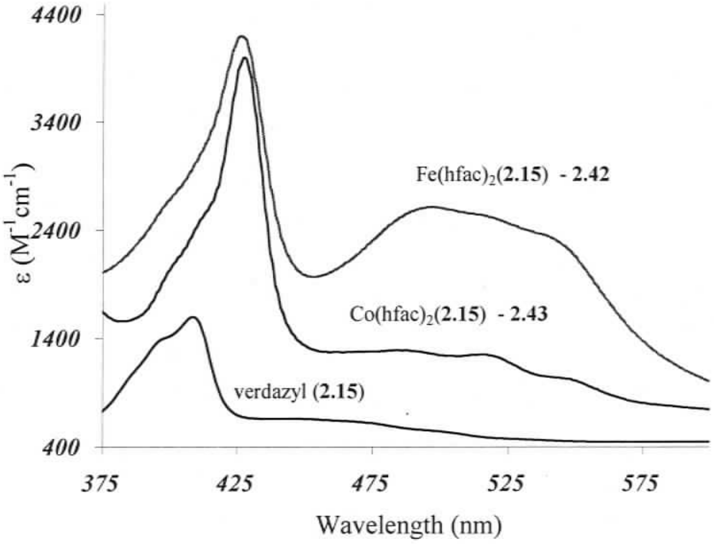

Figure 2.10 - UV-visible spectra of **2.15, 2.42,** and **2.43**

2.2.1 Magnetic properties of (hfac)$_2$M^{II}(2.15) complexes (M = Fe, Co)

The temperature dependence of the molar magnetic susceptibility was measured from 300 to 2 K for complexes **2.42** and **2.43**. The results are displayed in Figure 2.11 as χT versus T plots. The experimental data for both **2.42** and **2.43** were fitted to an asymmetrical binuclear model having a spin Hamiltonian of the form $H = -JS_{\mathrm{Metal}}S_{\mathrm{rad}}$.[3]

The room temperature χT value for **2.42** was 3.0 cm^3 K mol^{-1}, and this is lower than the spin-only value for non-interacting iron(II) and radical spins. From room temperature the χT product steadily decreases until about 75 K where it slowly decreases towards 25K. Below 25 K the χT product rapidly decreases. This magnetic behaviour is consistent with that of an antiferromagnetically coupled S_{rad}= 1/2, and S_{Fe} = 2 pair. Modeling the data for **2.42** resulted in the following parameters being obtained from the line of best fit: $g_{\mathrm{Fe}} = 1.996$, $g_{\mathrm{rad}}= 2.0037$ (fixed), $J_{\mathrm{Fe\text{-}rad}}= -66$ cm^{-1}, $\theta = -4.5$ K, $\rho = 0.15$, TIP = 150×10^{-6} ($R = 0.026$).

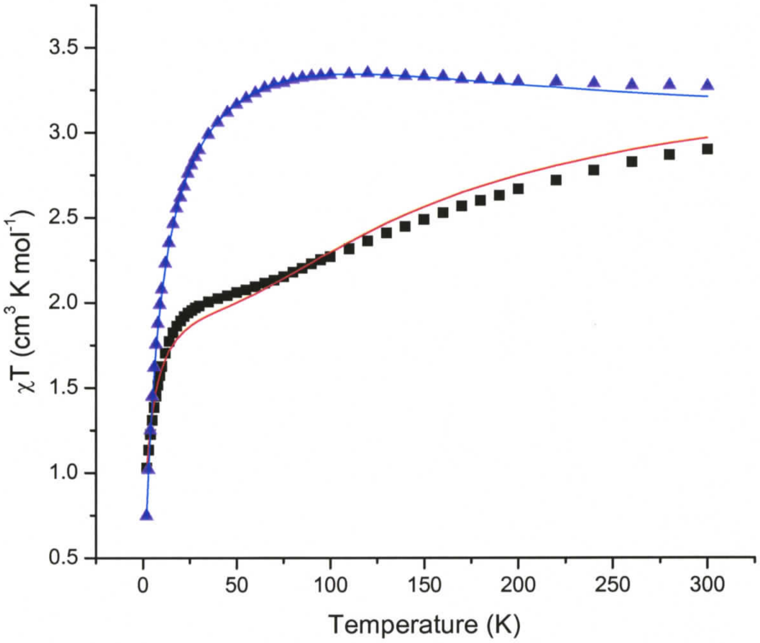

Figure 2.11 - χT vs T plot for M(hfac)$_2$pyvd; M = Fe(**2.42**, ■) and Co(**2.43**, ▲). Solid lines represent modeled fits to the experimental data

The model for **2.42** required the inclusion of a paramagnetic impurity parameter, ρ. The model was unable to replicate perfectly the experimental data, but the general features are similar. The modest differences between the experimental data and model suggest that it may be helpful to investigate the diamagnetic corrections.

In contrast to **2.42**, the room temperature χT value of **2.43** is 3.3 cm^3Kmol^{-1}. This is higher than the spin-only value for non-interacting cobalt(II) and radical spins, and corresponds to the expected value for an $S = 2$ system. The χT product did not vary significantly with temperature above 80 K. Below 50 K the χT product rapidly decreased. The magnetic behaviour of **2.43** was consistent with that of a ferromagnetically coupled $S_{rad} = 1/2$, $S_{Co} = 3/2$ pair and was modeled yielding the following best fit parameters: $g_{Co} = 2.41$, $g_{rad} = 2.0037$ (fixed), $J_{Co\text{-}rad} = +95\ cm^{-1}$, $\theta = -8.0$ K, TIP = 345×10^{-6} ($R = 0.008$).

Fitting magnetic data from complexes containing octahedral Co(II) is problematic because of the inherent temperature dependence of the Co(II) moment. Co(II) has several orbital contributions that affect the susceptibility and these contributions decrease as temperature is lowered. The fitting of **2.43** has omitted this orbital contribution and the binuclear model employed has exclusively spin-only context. These orbital contributions to the moment are believed to result in the rather large θ-values, but in the absence of crystallographic data it is difficult to rule out the possibility of intermolecular contacts.

The trends observed in the magnetic behaviour in this series of M(**2.15**)(hfac)$_2$ complexes suggest that the magnetic exchange follows the orbital orthogonality relationship. Despite the Fe^{2+} centre of **2.42** having two unpaired electrons of σ-symmetry, the two unpaired electrons in metal orbitals of π–character dominate resulting in orbital overlap, and hence antiferromagnetic exchange. Conversely, **2.43** has one unpaired electron in a metal orbital of π-symmetry, and two unpaired electrons in metal orbitals with σ-symmetry. The two orthogonal orbitals dominant the exchange pathway with the verdazyl, resulting in ferromagnetic exchange.

Table 2.3 - Magnetic exchange in M(**2.15**)(hfac)$_2$ complexes

Complex	***J*-value (cm^{-1})**
M= Ni – **2.31**	+240
M= Co – **2.43**	+95
M = Fe – **2.42**	-66
M = Mn – **2.30**	-45

2.3 Synthesis of N-heteroaromatic substituted verdazyl precursors

Previous discussions have shown that verdazyls behave as pyrimidine mimics. The following synthetic targets have been designed to further explore the nature of the metal-verdazyl interaction by expanding the library of verdazyl radicals of the *N*-heteroaromatic series and investigating their coordination chemistry.

2.3.1 General synthetic methodology

The synthetic approach taken to make 1,5-dimethyl-6-oxoverdazyl radicals is based on methodology established by Neugebauer[90] and modified by Hicks and coworkers.[131] When verdazyl radicals are functionalized with methyl substituents in the N1 or N5 position, and N-heteroaromatic substituents in the C3 position, they become suitable for metal coordination chemistry. Thus, as an extension of previous work[149] a new series of tetrazane and aldehyde precursors were prepared. Aldehyde precursors required to make these new tetrazanes and verdazyls are presented in Figure 2.12.

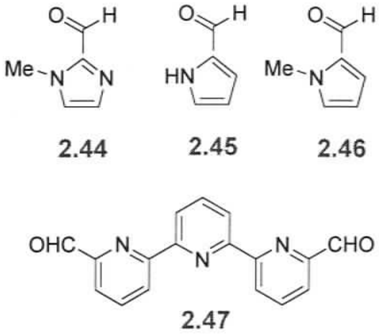

Figure 2.12 - Aldehydes used in the syntheses of N-heterocyclic verdazyl radicals.

2.3.2 Aldehyde synthesis

Aldehydes **2.44, 2.45,** and **2.46** were purchased commercially. The synthesis of **2.47** begins from the commercially available 2,6-dibromopyridine, where mono-lithiation of the dibromopyridine, followed by quenching the anion with DMF results in 6-bromo-pyridine-2-carbaldehyde (**2.48**) in excellent yields. The mono-lithiation of dibromopyridine is by no means trivial.[152-156] There have been two syntheses of **2.48**,[152,

[154] but Scheme 2.4 gives the highest yields and the most thorough characterization. The aldehyde is then protected using an existing procedure[157] to yield **2.49**.

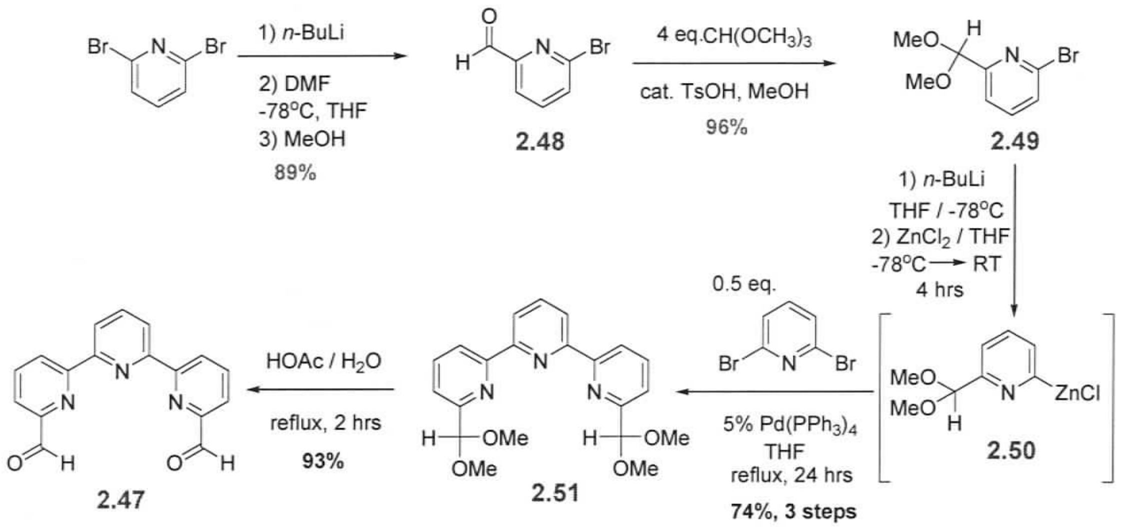

Scheme 2.4 – Synthesis of terpyridine dialdehyde **2.47**

The protected aldehyde **2.49** can then be lithiated and converted to the Negishi reagent (**2.50**) that is then coupled to 2,6-dibromopyridine *in situ* using the Negishi Coupling[158-161] procedure. Less than 0.5 equivalents of dibromopyridine were used to avoid the production of 6-bromo-2,2'-bipyridine as a by-product. The terpyridine ligand **2.51,** precipitates from THF as a zinc complex. This results in a solid, that when extracted using EDTA, yields the protected dialdehyde **2.51** in very high purity and good yield. Similar techniques have been applied to the construction of various terpyridines.[161] The deprotection of **2.51** gives the dialdehyde **2.47.**[162, 163]

2.3.3 Tetrazane synthesis using carbonic acid bis(1-methylhydrazide)

Hicks and coworkers[131] have previously described an efficient synthetic strategy for the generation of carbonic acid bis(1-methylhydrazide) (**2.52**). This strategy is depicted in Scheme 2.5. Triphosgene can readily be reacted with methylhydrazine at low temperatures to give **2.52**. Excess methylhydrazine is used as a base to sequester the HCl produced in the reaction.

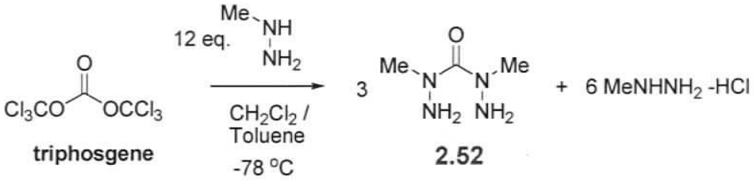

Scheme 2.5 - Synthesis of carbonic acid bis(1-methylhydrazide) **2.52**.

Bishydrazide **2.52** is an essential component in the modified Neugebauer synthesis of tetrazanes (Scheme 2.2). All tetrazanes were prepared using the general conditions provided in Scheme 2.6. Typically, to a gently refluxing concentrated solution of **2.52** in methanol was added a dilute methanolic solution of the aldehyde dropwise. Refluxing of the reaction mixture was generally continued for more than 12 hours, followed by evaporation of the solvent and trituration of the product using ethyl acetate to afford tetrazanes with yields above 70% in most cases.

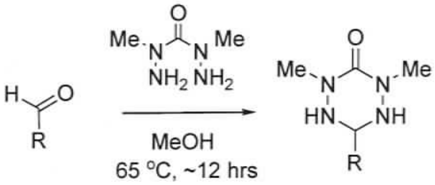

Scheme 2.6 - General preparation of precursor tetrazanes.

Lower yields are obtained if aldehyde concentration in solution is disproportionately high, likely owing to the formation of bis-imine side products (Figure 2.13). In the case of dialdehydes it is even more critical to maintain an excess of **2.52**, because of the oligo-imine side products that can be generated (Scheme 2.6b).

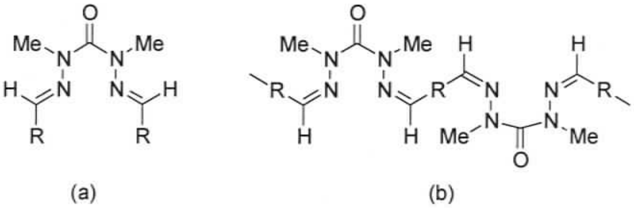

Figure 2.13 - Potential bis-imine (a) or oligo-imine (b) side products in the preparation of tetrazanes.

Using the method depicted in Scheme 2.6, tetrazanes **2.53**, **2.54**, **2.55**, and **2.56** were prepared. Characterization of all tetrazanes was accomplished by $^1H/^{13}C$ NMR, FT-IR spectroscopies, MS, and elemental analysis. In general, these tetrazanes all share the same spectroscopic properties. Therefore, the spectroscopic properties of bis-tetrazane

2.56 will be discussed as a representative sample of N-heteroaromatic substituted tetrazanes.

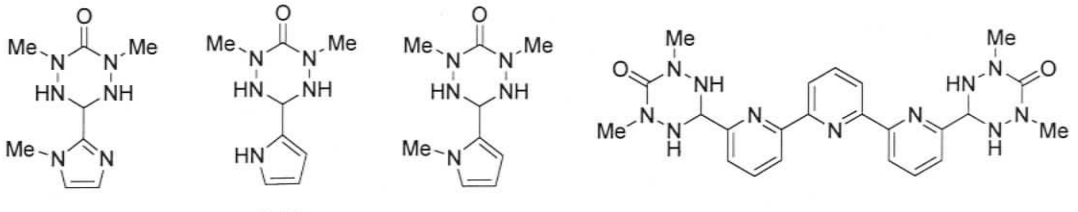

2.53 **2.54** **2.55** **2.56**

Figure 2.14 - N-heteroaromatic tetrazanes

The ^{1}H–NMR spectrum of tetrazane **2.56** exhibits a degree of solvent dependence. In chloroform the tetrazane ring protons do not show any coupling and are rather broad in nature. In Figure 2.15, tetrazane proton resonances show up in their typical locations; a large methyl singlet (b, 3.05 ppm), a triplet due to the C3 proton (d, 5.05 ppm), and a doublet for N-H protons (c, 5.85 ppm). Using homo- and heteronuclear correlation spectroscopies, the aromatic protons have also been assigned in Figure 2.15

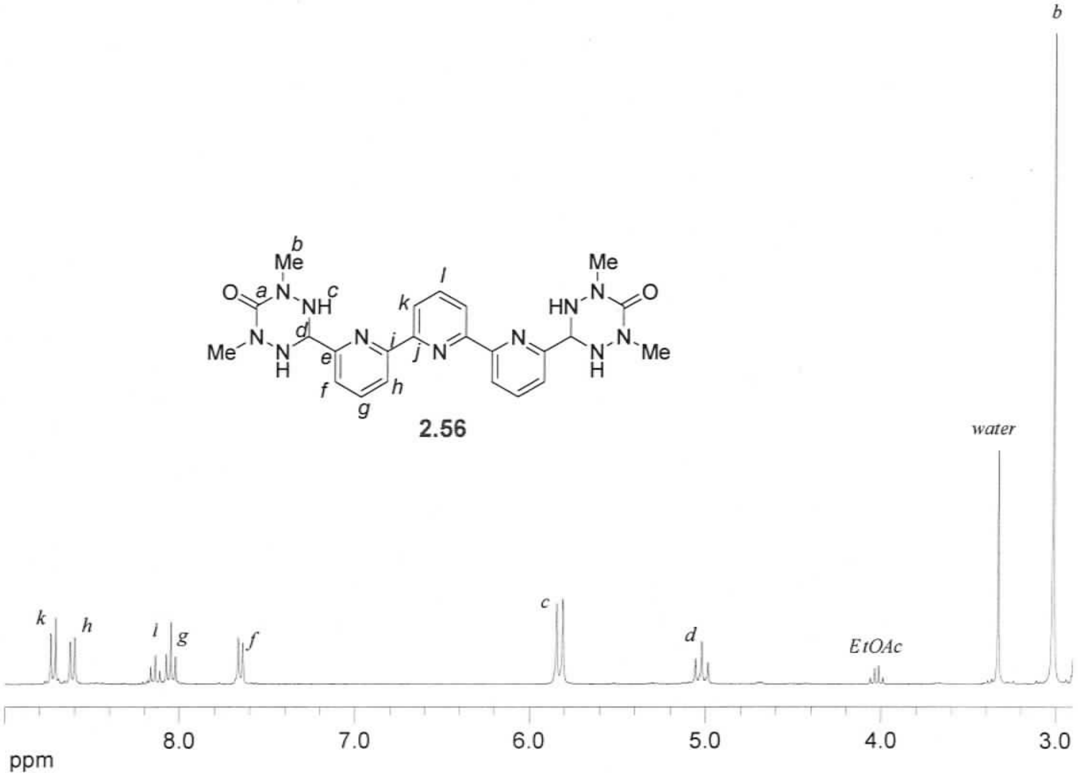

Figure 2.15 - ^{1}H-NMR of **2.56** in DMSO-d^6 (solvent peak at 2.50ppm)

Typical ^{13}C-NMR resonances for tetrazanes with aromatic substituents are the methyl signal (b), a C3 tetrazane ring carbon (d), and the carbonyl resonance (a) (Figure 2.16). The upfield carbonyl shift is typical of urea-like carbonyls. Using homo- and heteronuclear correlation spectroscopies, the aromatic carbons have also been assigned in Figure 2.16.

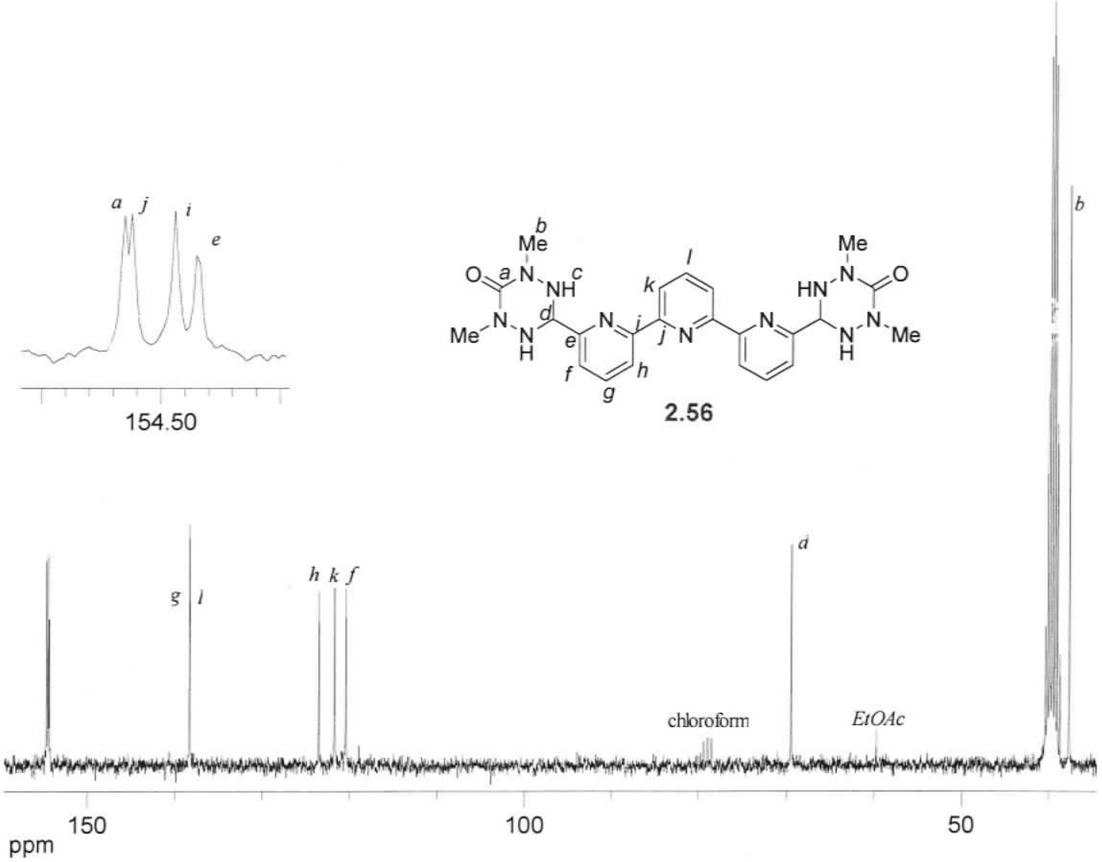

Figure 2.16 - ^{13}C-NMR of **2.56** in DMSO-d^6 (solvent peak at 39.5ppm)

In the FT-IR spectra of tetrazanes, diagnostic peaks include the strong carbonyl stretch and the variable strength secondary amine stretching frequency. In the FT-IR of **2.56** (Figure 2.17) both tetrazane elements are present; a weak NH stretch of the amine at 3234 cm^{-1} and the carbonyl stretch seen at 1636 cm^{-1}. The low carbonyl frequency is due to its conjugation with the adjacent amide nitrogens and is consistent with other tetrazanes of this type.

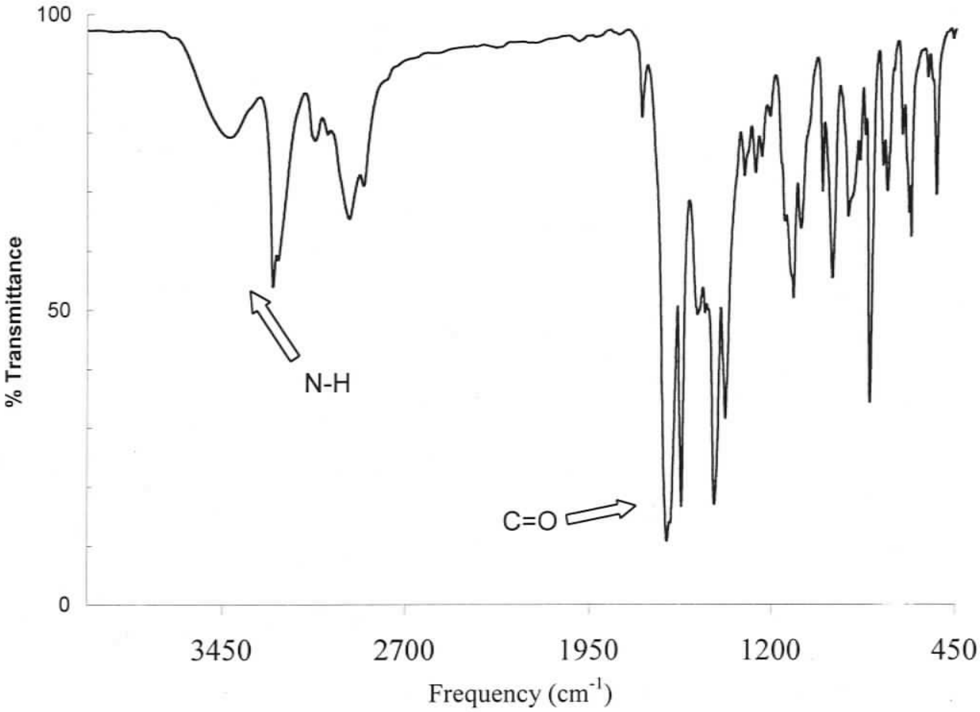

Figure 2.17 - FT-IR spectrum **2.56** (KBr disc, y-axis is in units of percent transmittance)

Low resolution liquid secondary ion mass spectrometry (LR-LSI-MS) was used to confirm the suggested formulations of all tetrazanes and high resolution liquid secondary ion mass spectrometry (HR-LSI-MS) succeeded in characterizing the mass of the molecular ions (M+) to four decimal places. Typically, *N*-heteroaromatic tetrazanes with high molecular weights like **2.56** are subjected to LSIMS because their low volatility prevents analysis using EI.

2.4 *N*-heteroaromatic verdazyl radicals: Synthesis, characterization and electronic properties

2.4.1 Oxidation of tetrazanes

There are many oxidants that can be used in the conversion of tetrazanes to verdazyls. The choice of oxidant is primarily pragmatic, as the greatest challenge is often the purification of the verdazyl. If the verdazyl radical is readily separated from the reaction mixture, then the oxidation reaction (Scheme 2.7) is often done homogeneously, where the oxidant and tetrazane solubility determine which solvent will be used.

Occasionally, difficulty in separating the verdazyl from the oxidant requires the use of a heterogeneous oxidant, which is much easier to remove from the reaction mixture. Typically, oxidations have been carried out in halogenated or aqueous solvents, largely due to the stability of these solvents to oxidation/reduction.

In this work, the only oxidant employed using heterogeneous conditions was silver(I) in the form of Fetizon's reagent[164] (Ag_2CO_3 on Celite). Although slower to react, the Fetizon reagent is particularly useful when the oxidant and the verdazyl are difficult to separate using column chromatography. The byproducts of the Fetizon oxidation are silver metal and perhaps unreacted tetrazane, which are easily separated from the verdazyl using column chromatography.

Oxidation of the tetrazane, if the verdazyl is stable, can afford verdazyls in good to excellent yields (50-95%). In this work ferricyanide, periodate, benzoquinone, and silver (I) have been used as oxidants.

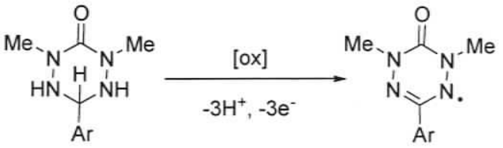

Scheme 2.7 - Oxidation of tetrazanes in the preparation of verdazyls

The oxidation of the tetrazane (Scheme 2.7) liberates three protons; therefore the oxidative conditions require the presence of a base. In the case of Ag^+ and ferricyanide, an external base is added to the reaction to sequester the acid produced.

2.4.2 Synthesis of *N*-heteroaromatic verdazyl radicals

2.4.2.1 Imidazole-substituted verdazyls

The study of electron rich, 5-membered heteroaromatic substituted verdazyls is the direct extension of research based on imidazole substituted verdazyl radicals synthesized previously in our group. The imidazole verdazyl was never effectively shown to coordinate to octahedral metal centres. However, it was hypothesized that methylation of the imidazole ring would increase the nucleophilicity and donating ability of the imidazole substituent owing to the electron donating ability of the methyl group.

Furthermore, the substitution of the acidic imidazole hydrogen should prohibit any multinuclear oligomerization.

The radical **2.57** was generated from the highly water soluble **2.53** using periodate as the oxidant. Verdazyl **2.57** was isolated in good yields.

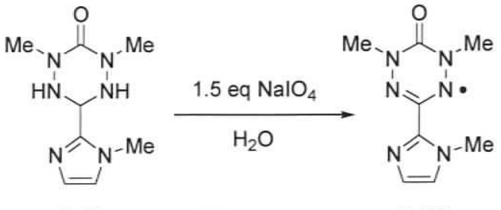

2.53 **2.57**

Scheme 2.8 - Oxidation of **2.53** to yield verdazyl **2.57**

2.4.2.2 Pyrrole-substituted verdazyls

Like the imidazole tetrazanes, pyrrole tetrazanes, upon oxidation and deprotonation of the pyrrole ring, would yield an interesting class of anionic verdazyls. Unfortunately, unlike their imidazole counterparts, the pyrrole verdazyl radicals are much more difficult to isolate as pure compounds. Initial attempts to generate **2.58** were performed in water using periodate, but did not lead to the desired product. Instead it appeared by MS as though the pyrrole unit oligomerized to yield some sort of larger molecular weight system, evidenced by the fact that there was a repeating unit (m/z = 197). No conditions were found in protic media to successfully generate **2.58**.

After several attempts, it was found that **2.58** could be generated and isolated in an impure form via the heterogeneous Fetizon reagent (Scheme 2.9). EPR, MS, and IR all confirmed the structural elements. Unfortunately, all attempts to purify the radical using column chromatography failed as the crude product rapidly lost colour and decomposed.

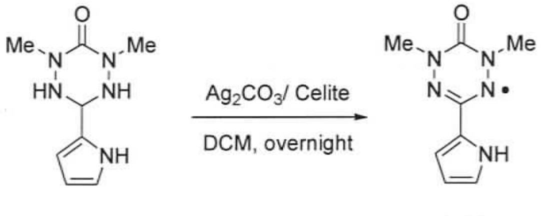

2.54 **2.58**

Scheme 2.9 – Oxidation of **2.54** to yield verdazyl **2.58**.

Owing to the instability of the pyrrole derivative, a methylated pyrrole derivative was prepared. Although this radical will not serve as a ligand, it is a useful derivative to explore the nature of the instability of pyrrole verdazyls. It was hypothesized that protecting the pyrrole nitrogen would eliminate the possibility of oligomerization and prevent reactivity of the pyrrole nitrogen.

Once again, the Fetizon reagent was used to oxidize **2.55** (Scheme 2.10), as periodate in water failed to generate the verdazyl. The methylation strategy seemed to be more successful as the verdazyl **2.59** was isolated in moderate yields. However, despite **2.59** appearing to be more stable towards column chromatography, elemental analysis was not able to confirm the desired purity. Although it is possible that the product could be decomposing on the column, it can be observed that the brilliant purple/red colour of the radical is lost over a few days, even in the solid state. Once again EPR, MS, and IR all confirmed the structural elements of **2.59.**

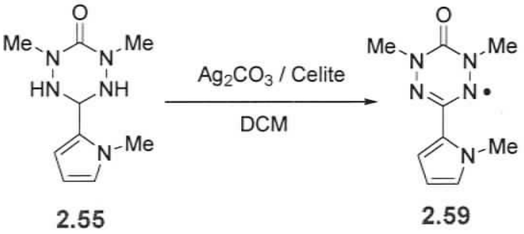

Scheme 2.10 – Oxidation of **2.55** to yield verdazyl **2.59**.

2.4.2.3 Synthesis of Oligopyridine-diradicals

The terpyridine diradical is a third compound in the series of oligopyridine diradicals, based on previously prepared diradicals **2.37** and **2.38**. Verdazyl **2.60** was prepared using ferricyanide as an oxidant because **2.56** has good solubility in DMF. The yields were variable, but the product was fully characterized with the exception of elemental analysis. Unfortunately the purity of this compound was low and attempts to purify it using column chromatography failed due to the affinity of **2.60** for the solid phase. It was also demonstrated that benzoquinone and Fetizon's reagent were successful oxidants, but once again the desired level of purity was not reached.

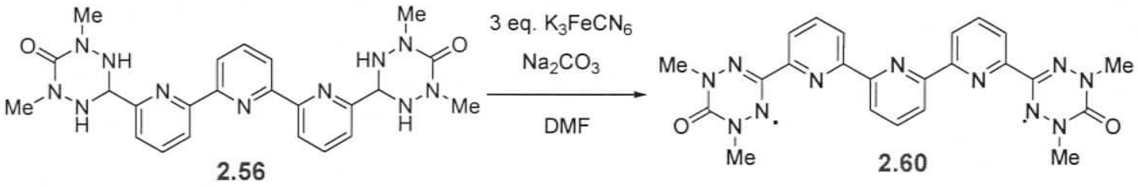

Scheme 2.11 - Oxidation of **2.56** to yield verdazyl **2.60**.

2.4.3 Electronic properties of *N*-heteroaromatic verdazyls

To gain further insight into the electronic structure of selected verdazyl radicals, their electronic nature was investigated using cyclic voltammetry and EPR. Possibly owing to the impure samples, cyclic voltammograms were complicated and had no indication of reversible behaviour. EPR studies suggest that the impurities are diamagnetic in nature, as quality EPR spectra of the radicals were obtained.

EPR spectra of the verdazyl radicals were recorded at room temperature and then simulated in order to determine the electron *g*-factors and hyperfine coupling constants (*a*). The spectra were found to be similar to previously reported 6-oxoverdazyl radicals, with hyperfine coupling (hfc) to four nearly equivalent nitrogen atoms of the verdazyl ring, and to the six protons of the methyl substituents.[112] The EPR spectrum of **2.59** represents one of the better resolved EPR spectra and is presented in Figure 2.18. The hyperfine coupling (hfc) reported in Table 2.4 shows that all of the verdazyls (even the diradical **2.60**) have a similar spin distribution, and the experimental spectra was simulated without incorporating any coupling to the C3 verdazyl substituent. This implies that any spin redistribution onto the C3 substituent is less than the spectral resolution (< 1 G). This is consistent with a nodal plane in the verdazyl SOMO, as predicted by HMO calculations.[165] The diradical **2.60** shows no evidence of radical-radical coupling at room temperature, although low temperature studies would be needed to determine the true multiplicity of the ground state.

Figure 2.18 - EPR spectrum of **2.59** in DCM at 298 K. The total spectral width is 80G. Experimental spectrum left a); simulated spectrum right b).

Table 2.4 - EPR parameters of heteroaromatic verdazyl radicals.

Compound	$a_{N2,4}$ (G)	$a_{N1,5}$ (G)	$a_{(methyl)}$ (G)	g-factor
2.57	6.5	5.3	5.3	2.0037
2.58	6.5	5.3	5.3	2.0038
2.59	6.5	5.3	5.3	2.0038
2.60	6.5	5.3	5.3	2.0039

2.5 Metal-radical complexes involving verdazyl radicals

2.5.1 Copper – imidazole verdazyl complexes

Copper(I) is a diamagnetic metal ion that often adopts tetrahedral coordination geometries. Although using a diamagnetic centre precludes metal-radical exchange, homoleptic bis-verdazyl complexes using diamagnetic transition metals allow for the investigation of the magnetic exchange between the coordinated verdazyls through the diamagnetic metal centre.

Tetrahedral copper complexes with their large coordination (109.5°) angles may require ligands with larger chelate angles. **2.15** has been discussed as a bipyridyl mimic because it has similar angles and distances between the ligating pair of nitrogens. Verdazyls with imidazole (or pyrrole) substituents possess a larger bite angle and may be more suitable as ligands for tetrahedral geometries (Figure 2.19). A typical ligand such as

2.15 has an N-N distance of 2.7Å, while an imidazole functionalized verdazyl has a much larger bite angle leading to an N-N distance of 2.9Å.

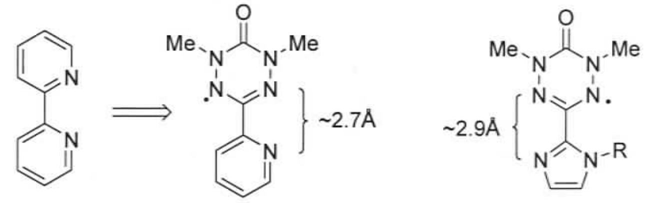

bipyridyl

2.15

R = H **2.35**
R = Me **2.57**

Figure 2.19 - Ligating distances in bidentate verdazyl radicals

Attempts at making metal complexes of imidazole verdazyls **2.35** and **2.57** using octahedral late transition metals were unsuccessful. However, tetrahedral copper (I) complexes using **2.35** and **2.57** were successfully prepared (Scheme 2.12). Reaction of two equivalents of **2.35** or **2.57**, with freshly prepared [Cu(CH_3CN)$_4$]PF_6 in acetonitrile provided complexes **2.61** or **2.62**, respectively as green powders (Scheme 2.12). Recrystallization afforded a microcrystalline solid but unfortunately x-ray quality crystals of this complex were not obtained after repeated recrystallization attempts. The structure was confirmed by elemental analysis, LSIMS, and FT-IR and UV-visible spectroscopies.

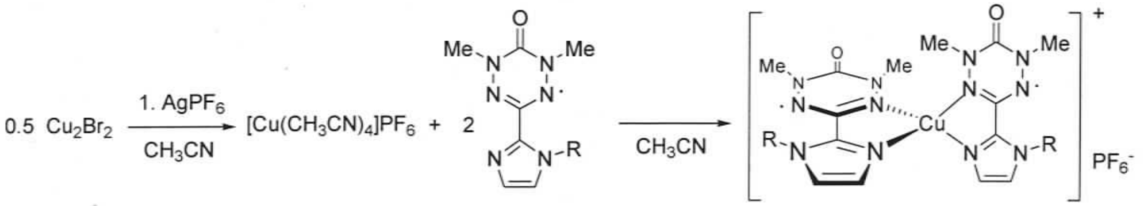

R = H **2.35**
R = Me **2.57**

R = H **2.61**
R = Me **2.62**

Scheme 2.12 - Preparation of [Cu(imidazole verdazyl)$_2$]PF_6 complexes.

Without a suitable crystal structure of the imidazole copper complexes the magnetic behaviour was not studied, but other spectroscopic properties suggest that these imidazole verdazyl radicals have similar features to the pyridyl verdazyl analogues. From UV-Vis analysis there is a modest bathochromic shift (Figure 2.20) between the free ligand and **2.62**. Bathochromic shifts are commonly observed for metal-verdazyl complexes.

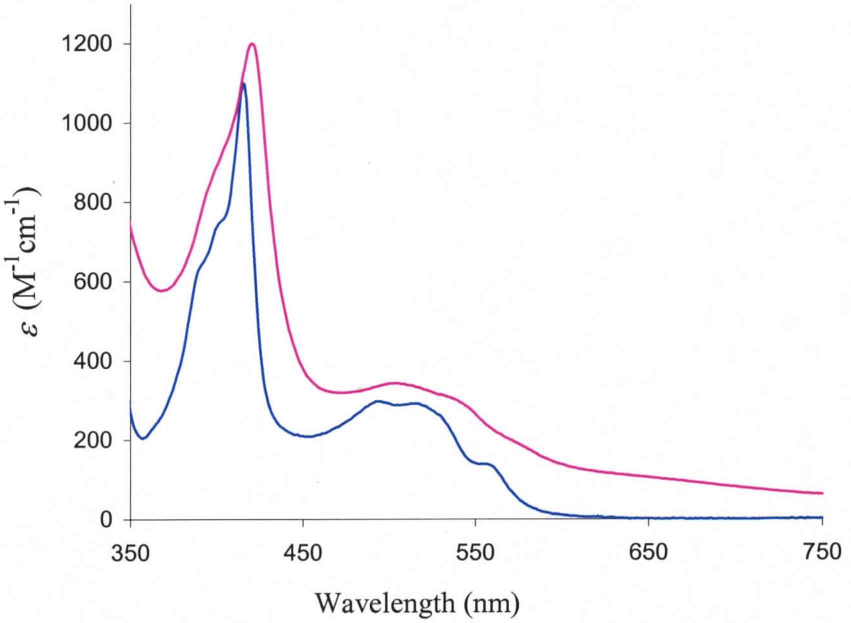

Figure 2.20 - UV-Vis of radical **2.57** (blue) and radical-Cu complex **2.62** (pink)

2.5.2 Attempted coordination of 2.60

A nitronyl-nitroxide diradical with a similar framework to ligand **2.60** has been previously prepared,[166] but there are no known transition metal complexes of terpyridine spaced diradicals. In 2001, Hicks and coworkers reported[167] some rather unusual magnetic properties from a co-crystallized sample of **2.15** and hydroquinone. Structural analysis showed that the verdazyls were stacked in a head-to-tale arrangement (Figure 2.21a). These stacks were insulated from each other by hydroquinone. The magnetic analysis of this material showed that there was strong antiferromagnetic coupling (J_{inter} = -58 cm^{-1}) between the radical and the authors surmised that the pyridine behaves as a magnetic coupling unit.

One advantage of diradical **2.60** over the nitronyl nitroxide analogue is that the planar features of the verdazyl ring should be less sterically demanding, and readily able to participate in π-stacking. Upon coordination of diradical **2.60** to a diamagnetic square planar metal ion (Pd or Pt), it may be possible to generate a molecular π-stacked diradical. It is predicted that metal complex **2.63** would have π-stacking distances similar to those observed in the organic solid state, making this a very useful molecule to probe the interactions between radicals that are separated by a pyridyl spacer (Figure 2.21b).

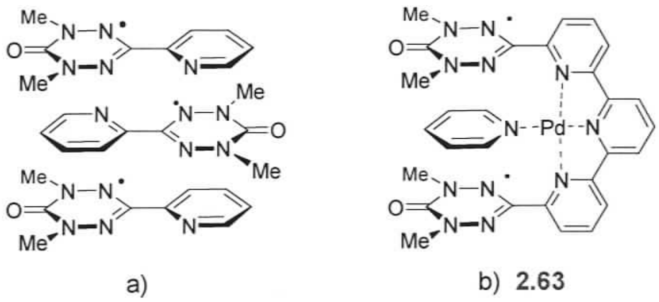

a)

b) **2.63**

Figure 2.21 – a) intermolecular π-stacking of **2.15** and b) possible intramolecular π-stacking using terpyridine-based diradical **2.60**

2.60 was also designed as the third molecule in a series of oligopyridine bridged diradicals, where the stability of the diradical modestly improves as the number of pyridyl units increases. Although diradical **2.60** is more stable than **2.37** and **2.38**, the radical is by no means robust. All attempts to coordinate **2.60** have been unsuccessful. This may be largely due to the instability of the diradical species. A demonstrative experiment that shows the instability of **2.60** is depicted in Scheme 2.13.

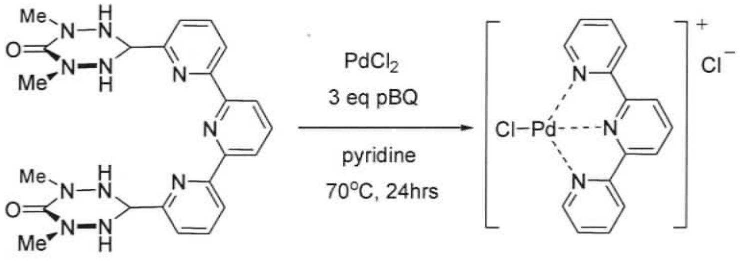

2.56

2.64

Scheme 2.13 – Attempted synthesis of a palladium coordination complex of **2.56**

An *in situ* oxidation-coordination was attempted using the tetrazane precursor **2.56**. While the ideal product would have been **2.63**, a surprising result emerged. Although not a quantitative yield, a significant amount (~70%) of **2.64** was recovered upon workup. This result suggests that the coordinated diradical is highly unstable and rapidly decomposes in the presence of a metal and oxidant to yield a coordinated terpyridine.

2.6 Summary

The imidazole-based radicals have been shown to effectively ligate to copper (I) centres. The homoleptic copper diradical complex **2.61** may prove to be a very interesting molecular building block, as **2.61** could be deprotonated and coordinated to other metal ions leading to 3D networks. Furthermore, magnetic studies using octahedral metal complexes of **2.15** have shown that the choice of metal dictates the nature of the interaction, and the verdazyl-metal magnetic exchange can be readily understood in terms of orbital orthogonality.

Generally, it has been shown that coordination to the metal centre helps to stabilize the verdazyl ligand. Recent attempts to coordinate diradicals such as **2.60** suggest that for some unstable radicals certain metal coordination may facilitate decomposition. In the case of diradicals, they seem to be stabilized by increasing the distance between radical centres, yet they are still significantly less stable than mono-radicals.

Although the electronic communication between metals and radicals is less understood, generally most *mono*-verdazyl radicals have the same electronic properties. However, it would appear that the C3 substituent significantly perturbs the electronics and stability of the verdazyl ring. It is uncertain if the pyrrole substituted verdazyls are less stable owing to the pyrrole unit or the electronic influence that they exert on the verdazyl ring. Regardless, pyrrole substituted verdazyls are not particularly well suited for materials chemistry.

The challenge of making more diverse ligand topologies, and extending the electronic and magnetic properties of these interesting molecules into 2- and 3-dimensions is the focus of the following chapter.

2.7 Experimental section

2.7.1 General synthetic procedures

Unless stated otherwise, all reactions and manipulations were carried out in air. Solvents were dried and distilled under argon prior to use (CH_2Cl_2 and CH_3CN from CaH_2; toluene, diethyl ether, and THF from sodium/benzophenone). All reagents were purchased from Aldrich or Strem Chemicals and used as received unless otherwise stated. Literature compounds that have been described herein are referenced in the appropriate sections that follow. $^1H/^{13}C$ NMR spectra were recorded on a Bruker AMX-300 MHz instrument unless otherwise stated. FT-IR spectra were recorded in solution using DCM as a solvent and NaCl cell or as KBr pressed discs on a Perkin-Elmer Spectrum One FT-IR spectrometer. EPR spectra were recorded in dilute deoxygenated (three freeze-pump-thaw cycles) solutions (~10^{-4} M) on a Bruker AMX360 spectrometer, and the spectra simulated using the WinEPR SimFonia program. Elemental analyses were carried out by Canadian Microanalytical Services Ltd., Vancouver, BC, Canada. Cyclic voltammetry (CV) experiments were performed with a Bioanalytical Systems CV50 voltammetric analyzer. The electrochemical cell consists of a three electrode setup containing DCM solutions of analyte (~1 mM), electrolyte (0.1 M $Bu_4N^+BF_4^-$) and ferrocene (stoichiometric with analyte), the last of which was added as an internal reference. UV-visible spectra were recorded on a Cary 5 spectrometer. Molar extinction coefficients were measured by taking the average extinction coefficient from two known concentrations. Mass spectra were recorded on a Finnigan 3300 or a Kratos Concept II spectrometer using electron impact (EI) or liquid secondary ion (LSIMS) sources. Melting points were recorded (uncorrected) using a Gallenkamp melting point apparatus. X-ray crystallography (chapter four and chapter five) was performed by the University of Alberta X-ray Crystallography Laboratory. Data was collected using a Bruker PLATFORM diffractometer equipped with a SMART 1000 CCD area detector. The structures were fully solved and refined by either Dr. Michael Ferguson or Dr. Robert McDonald. Full structure reports are given in the appendix of this dissertation.

2.7.2 Magnetic measurements

All magnetic data presented was obtained by Professor Laurence Thompson at the Memorial University of Newfoundland (St. John's, Nfld.). In general, variable temperature magnetic data (2-300 K) were obtained with a Quantum Design MPMS5S SQUID (superconducting quantum interference device) magnetometer operating at 0.1–0.5 T. Calibrations were carried out with a palladium standard cylinder and temperature errors were determined with $[H_2TMEN][CuCl_4]$.

In most cases magnetic data modeling was accomplished using the computer program Microcal Origin 7.0. For **2.42** and **2.43,** magnetic modeling was accomplished using the computer program MAGMUN, developed by Prof. Laurence K. Thompson and colleagues (www.ucs.mun.ca/~lthomp/). Unless otherwise stated, all models were derived using the appropriate spin Hamiltonian describing the spin system under investigation.[3]

Parameters used in magnetic modeling, other than the previously described *J*, are defined as follows:

ρ = fraction of paramagnetic impurity

θ = intermolecular interaction parameter

TIP = temperature independant paramagnetism

g_{rad} = Landé *g*-factor for the verdazyl radical component of the spin system (fixed at 2.0037 based on EPR studies of the free verdazyl ligands).

g_M = Landé *g*-factor for the transition metal component of the spin system.

2.7.3 Synthesis

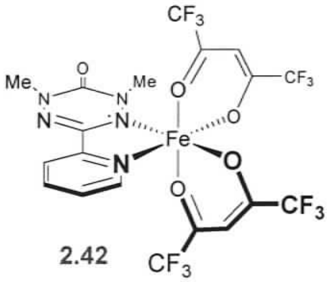

2.42

1,5-Dimethyl-3-(pyridin-2′-yl)-6-oxoverdazylbis-(1,1,1,5,5,5-hexafluoroacetylacetonato)iron(II) (2.42) - A solution of **2.15:hydroquinone**[149](172.0 mg, 0.55 mmol) in 15 mL of CH_2Cl_2 was added dropwise to a solution of $Fe(hfac)_2{\bullet}2H_20$ (276.9 mg, 0.55 mmol) in 40 mL of heptane. Immediately the reaction mixture turned deep red. After stirring for 45 min. a precipitate formed and the reaction mixture was filtered in air. The solvent was removed *in vacuo* leaving a deep red microcrystalline solid that was recrystallized from hexanes, yield 313 mg (84%). IR (KBr): 1715(s), 1637(s), 1602(m), 1555(m), 1528(m), 1475(s), 1410(w), 1347(m), 1256(s), 1207(s), 1143(s), 1099(m), 1051(w), 1031 (w), 1019(w), 949(w), 795(m), 754(w), 742(w), 714(w), 666(s), 645(w), 586(m), 547(w) 538(w) cm^{-1}. Anal. Calculated for $C_{19}H_{12}N_5O_5F_{12}Fe$: C, 33.85; H, 1.79; N, 10.39. Found: C, 34.22; H, 1.90; N, 10.40. λ_{max} (CH_2Cl_2) (ε($M^{-1}cm^{-1}$)): 426 nm (4240). MS (FAB LR): *m/z* 674 ($M + H^+$), 654 (M^+ – **2.15**), 204 (**2.15**). Mp. 100-103 °C (decomposes).

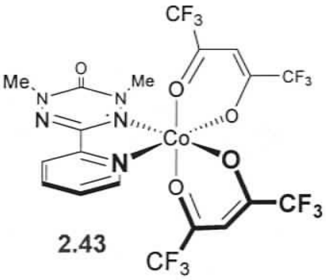

2.43

1,5-Dimethyl-3-(pyridin-2′-yl)-6-oxoverdazylbis-(1,1,1,5,5,5-hexafluoroacetylacetonato)cobalt(II)) (2.43) - A solution of **2.15:hydroquinone**[149] (315.0 mg, 1.0 mmol) in 20 mL of CH_2Cl_2 was added dropwise to a solution of $Co(hfac)_2{\bullet}2H_20$ (514 mg, 1.0 mmol) in 50 mL of heptane. Immediately the reaction mixture turned red. After stirring for 45 min. a precipitate formed and the reaction mixture was filtered in air. The solvent was removed *in vacuo* leaving a bright red needle-like solid that was recrystallized from hexanes, yield 577 mg (85%). IR (KBr): 1713(s), 1641(s), 1604(s), 1558(m), 1531(s), 1456(s), 1411(m), 1349(m), 1255(s), 1210(s), 1143(s), 1098(m), 1053(w), 1034 (w), 948(w), 795(m), 754(w), 743(w), 714(w), 669(s), 647(w), 586(m), 549(w) 538(w) cm^{-1}. Anal. Calculated for $C_{19}H_{12}N_5O_5F_{12}Co$: C, 33.70; H, 1.79; N, 10.34. Found: C, 33.59; H, 1.90; N, 10.34. λ_{max} (CH_2Cl_2) (ε($M^{-1}cm^{-1}$)): 427 nm (4054). MS (EI LR): *m/z* 676 (M^+), 658 (M^+ – HF), 470 (M^+ – hfac). Mp. 149-152 °C (decomposes).

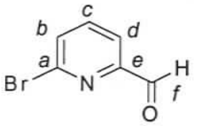

2.48

6-Bromopyridine-2-carbaldehyde[152, 154] **(2.48)** - *n*-BuLi (1.6M in hexanes, 26.6 mL) was diluted by THF (50 mL) and cooled to –75 °C. To this stirring mixture, a solution of dibromopyridine (10 g, 42.2 mmol) in THF (35 mL) was added dropwise, maintaining a temperature at/or below –70 °C (~1.5 hours). Once the dropwise addition was complete the resulting dark green solution (–70 °C) was stirred for 30 min. Then over a 30 sec. period, excess anhydrous DMF (4.9 mL, 63.3 mmol) was added.

Upon the electrophile addition the reaction temperature elevated to –40 °C, and the dark green solution became a dark turquoise colour. The mixture was then cooled to –70 °C and the acetone/dry ice bath was removed and the reaction warmed to 0 °C. The reaction was then quenched with MeOH (30 mL) resulting in a yellow transparent solution. The reaction mixture was then extracted from aqueous saturated $NaHCO_3$ (100 mL) with CH_2Cl_2 (3× 75 mL). The organic fractions were combined and the solvent was removed under reduced pressure. The crude aldehyde was purified using column chromatography (silica, CH_2Cl_2, $R_f = 0.50$) yielding 7.4g (94.2%) of the aldehyde product (pure by TLC and ^{1}H-NMR). For crystalline **2.49** the product can be recrystallized from hexane. ^{1}H NMR ($CDCl_3$): δ 9.97 (s, 1H, H_f), 7.19 (dd, $J = 6.5$, 1.8 Hz, 1H, H_c), 7.76–7.65 (m, 2H, H_d, H_b). ^{13}C NMR ($CDCl_3$): δ 191.8 (C_f), 153.7(C_e), 142.7(C_a), 139.6(C_c), 132.9(C_d), 120.5(C_b). FT-IR (KBr): 3040 (w), 2872 (w), 1731 (s), 1574 (m), 1554 (m), 1435 (s), 1412 (m), 1351 (w), 1219 (m), 1212 (m), 1163 (w), 1118 (s), 986 (m), 856 (m), 796 (s), 708 (m), 633 (m) cm^{-1}. Anal. Calculated for C_6H_4BrNO: C, 38.74; H, 2.17; N, 7.53. Found: C, 38.89; H, 2.19; N, 7.51. λ_{max} (MeOH) (ε($M^{-1}cm^{-1}$)): 268 nm (6.7×10^3). MS (LSIMS): *m/z* 186, 188 {$(MH)^+$, 100%}. HR-MS: 184.9474 +/- 0.0003 (184.9476 for M^+ C_6H_4BrNO). Mp 80-81 °C.

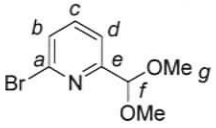

2.49

2-Bromo-6-(dimethoxymethyl) pyridine[157] **(2.49)** – **2.48** (15.0 g, 80.6 mmol) was combined with MeOH (150 mL, sieve dried), a catalytic amount of *para*-tolylsulphonic acid hydrate (300mg) and trimethylorthoformate (35 mL, 322.0 mmol) resulting in a yellow solution. This mixture was then heated to reflux for 4 hours resulting in a dark green/blue solution. Cooling the mixture to room temperature and removing most of the solvent under reduced pressure gave a crude liquid product. The product was distilled under reduced pressure (bp. 85 °C @ 1.5 mm) to yield **2.49** as a clear colourless liquid, 18.0 g (96.0%). ^{1}H NMR ($CDCl_3$): δ 7.55 (t, J = 7.6 Hz, 1H, H_c), 7.47 (d, $J = 7.6$ Hz, 1H, H_d), 7.41(d, $J = 7.6$ Hz, 1H, H_b), 5.25 (s, 1H, H_f), 3.36 (s, 6H, H_g). ^{13}C NMR ($CDCl_3$): δ 158.9(C_e), 141.5(C_a), 139.0(C_c), 128.1(C_d), 120.1(C_b), 103.7(C_f), 54.1(C_g). FT-IR (Neat): 3078 (w), 2993 (m), 2935 (s), 2830 (s), 1581 (s), 1557 (s), 1437 (s), 1408 (s), 1335 (s), 1271 (w), 1194 (s), 1155 (s), 1123 (br s), 1061 (br s), 982 (s), 921 (m), 880 (w), 795 (s), 750 (m), 712 (m), 653 (w), 638 (w), 618 (w) cm^{-1}. Anal. Calculated for $C_8H_{10}BrNO_2$: C, 41.40; H, 4.34; N, 6.04. Found: C, 41.01; H, 4.20; N, 5.82. λ_{max} (MeOH) (ε(M^{-1}cm^{-1})): 268 nm (5.5×10^3). MS (LSIMS): *m/z* 201, 157, 233 {(MH)$^+$, 100%}. HR-MS: 230.9892 +/- 0.0006 (230.9895 for M$^+$ $C_8H_{10}BrNO_2$).

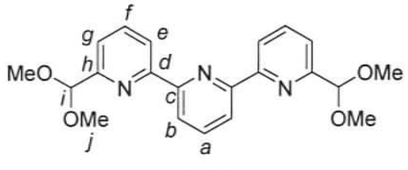

2.51

6,6''-Bis-dimethoxymethyl-[2,2';6',2'']terpyridine[161] **(2.51)** - *n*-BuLi (1.6M in hexanes, 15.3 mL, 24.6 mmol) was solubilized in THF (25 mL) and cooled to –75 °C. To this, a solution of **2.59** (5.7 g, 24.6mmol) in THF (15 mL) was added dropwise, maintaining a temperature at/or below –70 °C. Once the dropwise addition was complete the resulting dark red solution was stirred for 30 min. Then over a 20 min period a cold (0 °C) solution of zinc chloride (1.0M in Et_2O, 27 mL) was added maintaining a temperature at/or below –70 °C. After the addition was complete, the reaction was warmed to 0 °C and $Pd(PPh_3)_4$ (0.57 g, 2 mol%) and dibromopyridine (2.21 g, 9.3 mmol) were added. The reaction mixture was then stirred for 30 min followed by refluxing under argon for ~20 hrs, resulting in a large quantity of white precipitate. After leaving the mixture in a freezer overnight, the cold mixture was filtered and washed with cold THF. The precipitate was then solubilized in an aqueous saturated $NaHCO_3$ solution and extracted vigorously from a saturated EDTA solution using DCM. The organic fractions were then dried over $MgSO_4$, and the solvent removed under reduced pressure yielding 2.8g of **2.51** (78.6%). ^{1}H NMR ($CDCl_3$): δ 8.56 (d, J = 7.5 Hz, 2H, H_e), 8.50 (d, J = 7.5 Hz, 2H, H_b), 7.90 (t, J = 7.5 Hz, 1H, H_a), 7.87 (t, J = 7.5 Hz, 2H, H_f), 7.56 (d, J = 7.5 Hz, 2H, H_g). ^{13}C NMR ($CDCl_3$): δ 156.9(C_h), 155.7(C_d), 155.3(C_c), 137.9(C_a), 137.6(C_f), 121.5(C_e), 121.2(C_g), 121.0(C_b), 104.8(C_i), 54.1(C_j). FT-IR (KBr): 2994 (m), 2936 (m), 2890 (m), 2833 (m), 1567 (s), 1434 (s), 1357 (m), 1338 (s), 1254 (m), 1197 (s), 1114 (s), 1059 (br. s), 984 (s), 921 (m), 830 (m), 790 (s), 746 (m), 697 (m), 633 (s) cm^{-1}. Anal. Calculated for $C_{21}H_{23}N_3O_4$: C, 66.13; H, 6.08; N, 11.02. Found: C, 65.81; H, 6.10; N, 10.91. λ_{max} ($CHCl_3$) (ε(M^{-1}cm^{-1})): 283 nm (4.3×10^4). MS (LSIMS): *m/z* 382 {(MH)$^+$, 100%}, 350 {(M-CH_3O)$^+$, 90%}. HR-MS: 382.1767 +/- 0.0012 (382.1767 for MH$^+$ $C_{21}H_{24}N_3O_4$). Mp 82-84 °C.

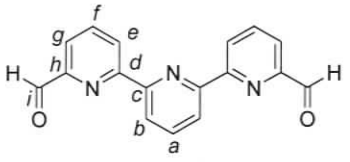

2.47

[2,2';6',2'']Terpyridine-6,6''-dicarbaldehyde[162, 163, 166, 168] **(2.47)** - Acetic acid (15 mL) and water (25 mL) were combined with **2.51** (2.0 g, 5.2 mmol) resulting in a milky white mixture. This mixture was stirred vigorously and heated to reflux for 1hr. After cooling to room temperature the solution was evaporated to near dryness and (neutralized) extracted from a saturated $NaHCO_3$ solution using $CHCl_3$ (3 × 50 mL). The organic extracts were combined, dried over $MgSO_4$, and the solvent removed under reduced pressure to yield 1.4g of **2.47** (92.3%). Higher purity can be achieved by recrystallizing from $CHCl_3$. ^{1}H NMR [500MHz] ($CDCl_3$): δ 10.19 (s, 2H, H_i), 8.84 (dd, J = 7.5, 1.4 Hz, 2H, H_g), 8.65 (d, J = 7.5, 2H, H_e), 8.08-7.99 (m, 5H, H_f, H_a, H_b). ^{13}C NMR ($CDCl_3$): δ 193.9(C_i), 156.7(C_h), 154.7(C_c) 152.6(C_d), 138.5(C_a), 138.2(C_f), 125.38(C_g), 122.1(C_e), 121.8(C_b). FT-IR (KBr): 3079 (m), 2855 (m), 1722 (s), 1584 (s), 1575 (s), 1563 (m), 1460 (m), 1451 (m), 1435 (s), 1386 (w), 1347 (m), 1284 (w), 1257 (m), 1218 (m), 1151 (w), 1110 (m), 1074 (m), 992 (m), 922 (w), 867 (m), 792 (s), 728 (m), 671 (m), 633 (m) cm^{-1}. Anal. Calculated for $C_{17}H_{11}N_3O_2$: C, 70.58; H, 3.83; N, 14.53. Found: C, 70.35; H, 3.77; N, 15.32. λ_{max} ($CHCl_3$) (ε($M^{-1}cm^{-1}$)): 292 nm (4.2×10^4). MS (EI): m/z 289 {$(M)^+$, 100%}, 289 {$(M\text{-}CHO)^+$, 60%}. HR-MS: 290.0931 +/- 0.0002 (290.0930 for MH^+ $C_{17}H_{12}N_3O_2$). Mp 231-232 °C (decomp. 234 °C).

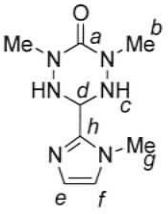

2.53

2,4-Dimethyl-6-(1-methyl-1H-imidazol-2-yl)-[1,2,4,5]tetrazinan-3-one (2.53) - To a gently refluxing solution of **2.52** (2.146 g, 18.2 mmol) in methanol (10 mL) was added dropwise (over 3 hours) a solution of **2.44** (2.0 g, 18.2 mmol) in methanol (200 mL). After the addition was complete the reaction was gently heated to reflux overnight (10 hours). The reaction mixture (light yellow) was then cooled and the solvent removed under reduced pressure. The resulting solid was then purified via repeated trituration using EtOAc to yield pure **2.53**. More product was collected from the EtOAc washings by precipitating the product with Et_2O (2.96 g, 77.5%). ^{1}H NMR (DMSO): δ 7.14 (s, 1H, H_e), 6.83 (s, 1H, H_f), 5.58 (d, 2H, J=11Hz, H_c), 5.07 (t, 1H, J=11Hz, H_d), 3.68 (s, 3H, H_g), 2.95 (s, 6H, H_b) ^{13}C NMR ($CDCl_3$): δ 154.6(C_a), 141.7(C_h), 128.0(C_e), 122.3(C_f), 63.0(C_d), 38.1(C_b), 32.9(C_g) ppm. FT-IR (KBr): 3200 (m), 3142 (m), 3118 (m), 2951 (m), 1633 (s), 1537 (m), 1491 (s), 1440 (s), 1385 (m), 1314 (w), 1284 (m), 1274 (m), 1192 (m), 1166 (w), 1124 (m), 1082 (m), 1046 (w), 963 (s), 949 (m), 903 (s), 887 (s), 749 (m), 739 (m), 727 (s), 684 (m), 639 (m), 582 (m), 535 (m), 461 (w) cm^{-1}. Anal. Calculated for $C_8H_{14}N_6O$: C, 45.70; H, 6.71; N, 39.97. Found: C, 45.75; H, 6.74; N, 40.41. $\lambda_{max}(CH_2Cl_2)(\varepsilon(M^{-1}cm^{-1})$: 229 nm (6.0×10^3). MS (EI): *m/z* 210 {M^+, 50%}. HR-MS: 210.1227 +/- 0.0002 (210.1229 for M^+ $C_8H_{14}N_6O$). Mp 176 °C (decomposes).

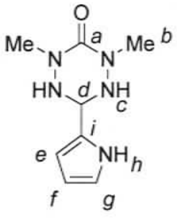

2.54

2,4-Dimethyl-6-(1H-pyrrol-2-yl)-[1,2,4,5]tetrazinan-3-one (2.54) - To a gently refluxing solution of **2.52** (2.0 g, 16.9 mmol) in methanol (10 mL) was added dropwise (over 3 hours) a solution of **2.45** (1.61 g, 16.9 mmol) in methanol (200 mL). After the addition was complete the reaction was gently heated to reflux overnight (10 hours). The reaction mixture (light yellow) was then cooled and the solvent removed under reduced pressure. The resulting solid was then purified via repeated trituration using EtOAc to yield pure **2.54** (2.3 g, 70%). ^{1}H NMR (DMSO): δ 10.70 (s, 1H, H_h), 6.67 (d, 1H, *J*=1.6Hz, H_g), 6.02 (s, 1H, H_e), 5.97 (dd, 1H, *J*=1.6, 1Hz, H_f), 5.55 (d, 2H, *J*=8.5Hz, H_c), 4.84 (t, 1H, *J*=8.5Hz, H_d), 2.94 (s, 6H, H_b) ^{13}C NMR (DMSO): δ 154.4(C_a), 126.6(C_i), 117.6(C_g), 107.4(C_e), 105.6(C_f), 64.7(C_d), 37.8(C_b) ppm. FT-IR (KBr): 3266 (s), 3248 (s), 3149 (m), 3127 (m), 3112 (m), 2980 (m), 2930 (m), 2874 (m), 1586 (s), 1573 (s), 1510 (s), 1492 (s), 1430 (s), 1398 (s), 1388 (s), 1346 (m), 1320 (m), 1238 (m), 1220 (m), 1119 (s), 1084 (m), 1062 (w), 1042 (w), 1022 (w), 974 (s), 938 (w), 883 (w), 865 (m), 807 (m), 748 (m), 729 (m), 715 (m), 679 (m), 607 (m), 562 (m), 538 (m) cm^{-1}. Anal. Calculated for $C_8H_{13}N_5O$: C, 49.22; H, 6.71; N, 35.87. Found: C, 49.26; H, 6.57; N, 35.85. $\lambda_{max}(CHCl_3)(\varepsilon(M^{-1}cm^{-1})$: 307 nm (4.9×10^3) MS (EI): *m/z* 195 {M^+, 90%}, 93 {$[M-102]^+$, 100%}. HR-MS: 195.1120 +/- 0.0009 (195.1120 for M^+ $C_8H_{13}N_5O$). Mp 143-146 °C.

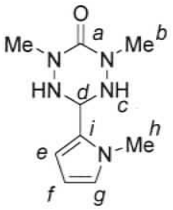

2.55

2,4-Dimethyl-6-(1-methyl-1H-pyrrol-2-yl)-[1,2,4,5]tetrazinan-3-one (2.55) - To a gently refluxing solution of **2.52** (2.165 g, 18.3 mmol) in methanol (10 mL) was added dropwise (over 3 hours) to a solution of **2.46** (2.0g, 18.3 mmol) in methanol (200 mL). After the addition was complete the reaction was gently heated to reflux overnight (10 hours).

The reaction mixture (light yellow) was then cooled and the solvent removed under reduced pressure . The resulting solid was then purified via repeated trituration using $CHCl_3$ or EtOAc to yield pure **2.55**. More product was collected from the EtOAc washings by precipitating the product with Et_2O (2.87 g, 74.8%). ^1H NMR (DMSO): δ 6.69 (dd, 1H, *J*=2.0, 1.0Hz, H_g), 6.02 (dd, 1H, *J*=2.0, 1.0Hz, H_e), 5.91 (dd, 1H, *J*=2.0, 1.0Hz, H_f), 5.50 (d, 2H, *J*=10Hz, H_c), 4.89 (t, 1H, *J*=10Hz, H_d), 3.63 (s, 3H, H_h), 2.95 (s, 6H, H_b) ^{13}C NMR (DMSO): δ 154.6(C_a), 126.9(C_i), 122.7(C_g), 106.4(C_e), 106.1(C_f), 63.6(C_i), 37.7(C_d), 33.8(C_h) ppm. FT-IR (KBr): 3259 (s), 3246 (s), 3123 (s), 3098 (s), 2975 (m), 2906 (m), 2874 (m), 1599 (s), 1595 (m), 1554 (s), 1509 (s), 1485 (s), 1432 (s), 1387 (s), 1347 (m), 1316 (m), 1295 (m), 1228 (m), 1166 (w), 1126 (s), 1101 (m), 1089 (m), 1056 (m), 1033 (m), 1010 (m), 972 (s), 934 (m), 862 (m), 798 (m), 788 (m), 739 (s), 727 (s), 689 (m), 678 (m), 625 (w), 613 (w), 549 (m), 531 (m) cm^{-1}. Anal. Calculated for $C_9H_{15}N_5O$: C, 51.66; H, 7.23; N, 33.47. Found: C, 51.77; H, 7.40; N, 33.48. $\lambda_{max}(CH_2Cl_2)(\varepsilon(M^{-1}cm^{-1})$: 306 nm ($5.0\times 10^3$). MS (EI): *m/z* 209 {$M^+$, 100%}, 106 {$[M-103]^+$, 90%}. HR-MS: 209.1274 +/- 0.0002 (209.1277 for M^+ $C_9H_{15}N_5O$). Mp 147-150 °C.

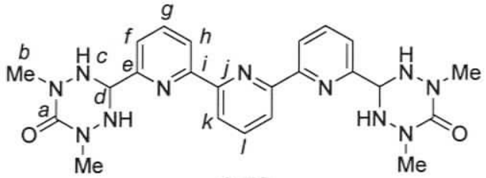

2.56

[2,2';6',2'']Terpyridine-6,6''-bis(1,5-dimethyl-1,2,4,5-tetrazane-6-oxide-3-yl) (2.56) - **2.52** (1.02 g, 8.6 mmol) was solubilized in 15 mL of MeOH/$CHCl_3$ (1:1) and gently heated to reflux. To this gently refluxing solution **2.47** (1.25 g, 4.32 mmol) in $CHCl_3$/MeOH (1:1), (175 mL) was added dropwise over 3hrs using a pressure equalizing dropping funnel. After the addition was complete the reaction was gently heated to reflux overnight (10 hrs). The solution was then cooled and solvent removed to yield a white/yellow solid. The product was triturated using hot ethyl acetate, yielding 1.7 g (80.4%) of **2.56**. ^1H NMR (DMSO): *δ* 8.72 (d, *J* = 8 Hz, 2H, H_h), 8.61 (d, *J* = 8 Hz, 2H, H_k), 8.14 (t, *J* = 8 Hz, 1H, H_l), 8.05 (t, *J* = 8 Hz, 2H, H_g), 7.65 (d, *J* = 8 Hz, 2H, H_f), 5.83 (d, *J* = 10.5 Hz, 4H, H_c), 5.02 (t, *J* = 10.5 Hz, 2H, H_d), 3.01 (s, 12H, H_b). ^{13}C NMR (MeOH): *δ* 157.2(C_a), 156.9(C_e), 156.3(C_i), 155.2(C_j), 139.6(C_g), 139.4(C_l), 124.9(C_f), 122.9(C_h), 122.4(C_k), 70.7(C_d), 38.4(C_b). FT-IR (KBr): 3421 (m), 3242 (m), 3073 (w), 2931 (m), 2871 (w), 1628 (s), 1569 (s), 1504 (m), 1434 (s), 1389 (m), 1312 (w), 1267 (w), 1241 (w), 1110 (br m), 1080 (m), 992 (w), 952 (w), 888 (w), 800 (m), 731 (w), 633 (w), 530 (w) cm^{-1}. Anal. Calculated for $C_{23}H_{27}N_{11}O_2$: C, 56.43; H, 5.56; N, 31.47. Found: C, 56.18; H, 5.76; N, 31.50. λ_{max} ($CHCl_3$) ($\varepsilon(M^{-1}cm^{-1})$): 290 nm ($5.8\times10^4$). MS (LSIMS): *m/z* 490{$(MH)^+$, 100%}. HR-MS: 490.2437 +/- 0.0010 (490.2427 for MH^+ $C_{23}H_{28}N_{11}O_2$). Mp 199-201 °C (decomp).

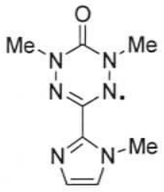

2.57

1,5-Dimethyl-3-(1-methyl-1H-pyrrol-2-yl)-6-oxoverdazyl (2.57) - To a vigorously stirred 'near solution' of **2.53** (0.15 g, 0.71 mmol) in distilled water (20 mL) was added quickly dropwise (via a pipette) an aqueous solution (10 mL) of $NaIO_4$ (0.229 g, 1.07 mmol) resulting in a deep cherry red solution. Stirring was continued for 10 min and then the reaction mixture was cooled in an ice bath for 30 min. This resulted in the precipitation of a microcrystalline red solid **2.57**. The red product was isolated by vacuum filtration, washed with ~30 mL of cold distilled water, and air dried to yield (0.103 g, 68%). FT-IR (KBr): 3131 (m), 3115 (m), 3031 (w), 2957 (w), 1674 (s), 1489 (m), 1464 (m), 1424 (m), 1382 (m), 1288 (m), 1259 (m), 1147 (m), 1088 (w), 1048 (m), 1021 (m), 993 (w), 914 (m), 769 (m), 728 (m), 717 (m), 687 (w), 643 (m), 623 (m), 593 (w), 547 (m), 536 (m) cm^{-1}. Anal. Calculated for $C_8H_{11}N_6O$: C, 46.37; H, 5.35; N, 40.56. Found: C, 46.20; H, 5.38; N, 40.68. $\lambda_{max}(CH_2Cl_2)(\varepsilon(M^{-1}cm^{-1})$: 415 nm ($1.1\times 10^3$), 493 nm ($4.1\times 10^2$). MS (LSIMS): *m/z* 207 {MH^+, 100%}, 107 {80%}. HR-MS: 207.0991 +/- 0.0003 (207.0994 for M^+ $C_8H_{11}N_6O$). Mp 165 °C (decomposes).

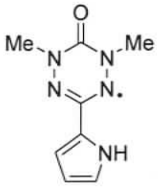

2.58

1,5-Dimethyl-3-(1H-pyrrol-2-yl)-6-oxoverdazyl (2.58) – **2.54** (100 mg, 0.52 mmol) was solubilized in DCM and excess silver carbonate (430 mg, 1.5 mmol) and Celite (2 g) was added to the reaction which was stirred at room temperature overnight 12 hrs. The reaction mixture was then filtered through a 2.5 cm plug of neutral alumina and the solvent removed under reduced pressure to yield the crude **2.58**. Unfortunately attempts to purify the product using column chromatography resulted in decomposition of the material, thus the crude was analyzed and was obtained in quantitative yields. FT-IR (KBr): 3401 (m), 2974 (w), 2938 (w), 2877 (w), 1676 (s), 1618 (m), 1560 (w), 1453 (m), 1433 (m), 1385 (m), 1345 (m), 1116 (m), 1089 (w), 1031 (m), 921 (w), 882 (w), 818 (w), 738 (m), 602 (w), 558 (w) cm^{-1}. Anal. Calculated for $C_8H_{10}N_5O$: C, 49.99; H, 5.24; N, 36.44. Found: C, 50.41; H, 5.80; N, 36.38. $\lambda_{max}(CH_2Cl_2)(\varepsilon(M^{-1}cm^{-1})$: 422 nm (9.7× 10^2), 565 nm (6.2× 10^2). MS (EI): *m/z* 193 {MH^+, 100%}, 192 {M^+, 30%}. HR-MS: 193.0961 +/- 0.0009 (193.0964 for MH^+ $C_8H_{11}N_5O$).

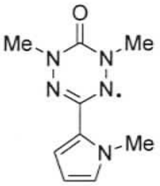
2.59

1,5-Dimethyl-3-(1-methyl-1H-pyrrol-2-yl)-6-oxoverdazyl (2.59) – **2.55** (100 mg, 0.49 mmol) was solubilized in DCM and excess silver carbonate (410 mg, 1.5 mmol) and Celite (2g) was added. The reaction was stirred at room temperature overnight (12 hrs). The reaction mixture was then rapidly filtered through a 2.5 cm plug of neutral alumina, and the solvent removed under reduced pressure to yield the crude **2.59**. Unfortunately attempts to purify the product using column chromatography resulted in decomposition of the material, thus the crude was analyzed and obtained in quantitative yields. FT-IR (KBr): 3108 (w), 2939 (w), 1682 (s), 1614 (m), 1533 (w), 1466 (m), 1437 (m), 1382 (m), 1337 (m), 1259 (m), 1092 (w), 1054 (m), 966 (w), 884 (w), 803 (w), 730 (s), 607 (w), 556 (w), 487 (w) cm^{-1}. Anal. Calculated for $C_9H_{12}N_5O$: C, 52.42; H, 5.87; N, 33.96. Found: C, 53.05; H, 6.38; N, 33.38. $\lambda_{max}(CH_2Cl_2)(\varepsilon(M^{-1}cm^{-1})$: 423 nm (1.0 × 10^3), 562 nm (5.8 × 10^2). MS (EI): *m/z* 207 {MH^+, 100%}, 206 {$[M]^+$, 30%}, 107{$[M-C_3H_6N_3O]^+$, 90%}. HR-MS: 207.1117 +/- 0.0003 (207.1120 for MH^+ $C_9H_{13}N_5O$).

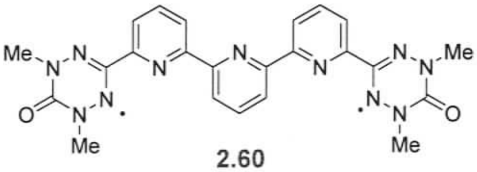
2.60

[2,2';6',2'']Terpyridine-6,6''-bis(1,5-dimethyl-6-oxoverdazyl-3-yl) (2.60) - A vigorously stirred slurry of **2.56** (0.15 g, 0.31 mmol) in DMF (8 mL) was heated until complete dissolution of the solid was observed. A solution of $K_3Fe(CN)_6$ (0.61 g, 1.84 mmol) in aqueous Na_2CO_3 solution (10 mL, 0.5 M) was added by pipette in large portions resulting in a colour change to deep orange and the precipitation of a white solid. Distilled water (~10 mL) was added to the mixture to dissolve the white precipitate. The reaction was then left to stir for 30 min and then put in an ice bath for 30 min after which time it was filtered and washed with water, followed by diethyl ether, yielding **2.60**, 0.105g (70.9%). FT-IR (KBr): 3066 (m), 2938 (m), 1693 (s), 1563 (s), 1537 (s), 1460 (s), 1370 (s), 1258 (m), 1173 (w), 1152 (w), 1124 (w), 1078 (w), 1027 (w), 993 (w), 820 (m), 763 (m), 737 (w), 701 (m) 638 (m), 540 (m) cm^{-1}. Anal. Calculated for $C_{23}H_{21}N_{11}O_2$: C, 57.14; H, 4.38; N, 31.87. Found: C, 56.30; H, 4.44; N, 31.06. λ_{max} ($CHCl_3$) ($\varepsilon(M^{-1}cm^{-1})$): 297 nm ($4.6\times10^4$), 401 nm ($2.2\times10^3$). MS (LSIMS): *m/z* 484 {$(MH)^+$, 100%}, 384 {$(MH-C_3H_6N_3O)^+$, 50%}. HR-MS: 484.1959 +/- 0.0010 (484.1958 for MH^+ $C_{23}H_{22}N_{11}O_2$). mp 160 °C (decomposes).

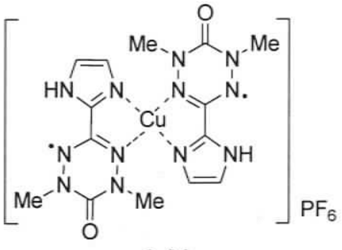

2.61

Bis-(1,5-dimethyl-3-{*1H*-imidazol-2'-yl}-6-oxoverdazyl)-copper (I) hexafluorophosphate (2.61) - To a green solution of Cu_2Br_2 (82 mg, 0.29 mmol) in MeCN (10 mL), was added silver hexafluorophosphate (145 mg, 0.57 mmol) in MeCN (5 mL) resulting in the formation of a gray precipitate (AgCl). The precipitate was filtered away, and to the filtrate was added a solution of **2.35**[149] (225 mg, 1.15 mmol) in MeCN (5 mL) resulting in a dark red/brown solution. The solution volume was reduced and the product was precipitated with Et_2O. The product was then recrystallized twice from acetone/Et_2O (240 mg, 70.4%). FT-IR (KBr): 3133 (w), 2951 (w), 1693 (s), 1574 (w), 1486 (m), 1403 (w), 1367 (w), 1294 (m), 1271 (m), 1129 (w), 1101 (m), 1041 (w), 1002 (w), 924 (w), 843 (s), 766 (w), 730 (w), 715 (w), 641 (w), 618 (w), 559 (m), 546 (m), 536 (m), 505 (w), 493 (w) cm^{-1}. Anal. Calculated for $C_{14}H_{18}CuF_6N_{12}O_2P$: C, 28.27; H, 3.05; N, 28.25. Found: C, 28.38; H, 3.00; N, 28.19. λ_{max}(MeOH)($\varepsilon(M^{-1}cm^{-1})$): 420 nm ($3.6 \times 10^3$), 505 nm ($1.0 \times 10^3$). MS (LSIMS): *m/z* 449 {$[M-PF_6]^+$, 100%}, 256 {$[M-C_7H_9N_6OPF_6]^+$, 85%}. HR-MS: 449.0968 +/- 0.0015 (449.1072 for $[M-PF_6]^+$ $C_{14}H_{18}CuN_{12}O_2$). Mp 182 °C (decomposes).

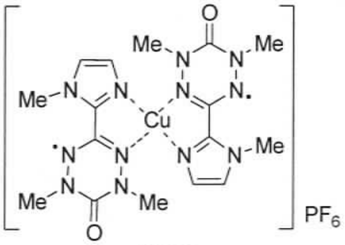

2.62

Bis-(1,5-dimethyl-3-{*N*-methyl-imidazol-2'-yl}-6-oxoverdazyl)-copper (I) hexafluorophosphate (2.62) - To a green solution of Cu_2Br_2 (173 mg, 0.6 mmol) in MeCN (20 mL) was added silver hexafluorophosphate (305 mg, 1.21 mmol) in MeCN (5 mL) resulting in the formation of a gray precipitate (AgCl). The precipitate was filtered away and to the filtrate was added a solution of **2.59** (500 mg, 2.42 mmol) in MeCN (10 mL) resulting in a dark brown solution. The solution volume was reduced and the product was precipitated using Et_2O. The product was then recrystallized twice from acetone/Et_2O (490 mg, 65.1%). FT-IR (KBr): 3153 (m), 2952 (m), 1698 (s), 1543 (w), 1461 (m), 1425 (m), 1365 (m), 1285 (m), 1171 (w), 1113 (w), 1051 (w), 992 (w), 959 (w), 843 (s), 767 (m), 727 (m), 638 (w), 558 (s), 492 (w) cm^{-1}. Anal. Calculated for $C_{16}H_{22}CuF_6N_{12}O_2P$: C, 30.85; H, 3.56; N, 26.98. Found: C, 31.18; H, 3.18; N, 27.28. λ_{max}(MeOH)(ε($M^{-1}cm^{-1}$): 416 nm (1.2×10^3). MS (LSIMS): *m/z* 477 {$[M-PF_6]^+$, 100%}, 462 {$[M-CH_3PF_6]^+$, 30%}. HR-MS: 476.1297 +/- 0.0010 (476.1306 for $[M-H-PF_6]^+$ $C_{16}H_{22}CuF_6N_{12}O_2P$). Mp 172 °C (decomposes).

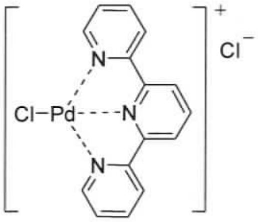

2.64

Dichloro-palladium(II) terpyridine[169] **(2.64)** - Palladium dichloride (50 mg, 0.28 mmol) was solubilized in a heated (~60 °C) solution of pyridine (25 mL). After approximately 15min, **2.60** (137 mg, 0.28 mmol) was powdered into the pyridine palladium solution. This yellow solution darkened to a bright orange, as **2.60** dissolved. After a second 15min interval, pBQ was added resulting in a dark red/orange solution. The reaction mixture was stirred overnight (14hrs) at 60 °C. A creamy white precipitate formed overnight, and was filtered and washed with pyridine and ether to yield **2.64** (80mg, 69.5%). The product was then characterized by ^1H- and ^{13}C-NMR and LSI-MS. The characterization was consistent with previous findings[170] and agreed with the expected formulation.

Chapter 3: Multitopic Verdazyl Radical Ligands as Paramagnetic Supramolecular Synthons

3.1 Metallosupramolecular self-assembly

In the last decade a large body of work has been dedicated to the generation of discrete inorganic architectures in order to further understand the principles of inorganic self-assembly.[171] The ability to controllably substitute different metal ions within a metallosupramolecular array has resulted in new materials possessing interesting electrochemical, optical, magnetic, and catalytic properties. It is also possible to generate molecular materials possessing multiple, cooperative physical properties. Furthermore, metal-directed self-assembly is capable of generating large complex architectures spontaneously, in a single step from molecular subunits. This synthetic variability should have a profound impact in nanotechnology.[172] These systems are not merely being studied because of their nanotechnological applications; a better understanding of solution thermodynamics has direct implications toward biological systems.

Typically, supramolecular architectures are comprised of subunits (or *tectons*[173]) that are connected via intermolecular interactions. Intermolecular interactions include; hydrogen bonding, π–π interactions, electrostatics, van der Waals forces, and solvophobic forces. Metallosupramolecules also make use of another type of interaction known as the coordinative bond. The connectivity (or bonding) between the subunits of supramolecular architectures should be reversible; this reversibility allows for thermodynamic control in the product distribution. Coordinative bond strengths are on the order of 10-30 kcal/mol,[174] significantly less than that of organic covalent bonds (73-111 kcal/mol). However, some inorganic self-assembled structures may display thermodynamic stabilities near to that of covalent structures.

In general, the process of metallosupramolecular self-assembly can be understood as the synthesis of discrete or extended coordination (metal-ligand) structures using rationally designed ligands. The resulting product should have a predictable and reproducible structure as dictated by the topological design of the ligand. Therefore, ligand topology is of great importance in metallosupramolecular architectures.[175] The topology is determined by the number and type of binding sites and the bond lengths and angles contained within the ligand.

The use of metal ions in supramolecular chemistry results in the incorporation of several unique features. Metal ions provide a diverse set of coordination environments that result in a wide range of architectural possibilities that are not present in traditional organic-based supramolecular chemistry. Also, the incorporation of metal ions introduces variable physical properties (photochemical, electrochemical, and magnetic) into the supramolecular structure. Finally, because of the range of binding strengths and dissociation kinetics in metal complexes, coordinative bonds allow for the reversible and dynamic assembly-disassembly of supramolecular architectures. This often leads to the most thermodynamically stable product.

Dynamic equilibrium is very important in discrete supramolecular chemistry. Factors such as concentration, temperature, pressure and presence of a catalyst are all *stress* factors, according to Le Chatelier's principle. Other factors such as entropic and solvation factors also play an important role in the generation of discrete supramolecular architectures. Structural modification of the ligands can destabilize the formation of extended systems and stabilize the desired supramolecular product. For example, rigid ligands functionalized with sterically hindered groups can alter the product distribution in self-assembly.[172] With topological design of the ligands being so important, oligopyridines have been studied extensively as ligands for use in coordination and metallosupramolecular chemistry.[176] Oligopyridines are readily synthesized and functionalized using conventional techniques. Their planar, rigid aromatic structure makes them ideal candidates for self assembly because they have few conformations in solution.

Oligopyridines have multiple binding sites, depending on the number of chelating nitrogens in the ligand. Increased chelation significantly lowers the free energy of the system, which ultimately increases the overall stability of the metal complex. When using chelating ligands there is often a positive enthalpy associated with chelation due to greater steric strain (compared to mono-dentate ligands). However, the greater overall stability occurs due to an entropic effect that is only partially canceled by the unfavourable enthalpy changes.

The transition metal complexes that will be discussed have metal ions in their 2+ oxidation state, thus counter *anions* are present. The most common counter ions used are the water soluble nitrate (NO_3^-) and perchlorate (ClO_4^-), as well as the organic soluble tetrafluoroborate (BF_4^-), hexafluorophosphate (PF_6^-), and triflate ($CF_3SO_3^-$). Counter ions play several major roles; they occupy space in the solid state, and they help determine the solubility of the complex in solution. Ideally the anions are innocent, which means they must not compete for binding to the metal during the self-assembly process. As entropic solvent effects play a key role in self-assembly, so too does the counterion because it is responsible for solubility and it occupies space. Therefore the solid state structure, to some extent, relies on the size of the counterion.

The use of metal ions at specific positions in a supramolecular array opens the door to a wide range of metallosupramolecular structures. Recent work with discrete metal complexes has demonstrated the feasibility of assembling molecular squares[177-179] or polygons,[180-185] cages or cubes,[186-193] ladders,[194] grids,[171, 195-202] catenanes,[203, 204] and metalloreceptors[205, 206] (Figure 3.1). Literature in metallosupramolecular chemistry is vast, but the remainder of this introduction to discrete metallosupramolecular structures will focus on metallosupramolecular grids.

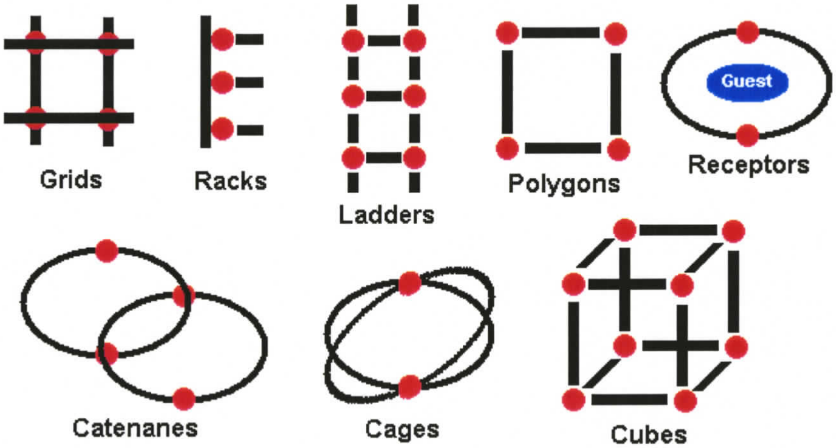

Figure 3.1 - Discrete Metallosupramolecular Structures (red - metal ion / black – ligand)

3.1.1 Metallosupramolecular grids

The 2 × 2 grid is one of the simplest and most well-studied discrete molecular architectures. The first 2 × 2 grid was created by Youinou and co-workers[207] and was assembled from a *bis*-bidentate ligand **3.1** and tetrahedral copper metal centres. As expected from thermodynamic considerations, a more robust and stable 2 × 2 grid would make use of a *bis*-tridentate ligand series (**3.2-3.4,** Figure 3.2). This was the strategy employed by Lehn and co-workers using octahedral metal centres.[208]

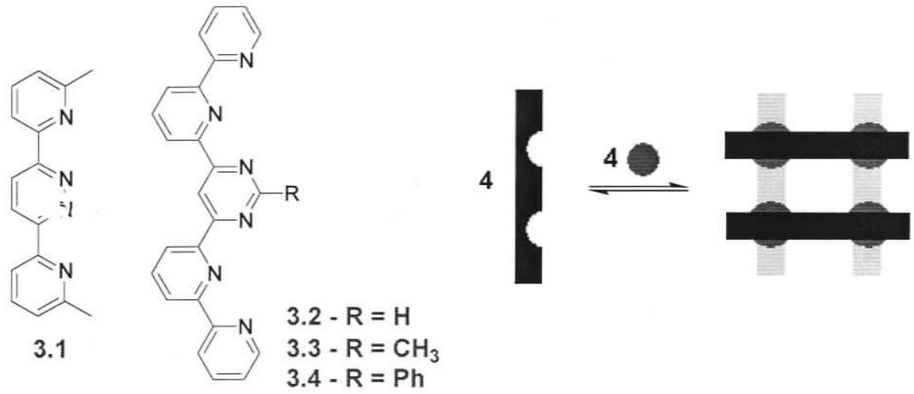

3.1

3.2 - R = H
3.3 - R = CH_3
3.4 - R = Ph

Figure 3.2 - 2 × 2 Grid Self-Assembly using rationally designed ligands

Designing supramolecular grids is more than an aesthetic pursuit of molecular symmetry.[209] Grids have the potential to serve as molecular storage devices and this directly translates into storage media for electronics. Consider a hypothetical 2 × 2 grid based on ligand **3.4**. The ligand is approximately 2 nm long. This translates into a grid area of 4 nm^2. Assuming these grids could be close packed on a one square inch surface, the resulting surface would contain 160×10^{12} grids. If each grid behaves as an addressable unit, this translates to 160 terabits of possible storage density. It is conceivable to use four different metal centres in a 2 × 2 grid where this would translate to a modest 4-fold increase in capacity. This notion of grids being *locally addressable*[176] is a reasonable concept, but as of yet there have been no methods proposed to read this addressable information. The utility of these grids may still exist merely in science fiction.

Since the synthesis and the use of the *bis*-tridentate ligand system **3.2** in 1997, Lehn and co-workers have made several strides in extending the understanding, as well as the size and complexity of these structures. The design of the ligand is crucial for controlling the structure and properties of the final assemblies. With Lehn's particular ligand system (**3.2-3.4**) the substituent R in the C2 position on the pyrimidine ring plays a very important role. With ligand **3.2**, it is found that the parallel ligands in the grid tend to cant inwards to fill the space. In contrast, the grid based on ligand **3.3** tends to produce the opposite effect, as the ligands start to cant outwards. This effect is attributed to the steric bulk of the methyl groups.[195] When ligand **3.4** is used to assemble the grid, not only does the phenyl substituent have the necessary thickness to occupy the void, but it also stabilizes the complex through π-stacking between the π system of the pyridyl rings on one ligand and the phenyl substituent on another ligand. Introduction of the C2 substituent of **3.2** also plays a role in increasing the solubility of the pyridyl ligand system. This is essential because many unsubstituted polypyridyl systems have limited solubility. Furthermore, substitution of the phenyl ring can lead to tunable electronic characteristics.

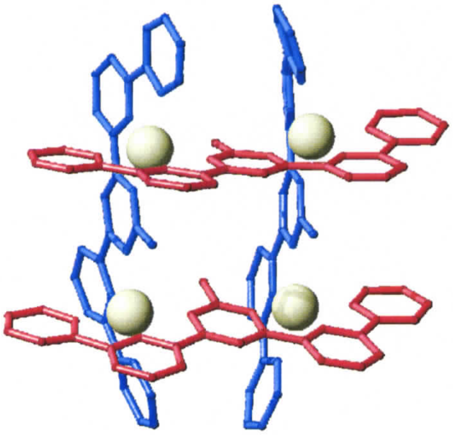

Figure 3.3 – Structure of tetranuclear cobalt 2 × 2 grid using bis-tridentate ligand **3.2**

2 × 2 grids have been synthesized using Zn^{2+}, Fe^{2+}, Co^{2+}, Ni^{2+}, Ru^{2+}, and Pb^{2+} ions. The introduction of zinc into these grids is particularly useful. The presence of a diamagnetic metal centre permits monitoring the solution dynamics of self-assembly. A variable temperature NMR study has shown that no significant dissociation of the complex takes place on the NMR timescale between 243 K and 333 K.[195]

The iron grid system was investigated for spin crossover behaviour using external stimuli including; temperature, pressure, and light. Spin crossover results from metal ions switching between high spin (HS; S=2) and low spin (LS; S=0) states. This system was found to be a multilevel switchable device with three magnetic levels (3HS/1LS, 1HS/3LS, 2HS/2LS).[198] Each of these three states was accessible by external perturbations and the spin states were monitored by variable temperature NMR, magnetic susceptibility, and Mössbauer spectroscopy.

The 2 × 2 cobalt grid also exhibited some interesting properties. It was found that the discrete grid complex could go through a ten-electron well-resolved, fully reversible reduction sequence at -20 °C.[195] This system was scanned 20 times with little observed decomposition. The analogous Fe^{2+} and Zn^{2+} systems decomposed under the same conditions.[199] There is evidence that suggests some modest dissociation of the metal complex occurred.

Although not a transition metal system, the Pb^{2+} 2 × 2 grid demonstrates a very important point regarding the thermodynamic stability and scope of metal sources that can be implemented in these discrete metal complexes. The large size of the Pb^{2+} ions and the comparatively long bonding distances may allow the generation of novel entities (including larger grid structures) not accessible with transition metal ions.[197]

With the intent of designing a grid system with tunable magnetic properties, a new type of *bis*–tridentate ligand (**3.5**) was designed by Lehn and co-workers[196]. The grid system that was analyzed was a Cu^{2+} 2 × 2 grid. The incorporation of the central oxygen atom in the ligand was meant to facilitate a strong antiferromagnetic coupling between copper centres based on the principle of super-exchange. However, magnetic measurements indicated only a very weak antiferromagnetic coupling of the copper ions due to insufficient overlap of the orbitals, which can be rationalized by considering the crystal structure of this grid complex.[196] The copper ion is in a distorted octahedral environment, therefore an unpaired electron resides in the $d_{x^2-y^2}$ orbital; where this orbital is in the N1-N2 plane (Figure 3.4). The $d_{x^2-y^2}$ orbitals of adjacent copper atoms do not overlap with the same oxygen; therefore there is no communication via super-exchange.

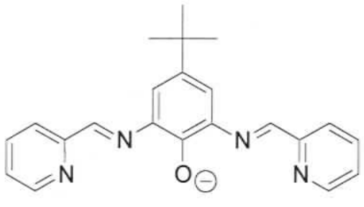

3.5

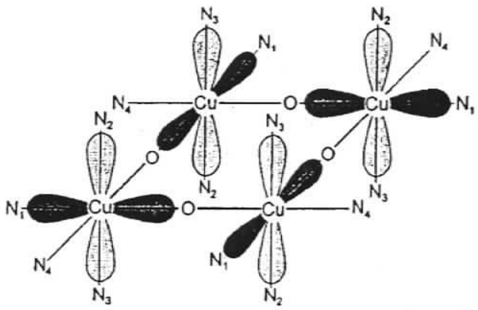

Figure 3.4 - Copper 2 × 2 Grid. Reproduced with permission from *Eur. J. Inorg. Chem.* **1999**, 517-522. Copyright 1999 Wiley-VCH.

Although Lehn and co-workers[196] did investigate the magnetic properties in one of their grid systems, Thompson and co-workers[210-217] can be credited with developing the understanding of magnetic exchange in grid systems. Thompson and coworkers have developed a wide array of grid and cluster[214, 218, 219] architectures using pyridyl hydrazone ligands. There are two major advantages to using hydrazone derived ligands; greater ligand flexibility and synthetic versatility. Using hydrazone methodologies leads to ligands that are synthetically versatile because they are readily modified by judiciously choosing different commercially available esters and aldehydes.

Thompson and coworkers have successfully synthesized and characterized 2 × 2 and 3 × 3 grid structures with most of their attention being focused on the larger grid structures. Increasing the nuclearity of discrete coordination structures is a desired approach to molecular magnetism[216] because increasing the number of paramagnetic metal centres could lead to high spin molecules. However, increasing the grid structure leads to a more challenging magnetic interpretation.

Thompson's homoleptic Cu(II) 2 × 2 grid[220] (Figure 3.5) was made using ligand **3.6**. Hydrazone derived **3.6** is unusual, as most grid ligands are made symmetrical to avoid stereoisomers upon coordination. Each of the copper ions are bridged by oxygen atoms, resulting in a straightforward magnetic interpretation (Figure 3.5c). Each copper is in a symmetrically equivalent position with two adjacent copper ions. As such, there is only one magnetic exchange parameter to consider and it was found that the interaction between the copper ions is weakly ferromagnetic ($J = 7.2$ cm^{-1}).

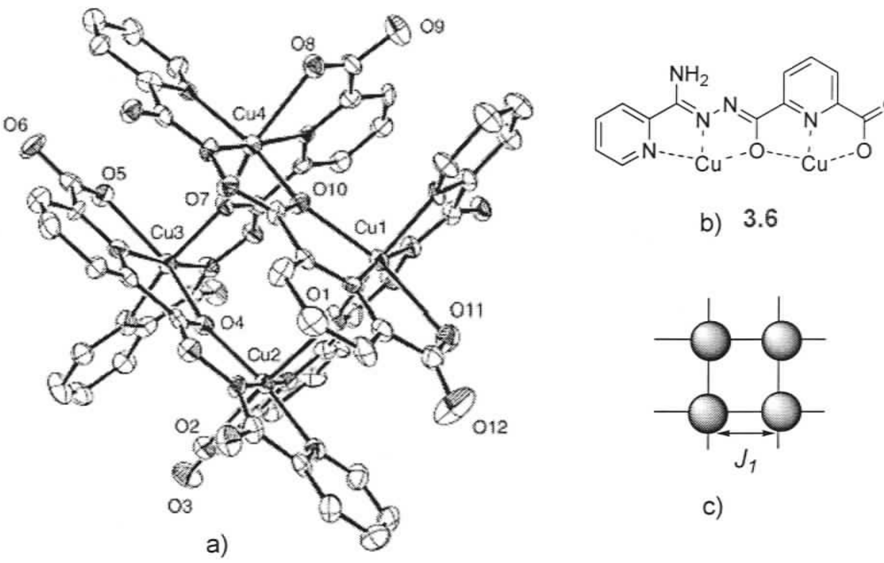

Figure 3.5 – a) Crystal structure of the 2 × 2 Cu(II) Grid with b) pyridyl hydrazone ligand **3.6** and c) magnetic interactions in the grid. Crystal structure reproduced with permission from *J. Chem. Soc.-Dalton Trans.* **2002,** *2462-2466*. Copyright 2002 Royal Society of Chemistry.

Thompson and co-workers have also produced several different 3 × 3 grids using ligands with similar topology to **3.7** (Figure 3.6b). Cu(II), Mn(II), Fe(III), and Zn(II) have all been successfully used to create M_9-type grids with similar structures to those depicted in Figure 3.6. In some cases non-homoleptic, less symmetrical[221] and mixed valent Mn(II)/Mn(III) 3 × 3 grids[210, 212] were also prepared.

Consider the magnetic interactions in Figure 3.6c where there are two distinct metal ion environments. The metal ions around the periphery of the grid, adjacent to two other metal ions, all have similar magnetic environments. From this magnetic symmetry only one magnetic exchange parameter (J_1) is needed to describe the interaction between the peripheral metal centres. However, the metal ion that is symmetrically centred has 8 adjacent metal ions, resulting in the need to consider a second magnetic exchange parameter (J_2). In all of the homoleptic grids studied[210, 215], it turns out that $| J_1 | > | J_2 |$ where $J_1 \sim -5\text{cm}^{-1}$, and $J_2 = 0$. In the case of the Mn(II) grid antiferromagnetic alignment results in a ground state that appears to be $S = 2.5$.

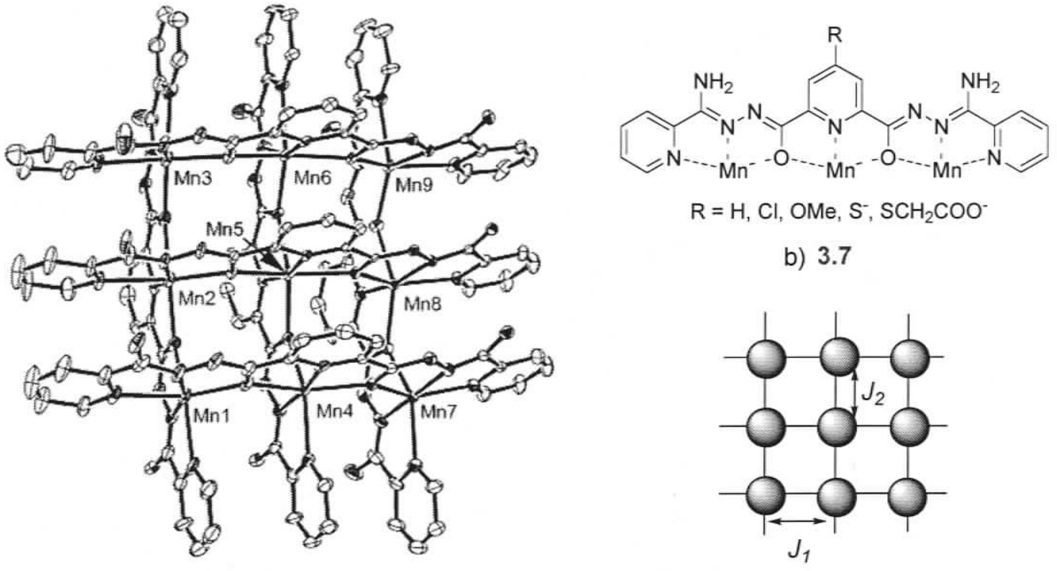

a)

b) **3.7**

c)

Figure 3.6 – a) Crystal structure of the 3×3 Mn(II)/Mn(III) Grid with b) pyridyl hydrazone ligand **3.7** and c) magnetic interactions in the grid. Crystal structure reproduced with permission from *Inorganic Chemistry,* **2004**, *43,* 7605-7616. Copyright 2004 American Chemical Society.

The Mn_9-polynuclear grids also exhibit good electrochemical reversibility in solution as shown using cyclic voltammetry. This prompted Thompson and coworkers to investigate the electrochemical stability of these systems on surfaces. Grids containing sulfur modified ligand derivatives of **3.7** have been attached to surfaces and are currently being explored for possible applications in data storage.[212]

3.1.2 Objectives

Thoughtful topological design of ligands can result in ligands that spontaneously form 2 × 2 grids architectures under thermodynamic control. Although there have been several metal ion variants, there has been very little consideration given to altering the pyridyl units of the ligand while maintaining the desired topology. In particular, all of the ligand systems produced to date are diamagnetic. In the study of electronic or magnetic communication between metal ions, diamagnetic ligands have limited utility.

For effective magnetic and electronic communication between metals in a grid system, a radical based ligand should be able to interact (ferromagnetically or antiferromagnetically) with one or more metals in a predictable fashion. The strength of this interaction should be strong and ideally multidirectional. Furthermore, increasing the number of cooperative 'spins' (radicals) may lead to high spin molecules that possess a magnetic dipole, which is necessary for magnetic applications.

The verdazyl radical represents a very interesting class of paramagnetic nitrogen containing heterocycles[88, 131, 222] that, based on previous discussions in Chapter 2, could be introduced effectively into a wide range of oligopyridine backbones. Most verdazyls and transition metal complexes of verdazyls are stable indefinitely in the solid state. This makes them excellent candidates for oligopyridine-based grid synthesis.

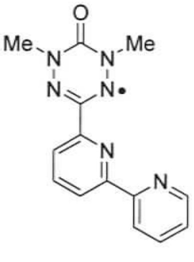

2.33

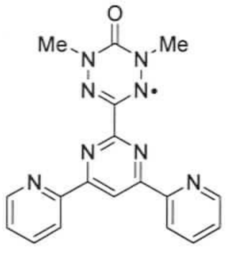

2.36

From previous studies, Hicks and coworkers have shown that verdazyls can be successfully incorporated into oligopyridine backbones to create tridentate[150] (**2.33**) and *bis*-tridentate[98] (**2.36**) ligands. The following series of novel oligopyridine–based *bis*-tridentate verdazyl radicals (Figure 3.7) are meant to serve as paramagnetic analogs to existing diamagnetic grid-forming ligands.

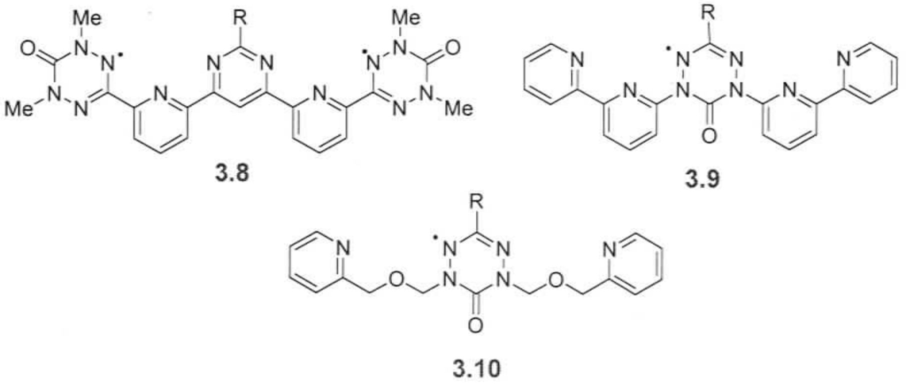

3.8

3.9

3.10

Figure 3.7 - Potentially grid forming *bis*-tridentate target ligands

All three targets depicted in Figure 3.7 are *bis*-tridentate ligands with topologies similar to Lehn and coworkers grid forming ligands (**3.2-3.4**).[223, 224] **3.8** and **3.9** have more rigid oligopyridine backbones, while **3.10** contains a more flexible ether linkage. While non-pyridyl based hydrazone backbones have been shown to be suitable ligand structures to form grids, to our knowledge the ether-containing ligands have yet to demonstrate the ability to self assemble into grid architectures.

The position of the verdazyl ring is an important consideration. In **3.8**, the ligand is a diradical with the verdazyls located at each end of the ligand. Ligands **3.9** and **3.10** possess only one radical positioned at the centre of the ligand, where it would serve as a bridge between the metal centres as seen in Figure 3.8.

Figure 3.8 - Possible 2 × 2 grid configurations using ligands: (A) **3.8**, (B) **3.9**, and **3.10**.

The location of the radical within the ligand has significant ramifications to the magnetic properties of a 2 × 2 grid that is formed. Previous investigations of verdazyl coordination complexes have shown that bridging verdazyl radicals are capable of coupling metals ferromagnetically.[225] However, diradical **3.8** does not have any predictable magnetic pattern, as it is uncertain what kind of interactions between metals would be present in ligands terminally substituted with verdazyls.

The design of 2D architectures, such as 2 × 2 grids, is a logical extension of small molecule (monometallic) complexes. To this end, 2D grids could be prepared by introducing verdazyl radicals into known grid forming topologies and combining them with paramagnetic metal ions using the tenets of metallosupramolecular chemistry. The remainder of this chapter will discuss the synthesis and characterization of these potential grid-forming ligands.

3.2 Synthesis and characterization of a *bis*-tridentate oligopyridine-based diradical

3.2.1 Pyrimidine synthesis using amidine-enone condensations

The enone-amidine condensation[226] method (Scheme 3.1) to form pyrimidines was chosen as a key component of the synthesis of **3.8**. This route can be used to synthesize oligopyridines containing pyrimidine moieties without the difficulties of handling Stille-type reagents.[223] The Stille-type couplings are highly toxic largely due to the use of alkyl tin derivatives. Furthermore, enone-amidine condensations can generate a library of pyrimidines that are functionalized in the 2-position. This could prove to be useful when tuning the topology of the oligopyridyl ligand.

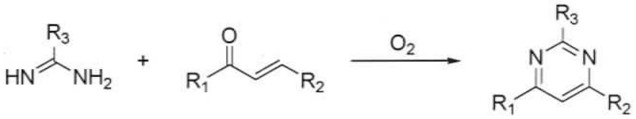

Scheme 3.1 – Amidine-enone condensation reaction

3.2.1.1 Enone-amidine condensations using acetamidine

There were several early attempts to create ligands with similar topologies to **3.8**. The first target ligand using the enone methodology was **3.11**, which is the direct verdazyl analog of Lehn's grid forming ligand **3.2**. The synthetic strategy (Scheme 3.1) leading to the dialdehyde **3.14** required lithiation of the dibromide **3.13** after the construction of the pyrimidyl ring. Typically this is done by condensing amidines with the crude enones, because the enones are difficult to purify using conventional or chromatographic techniques. Unfortunately this method did not yield the expected pyrimidyl ring **3.13**. Instead, the *tris*-pyridyl-pyridine **3.15** was the major product in moderate yields.

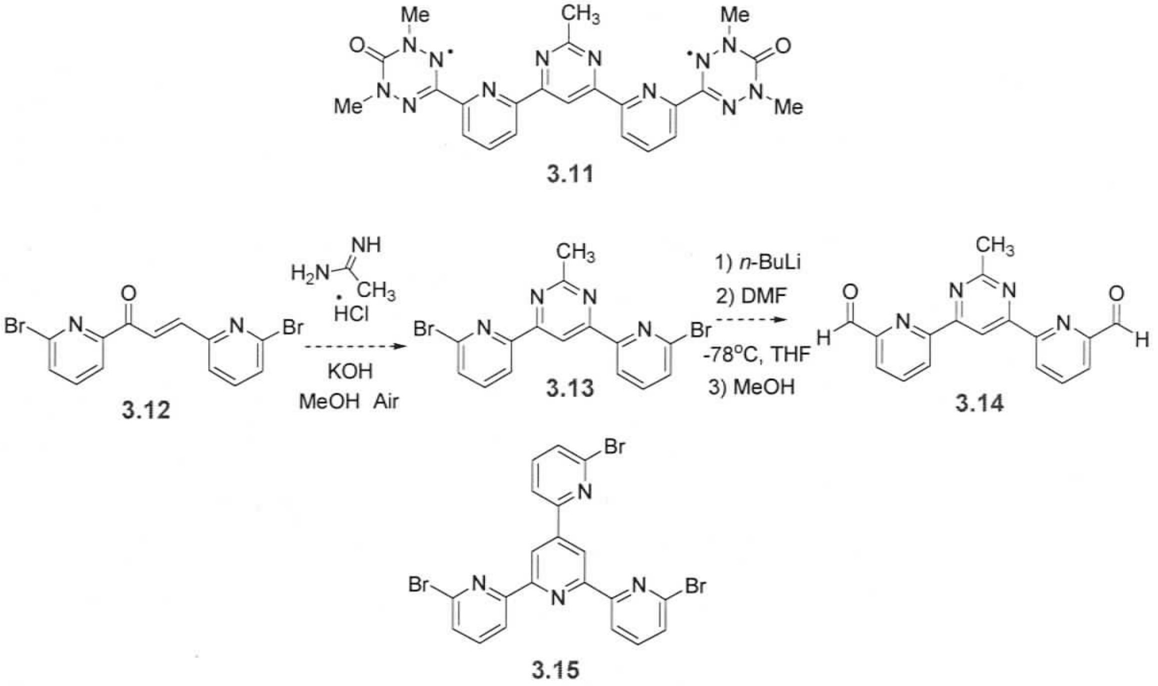

Scheme 3.2 – Attempted synthesis of 4,6-Bis-(6-bromo-pyridin-2-yl)-2-methyl-pyrimidine **3.13.**

It is hypothesized that due to the inability to purify the enone **3.12**, the presence of excess 2-bromo-6-acetylpyridine (from the enone condensation) could be the source of the third pyridyl equivalent needed to make product **3.15**. A proposed mechanism is given in Scheme 3.3. With the generation of the 1,5-diketone as an intermediate, acetamidine serves as the pyridine nitrogen source in **3.15**.

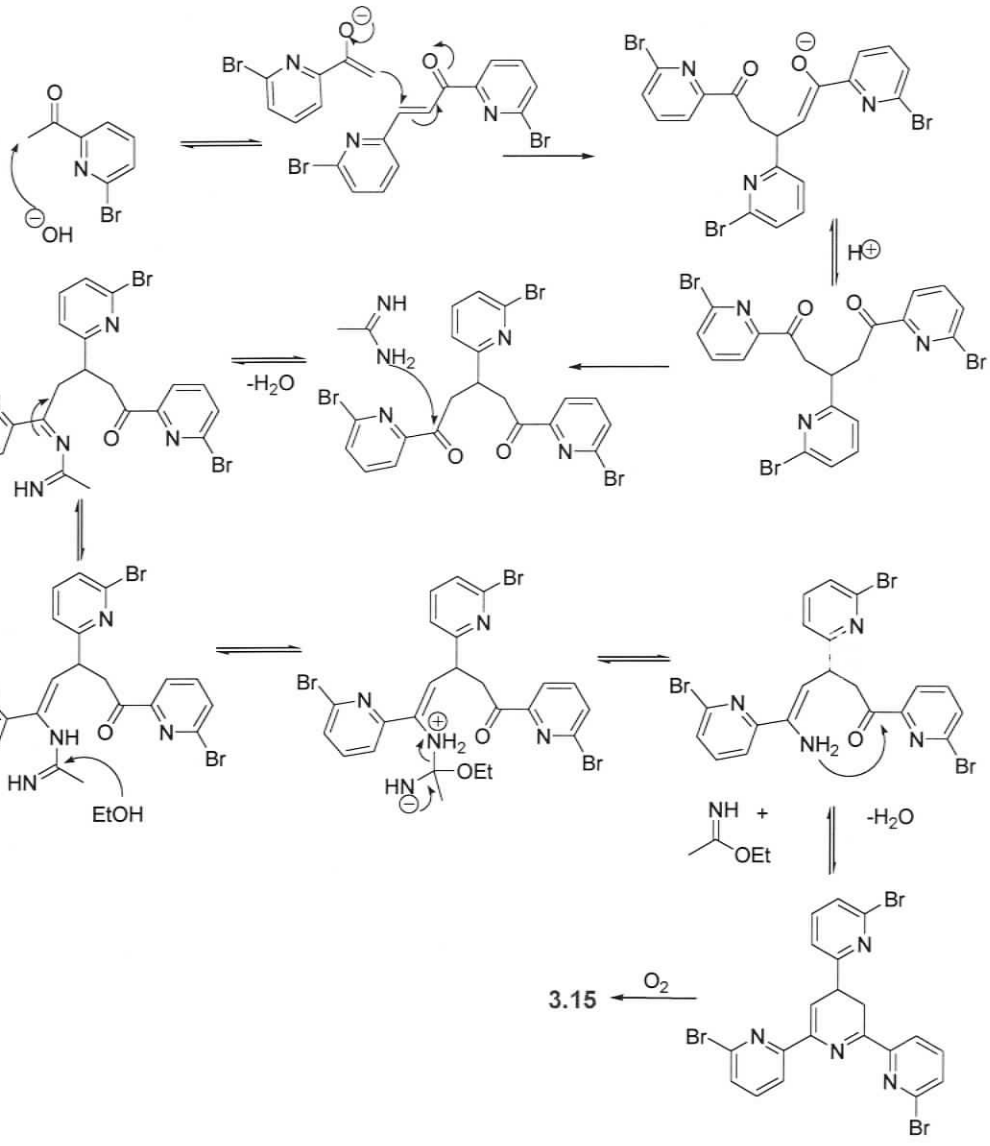

Scheme 3.3 – Proposed mechanism for the synthesis of **3.15.**

3.2.1.2 Lithiations involving benzene substituted pyrimidines

To avoid the formation of **3.15**, benzamidine was chosen as a new amidine source and 2-bromo-6-acetylpyridine was used as a limiting reagent in preparation of enone **3.12** (Scheme 3.4). This procedure, using existing literature methods,[227] yielded the benzene-substituted pyrimidine **3.16** in moderate yields. However, attempting to generate the desired aldehyde **3.17** using lithium-halogen exchange was unsuccessful as the only product isolated, in poor yields, was mono-aldehyde **3.18**. The lithiation of the phenyl ring over the metal-halogen exchange suggests that lithiation of the phenyl ring is the more energetically favoured route. There are several examples in the literature where Lewis bases coordinate to lithium and direct the lithiation to the *ortho*-position. This is the premise employed in directed-*ortho*-metalation[228-231] and it is believed the bipyridine binding pocket is behaving as an ortho-directing group to the phenyl ring.

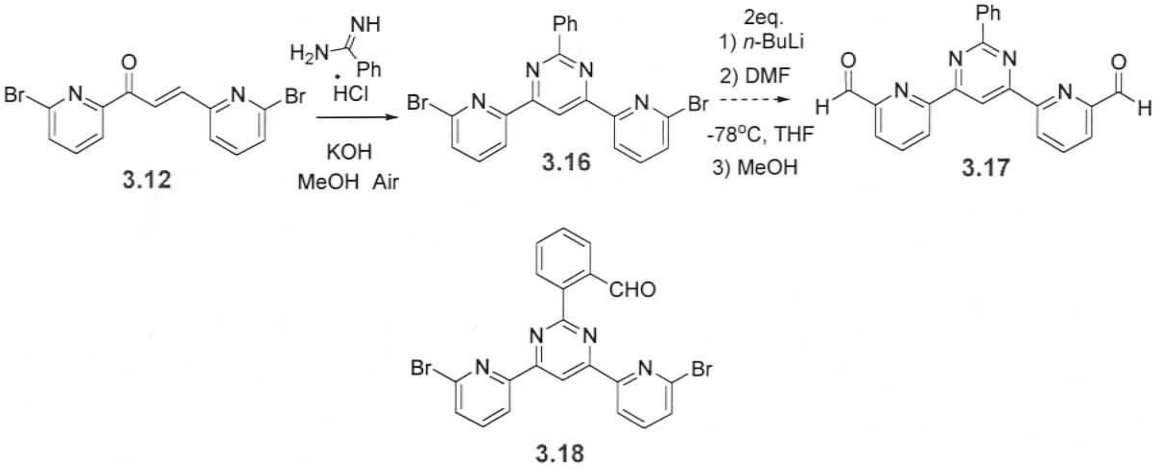

Scheme 3.4 - Attempted synthesis of 4,6-Bis-(6-pyridinylcarboxaldehyde-2-)-2-phenyl-pyrimidine **3.17**.

As can be seen from the previous two examples, the enone-amidine condensation methodology does not always lead to the desired product, but the ability to generate diverse 2-substituted pyrimidyl rings is readily achieved.

3.2.1.3 Synthesis of a synthetically useful amidine for pyrimidine construction

Another example of the synthetic versatility of the enone-amidine condensation methodology for generating 2-substituted pyrimidines is evident in the preparation of **3.21** (Scheme 3.5). **3.21** has been previously synthesized and is a synthetic precursor to verdazyl **2.36**.[149] Originally the condensation of enone **3.19** with acetamidine yielded the methyl substituted pyrimidine **3.20**. This methyl group was then oxidized using selenium dioxide. Unfortunately the use of selenium dioxide leads to over-oxidation and the carboxylic acid as the major product. The alternative route presented in Scheme 3.5b makes use of dimethoxyacetamidine **3.24** as a formyl-acetamidine equivalent. **3.24** can be generated in quantitative yields from the dimethoxyacetonitrile **3.23**, originally synthesized by Olah and coworkers.[232] Using methanol as a hydrolyzing agent, the nitrile can be readily converted to the amidine hydrochloride salt **3.24** via the *in situ* addition of ammonium chloride (Scheme 3.5c). While both routes to **3.21** are amenable to scale up, the yields using the dimethoxyacetamidine method are a factor of three higher. The yields are approximately the same after the condensation of the enone and amidine, but the dimethoxyacetamidine deprotection step is virtually quantitative and there are no observable side products as seen in the original oxidation route.

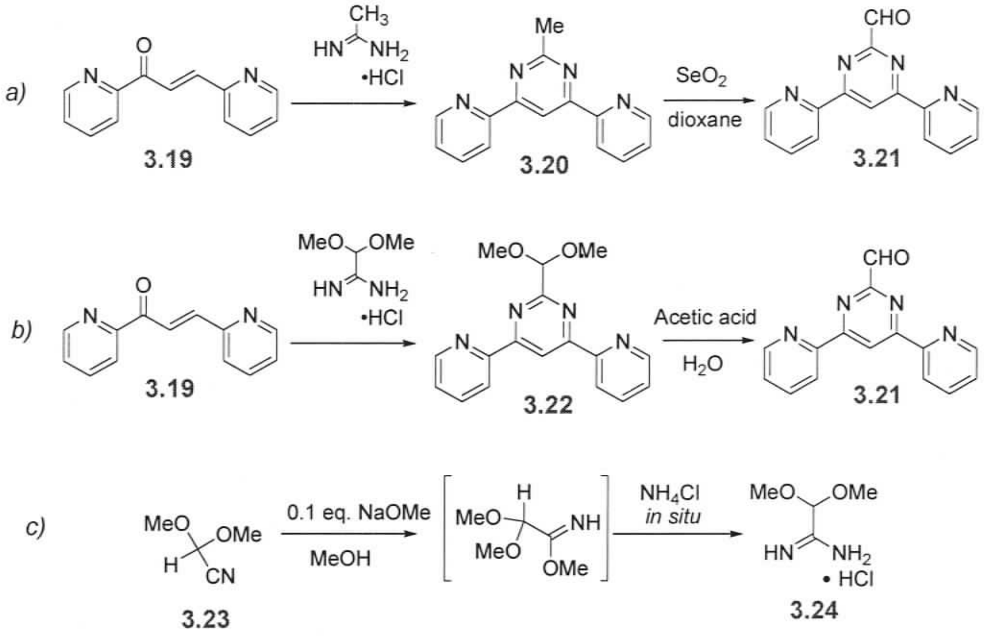

Scheme 3.5 –Dimethoxyacetamidine **3.23** as a synthetic equivalent; a) original method to **3.21**, b) dimethoxyacetamidine modified method to **3.21**, and c) preparation of dimethoxyacetamidine **3.24**.

The generation of **3.24** as a formyl equivalent represents a very useful synthon to generate 2-formyl-pyrimidines using the enone-amidine condensation. Although this concludes the digression of using amidines in pyrimidine synthesis, the synthesis and characterization of all novel acetamidines and derivatives are presented in further detail in the experimental section of this chapter.

3.2.2 Synthesis of **3.8**

Ultimately, **3.8** was prepared using the enone-amidine condensation strategy coupled with a protection-deprotection methodology similar to the one used in the preparation of diradical **2.60**. The synthetic sequence towards **3.8** (Scheme 3.6) begins from the commercially available dibromopyridine, where mono-lithiation followed by quenching the anion with DMF results in 6-bromo-pyridine-2-carbaldehyde **2.48** in excellent yields. The aldehyde **2.48** is then protected as the acetal[157] **2.49**. The acetal is functionalized further to an aldehyde **3.25** and ketone **3.26** using a metal-halogen exchange strategy followed by quenching with the appropriate electrophile. The aldehyde **3.25** and ketone **3.26** are then combined in a Claisen-Schmidt fashion,[227, 233] resulting in the enone **3.27**. Complete characterization of the enone was not possible, as this compound is unstable when subjected to column chromatography. The crude enone **3.27** was used *in situ* to construct the pyrimidine containing **3.28** by reacting **3.27** with benzamidine. Over three steps a moderate yield is achieved. The desired product precipitates from the reaction mixture and no significant purification is required.

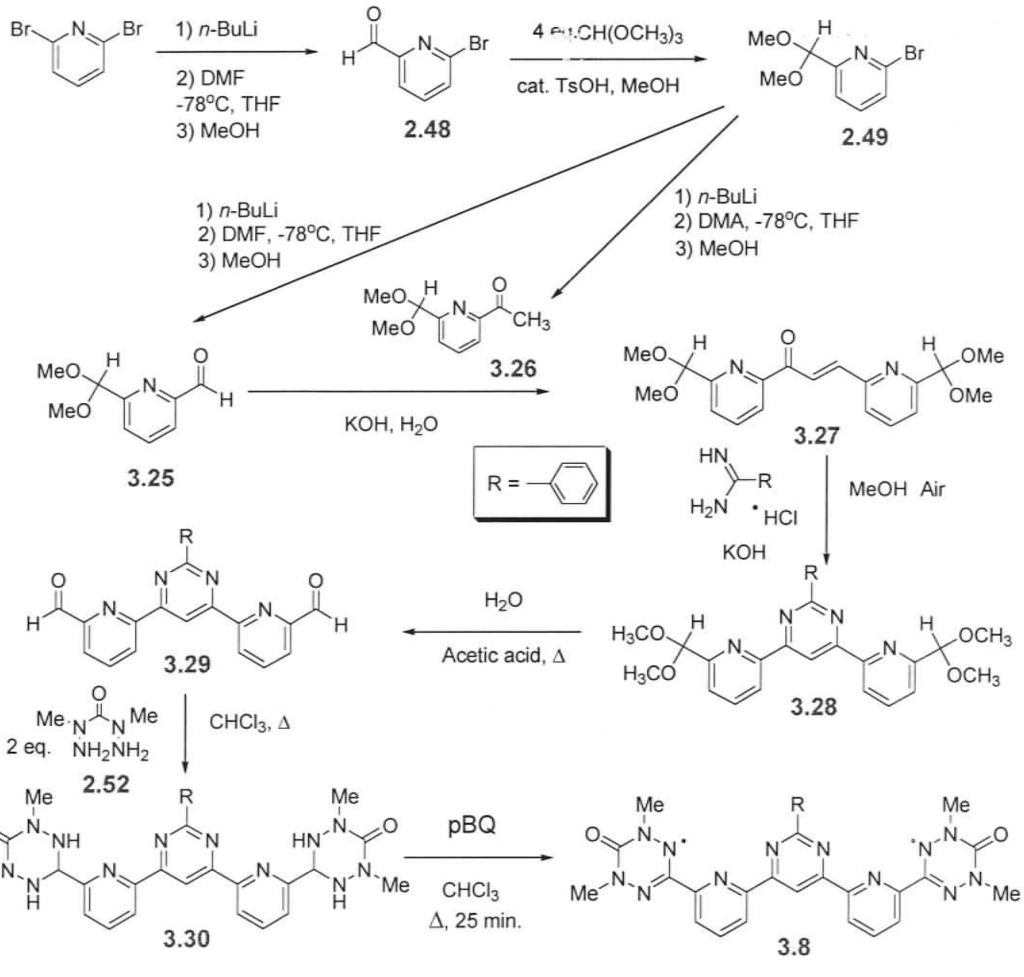

Scheme 3.6 – Synthetic scheme for the preparation of **3.8**.

The deprotection of **3.28** yielded the dialdehyde **3.29** and was followed by the condensation with **2.52** to yield the desired tetrazane **3.30**. The tetrazane is only soluble in chloroform, DMSO, and MeOH, thus *para*-benzoquinone (pBQ) was used as the oxidant to yield **3.8** with variable yields.

3.2.3 Characterization of diradical 3.8 and tetrazane precursor

3.2.3.1 Characterization of Tetrazane **3.30**

The tetrazane **3.30** is not very soluble in most organic solvents. Despite its low solubility, tetrazane **3.30** has been characterized by $^1H/^{13}C$ NMR, FT-IR, UV-Vis, high resolution mass spectrometry, and elemental analysis. Typically, NMR spectra of tetrazanes are acquired using DMSO as the solvent because using polar solvents tends to resolve the tetrazane NH proton signals and coupling to the C3 hydrogen is observed. In chlorinated solvents, these peaks become broad and coupling is no longer observed. The ^1H-NMR spectrum in $CHCl_3$ is presented in Figure 3.9.

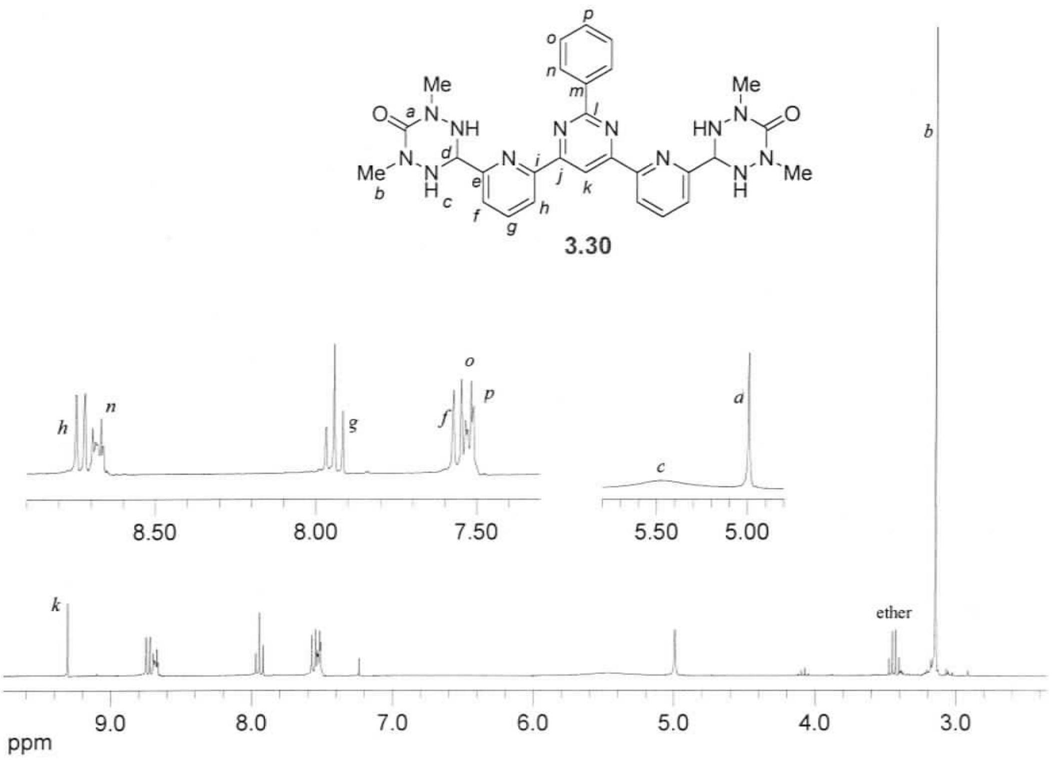

Figure 3.9 - ^1H-NMR spectrum of tetrazane **3.30** in $CDCl_3$ (7.23ppm).

The ^{13}C-NMR spectrum (Figure 3.10) is representative of oligopyridine-substituted tetrazanes. The key tetrazane peaks show up at 164.0 (C=O), 69.7 (C3), and 38.5 (N-CH_3) ppm. The remainder of the spectrum has been assigned to the aromatic peaks of the oligopyridine backbone.

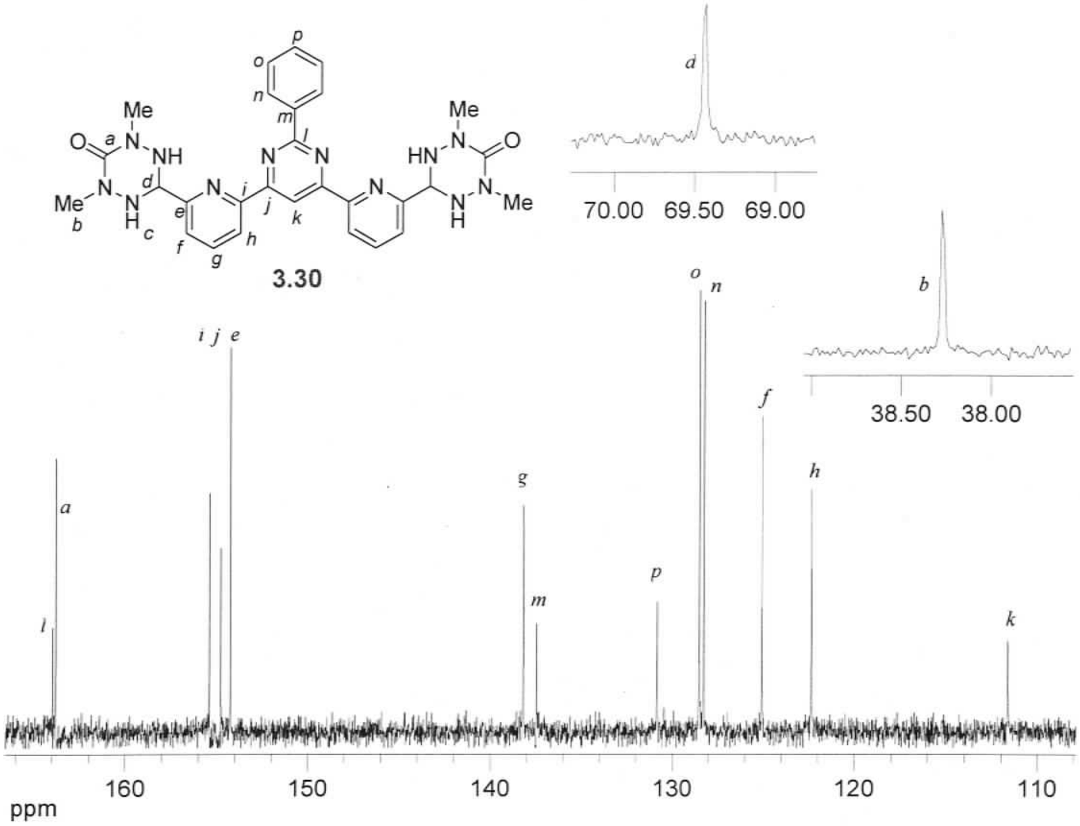

Figure 3.10 - ^{13}C-NMR spectrum of tetrazane **3.30** in $CDCl_3$

3.2.3.2 Electronic Properties of diradical **3.8**

Several oxidants were tested in the oxidation of **3.25**. Of these, *para*-benzoquinone (pBQ) was the most efficient and reproducible. The *bis*-verdazyl is not soluble in most solvents and is only partially soluble in chloroform. Owing to poor solubility **3.25** was not amenable to purification using column chromatography. Although unreacted benzoquinone was easily removed via trituration, the hydroquinone byproduct was more difficult to remove and resulted in poor elemental analysis values for diradical **3.8**.

The full characterization of diradicals is often a challenging pursuit, especially when purity is a problem. While there are several methods that confirm the existence of the diradical, it is often difficult to ascertain the degree of purity because integratable methods are not readily available for paramagnetic species. Diradical **3.8** was characterized by EPR, FT-IR, UV-Vis, and high resolution mass spectrometry. Although diradical **3.8** is stable in the solid state for many months, it is believed that the inability to purify the verdazyl leads to poor stability in solution. A simple UV-Vis experiment in degassed chloroform has shown that the verdazyl diradical completely decomposes over the period of one week. Although this is an acceptable rate of decomposition for most solution measurements, it has made it impossible to grow x-ray quality crystals for structural elucidation.

The ambient temperature EPR of **3.8** is given in Figure 3.11. As a result of the nodal plane in the verdazyl SOMO, little spin density escapes off the verdazyl heterocycle. The fairly large distance between the radical centres in **3.8** would significantly decrease communication between spins, resulting in a very small energy gap between the singlet and triplet states.[104, 229] **3.8** has a *g*-value of 2.0037, with a coupling pattern and hfc values identical to those of the mono-verdazyls described previously in Chapter 2. The parameters used in the simulation do not require any intramolecular radical coupling, which suggests that the intramolecular radical-radical coupling is negligible ($J_{intra} \approx 0$).

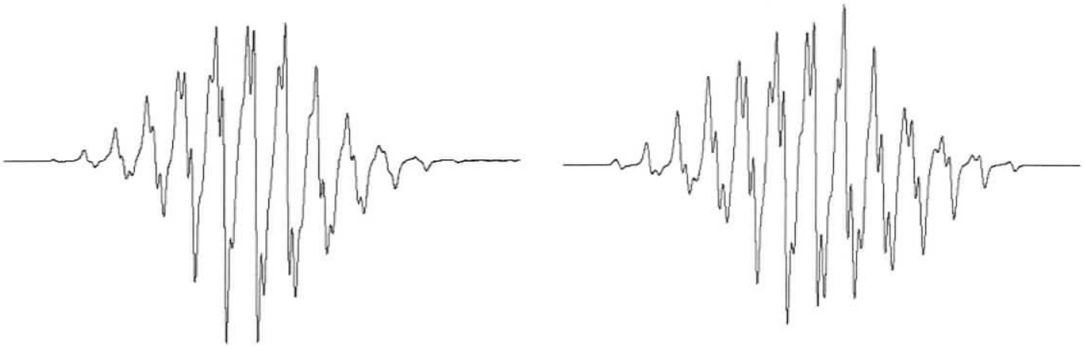

Figure 3.11 - EPR spectrum of **3.8** in $CHCl_3$ at 298 K. The total spectral width is 90 G. Experimental spectrum left; simulated spectrum right.

Upon forming the verdazyl ring system there is a 68 cm^{-1} (1626 to 1694 cm^{-1}) shift in the carbonyl stretching frequency (Figure 3.12). This is consistent with the formation of other verdazyl radicals as previously discussed in Chapter 2. IR is not amenable to quantitative study because impurities can be lost in the shoulders of peaks, therefore it is difficult to quantify the existence of impurities like tetrazines and starting materials, but the IR of the verdazyl does indicate that the major product is the diradical.

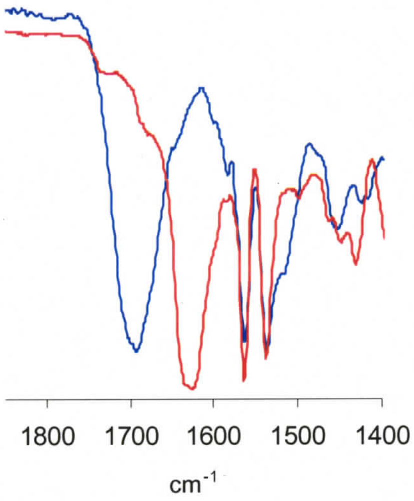

Figure 3.12 – FTIR (in KBr) spectra of bis-tetrazane **3.30** (red) and diradical **3.8** (blue)

3.2.4 Attempted Coordination of 3.8

There were primarily two methods employed in the attempted coordination of **3.8**. The first method, depicted in Scheme 3.7, involves the combination of octahedral metal salts with potentially grid forming ligand **3.8** in a 1:1 stoichiometry. Although several different metal salts (Co(II), Ni(II), Cu(II), Zn(II), and Ru(III)), counterions, and reaction conditions were employed no evidence of metal-radical coordination was observed. In some cases, dramatic colour changes suggested that coordination was occurring, but there was never any evidence of complexation by IR or mass spectrometry. In some cases there was no evidence of the radical in any of the reaction fractions, which could indicate that the diradical is decomposing during the attempted coordination.

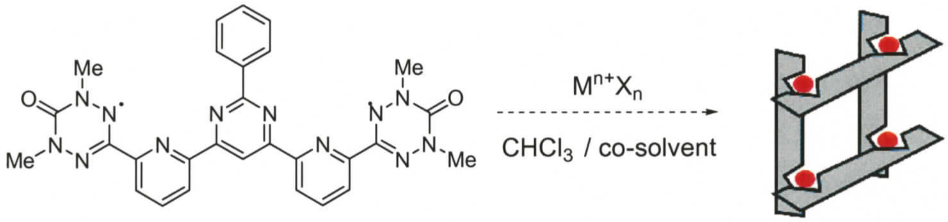

Scheme 3.7 – Method 1: Attempted preparation of 2 × 2 grid complex – model shows ideal grid structure

A significant challenge when trying to form metallosupramolecular discrete species, like grids, is the formation of coordination polymers and oligomers. Normally these metallosupramolecular reactions are carried out at significantly higher temperatures because elevated temperatures allow for reversible exploration of the potential energy surface. Despite oligomers being kinetically favoured, high temperatures favour disassembly and reassembly resulting in the thermodynamic and discrete species being formed. Verdazyl radicals are not particularly stable to elevated thermal conditions and complexation reactions at room temperature may result in significant amounts of oligomer formation.

The second strategy for the coordination of **3.8** avoids the possibility of oligomerization by using ancillary ligands. Several attempts to make bimetallic species using a variety of metal terpyridine salts were made. A model of the desired bimetallic species is presented in Scheme 3.8. Unfortunately, there was no evidence of radical coordination.

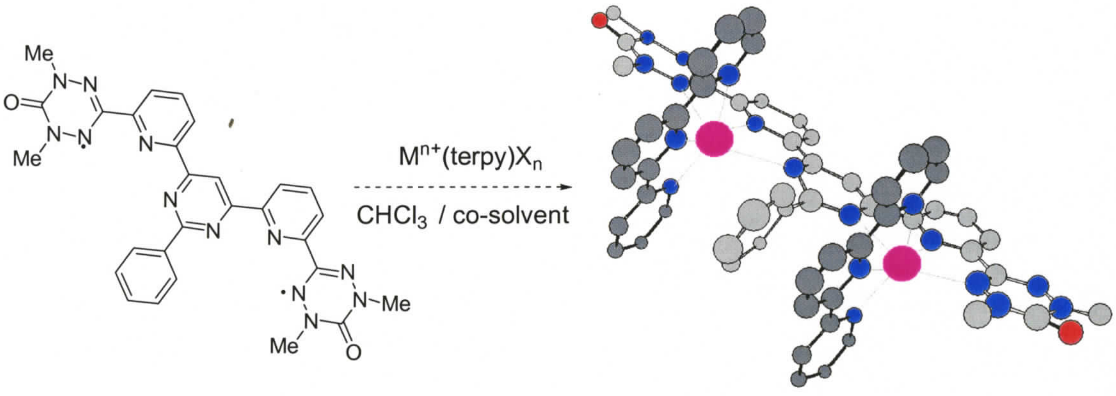

Scheme 3.8 – Attempted preparation of bimetallic complexes of diradical **3.8**

Previous investigations[143] have found that it is possible to form coordination complexes using tetrazanes as precursors. As the tetrazane oxidizes in solution to the leuco verdazyl or radical, coordination can occur *in situ* with the metal ion. This route is desirable because as the radical is formed it coordinates and becomes a more stable metal-radical complex. Furthermore, oxidations involving air should result in fewer impurities contaminating the system. This approach to coordination was applied to both metal complexation strategies, but unfortunately this approach has not yet led to any metal-radical complexes involving **3.8**.

3.3 Attempted syntheses of bis-tridentate mono-verdazyls

The instability of diradicals and the poor solubility of the oligopyridine backbone and diradical **3.8** led to the decision to investigate strategies to new *bis*-tridentate mono-verdazyls. Furthermore, the *bis*-tridentate mono-radicals **3.9** and **3.10** could lead to grids with unique magnetic exchange relationships.

Generally speaking, the attempted synthesis of **3.9** and **3.10** employ similar synthetic strategies that can be grouped into two categories. Preparing mono-verdazyls that are symmetrically substituted on the N1 and N5 nitrogens requires the synthesis of an organic spacer (Figure 3.13) that can be readily functionalized to either undergo C-N bond forming reactions or verdazyl ring construction.

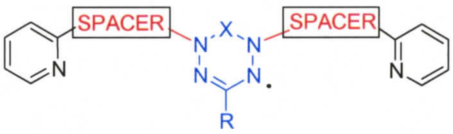

Figure 3.13 - Synthetic strategies in the design of *bis*-tridentate mono-verdazyls spacer modification or verdazyl ring construction

The remainder of this chapter will investigate the attempted synthesis of bis-tridentate mono-verdazyls by discussing various retrosynthetic strategies that have been explored. In many reactions synthetically simpler substrates were tested as proof of concept. The following sections present these retrosynthetic strategies, and include brief discussions of where these strategies failed.

3.3.1 The challenges involving *bis*-pyridyl carbohydrazides

The synthesis of oligo-pyridyl mono-verdazyls would be significantly less challenging if it were possible to prepare bis-hydrazides with pyridyl substituents (**3.31** and **3.32**). *Bis*-methylhydrazide **2.52** can be formed by reacting methylhydrazine with phosgene. The preparation of **2.52** is an example where the methyl electron donating groups increase the nucleophilicity of the hydrazines secondary amine nitrogen. This enhanced nucleophilicity favours carbohydrazides with substituents attached to the urea-type nitrogens (Scheme 3.9).

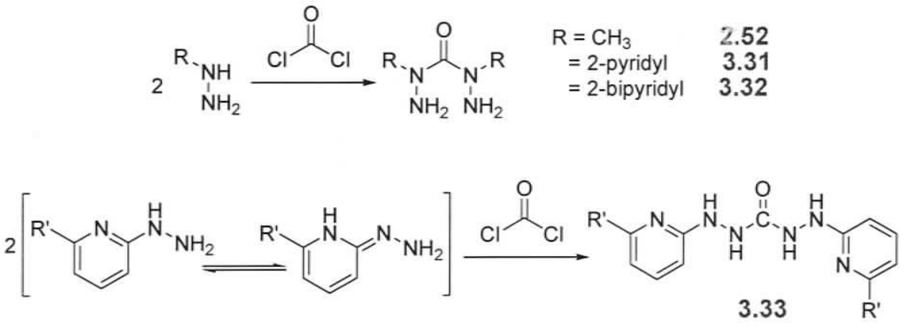

Scheme 3.9 – Attempted preparation of bis-pyridylhydrazides using phosgene

One of the many difficulties of using pyridyl hydrazines is that tautomerization between the pyridyl ring and the hydrazine substituent (Scheme 3.9) significantly diminishes the nucleophilicity of the secondary amine nitrogen. The reaction of pyridyl hydrazines with phosgene produces carbohydrazides like **3.33** (Scheme 3.9). This type of oligopyridyl carbohydrazide represents a 'dead end' in the formation of oligopyridyl-based tetrazanes, therefore a new set of synthetic strategies is needed.

3.3.2 Attempted synthesis of oligopyridine-based mono-verdazyl 3.9

3.3.2.1 Attempted hydrazone coupling to generate bis-hydrazides

When attempting to construct verdazyl rings, hydrazones appear to be excellent starting materials because of their nitrogenous nature. Scheme 3.10 depicts a possible retrosynthetic pathway for the creation of verdazyls using hydrazones. After a series of steps, retrosynthetic analysis of verdazyl **3.9** suggests that hydrazone **3.34** could be a suitable molecular precursor. Hydrazones are readily prepared by reacting ketones (or aldehydes) with hydrazines. This reaction is also reversible and therefore, hydrazones can be considered as protected hydrazines. Based on previous findings, a protected hydrazine would be a very attractive target because it should eliminate the formation of **3.33** upon reaction with phosgene.

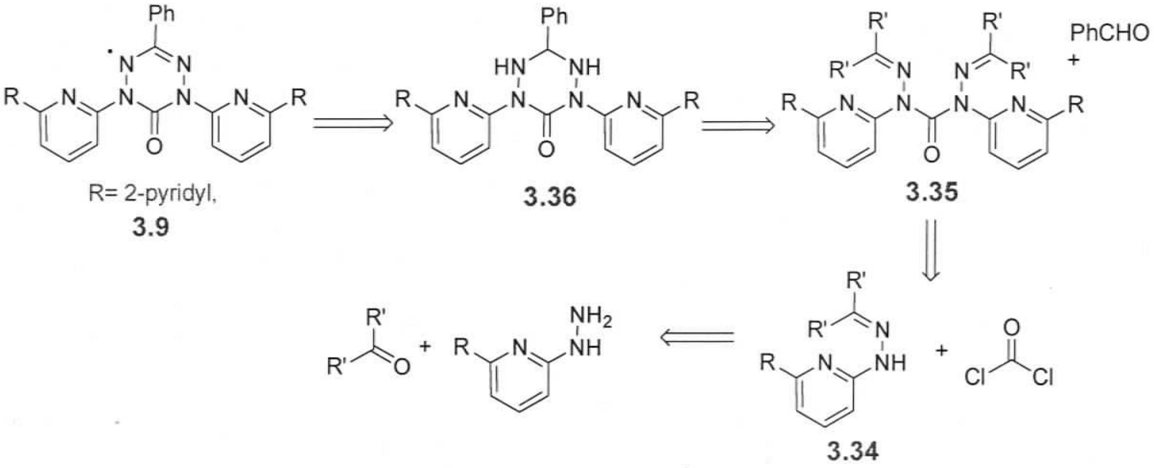

Scheme 3.10 – Retro-synthetic strategy for the formation of **3.9** using pyridyl hydrazones

In the forward direction hydrazone coupling using phosgene ideally would lead to the ketone-protected bis-pyridyl carbohydrazide **3.35**. Cleaving the hydrazone via hydrolysis and reacting the deprotected carbohydrazide with an aldehyde could lead to the tetrazane **3.36** which then could be oxidized to **3.9**. Scheme 3.11 depicts the synthetic route taken based on the retrosynthetic strategy presented in Scheme 3.10. After converting readily available pyridyl bromide **2.49** to the pyridyl hydrazine **3.37** using hydrazine **3.37** was protected with acetone resulting in the hydrazone **3.38**. Acetone as the hydrazone protecting group was chosen because its low boiling point could potentially simplify the workup after the deprotection step. However, the reaction of two equivalents of the hydrazone with the electrophilic phosgene did not generate the desired hydrazide adduct **3.35b**. Instead, an intramolecular cyclization generated a triazepinone derivative **3.39**.

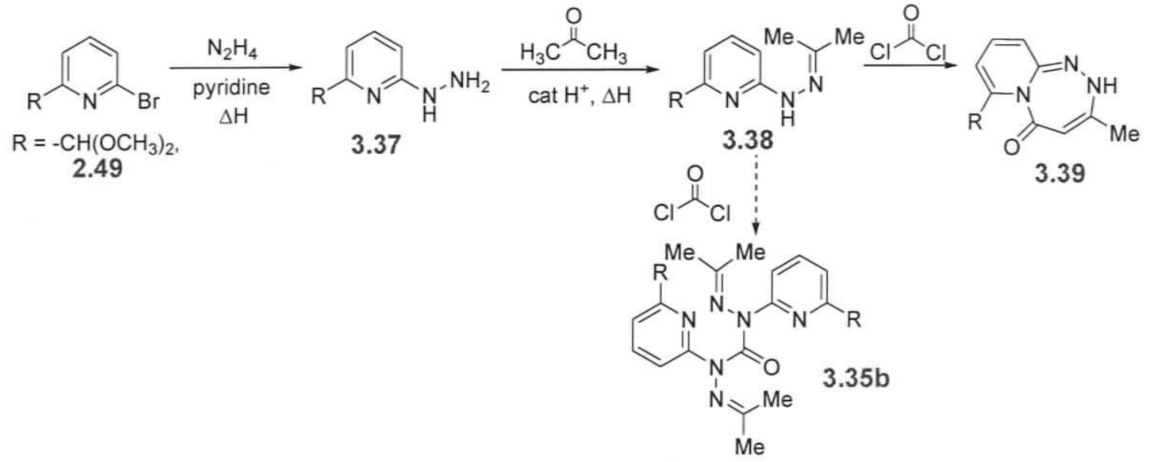

Scheme 3.11 – Synthesis of triazepinone **3.39**

Although the mechanism has not been studied in detail, based on the product distribution it appears that the pyridyl nitrogen is more nucleophilic than the NH of the hydrazone. One possible explanation for this is that there exists a more reactive tautomeric form of **3.38**. A possible mechanism for the formation of **3.39** is shown in Scheme 3.12.

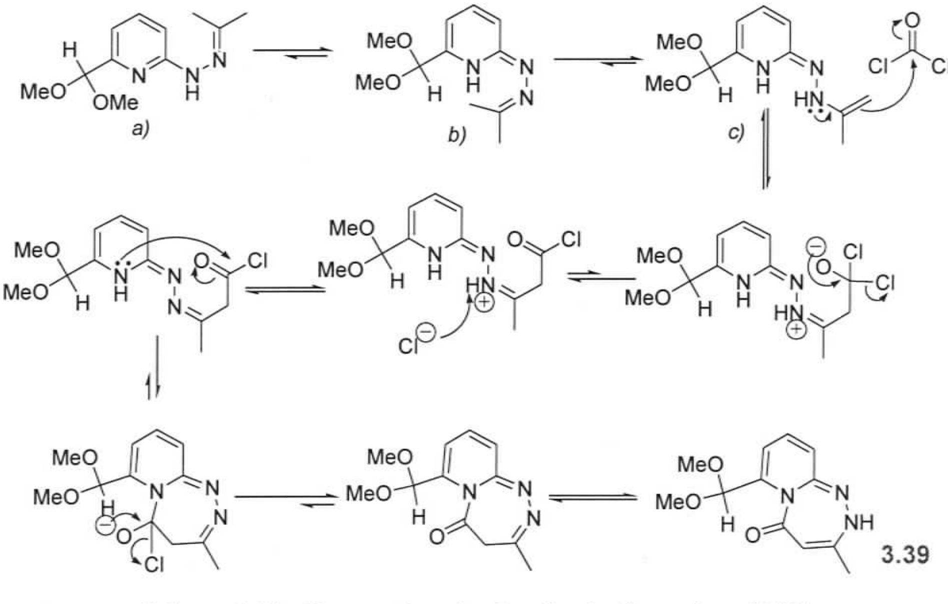

Scheme 3.12 – Proposed mechanism for the formation of **3.39**

Consider the isomers (*a,b,c*) depicted in Scheme 3.12. It is difficult to determine by ^{1}H - NMR whether *a* or *b* is the dominant solution structure, as both would have very similar NMR spectra. Even though *b* would possess a nucleophilic nitrogen in the pyridyl ring, it is proposed that tautomer *c* would be the most reactive of the equilibrium starting materials. After the initial nucleophilic attack, a second nucleophilic attack involving the nitrogen of the pyridyl ring closes the 7-membered ring, eventually leading to **3.39** as the product (Scheme 3.12). Although the 5-membered ring **3.40** is also a possible product, based on the upfield NMR shifts it appears as though the aromaticity of the pyridyl ring has been lost and **3.39** is the more accurate structural representation.

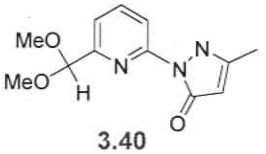

3.40

3.3.2.2 Chlorohydrazones as possible precursors

Scheme 3.13 depicts another possible route to the formation of symmetrically (N1, N5) substituted verdazyls. A second retrosynthetic analysis of verdazyl **3.9** suggests that chlorohydrazone **3.42** could be a suitable intermediate. Chlorohydrazones are readily prepared by chlorinating hydrazones (**3.43**). In the forward direction, these chlorohydrazones could be reacted with hydrazine to from hydrazino-hydrazones (**3.41**). Before oxidation to the verdazyls, a tetrazine ring could be formed using phosgene to close the hydrazino-hydrazone. Although this is not a formazan ring closure, there are strong similarities between these approaches.

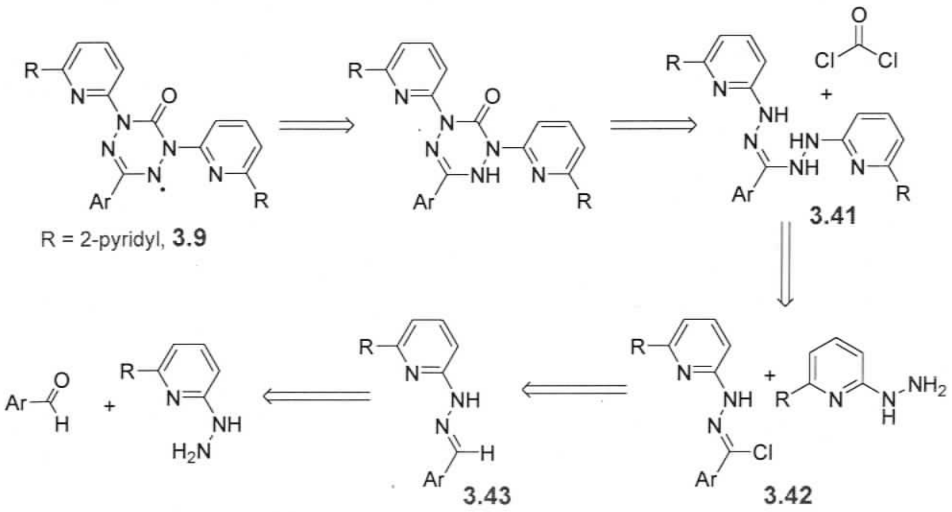

Scheme 3.13 - Retro-synthetic strategy for the formation of **3.9** using chlorohydrazones

In the synthetic direction (Scheme 3.14), insurmountable challenges were met in isolating the chlorinated hydrazone **3.45**. The attempted chlorination of **3.44** led quantitatively to the triazole ring **3.46**. Once again the pyridyl nitrogens appear to be nucleophilic menaces and the final product is yet another demonstration of the challenges in working with pyridyl aromatics.

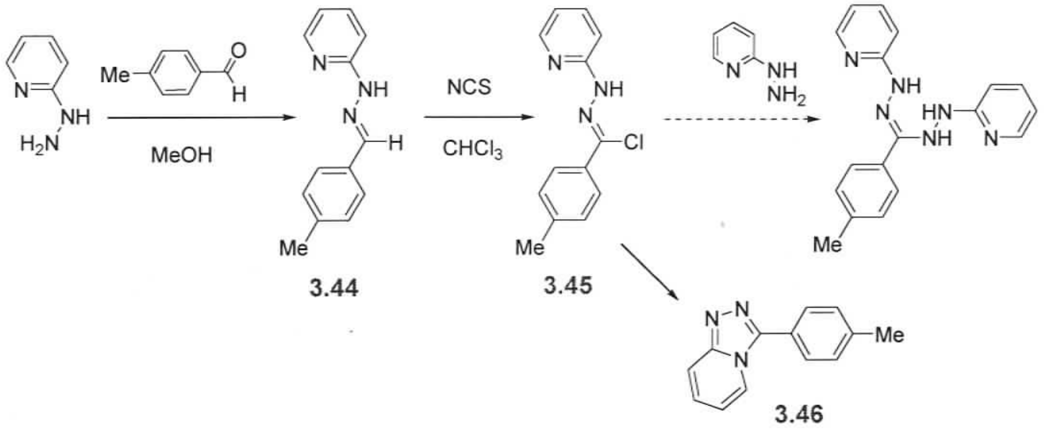

Scheme 3.14 – Attempted formation of chlorohydrazone **3.56**

Triazole **3.46** has been previously prepared using alternative methods,[234] but complementary characterization has been included in the experimental section. After the isolation of **3.46**, this route was abandoned without preparing hydrazones from other oligopyridyl hydrazines. The presence of the triazole-product is strong evidence suggesting the formation of the chlorinated derivative, but the driving force of this reaction is an intramolecular cyclization leading to a 10π electron aromatic which may be insurmountable regardless of the substituent on pyridyl ring.

3.3.2.3 C-N bond forming reactions

Different strategies for making verdazyl **3.9** have been discussed. In these strategies the ring is constructed from modified pendant spacers. Owing largely to the nucleophilicity of the pyridyl lone pair, these routes have been plagued with premature ring closures. Another possible strategy is to couple the pendant spacers directly to an existing tetrazane framework using carbon-nitrogen bond forming methodologies.

Carbon-nitrogen (C-N) bond forming reactions have been well studied under a variety of conditions using different substrates.[235-241] Although arylhalides have been shown to effectively couple hydrazides, bishydrazide coupling has not been studied.[242] Hydrazide coupling has been shown to be regiospecific and arylhalides couple exclusively to the urea-type nitrogens. The potential of C-N bond forming reactions is very attractive to the synthesis of verdazyls, especially 6-oxoverdazyls with symmetric N1 and N5 substituents. Using this C-N bond forming methodology two slightly different retrosynthetic schemes are presented in Scheme 3.15. The C-N coupling could either be done before tetrazane formation (route A) or after the ring as been formed (route B).

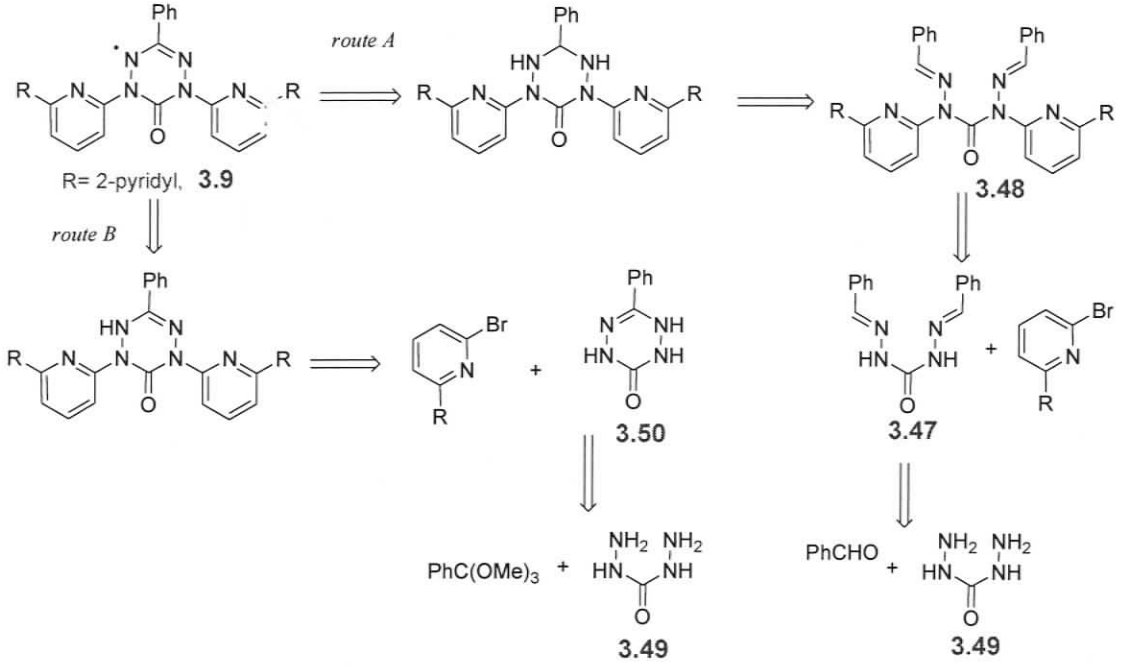

Scheme 3.15 - Retrosynthetic scheme for the formation of **3.9** using C-N bond forming strategies

3.3.2.3.1 Route A

A retrosynthetic analysis of route A suggests that *bis*-imine **3.47** could be a suitable intermediate. **3.47** can be readily prepared by condensing carbohydrazide **3.49** with an aldehyde. **3.48** could be formed by coupling two pyridyl pendant side arms onto **3.47**. The tetrazane could be formed by deprotection of the imine and cyclizing with one aldehyde equivalent before oxidizing the tetrazane to verdazyl **3.9**.

Given that both routes require a coupling step and carbohydrazide starting material, the initial coupling procedure was investigated using iodobenzene as a pendant spacer and *bis*-imine carbohydrazide **3.47**. Although adding pendant phenyl groups will not yield the desired final product presented in Scheme 3.15, it does serve as a proof-of-concept by using **3.47** as a substrate without consuming synthetically intensive starting materials like 6-bromo-2-2'-bipyridine. Scheme 3.16 shows the synthetic attempt using Buchwald's C-N bond forming methodology.[242] Unfortunately, this route failed as the major product was not the desired phenyl substituted carbohydrazide **3.51**, but instead a dibenzylidene-hydrazine **3.52**.[243]

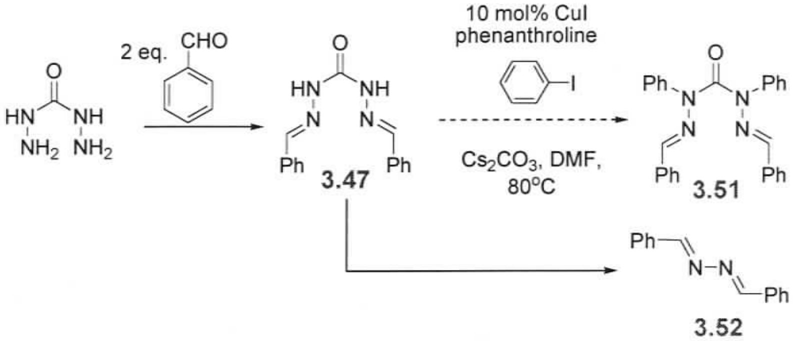

Scheme 3.16 – Attempted C-N bond forming reaction using carbohydrazide as a substrate

Given that **3.47** is stable under a variety of conditions and capable of ligating a metal, copper coordination may be responsible for the decomposition leading to **3.52**, which was isolated in low yields. One mechanistic argument to explain the presence of **3.52** is an oxidative addition of **3.47** to the copper catalyst, followed by a reductive elimination of the dibenzylidene-hydrazine **3.52**.

The formation of **3.52** could be avoided if C-N-bond forming reactions were conducted on substrates that were not capable of ligating to a metal centre. Therefore, a synthetic strategy involving tetrazine **3.50** was employed to prevent the decomposition of the substrate in the presence of a copper catalyst.

3.3.2.3.2 Route B

A retrosynthetic analysis (Scheme 3.15) of route B proposes phenyl-tetrazine **3.50** as a suitable substrate for the eventual formation of **3.9**, where **3.50** could be prepared from the reaction of carbohydrazide **3.49** with trimethylorthobenzoate. Coupling of two pyridyl pendant side arms to **3.50** would lead directly to a tetrazine precursor that may readily oxidize in air to yield **3.9**.

In the synthetic direction, **3.49** was reacted with trimethylorthobenzoate, but it did not result in tetrazine **3.50**. Instead **3.53** was formed in high yields (Scheme 3.17). This route to tetrazine **3.53**[244-246] is new, but the mechanism is not clear. In order to form the diphenyl tetrazine ring an equivalent of CO must be lost in the process.

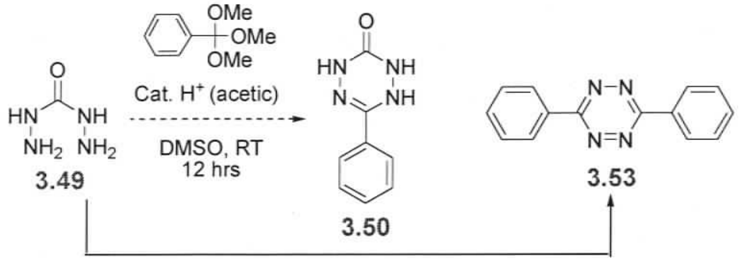

Scheme 3.17 – Attempted formation of tetrazine **3.50**

Introductory studies of C-N bond forming strategies have yet to successfully yield N1 and N5 symmetrically substituted tetrazanes and thus coupling reactions have not been attempted using oligopyridyl halides as pendant spacers. Although this initially appeared to be a very attractive route to **3.9**, it is unlikely that C-N bond forming will be an effective strategy without significant modification to the carbohydrazide starting material.

3.3.3 Attempted synthesis of ether-linked verdazyl

Synthetic challenges in the design of novel mono-verdazyls with pendant pyridyl spacers symmetrically substituted on the N1 and N5 ring positions led to the search for new spacers that could serve as potential ligands. Although ether-containing ligands similar to **3.10** have not been used to form grid structures, they could be effectively introduced as spacers in bis-tridentate ligands. Two retrosynthetic routes to **3.10** are presented in Scheme 3.18.

Retrosynthetic analysis of verdazyl **3.10** identifies hydrazine **3.55** as a suitable precursor. **3.55** is a modified spacer that could be used to construct a *bis*hydrazide **3.54** and eventually a verdazyl ring. Although **3.55** possesses a pyridyl substituent, the secondary amine of the hydrazine should be the more nucleophilic nitrogen and react with phosgene in a similar fashion to methyl hydrazine. Two different routes have been proposed to prepare **3.55**.

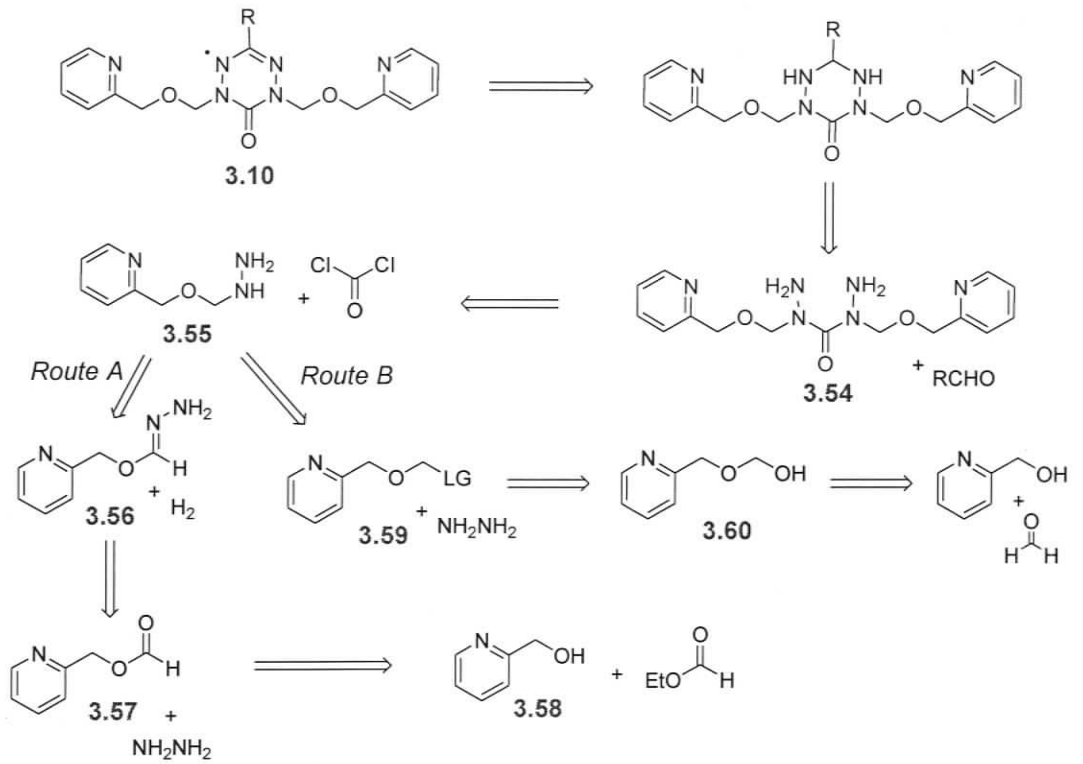

Scheme 3.18 – Retrosynthetic routes to **3.10**

3.3.3.1 Route A

Route A proposes that **3.55** could be formed via the reduction of hydrazone **3.56**, where the hydrazone is derived from the pyridyl formate ester **3.57**. The pyridyl ester **3.57** is simply prepared via a trans-esterification using pyridyl carbinol **3.58** and ethylformate. In the synthetic direction of route A (Scheme 3.19), the pyridyl formate ester[247] **3.57** was formed by reacting ethyl formate with **3.58**. Unfortunately, the reaction with hydrazine did not yield the desired hydrazone, but instead quantitatively yielded the starting material **3.58** and formic hydrazide.

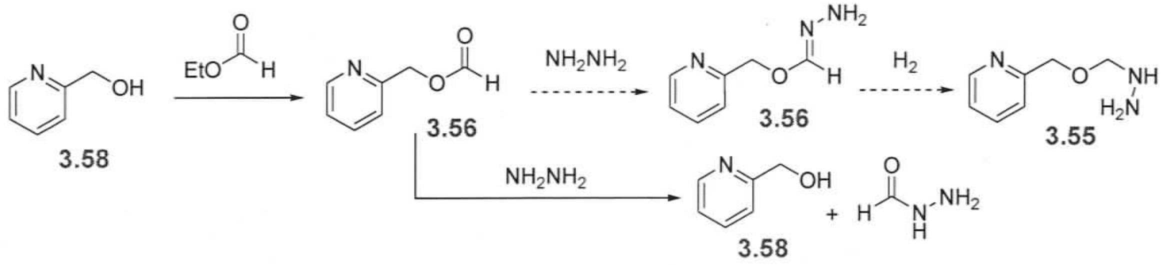

Scheme 3.19 – Synthetic challenges: Attempted synthesis of **3.55** using route A

3.3.3.2 Route B

The retrosynthetic analysis of Route B (Scheme 3.18) suggests that **3.55** could be formed if the leaving group (LG) on **3.59** was displaced by a hydrazine nucleophile. The pyridyl ether possessing a suitable leaving group (**3.59**) could be prepared via functional group conversion of a pyridyl ether alcohol **3.60**. Finally, the alcohol could be formed by reacting pyridyl carbinol **3.58** with formaldehyde.

In the synthetic direction of route B, the pyridyl ether **3.60** was not successfully isolated from the reaction of formaldehyde and pyridylmethanol **3.58**. Instead the starting materials were the only products isolated after workup. This suggests that the equilibrium (Scheme 3.20) lies heavily toward **3.58**. As of yet no attempts to shift the equilibrium towards **3.60** have been successful. The benzene derivative of **3.59** is known,^{248} and perhaps strategies used in its synthesis can be applied to the pyridyl derivative.

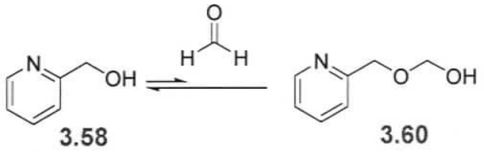

Scheme 3.20 – Attempted synthesis of **3.60** using route B

3.4 Summary

Oligopyridine verdazyls can be prepared with suitable structures necessary to form discrete metallosupramolecular grids and squares. Diradical **3.8** was the most studied potentially grid-forming ligand. Its preparation was simplified because it capitalized on existing bis-methylhydrazide methodologies, where verdazyl precursors are readily prepared from aldehyde starting materials.

Verdazyl radicals **3.9** and **3.10**, with symmetrically substituted N1 and N5 positions, proved much more difficult to prepare. Although several new synthetic strategies have been investigated, each of these strategies succumbed to either substrate decomposition or side product formation. Specifically, routes to form **3.9** using hydrazines or hydrazides have yielded heterocyclic side products owing to the nucleophilicity of the pyridine substituents.

The routes explored to make the ether-substituted verdazyl **3.10** have also been plagued with synthetic challenges. **3.10** is a very attractive ligand because of its unique ether topology, but attempts to make **3.10** show that pyridyl carbinol **3.58** is an excellent leaving group. This high lability of **3.58** could be indicative of future problems in pursuing this radical ligand. As spin density leaks onto the pendant groups, the positions indicated in Figure 3.14 will likely be very reactive under a variety of conditions, and towards nucleophiles.

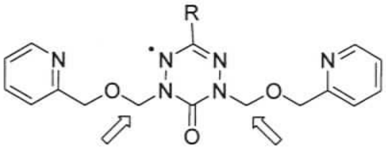

3.10

Figure 3.14- Possible reactive sites in **3.10**

Although diradical **3.8** has been successfully prepared and characterized, it represents another example of oligopyridine-based diradicals being unstable. Despite **3.8** possessing a radical-radical oligopyridine spacer with the topology necessary to form grids, it is has yet to demonstrate the ability to coordinate metal ions.

3.5 Experimental section

3.5.1 General synthetic procedures

Unless stated otherwise all general synthetic procedures employed are similar to those presented in section 2.7.1.

3.5.2 Synthesis

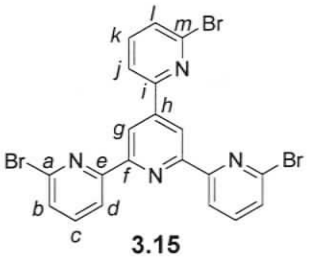

3.15

2,4,6-Tri(6-bromo-pyrid-2-yl) pyridine (3.15) – A 250 mL RBF was charged with crude 1,3-bis-(6-bromo-pyridin-2-yl)-propenone[227] (1.79 g, 4.8 mmol), acetylamidine (0.454 g, 4.8 mmol), NaOH (0.250 g), and EtOH (150 mL). The reaction was heated to reflux for 48 hours. A precipitate (KCl) formed, and was filtered from the reaction. The organic portion was then the solvent removed under reduced pressure and extracted from water using DCM. The organic layers were dried over $MgSO_4$, filtered, and the solvent removed under reduced pressure. The oily solid was then triturated twice with ether resulting in a white powder (0.89 g, 67.8%). **3.15** has limited solubility in DCM. ^1H NMR (DCM): δ 8.91 (s, 2H, H_g), 8.60 (d, 2H, J=7Hz, H_d), 8.06 (d, 1H, J=7Hz, H_l), 7.79-7.74 (m, 3H, H_c, H_k), 7.62-7.56 (m, 3H, H_j, H_b). ^{13}C NMR (DCM): δ 157.3 (C_f), 156.1 (C_i), 155.4 (C_e), 147.8 (C_h), 143.0 (C_m), 142.1 (C_a), 140.1 (C_k), 140.0 (C_c), 129.1 (C_l), 129.0 (C_g), 120.9 (C_j), 120.6 (C_b), 119.4 (C_d) ppm. FT-IR (KBr): 1605 (w), 1575 (s), 1547 (s), 1447 (s), 1420 (m), 1408 (m), 1382 (s), 1373 (m), 1270 (w), 1153 (m), 1124 (s), 1067 (w), 984 (m), 899 (w), 875 (m), 862 (w), 791 (s), 750 (w), 741 (w), 726 (w), 697 (m), 683 (w), 643 (w), 624 (m) cm^{-1}. Anal. Calculated for $C_{20}H_{11}Br_3N_4$: C, 43.91; H, 2.03; N, 10.24. Found: C, 44.12; H, 2.03; N, 10.29. $\lambda_{max}(CH_2Cl_2)(\varepsilon(M^{-1}cm^{-1})$: 299 ($2.1 \times 10^4$), 236 nm ($2.1\times 10^4$). MS (LSIMS): m/z 548 {M^+, 100%}, 218 {70%}. HR-MS: 543.8502 +/- 0.0015 (543.8534 for M^+ $C_{20}H_{11}Br_3N_4$). Mp 99-102 °C.

2-[4,6-Bis-(6-bromo-pyridin-2-yl)-pyrimidin-2-yl]-benzaldehyde (3.18) - 4,6-Bis-(6-bromo-pyridin-2-yl)-2-phenyl-pyrimidine[227] (1.0 g, 2.1 mmol) was solubilized in THF (50 mL) and cooled to –75 °C. To this stirring solution was added *n*-BuLi (1.6 M in hexanes, 2.7 mL) dropwise, maintaining a temperature at/or below –70 °C (~0.5 hours). Once the dropwise addition was complete the resulting red solution was stirred for 30 min. (at –70 °C). Then over a 30 second period excess anhydrous DMF (4.2 mL, 53.9 mmol) was added. Upon electrophile addition, the reaction temperature elevated to –40 °C and the red solution darkened. The mixture was then cooled to –70 °C, the acetone/dry ice bath was removed and the reaction warmed to 0 °C. The reaction was then quenched with MeOH (10 mL), resulting in a yellow transparent solution. The reaction mixture was then extracted from aqueous saturated $NaHCO_3$ (100 mL) with CH_2Cl_2 (3 × 75 mL). The organic fractions were combined and the solvent was removed under reduced pressure. The crude mixture was purified using column chromatography (basic alumina) using EtOAc as the eluent yielding 0.38 g (36.7%) of **3.18**. ^{1}H NMR ($CDCl_3$): δ 10.24 (s, 1H, H$_a$), 9.10 (s, 1H, H$_b$), 8.62 (d, $J = 8$ Hz, 2H, H$_c$), 7.69 (t, $J = 7$ Hz, 2H, H$_d$), 7.55-7.39 (m, 6H). Anal. Calculated for $C_{21}H_{12}Br_2N_4O$: C, 50.84; H, 2.44; N, 11.29. Found: C, 50.91; H, 2.61; N, 11.22. MS (LSIMS): *m/z* 496 {(MH)$^+$, 70%}, 466 {(M-CHO)$^+$, 40%}, 417 {(M-Br)$^+$, 100%}.

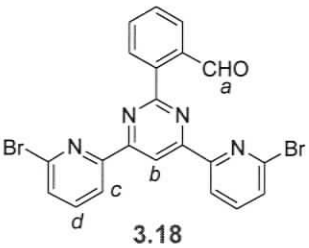

3.18

2-Dimethoxymethyl-4,6-di-pyridin-2-yl-pyrimidine (3.22) – 2-Pyridine carboxaldehyde (1.0 g, 9.34 mmol) was dissolved in distilled water (15 mL) yielding a yellow/orange solution. The solution was cooled to 0 °C and NaOH (0.71 g, 9.34 mmol) was added. A solution of 2-acetylpyridine (1.07 g, 8.87 mmol) in water (15 mL) was added dropwise over 30 min to the aldehyde solution. This resulted in an orange solution followed by the formation of a yellow precipitate. The mixture was stirred for 30 min and then the yellow precipitate was isolated by vacuum filtration and washed with distilled water. The tacky enone product was not characterized and was used without further purification. In a 250 mL RBF the enone solid was combined with dimethoxyacetamidine hydrochloride (1.44 g, 9.3 mmol) and suspended in absolute

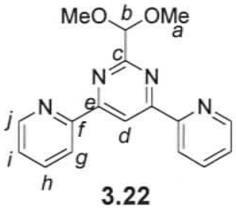

3.22

ethanol (100%, 50 mL). To this mixture was added NaOH (0.46 g, 1.6 mmol), which after gave a yellow solution. The reaction mixture was heated to reflux and stirred for 12 hours before the reaction mixture was left to cool to room temperature. A white precipitate (NaCl) was removed by filtration. The filtrate was the solvent removed under reduced pressure to dryness and the residue triturated with EtOAc. This organic fraction was then purified by column chromatography using EtOAc/B. Alumina (product - R_f = 0.77) to yield **3.22** (0.9 g, 33%). ^{1}H NMR ($CDCl_3$): δ 9.34 (s, 1H, H_d), 8.73 (d, 2H, *J*=5Hz, H_j), 8.57 (d, 2H, *J*=8Hz, H_g), 7.82 (t, 2H, *J*=8Hz, H_h), 7.37 (dd, 2H, *J*=8Hz, 5Hz, H_i), 5.60 (s, 1H, H_b), 3.56 (s, 6H, H_a) ^{13}C NMR ($CDCl_3$): δ 165.0 (C_c), 164.8 (C_e), 154.2 (C_f), 149.8 (C_j), 137.1 (C_h), 125.5 (C_g), 122.3 (C_i), 113.4 (C_d), 104.7 (C_b), 54.7 (C_a) ppm. FT-IR (KBr): 3054 (w), 3013 (w), 2988 (w), 2937 (w), 2823 (w), 1596 (s), 1579 (s), 1561 (s), 1537 (s), 1473 (m) 1434 (m), 1416 (m), 1371 (m), 1324 (m), 1277 (w), 1264 (w), 1229 (w), 1205 (m), 1129 (s), 1104 (m), 1087 (m), 1055 (s), 990 (m), 957 (m), 921 (m), 901 (m), 836 (m), 815 (m), 796 (s), 759 (s), 743 (m), 686 (w), 648 (m), 620 (m), 474 (w) cm^{-1}. Anal. Calculated for $C_{17}H_{15}N_4O_2$: C, 66.22; H, 5.23; N, 18.17. Found: C, 66.59; H, 5.19; N, 18.52. λ_{max}(CH_2Cl_2)(ε($M^{-1}cm^{-1}$)): 299 (2.1 × 10^4), 236 nm (2.1× 10^4). MS (LSIMS): *m/z* 309 {M^+, 70%}, 277 {$[M-CH_3O]^+$, 100%}. HR-MS: 309.1350 +/- 0.0010 (309.1352 for MH^+ $C_{17}H_{16}N_4O_2$). Mp 83-86 °C.

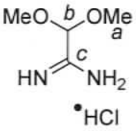

3.24

2,2-Dimethoxy-acetamidine-hydrochloride$^{249-251}$ **(3.24)** – Dimethoxyacetonitrile^{232} (0.5 g, 5.0 mmol) was solubilized in MeOH (50 mL) and to it was added a catalytic amount of NaOMe (0.027 g, 0.50 mmol) under argon. The reaction was stirred for 12 hours and then NH_4Cl (0.27 g, 5.0 mmol) was added and stirred for 8 more hours. The solvent was then removed *in vacuo* and the solid washed with diethyl ether to remove any excess nitrile. The resulting dry white solid is very hygroscopic. Yields are quantitative (0.75 g, 4.9 mmol). ^{1}H NMR (D_2O): δ 5.33 (s, 1H, H_b), 3.48 (s, 6H, H_a) ^{13}C NMR (D_2O): δ 165.7 (C_c), 97.6 (C_b), 55.1 (C_a) ppm. FT-IR (KBr): 3250 (s br), 2842 (m), 1701 (s), 1637 (m), 1450 (m), 1404 (m), 1346 (m), 1206 (m), 1124 (s), 1086 (s), 999 (m), 945 (w), 903 (w), 725 (m, br), 480 (w) cm^{-1}. Anal. Calculated for $C_4H_{11}ClN_2O_2$-H_2O: C, 27.83; H, 7.59; N, 16.23. Found: C, 28.06; H, 6.89; N, 16.28. MS (LSIMS): *m/z* 119 {$C_4H_{11}N_2O_2^+$, 15%}, 88 {$[C_4H_{11}N_2O_2-CH_3O]^+$, 100%}.

MS (EI): *m/z* 88 {$[MH-CH_3O]^+$, 100%}, 75 {$[C_3H_7O_2]^+$, 100%}, 43 {$[CH_3N_2]^+$, 35%}. HR-MS: 119.0826 +/- 0.0007 (119.0821 for MH^+ $C_4H_{11}N_2O_2$). Mp 56-63 °C.

6-Dimethoxymethyl-pyridine-2-carbaldehyde (3.25) - *n*-BuLi (1.6M in hexanes, 27.0 mL) was diluted in THF (50 mL) and cooled to –75 °C. To this stirring mixture, a solution of **2.49** (10 g, 43.1 mmol) in THF (20 mL) was added dropwise, maintaining a temperature at/or below –70 °C (~1.5 hours). Once the dropwise addition was complete the resulting dark red solution (–70 °C) was stirred for 30 min. Then over a 30 sec. period, excess anhydrous DMF (4.2 mL, 53.9 mmol) was added. Upon the electrophile addition the reaction temperature elevated to –40 °C and the dark red solution darkened further. The mixture was then cooled to –70 °C and the acetone/dry ice bath was removed and the reaction warmed to 0 °C. The reaction was quenched with MeOH (30 mL), resulting in a yellow transparent solution. The reaction mixture was extracted from aqueous saturated $NaHCO_3$ (100 mL) with CH_2Cl_2 (3 × 75 mL). The organic fractions were combined and the solvent was removed under reduced pressure. The crude aldehyde was purified using fractional vacuum distillation (47 °C at 1.5 mmHg) yielding 6.8 g (87.1%) of **3.25**. ^1H NMR ($CDCl_3$): δ 9.98 (s, 1H, H_h), 7.82-7.79 (m, 2H, H_e, H_f), 7.68 (t, $J = 4.5$ Hz, 1H, H_d), 5.34 (s, 1H, H_b), 3.32 (s, 6H, H_a). ^{13}C NMR ($CDCl_3$): δ 193.2 (C_h), 158.1 (C_g), 152.1 (C_e), 137.6 (C_e), 125.5 (C_f), 121.2 (C_d), 103.6 (C_b), 53.8 (C_a). FT-IR (Neat): 2937 (m), 2832 (m), 1713 (s), 1590 (m), 1445 (m), 1342 (m), 1286 (w), 1257 (w), 1208 (m), 1193 (m), 1111 (s), 1062 (s, br), 990 (m), 836 (m), 795 (m), 744 (w), 699 (w), 631 (m) cm^{-1}. Anal. Calculated for $C_9H_{11}NO_3$: C, 59.66; H, 6.12; N, 7.73. Found: C, 59.55; H, 6.02; N, 7.61. λ_{max} (MeOH) ($\varepsilon(M^{-1}cm^{-1})$): 268 nm ($6.7\times10^3$). MS (LSIMS): *m/z* 150 {$(M-OMe)^+$, 100%}, 152 {$(M-CHO)^+$, 100%}, 182 {$(MH)^+$, 100%}. HR-MS: 182.0822 +/- 0.0005 (182.0817 for MH^+ $C_9H_{12}NO_3$).

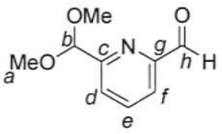

3.25

1-(6-Dimethoxymethyl-pyridin-2-yl)-ethanone (3.26) - *n*-BuLi (1.6 M in hexanes, 27.0 mL) was diluted by THF (70 mL) and cooled to –75 °C. To this stirring mixture, a solution of **2.49** (10 g, 43.1 mmol) in THF (20 mL) was added dropwise, maintaining a temperature at/or below –70 °C (~1.5 hours). Once the dropwise addition was complete the resulting dark red solution (–70 °C) was stirred for 30 min. Then over a 30 second

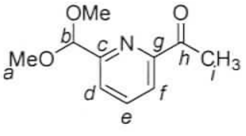

3.26

period excess anhydrous dimethylacetamide (DMA) (5.0 mL, 53.9 mmol) was added. Upon the electrophile addition the reaction temperature elevated to –40 °C and the dark red solution darkened further. The mixture was then cooled to –70 °C and the acetone dry ice bath was removed and the reaction warmed to 0 °C. The reaction was then quenched with MeOH (30 mL) resulting in a yellow transparent solution. The reaction mixture was then extracted from aqueous saturated $NaHCO_3$ (100 mL) with CH_2Cl_2 (3 × 75 mL). The organic fractions were combined and the solvent was removed under reduced pressure. The crude ketone was purified using fractional vacuum distillation (71 °C at 1.5 mmHg) yielding 5.7 g (67.8%) of **3.26**. ^{1}H NMR ($CDCl_3$): δ 7.90 (dd, J = 7.5, 1.0 Hz. 1H, H_f), 7.78 (t, J = 7.5 Hz, 1H, H_e), 7.64 (dd, J = 7.5, 1.0 Hz, 1H, H_d). 5.30 (s, 1H, H_b), 3.36 (s, 6H, H_a), 2.64 (s, 3H, H_i). ^{13}C NMR ($CDCl_3$): δ 200.1 (C_h), 157.1 (C_g), 152.9 (C_c), 137.5 (C_e), 124.6 (C_f), 121.4 (C_d), 104.4 (C_b), 54.1 (C_a), 25.7 (C_i). FT-IR (Neat): 2936 (m), 2831 (m), 1700 (s), 1586 (m), 1454 (m), 1420 (m), 1360 (s), 1293 (m), 1217 (m), 1193 (m), 1113 (s), 1062 (s, br), 987 (m), 959 (w), 928 (w), 817 (m), 772 (w), 594 (m) cm^{-1}. Anal. Calculated for $C_{10}H_{13}NO_3$: C, 61.53; H, 6.71; N, 7.18. Found: C, 61.91; H, 6.53; N, 7.11. λ_{max} (MeOH) (ε(M^{-1}cm^{-1})): 261 nm (8.1×10^3). MS (LSIMS): *m/z* 196 {(MH)$^+$, 50%}, 164 {100%}. HR-MS: 196.0970 +/- 0.0004 (196.0973 for MH$^+$ $C_{10}H_{13}NO_3$).

4,6-Bis-(6-dimethoxymethyl-pyridin-2-yl)-2-phenyl-pyrimidine (3.28) – **3.25** (2.05 g 11.3 mmol) was suspended (and vigorously stirred) in an aqueous KOH (1.2g, 21.5mmol) solution (75 mL). To this emulsion, a solution of **3.26** (2.1 g, 10.7 mmol) in MeOH (25 mL) was added slowly (over 3hrs) via dropwise addition (at 0 °C). The resulting enone obtained was yellow gum-like product and after several attempts could not be isolated as pure material. The near solid product was then extracted from aqueous with DCM (3 × 30 mL) and the organic fractions dried over $MgSO_4$ before the solvent was removed under reduced pressure. The enone (yellow oil)

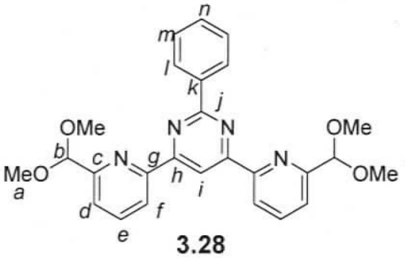

3.28

was then solubilized in MeOH (150 mL) and combined with benzamidine hydrochloride (1.68 g, 10.7 mmol) and KOH (1.2 g, 21.5 mmol). The reaction was allowed to stir at room temperature for 3 hrs and gently heated to reflux for 4 hrs. During the reflux air was bubbled through the mixture. After the reflux, the yellow solution became a bright red/salmon colour. The mixture was cooled to 0 °C in an ice bath and the resulting precipitate collected, and washed with ice-cold methanol (3 × 20 mL) resulting in pure product 1.93 g (39.2% based on ketone) by ^{1}H-NMR. The product can be further purified by chromatography (N. alumina, $CHCl_3$, $R_f = 0.6$) or by recrystallization from hexane. ^{1}H NMR ($CDCl_3$): δ 9.30 (s, 1H, H_i), 8.70 (m, 4H, H_f, H_l), 7.95 (t, $J = 7.7$ Hz, 2H, H_e), 7.69 (d, J = 7.7, 2H, H_d), 7.53 (m, 3H, H_m, H_n), 5.53 (s, 2H, H_b), 3.49 (s, 12H, H_a). ^{13}C NMR ($CDCl_3$): δ 164.3 (C_j), 164.1 (C_g), 157.6 (C_c), 154.3 (C_h), 138.1 (C_k), 137.8 (C_e), 130.9 (C_n), 128.7 (C_l), 128.4 (C_m), 122.8 (C_d), 122.0 (C_f), 112.2 (C_i), 105.0 (C_b), 54.3 (C_a). FT-IR (KBr): 2936 (m), 2831 (m), 1700 (s), 1586 (m), 1454 (m), 1420 (m), 1360 (s), 1293 (m), 1217 (m), 1193 (m), 1113 (s), 1062 (s, br), 987 (m), 959 (w), 928 (w), 817 (m), 772 (w), 594 (m) cm^{-1}. Anal. Calculated for $C_{26}H_{26}N_4O_4$: C, 68.11; H, 5.72; N, 12.22. Found: C, 67.72; H, 5.66; N, 12.23. λ_{max} ($CHCl_3$) (ε($M^{-1}cm^{-1}$)): 272 nm (1.5×10^5), 319 nm (4.8×10^3) . MS (LSIMS): *m/z* 459 {$(MH)^+$, 70%}, 428 {$(MH\text{-}OCH_3)^+$, 20%}, 381 {$(M\text{-}Ph)^+$, 100%}. HR-MS: 459.2034 +/- 0.0013 (459.2032 for MH^+ $C_{26}H_{27}N_4O_4$). Mp 152-154 °C.

6-[6-(6-Formylpyridin-2-yl)-2-phenylpyrimidin-4-yl]-pyridine-2-carbaldehyde (3.29)

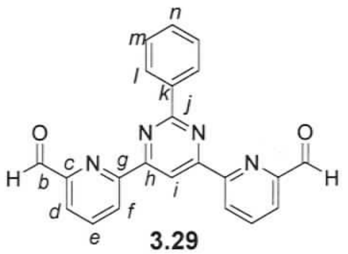

3.29

- Acetic acid (15 mL) and water (25 mL) were combined with **3.28** (1.5 g, 3.3 mmol) resulting in a milky white mixture. This mixture was stirred vigorously and heated to reflux for 1hr, over which time the mixture became transparent and slightly yellow. Within minutes of becoming clear, a white precipitate formed. After cooling to room temperature the solution was evaporated to near dryness, neutralized, and extracted from a sat. $NaHCO_3$ solution using $CHCl_3$ (3 × 50 mL). The organic extracts were combined, dried over $MgSO_4$ and the solvent removed under reduced pressure to yield 1.14 g of **3.29** (95.1%). Elemental purity can be achieved using column chromatography (N.

Alumina/$CHCl_3$ – $R_f = 0.60$) or by recrystallizing from MeOH. ^1H NMR ($CDCl_3$): δ 10.28 (s, 2H, H_c), 9.43 (s, 1H, H_i), 8.97-8.91 (m, 2H, H_f), 8.71-8.68 (m, 2H, H_l), 8.11-8.06 (m, 4H, H_d, H_e), 7.58-7.53 (m, 3H, H_m, H_n). ^{13}C NMR ($CDCl_3$): δ 193.6 (C_b), 164.6 (C_j), 163.7 (C_c), 155.3 (C_g), 152.9 (C_h), 138.4 (C_e), 137.6 (C_k), 131.3 (C_n), 128.9 (C_l), 128.6 (C_m), 126.1 (C_d), 123.1 (C_f), 111.7 (C_i). FT-IR (KBr): 2824 (w), 1715 (s), 1584 (m), 1561 (s), 1538 (s), 1460 (w), 1446 (m), 1372 (s), 1345 (m), 1221 (m), 1148 (w), 1072 (w), 993 (w), 895 (w), 815 (m), 806 (w), 760 (m), 706 (m), 695 (m), 654 (m), 632 (m) cm^{-1}. Anal. Calculated for $C_{22}H_{14}N_4O_2$: C, 72.12; H, 3.85; N, 15.29. Found: C, 71.88; H, 4.02; N, 15.07. λ_{max} ($CHCl_3$) ($\varepsilon(M^{-1}cm^{-1})$): 270 ($3.3\times10^4$), 322 nm ($8.6\times10^3$). MS (LSIMS): *m/z* 367 {$(MH)^+$, 100%}, 289 {$(M\text{-phenyl})^+$, 30%}. HR-MS: 367.1200 +/- 0.0010 (367.1195 for MH^+ $C_{22}H_{15}N_4O_2$). Mp 206-208 °C.

4,6-Bis-[6-(1,5-dimethyl-1,2,4,5-tetrazane-6-oxide-3-yl)-pyridin-2-yl]-2-phenyl-pyrimidine (3.30) – **2.52** (0.485 g, 4.10 mmol) was solubilized in 15 mL of MeOH/$CHCl_3$ (1:1) and the solution was gently heated to reflux. To this gently refluxing solution was added **3.29** (0.75 g, 2.05 mmol) in $CHCl_3$/MeOH (1:1) (175 mL) dropwise over 5hrs using a pressure equalizing dropping funnel. After the addition was complete the reaction was gently heated to reflux overnight (10 hrs). The solution (yellow) was then cooled and solvent removed to yield a white/yellow solid. The product was triturated with hot ethyl acetate, yielding 0.99 g of **3.30** (85.3%). ^1H NMR ($CDCl_3$): δ 9.29 (s, 1H, H_k), 8.76-8.66 (m, 4H, H_h, H_n), 7.96 (t, J = 7.8 Hz, 2H, H_g), 7.59-7.53 (m, 5H, H_f, H_o, H_p), 5.56 (br. s, 4H, H_c), 5.03 (s, 2H, H_d), 3.16 (s, 12H, H_b). ^{13}C NMR ($CDCl_3$): δ 164.2 (C_l), 164.0 (C_a), 155.6 (C_i), 155.0 (C_j), 154.5 (C_e), 138.4 (C_g), 137.7 (C_m), 131.1 (C_p), 128.8 (C_o), 128.5 (C_n), 125.3 (C_f) 122.0 (C_h), 111.9 (C_k), 69.7 (C_d), 38.5 (C_b). FT-IR (KBr): 3415 (m), 3229 (m), 2963 (w) 1627 (s), 1563 (s), 1538 (s), 1459 (m), 1448 (m), 1431 (m), 1373 (s), 1261 (m), 1095 (br m), 951 (m), 817 (m), 763 (w), 702 (w), 648 (m), 530 (w) cm^{-1}. Anal. Calculated for $C_{28}H_{30}N_{12}O_2$: C, 59.35; H, 5.34; N, 29.66. Found: C, 59.42; H, 5.46; N, 29.71. λ_{max} ($CHCl_3$) ($\varepsilon(M^{-1}cm^{-1})$): 273 ($3.7\times10^4$), 321 nm ($1.2\times10^4$). MS (LSIMS):

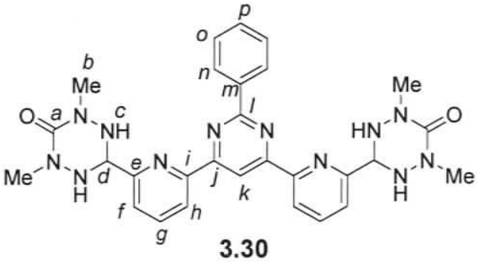

3.30

m/z 567{$(MH)^+$, 100%}, 495 {$(M\text{-}C_2H_4ON_2)^+$, 40%}. HR-MS: 567.2689 +/- 0.0008 (567.2693 for MH^+ $C_{28}H_{31}N_{12}O_2$). Mp 171-172 °C (decomp).

4,6-Bis-[6-(1,5-dimethyl-6-oxoverdazyl-3-yl)-pyridin-2-yl]-2-phenyl-pyrimidine (3.8) – *para*-Benzoquinone (*p*BQ) (0.12 g, 1.06 mmol) was added to a solution of **3.30** (0.20 g, 0.35 mmol) in $CHCl_3$ (25 mL) and the yellow solution was heated to reflux for 25 minutes. The resulting deep red solution was cooled to room temperature and the solvent removed under reduced pressure. The crude material was then triturated using hot ethyl acetate (3 × 10 mL), yielding **3.8** (0.135g 68.2%). FT-IR (KBr): 3253 (w), 3066 (w), 2938 (w), 1693 (s), 1563 (s), 1536 (s), 1460 (m), 1426 (m), 1369 (s), 1255 (m), 993 (w), 821 (m), 764 (w), 637 (m) cm^{-1}. Anal. Calculated for $C_{28}H_{24}N_{12}O_2$: C, 59.99; H, 4.32; N, 29.98. Found: C, 59.17; H, 4.33; N, 28.23. λ_{max} ($CHCl_3$) ($\varepsilon(M^{-1}cm^{-1})$): 264 ($4.1\times10^4$), 318 ($1.5\times10^4$), 399 nm ($2.3\times10^3$). MS (LSIMS): *m/z* 560{$(M)^+$, 100%}. HR-MS: 560.2142 +/- 0.0005 (566.2145 for MH^+ $C_{28}H_{31}N_{12}O_2$). Mp 161-166 °C (decomposes over the range).

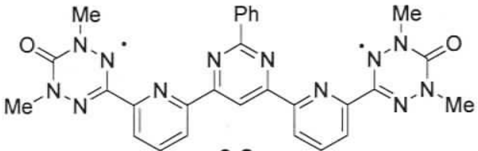

3.8

(6-Dimethoxymethyl-pyridin-2-yl)-hydrazine (3.37) – A 50 mL RBF was charged with **2.49** (3 g, 12.9 mmol), hydrazine (8 mL, 272 mmol) and pyridine (35 mL) and heated to reflux overnight (12 hrs).[252] The reaction was cooled to room temperature, then concentrated under vacuum. The resulting solid was solubilized in water and extracted with DCM, dried over $MgSO_4$, filtered, and the solvent removed under reduced pressure to quantitatively yield a white waxy solid (2.37 g, 100%). ^1H NMR ($CDCl_3$): δ 7.46 (t, 1H, *J*=7Hz, H_e), 6.85 (d, 1H, *J*=7Hz, H_f), 6.67 (d, 1H, *J*=8Hz, H_d), 6.20 (s, 1H, H_h), 5.17 (s, 1H, H_b), 3.69 (s, 2H, H_i), 3.33 (s, 6H, H_a). ^{13}C NMR ($CDCl_3$): δ 161.2 (C_g), 154.9 (C_c), 137.9 (C_e), 111.7 (C_f), 106.7 (C_d), 103.8 (C_b), 53.4 (C_a) ppm. FT-IR (KBr): 3583 (w), 3337 (m), 3085 (m), 3051 (m), 3020 (m), 2935 (m), 2831 (m), 1601 (s), 1582 (m), 1557 (m), 1496 (s), 1437 (m), 1408 (m), 1336 (m), 1310 (m), 1265 (m), 1195 (m), 1179 (m), 1155 (m), 1124 (s), 1109 (m), 1059 (s), 984 (m), 921 (m), 881 (m), 795 (m), 754 (s), 711 (m), 695 (s), 665 (m), 654 (m), 639 (m), 618 (m) cm^{-1}. Anal. Calculated for

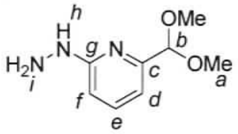

3.37

$C_8H_{13}N_3O_2$: C, 52.45; H, 7.15; N, 22.94. Found: C, 55.81; H, 7.29; N, 22.65. $\lambda_{max}(CH_2Cl_2)(\varepsilon(M^{-1}cm^{-1})$: 238 nm ($1.0 \times 10^4$), 295 nm ($3.7 \times 10^3$). MS (LSIMS): *m/z* 184 {MH^+, 50%}, 152 {$[M-CH_3O]^+$, 100%}. HR-MS: 183.1007 +/- 0.0002 (183.1008 for M^+ $C_8H_{13}N_3O_2$). Mp. 39-44 °C.

***N*-(6-Dimethoxymethyl-pyridin-2-yl)-N'-isopropylidene-hydrazine (3.38)** – A 50 mL RBF was charged with **3.37** (1.58 g, 8.6 mmol), acetone (0.7 mL, 9.5 mmol) EtOH (25 mL), and a catalytic amount of acetic acid. The solution was heated to reflux overnight (12 hrs).[253] The reaction was cooled to room temperature and concentrated under vacuum to yield an orange oil (1.93 g, 99.8%). ^1H NMR ($CDCl_3$): δ 7.78 (s, 1H, H_h), 7.53 (t, 1H, *J*=8Hz, H_e), 7.15 (d, 1H, *J*=8Hz, H_d), 6.89 (d, 1H, *J*=7Hz, H_f), 5.17 (s, 1H, H_b), 3.32 (s, 6H, H_a), 1.98 (s, 3H, H_j or H_k), 1.82 (s, 3H, H_k or H_j). ^{13}C NMR ($CDCl_3$): δ 157.2 (C_g), 154.5 (C_c), 145.7 (C_i), 138.4 (C_e), 112.7 (C_f), 107.2 (C_d), 103.3 (C_b), 53.2 (C_a), 25.2 (C_k or C_j), 16.1 (C_j or C_k) ppm. FT-IR (KBr): 3240 (m), 3085 (w), 2994 (m), 2940 (m), 2913 (m), 2828 (m), 1593 (s), 1573 (s), 1514 (s), 1441 (s), 1365 (m), 1322 (s), 1276 (m), 1253 (s), 1128 (s), 1093 (m), 1045 (m), 1030 (m), 982 (m), 880 (w), 861 (w), 817 (w), 775 (s), 745 (w), 670 (w), 643 (w), 625 (m), 546 (w), 523 (w) cm^{-1}. Anal. Calculated for $C_{11}H_{17}N_3O_2$: C, 59.17; H, 7.67; N, 18.82. Found: C, 58.82; H, 7.89; N, 18.52. $\lambda_{max}(CH_2Cl_2)(\varepsilon(M^{-1}cm^{-1})$: 267 ($3.1\times 10^4$), 304 nm ($6.0 \times 10^3$). MS (LSIMS): *m/z* 224 {MH^+, 100%}, 192 {$[M-CH_3O]^+$, 95%}. HR-MS: 223.1322 +/- 0.0003 (223.1321 for M^+ $C_{11}H_{17}N_3O_2$).

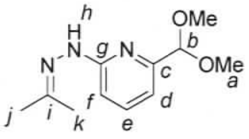

3.38

7-Dimethoxymethyl-3-methyl-2H-pyrido[2,1-c][1,2,4]triazepin-5-one (3.39) – A 250ml RBF was charged with **3.38** (1.93 g, 8.62 mmol), pyridine (0.7 mL, 8.62 mmol), and toluene (30 mL). To this solution was added dropwise a toluene-phosgene solution (20% by weight, 2.28 mL, 4.31 mmol). The reaction became slightly darker in colour and a precipitate formed (pyridine-HCl) over the 45 min addition of the phosgene solution. Water (25 mL) was added to quench the reaction and the product was extracted using DCM (3×75 mL). The organic layers were dried over $MgSO_4$, filtered,

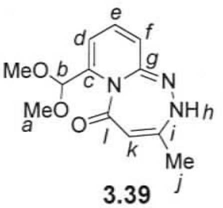

3.39

and the solvent removed under reduced pressure. The oily solid was then recrystallized twice from hexane resulting in a yellow crystalline powder (0.69 g, 64.2%). ^{1}H NMR ($CDCl_3$): δ 6.98 (d, 1H, J=1Hz, H_d), 6.96 (s, 2H, H_e), 6.64 (td, 1H, J= 4Hz, 1Hz, H_f), 6.38 (s, 1H, H_h), 5.76 (s, 1H, H_k), 4.85 (s, 1H, H_b), 3.45 (s, 6H, H_a), 2.24 (s, 3H, H_j). ^{13}C NMR ($CDCl_3$): δ 147.7 (C_l), 141.8 (C_i), 139.0 (C_g), 137.1 (C_c), 129.5 (C_e), 115.8 (C_f), 108.5 (C_d), 102.9 (C_b), 97.2 (C_k), 54.8 (C_a), 20.4 (C_j) ppm. FT-IR (KBr): 3406 (w), 3240 (m), 3080 (m), 3038 (m), 2989 (m), 2958 (m), 2933 (m), 2905 (m), 2829 (m), 1715 (s), 1653 (m), 1643 (m), 1558 (s), 1443 (m), 1398 (m), 1381 (m), 1339 (s), 1255 (m), 1228 (w), 1212 (m), 1192 (m), 1167 (m), 1143 (m), 1104 (s), 1081 (s), 1042 (m), 992 (m), 963 (s), 901 (m), 861 (m), 830 (m), 800 (s), 745 (w), 693 (w), 682 (w), 636 (w), 601 (w), 545 (w), 529 (w), 507 (w), 489 (w) cm^{-1}. Anal. Calculated for $C_{12}H_{15}N_3O_2$: C, 57.82; H, 6.07; N, 16.86. Found: C, 58.18; H, 6.04; N, 17.00. λ_{max}(CH_2Cl_2)(ε($M^{-1}cm^{-1}$): 243 (2.0×10^4), 351 nm (5.5×10^3). MS (LSIMS): *m/z* 249 {M^+, 70%}, 218 {$[M-CH_3O]^+$, 100%}. HR-MS: 249.1113 +/- 0.0005 (249.1113 for M^+ $C_{12}H_{15}N_3O_2$). Mp 99-102 °C.

3-*para*-Tolyl-[1,2,4]triazolo[4,3-a]pyridine[234] **(3.46)** – In a 100 mL 2-neck RBF equipped with an argon inlet, *N*-(4-Methyl-benzylidene)-*N′*-pyridin-2-yl-hydrazine[234] **3.44** (1.00 g, 4.7 mmol) was solubilized in $CHCl_3$ (50 mL). To this was added NCS (0.67 g, 5 mmol) and the reaction was allowed to stir at room temperature for 2 hours over which time a white precipitate formed. The precipitate was filtered from the reaction and washed with DCM to yield **3.46** as white solid. More of the product was collected by extracting the product from water using chloroform (1.03 g, 88.6%). ^{1}H NMR ($CDCl_3$): δ 8.21 (d, 1H, J=6Hz), 7.75 (d, 1H, J=8Hz), 7.66 (d, 2H, J=8Hz), 7.32 (d, 2H, J=8Hz), 7.20 (dd, 1H, J=6Hz), 6.78 (t, 1H, J= 7Hz), 2.38 (s, 3H). ^{13}C NMR ($CDCl_3$): δ 150.7, 147.1, 140.6, 130.2, 128.3, 127.2, 123.9, 122.9, 117.0, 114.2, 21.7 ppm. FT-IR (KBr): 3135 (w), 3108 (m), 3027 (w), 2971 (m), 2948 (w), 1633 (s), 1613 (w), 1497 (s), 1466 (s), 1445 (m), 1409 (m), 1370 (s), 1316 (m), 1303 (m), 1277 (m), 1190 (w), 1137 (w), 1116 (m), 1071 (s), 1048 (m), 1005 (s), 985 (m), 922 (w), 824 (s), 774 (m), 749 (s), 738 (s), 716 (s), 695 (m), 663 (w), 594 (w), 570 (m), 526 (m), 487 (m) cm^{-1}. MS (EI): *m/z* 209 {M^+, 100%}. Mp 213 °C (decomposes).

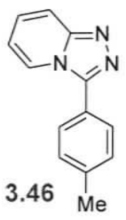

3.46

3.5.3 Attempted preparation of coordination complexes involving **3.8**

3.5.3.1 General procedure for bimetallics

The tetrazane **3.30** or verdazyl **3.8** (typically 0.1-0.2mmol) was solubilized in MeOH (10 mL) with the aid of a minimal amount of $CHCl_3$. To this solution was added a solution of the metal salt M^{n+}(terpy)X_n (2 equivalents) in MeOH (10 mL). Some metal salts required the addition of a minimal amount of MeCN to aid solubility. DMF was also used as a solvent replacement for methanol. The higher boiling point of DMF allows for higher refluxing temperatures. Metal salts used in the trials include Ru(terpy)Cl_3[254], Co(terpy)Cl_2, and Zn(terpy)Cl_2[169].

The reaction was stirred under a variety of conditions. Under ambient conditions the solution mixture was allowed to stand for up to 6 days and under more vigorous conditions (refluxing), the reactions were left up to 16 hours. If a precipitate formed, the solid was isolated via filtration and characterized using FT-IR; otherwise, the solvent was removed *in vacuo* and solubility of the residual solid examined. Depending on the solubility of the solid, anion metathesis was done using saturated solutions of KPF_6, $NaBF_4$. If the solids were organic soluble, $AgPF_6$, $AgBF_4$, or AgOTf were used to generate the metathesis product. The metathesis products, in all cases, were washed with $CHCl_3$ and Et_2O to remove any residual organics. Often the products were recrystallized from suitable solvents. The metathesis product was analyzed by FT-IR. If the IR showed the presence of a ketone signal, it was submitted for ESI-MS or LSI-MS.

3.5.3.2 General procedure for grids

In order to synthesize 2 × 2 grids the procedure in section 3.5.3.1 (above) was modified slightly where the metal:ligand ratio was adjusted to 1:1, where this stoichiometry is preferred for grid formation. The metal salts tested were $NiCl_2$, $Ni(ClO_4)_2$, $Ni(PF_6)_2$, $CoCl_2$, $Co(ClO_4)_2$, $Co(OTf)_2$, $ZnCl_2$, $Zn(ClO_4)_2$, and $RuCl_3$.

Reaction conditions and solvents employed in attempted grid formation were identical to the procedure for the preparation of the bimetallics (Section 3.5.3.1).

Chapter 4: Ferrocenyl Verdazyls

4.1 Introduction to ferrocene-radical complexes

4.1.1 Objectives

There have been many studies on the magnetic interactions in metal-radical assemblies, but few studies have investigated other forms of electronic interactions between metals and radicals. Valence tautomerism is perhaps the most well studied example of metal-radical electronic communication. Previous chapters have explored the potential of the verdazyl radical as a ligand directly coordinated to metal ion in order to obtain strong magnetic interactions. However, the more general aspects of the electronic structure of these C3-substituted *N*-heterocyclic verdazyl complexes have not been studied because for the most part, verdazyl radicals substituted with electron-withdrawing groups are not electrochemically stable.

This chapter focuses on the synthesis and characterization of verdazyls that possess ferrocenyl moieties. Ferrocene verdazyls have been designed to investigate the indirect interactions between electrophores. By substituting the verdazyl radical in the C3 position with ferrocenyl moieties the electroactive nature of the verdazyl can be probed in two ways. Ferrocene can be chemically altered to increase or decrease its electron donating ability, and because ferrocene is a well-established redox active species, coupling it to an electroactive verdazyl radical may result in valence tautomerism.

4.1.2 Ferrocene-based radical assemblies

From the initial elucidation of the structure of ferrocene in 1951 by Fischer and Wilkinson, transition metal cyclopentadienyl complexes have constituted a major area in the development of organometallic chemistry.[255, 256] Ferrocene compounds have found applications as chiral auxiliaries and ligand scaffolds for transition metal-mediated homogeneous catalysis;[257-259] redox probes in biochemistry,[260] organometallic and inorganic chemistry;[261-263] and materials chemistry as charge transfer complexes[264] and organometallic polymers.[265-267]

Ferrocene is an 18-electron transition metal complex that is popular because of its remarkable chemical stability, redox activity, and synthetic versatility. Ferrocene is soluble in most organic solvents, and is stable to air, water, acids, and bases. Ferrocene is readily functionalized[268] and possesses a tunable and reversible oxidation potential that can be readily converted between ferrocene and the ferrocenium cation.

The first studies to use ferrocene as a magnetic building block were focused on the charge transfer (CT) salts involving ferrocenium cations and radical anions.[264] In these charge transfer complexes the ferrocene unit serves as an electron donor, and a quinone-based molecule as an electron acceptor. A variety of electron rich methylated ferrocene derivatives have been studied with DDQ[269], TCNQ[40, 270, 271], and TCNE[38, 39, 272] as oxidants and in 1987 the discovery of the first organometallic bulk ferromagnet, $[FeCp^*_2]^+[TCNE]^{\cdot-}$ was made by Miller and coworkers.[41] It is important to note that these ferrocene-radical assemblies are CT salts and the two spin containing entities are not covalently bound to one another.

4.1.2.1 Ferrocene-nitronyl nitroxides

Ferrocene-substituted radical anions with short lifetimes have been generated electrochemically,[273] but the first ferrocene covalently bound to a stable radical was reported by Iwamura and co-workers[274] in 1991. The original experiment was an attempt to make donor-acceptor systems based on ferrocene-TCNQ (CT) salts. Ideally it was thought that the combination of a stable radical with ferrocene would result in a strongly coupled triplet diradical after the ferrocene was oxidized by a polynitrile. This incorporation of stable radical moieties would lead to the addition or at least incomplete cancellation of the total spin, leading to ferrimagnetism. Iwamura and coworkers decided to study compound **4.1** where the ferrocene was covalently bound to a nitronyl-nitroxide fragment. Electrochemical investigations using **4.1** suggested that the radical is a modest electron withdrawing group and DDQ would be an ideal oxidant, because its oxidizing power would allow for oxidation of the ferrocenyl moiety (0.19 V vs. Fc/Fc^+) but not the nitronyl nitroxide radical (0.53 V vs Fc/Fc^+). Oxidation of the ferrocenyl radical with DDQ resulted in a corresponding 1:1 CT salt that displayed complex temperature-dependant magnetic behaviour due to DDQ radical anion dimerization. The authors were able to determine that there was weak intramolecular antiferromagnetic ($J_{Fc\text{-}rad}$= -25 cm^{-1}) coupling between the ferrocenium cation and nitronyl-nitroxide, where spin polarization dominated the exchange mechanism; this is consistent with theoretical predictions.[275] The dimerization of the DDQ radical anion and the weak antiferromagnetic coupling between the radical and the ferrocenium cation led to the authors abandoning this focus for ferrocene stable radical-based CT complexes.

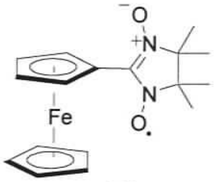

4.1

Nitronyl-nitroxide substituted ferrocene **4.1** was studied in more detail in the late 1990s by Veciana and coworkers.[276] The most relevant structural features[277] of the ferrocenyl nitronyl-nitroxide was dimer formation caused by complementary weak C-H···O-N hydrogen bonds between a pair of neighboring radicals. As a result the ferrocene nitronyl-nitroxide showed weak antiferromagnetic behaviour (J_{inter} = -0.5 cm^{-1}), consistent with the weak hydrogen bonding in the solid state.

An electrochemical investigation of the ferrocenyl nitronyl-nitroxide radical in solution demonstrated two reversible waves. The first oxidation was assigned to ferrocene (0.17 V vs. Fc/Fc$^+$) and the second to the radical (0.50 V vs Fc/Fc$^+$). This is consistent with the observations made by Iwamura.[274] The nitroxide family of radicals is generally not stable to reduction and as a result the attempted reduction of **4.1** was seen to be an irreversible process. Veciana and coworkers also electrochemically studied model compounds **4.2** and **4.3**, and noted that the presence of the ferrocenyl moiety increases the oxidation potential of the radical moiety by ~0.16 V. This result is somewhat surprising considering that ferrocene behaves like an electron-rich aromatic and should decrease the oxidation potential of the radical. However, because the ferrocene is oxidized to ferrocenium prior to the radical oxidation the ferrocene unit becomes a much poorer electron donating group.

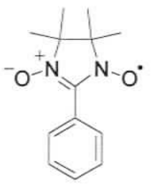

4.2

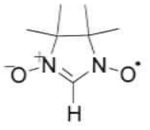

4.3

Variable-temperature EPR investigations[276] of **4.1** also concluded that there is a nonzero spin density on the iron centre as determined from low intensity satellite bands (enhanced in a ruthenocene derivative) in the room temperature spectrum. This result is rather surprising considering there is no significant coupling with the protons of the cyclopentadienyl rings, but the authors concluded that with larger nuclear magnetic moments of the metal nuclei it makes the observation of the hyperfine coupling between the radical and metal ion possible. The mechanism through which this small spin density appears on the metal nuclei is different depending on the experimental conditions and the conformations of the free radical. It is likely that under isotropic conditions the dominant mechanism for a freely rotating radical interaction would be spin polarization through covalent bonds. Under anisotropic conditions in a frozen solution it is also possible that some conformations lead to direct overlap between the radical unit and the d-orbitals.

4.1.2.2 Ferrocene-triphenylmethyl radicals

After investigating the nitronyl-nitroxide ferrocene derivatives, Veciana and coworkers turned their attention towards a new radical system based on ferrocene - triphenylmethyl radicals **4.4**.[278] Electrochemical investigations of **4.4** showed two reversible waves; one owing to the oxidation of the ferrocenyl moiety (0.59 V vs. Ag/AgCl) and the other to the reduction of the radical (-0.18 V vs Ag/AgCl).

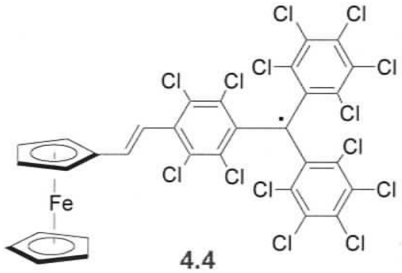

4.4

In the solid state UV-Vis a broad intervalence transition band at 1020 nm was observed and suggested that an intramolecular electron transfer process could be induced by light irradiation. This charge transfer was confirmed thermally using variable temperature Mössbauer spectroscopy. The ferrocene-radical derivative **4.4** undergoes a reversible temperature dependant valence tautomerism as depicted in Figure 4.1.

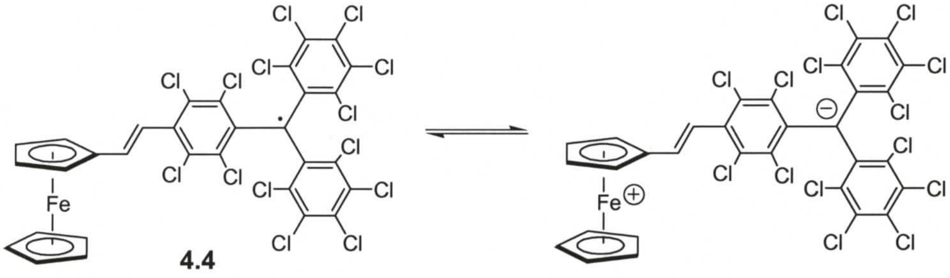

Figure 4.1 - Valence tautomerism in the ferrocene triphenylmethyl radical

Mössbauer spectroscopy is a useful technique used to determine the oxidation state and ligand field environment of iron. Figure 4.2 presents a series of Mössbauer spectra taken at various temperatures. These spectra demonstrate the effect of raising the temperature on the valence tautomerism presented in Figure 4.1. At 2 K Mössbauer data suggests that only Fe^{2+} (Figure 4.2, red envelope) is present in the sample, but as the temperature is raised to 78 and 200 K there is an increasing proportion of Fe^{3+} (Figure 4.2, blue envelope) present in the sample. At room temperature (293 K) there is nearly an equal distribution of the equilibrium structures.

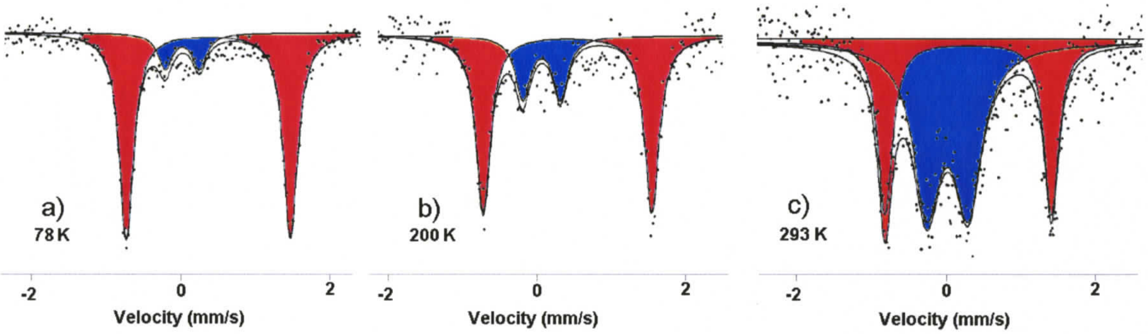

Figure 4.2 - Mössbauer spectra of **4.4** a) 78 K, b) 200 K, c) 293 K. (y-axis – relative transmission). Reproduced with permission from *J. Am. Chem. Soc*, 2003, *125*, 1462-1463. Copyright 2003 American Chemical Society.

Valence tautomerism results in subtle changes in the magnetization data of radical **4.4**. Veciana and co-workers[279] observed a rather high room temperature magnetic moment ($_{\text{experimental}}\mu_{eff} = 2.28$; $_{\text{theoretical}}\mu_{eff} = 1.73$) in **4.4** and attributed this high μ_{eff} value to significant orbital contributions from remnant $[Fe^{III}Cp_2]^+$. This assignment is consistent with the large amount of ferrocenium cation present as seen in the Mössbauer spectrum.

The currently accepted belief in the ferrocene community[280] suggests that the HOMO of ferrocene has a e_{2g} symmetry (Figure 4.3b) which contrasts the previously understood molecular orbital diagram[255] that described the ferrocene HOMO as having a_{1g} symmetry (Figure 4.3a). This more modern description of the FMO diagram for ferrocene correlates well to the experimentally determined ground state for ferrocenium as depicted in Figure 4.3c. By looking at the FMO of ferrocenium, it may not be clear why the magnetic moment in the solid state of Veciana's ferrocenium would exceed its 'spin-only' value of 1.73.

The observation of a higher than expected magnetic susceptibility in the ferrocenium cation system has been thoroughly studied.[281-284] These studies concluded that the $^2E_{2g}$ state of ferrocenium ion is split into two Kramers doublets under the influence of spin-orbit coupling. Furthermore, thermal population[285] of the $^2A_{1g}$ state leads to another thermally accessible electronic configuration. These multiple electronic configurations result in an effective moment that is the sum of multiple orbital components resulting in a higher than expected μ_{eff}.[286]

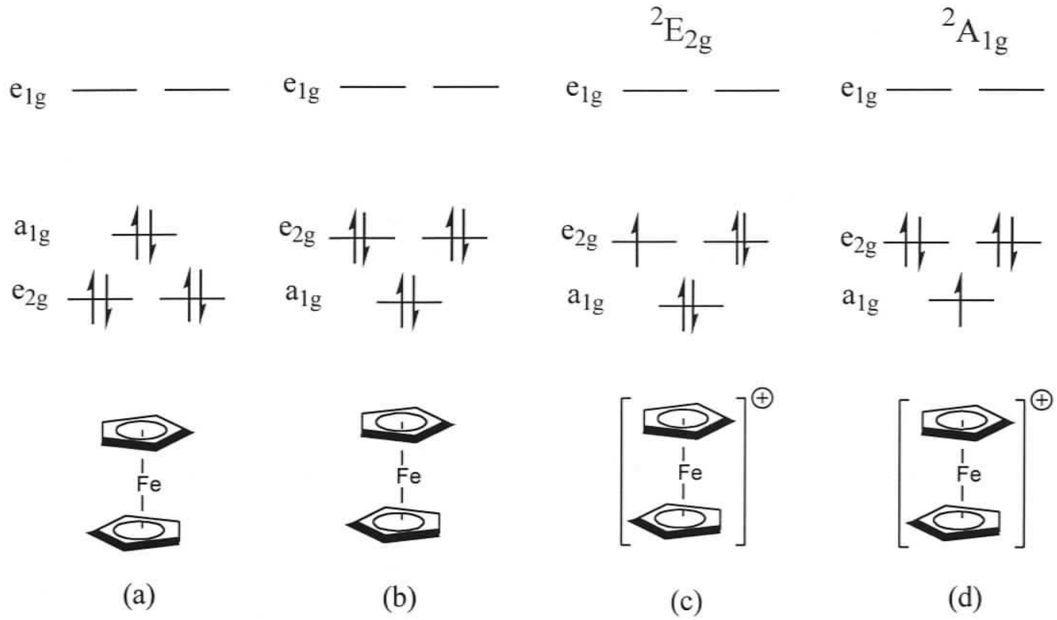

(a) (b) (c) (d)

Figure 4.3 - Frontier molecular orbital (FMO) schemes for ferrocene (pre-1990) (a); revised FMO of ferrocene (b); experimentally determined ground state configuration of ferrocenium (c); thermally populated excited state of ferrocenium (d)

Subsequent to the initial discovery of valence tautomerism in the ferrocene-triphenyl methyl radical, Veciana and coworkers[287] made modifications to their triphenylmethyl radical system **4.4** by replacing the alkene spacer with an imine linkage (as seen in **4.5**). This new conjugated bridge was expected to experience reversible photo-induced structural changes. Ideally these induced changes in geometry would have controllable changes in magnetic behaviour. Although isomerism was not observed in the solid state, the *cis*- and *trans*-isomers were identified in solution using UV-Vis spectroscopy.

A nonamethylated ferrocene derivative **4.6** was also presented and valence tautomerism was observed in this case because of the capacity of the methylated ferrocene to serve as an electron donor. This experimental observation is also supported by theoretical calculations. Oddly, there was no intervalence band transition observed in the non-methylated derivatives (**4.5**; *cis or trans*). The authors concede that these bands for the non-methylated derivatives are hidden in the tails of radical absorption, but no Mössbauer data was provided to help support this claim.

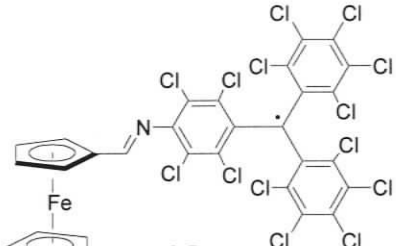

4.5

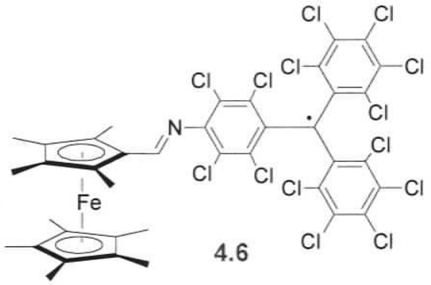

4.6

Electrochemical data showed that the triphenylmethyl radical component was fully reversible to oxidation (1.05 V vs Ag/AgCl) and reduction (-0.66 V vs Ag/AgCl) and the radical oxidation/reduction potentials are not effected by methylation of the ferrocene moiety.

4.1.2.3 Other ferrocene-substituted radicals

Ferrocene-TEMPO derivative **4.7** was studied as part of a large suite of arylmethylamino-TEMPO derivatives[288] and **4.7** was found to exhibit weak intermolecular antiferromagnetic exchange in the solid state based on a negative Weiss constant. This is consistent with the observations seen in the nitronyl-nitroxide ferrocene derivative. No other characterization was reported for **4.7**.

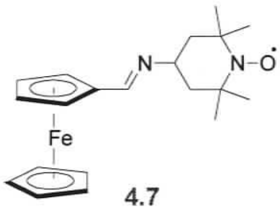

4.7

The ferrocene-substituted enol radical **4.8** has been prepared chemically in solution,[289] but has not been isolated in the solid state. The radical is stabilized similarly to **4.4**, but it does have some interesting differences. The radical is stabilized with an enol functionality and there is an alkyne linkage to the ferrocene. These unique structural and stabilizing moieties may inspire further development of other organometallic-radical hybrids.

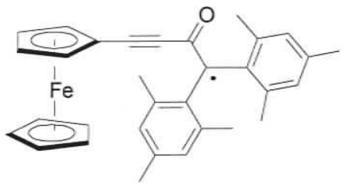

4.8

4.9 and **4.10** represent other paramagnetic ferrocene derivatives that share a common feature. Both organic radicals are generated in the excited state. The electron rich diarylamino-substituted ferrocene derivative **4.9** is an intriguing variation of substituted ferrocenes. The addition of a diarylamino electron donor results in large perturbations to the frontier molecular orbital energies of ferrocene.[290] This effect can be studied electrochemically or by electronic absorption spectroscopy. The authors[291] investigated **4.9** and determined from magnetic measurements that the cation is principally isolated on the ferrocene moiety (μ_{eff} = 2.1), but a low energy (938 nm) ligand-to-metal-charge transfer band could suggest a low energy excited state where the radical cation is nitrogen centred (Figure 4.4).

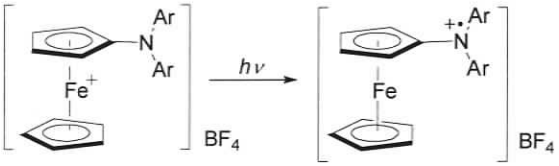

4.9

Figure 4.4 - Metal-to-ligand charge transfer in **4.9**

Charge separation was investigated in compound **4.10**. Although the ferrocene substituent is not a radical, photochemically a diradical can be generated in the excited state. In the presence of yttrium triflate a charge separated lifetime can be as long as 83 μs.[292] The authors observed this result by examining the charge transfer band at 700 nm (600 nm in the absence of yttrium triflate) using time-resolved absorption spectroscopy after laser pulse excitation (355 nm). **4.10** was also studied electrochemically. Based on two reversible one electron (E_{ox} – 0.47 V vs SCE for Fc/Fc^+ couple and E_{red} = -0.81 V for $AQ/AQ^{\cdot-}$ couple) waves it was determined that no thermal electron transfer would occur due to high endothermicity.

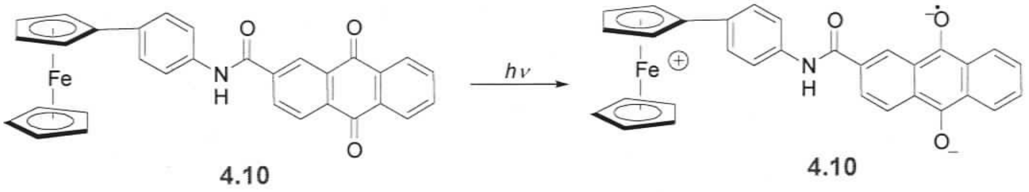

Figure 4.5 - Excited state charge separation in **4.10**

Radicals covalently linked to ferrocene have interesting properties owing to the electroactive nature of both the ferrocene and attached radical unit. Using this ferrocene scaffold perhaps new properties can be observed by altering the radical component. To this end, the remainder of the chapter focuses on synthesis and properties of a new class of ferrocene radicals using the verdazyl moiety as an electroactive substituent.

4.2 Synthesis of ferrocenyl verdazyls

4.2.1 General methodology

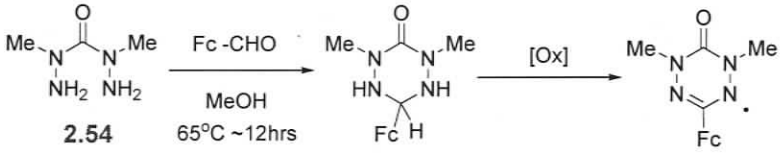

Scheme 4.1 - General methodology to ferrocenyl verdazyls

Using existing strategies for verdazyl synthesis (Scheme 4.1) the ferrocenyl aldehydes (Figure 4.6) were identified as precursors for condensation with carbonic acid bis(1-methylhydrazide).[131] The resulting tetrazanes were then oxidized to form a series of ferrocenyl verdazyls. In our synthetic strategy the ferrocenyl aldehydes (Figure 4.6) were chosen because of their varying electron donating effects dictated by degree and pattern of methylation.

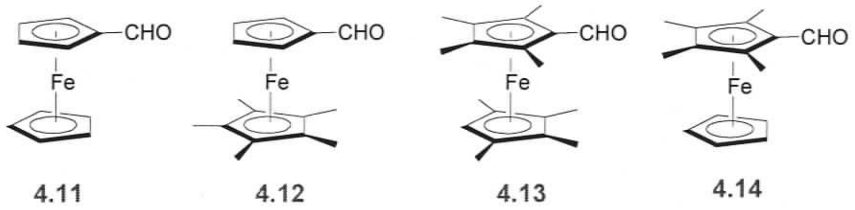

Figure 4.6 - Formylferrocenes used in the study of ferrocenyl verdazyls

4.2.2 Aldehyde synthesis

Three of the aldehydes (**4.11 - 4.13,** Figure 4.6) are known compounds. Ferrocene carboxaldehyde is commercially available, but instead it was synthesized from ferrocene an existing procedure.[293] The aldehyde was prepared via a low temperature lithiation using the mixture of *tert*-butoxide and *tert*-butyllithium as presented in Scheme 4.2.

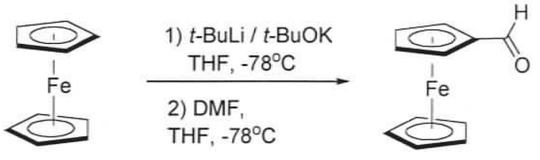

4.11

Scheme 4.2 - Synthesis of ferrocene carboxaldehyde

The pentamethylferrocenyl aldehyde **4.12** was prepared using an existing ancillary ligand strategy[294, 295] (Scheme 4.3) for the preparation of asymmetrically substituted ferrocenes. The lithiated pentamethylcyclopentadienyl ligand was added to a solution of *bis*(acetylacetonato-)iron(II)[296] in THF, resulting in the pentamethylcyclopentadienyl-iron(II) acetylacetonate adduct (**4.15**).[297] **4.15** is thermally stable in a THF solution, but it is highly sensitive to atmospheric oxidation and it was not isolated. To this mixture was added a cold solution of lithium cyclopentadienyl carboxaldehyde[298] resulting in pentamethylformylferrocene **4.12**. The yield for this sequence varies depending on the temperature gradients employed and the purity of the iron *bis*-acetylacetonate used. Low yields (10-25%) were obtained in all trials.

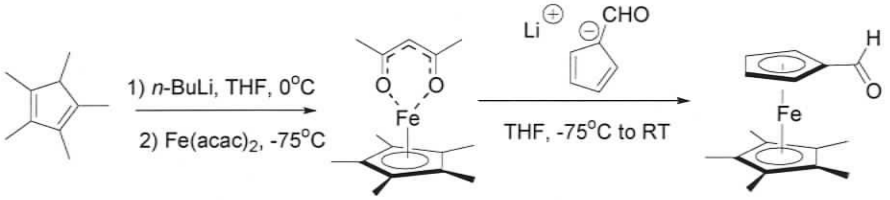

4.15

4.12

Scheme 4.3 - Synthesis of 1,2,3,4,5-pentamethyl-1'-formylferrocene, **4.2.**

Octamethylformyl ferrocene **4.13** was prepared by lithiating tetramethylcyclopentadiene and combining it with iron (II) chloride (Scheme 4.4). This resulted in the symmetrically-substituted octamethylferrocene.[299] Octamethylferrocene

4.16 is an electron rich aromatic and as such lithiations become more challenging because of the reactivity of the anion formed.[300] However, electron-rich aromatics can be formylated without the need to deprotonate using the *Vilsmeier-Haack* procedure.[301] The literature[302] variation to the Vilsmeier method results in the formylferrocene derivative **4.13**, where the strong electron withdrawing effect of the newly generated aldehyde prohibits multiple formylations.

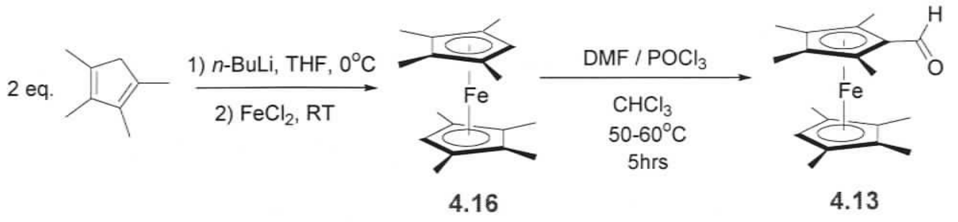

Scheme 4.4 - Synthesis of octamethyl-1-formylferrocene, **4.13**

Scheme 4.5 outlines the proposed route and the challenges in synthesizing tetramethylferrocenyl aldehyde **4.14.** There is only one known literature[303] route to tetramethylferrocene and in this case the product was isolated in low yields using gas phase low temperature methods. Literature methods exist to make pentamethylformylferrocene (**4.12**) via iron carbonyl dimers.[304, 305] It was hypothesized that this method could be applied to the synthesis of tetramethylformylferrocenes.

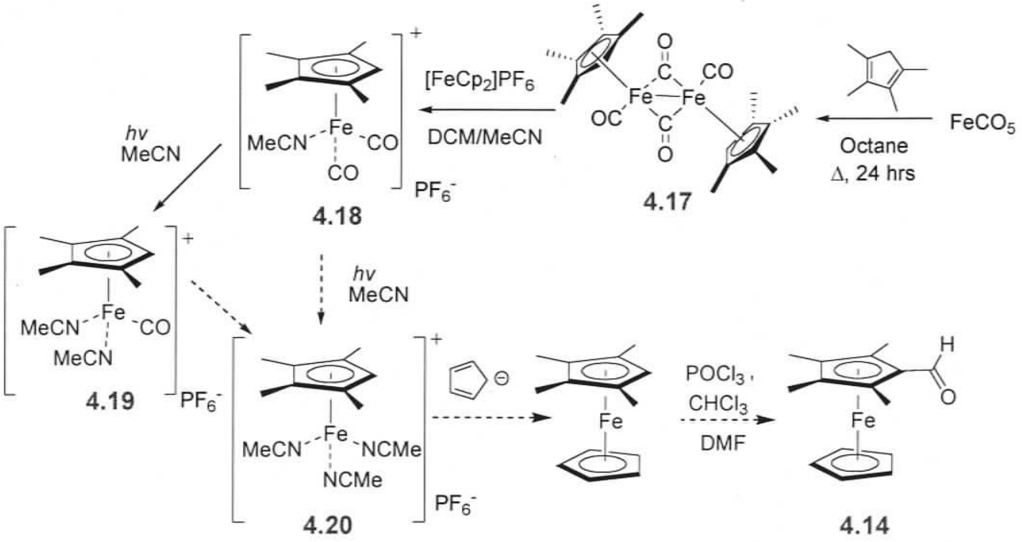

Scheme 4.5 - Attempted preparation of 2,3,4,5-tetramethyl-1-formylferrocene, **4.5.**

The tetramethyl cyclopentadienyl iron carbonyl dimer[306] (**4.17**) was readily converted into the monomer (**4.18**) via oxidation using ferrocenium hexafluorophosphate. Piano stool-type dicarbonyl complex **4.18** was exhaustively irradiated under a variety of conditions, yet, despite these attempts there was no indication of tris-acetonitrile formation (**4.20**). Either **4.18** decomposed or the monocarbonyl **4.19** was isolated. As of yet we have not been able to overcome the synthetic challenges in preparation of asymmetrically substituted tetramethylferrocene.

4.2.3 Synthesis and characterization of ferrocenyl tetrazanes

With few exceptions, aldehydes can be condensed with carbonic acid *bis*(1-methylhydrazide)[131] **2.52** to form tetrazanes under the appropriate conditions. These conditions usually involve controlled aldehyde addition to prevent the competition with imine byproducts. The following ferrocenyl tetrazanes (Figure 4.7) were synthesized by condensation of the previously discussed aldehydes (Figure 4.6).

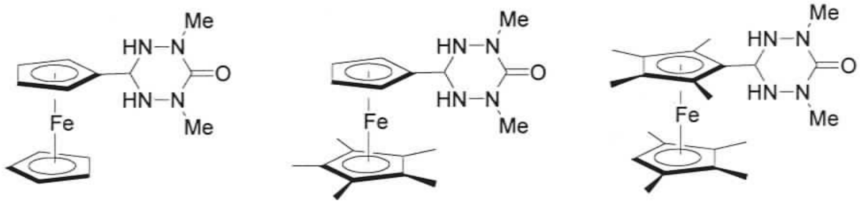

4.21 **4.22** **4.23**

Figure 4.7- Ferrocenyl tetrazanes

Ferrocenyl tetrazanes **4.21** and **4.22** were synthesized in moderate to good yield, with no observation of competing equilibrium or imine formation. Characterization of all tetrazanes was accomplished by $^{1}H/^{13}C$ NMR, FT-IR and UV-Vis spectroscopies, MS, and elemental analysis and detailed characterization is presented in the experimental section 4.6.

4.2.3.1 Octamethylferrocenyl tetrazane, **4.23**

In some cases imine side products are not avoided by simply controlling reaction conditions. The electron donating ability of the aldehyde substituent also influences the relative yields of imine products; electron-rich C3 groups (Scheme 4.6) tend to favour imine formation. Condensations involving electron rich aromatic aldehydes have increased levels of imine formation that considerably lower the yield of the tetrazane. The mechanism for tetrazane formation (Scheme 4.6) goes through an imine intermediate, where the electron rich substituents tend to stabilize the imine side product. Electron donating groups attached to the imine decrease the electrophilicity of the imine carbon, thus favouring the mono-imine over the cyclic tetrazane.

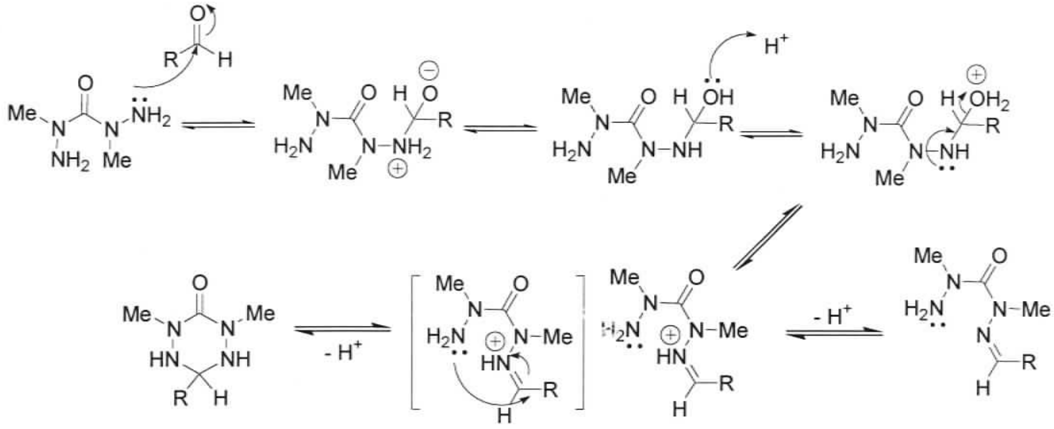

Scheme 4.6 - A mechanistic interpretation of the competing equilibria in the formation of imines and tetrazanes.

The tetrazane ring closing reaction in Scheme 4.6 is reversible, as was observed in the preparation of **4.23**. In non-polar solvents equilibrium (Figure 4.8) is instantly established between the octamethylferrocene tetrazane **4.23** and the corresponding imine isomer **4.24**. In polar solvents (MeOH, DMSO) this equilibrium is established over approximately 3 hours. This reversibility is attributed to the electron rich octamethylferrocene decreasing the electrophilicity of the C3 carbon. This ring-chain tautomerism has been recently observed in other ferrocenyl compounds based on 2-ferrocenyl-2,4-dihydro-1*H*-3,1-benzoxazines.[307]

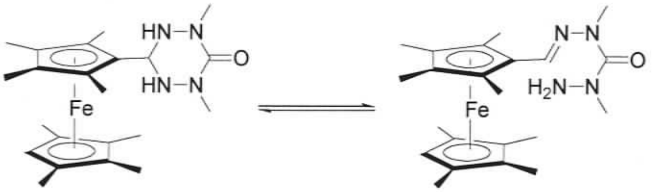

4.23

4.24

Figure 4.8 – Equilibrium between octamethylferrocenyl tetrazane and corresponding imine

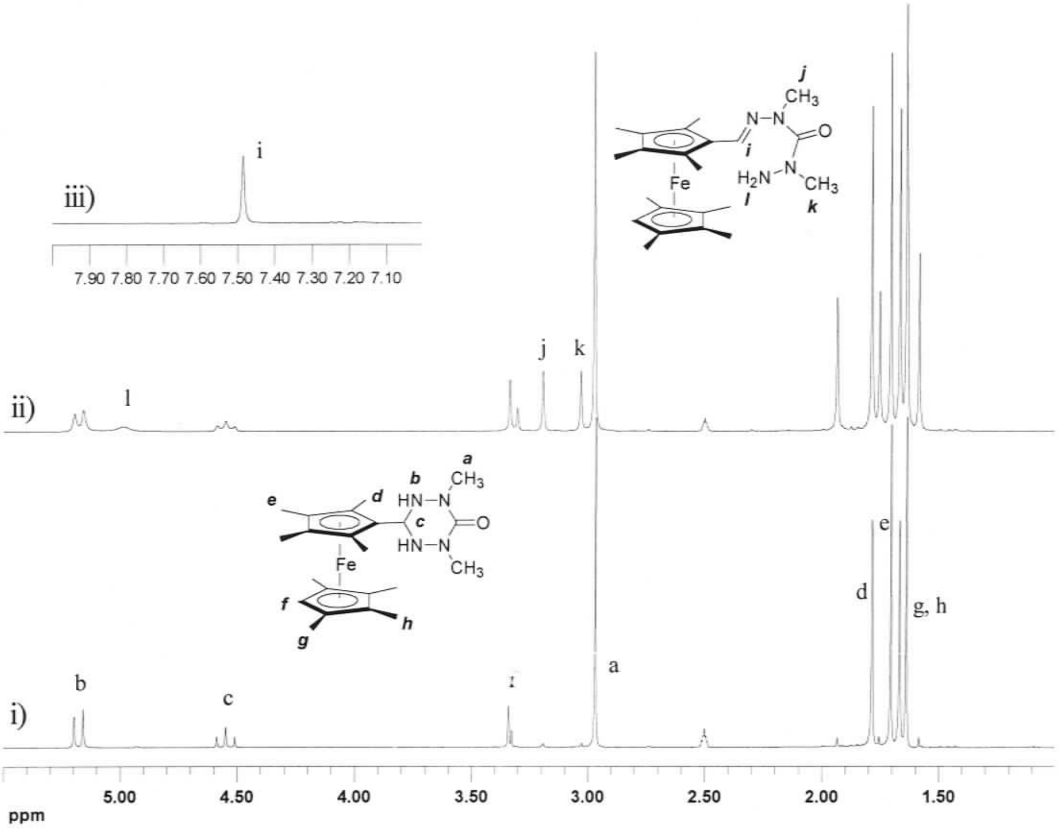

Figure 4.9 - ^{1}H-NMR spectra of **4.23** in DMSO-d^6; i) 5 minutes in solution; ii) 3hrs in solution; (iii) inset shows the presence of the imine hydrogen in the mixture.

This equilibrium can be monitored using ^{1}H-NMR spectroscopy. Figure 4.9 shows the assigned spectrum of **4.23**. Once equilibrium is established, the relative percentage of tetrazane to imine is about 65:35 by ^{1}H integration. The imine side product can be observed (Figure 4.9) from the presence of the imine hydrogen (i), primary amine (l), and asymmetry of the carbohydrazide methyl signals (j, k).

Conveniently, the tetrazanes are much less soluble than their imine side products, and **4.23** was selectively crystallized from a cold saturated toluene solution, yielding x-ray quality crystals. An ORTEP of **4.23** is shown in Figure 4.10. The Cp units of the ferrocene are eclipsed and the tetrazane adopts the energetically favoured *trans*-'chair' conformation. All bond lengths and angles within the tetrazane are consistent with previously reported tetrazanes[149] and a selection of bond lengths and angles is presented in Table 4.1. Attempts were made to isolate the imine side product as a crystalline solid; however, due to its high solubility this was not possible.

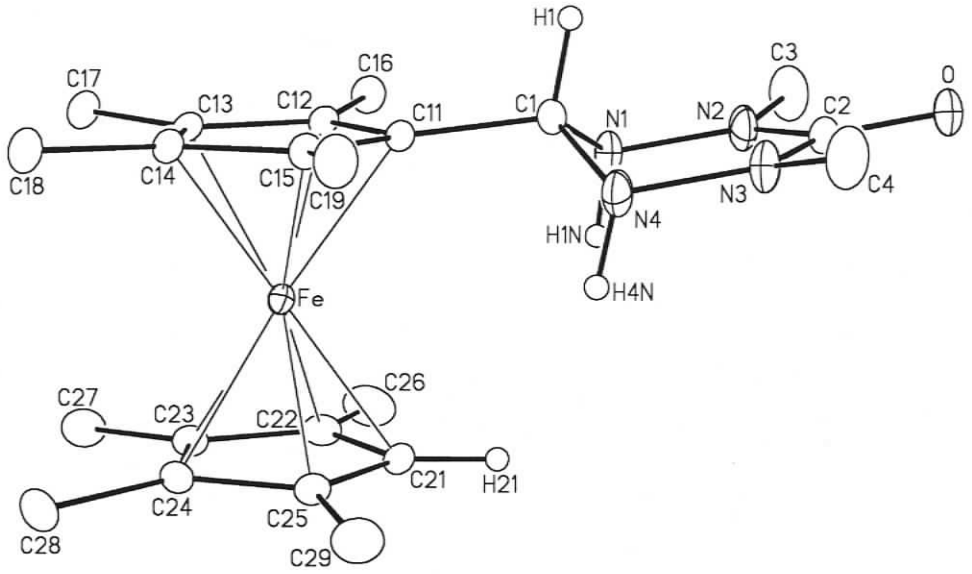

Figure 4.10 - ORTEP diagram of the molecular structure of **4.23** (Gaussian ellipsoids at the 20% probability level; the hydrogen atoms of the methyl groups are not shown.)

Table 4.1 - Selected bond distances and angles for the structure of tetrazane 4.23 (estimated standard deviations in parentheses)

Atoms	Distance (Å)	Atoms	Angle (deg.)
O-C(2)	1.240(2)	N(2)-N(1)-C(1)	108.71(16)
N(1)-N(2)	1.427(2)	N(1)-N(2)-C(3)	114.50(19)
N(1)-C(1)	1.457(2)	C(2)-N(2)-C(3)	122.6(2)
N(1)-H(1)N	0.89(2)	N(4)-N(3)-C(2)	122.68(17)
N(2)-C(3)	1.429(3)	C(2)-N(3)-C(4)	122.0(2)
N(3)-N(4)	1.426(2)	N(3)-N(4)-C(1)	109.08(16)
N(3)-C(2)	1.355(3)	N(1)-C(1)-N(4)	110.92(16)
N(3)-C(4)	1.442(3)	N(1)-C(1)-C(11)	112.01(15)
N(4)-C(1)	1.456(2)	O-C(2)-N(2)	121.4(2)
C(1)-C(11)	1.513(2)	N(2)-C(2)-N(3)	117.74(17)

To avoid imine formation an attempt was made to shift the tetrazane-imine equilibrium by oxidizing the octamethylferrocenyl moiety of the tetrazane **4.23**. This could sufficiently decrease the electron donating ability of the ferrocene, destabilizing the imine and favouring the tetrazane as the dominant solution structure (Scheme 4.7). However, upon oxidation using ferrocenium hexafluorophosphate ($FcPF_6$), the product was not the octamethylferrocenium cation **4.25**. Instead a ferrocenium disproportionation product **4.26** resulting from the reaction of the octamethylferrocene imine side product **4.24** and octamethylformylferrocene was observed. Serendipitously, the *bis*-imine product **4.26** was isolated as a ferrocenium salt.

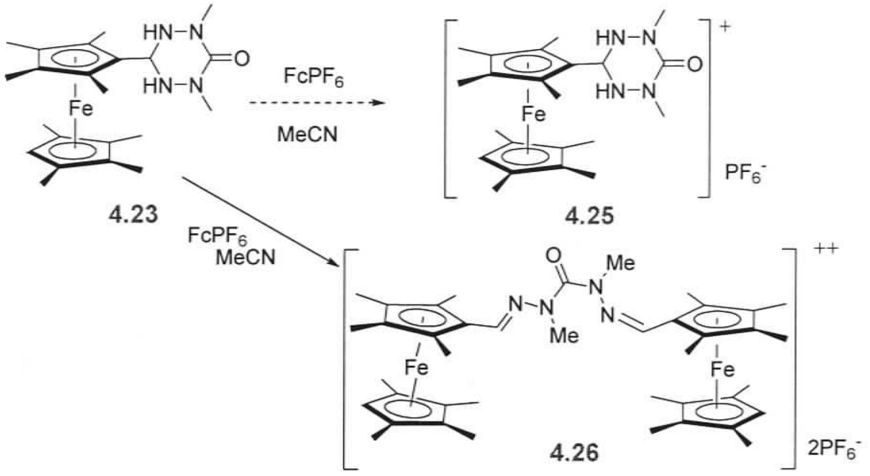

Scheme 4.7 - Octamethylferrocenyl tetrazane products upon oxidation by ferrocenium hexafluorophosphate

Compound **4.26** was isolated as a green crystalline solid and analyzed by x-ray crystallography. An ORTEP of **4.26** is shown in Figure 4.11 and a listing of bond lengths and angles follows in Table 4.2. The ferrocene hydrogen atoms and PF_6 counter ions are omitted for clarity. The crystal structure of **4.26** has several notable conformational features. One of the ferrocenyl units has staggered Cp rings, and the other adopts an eclipsed geometry. The open chain between the ferrocenyl units has two *trans*-imine functionalities and the substituents of the urea nitrogens also adopt a *trans*-configuration.

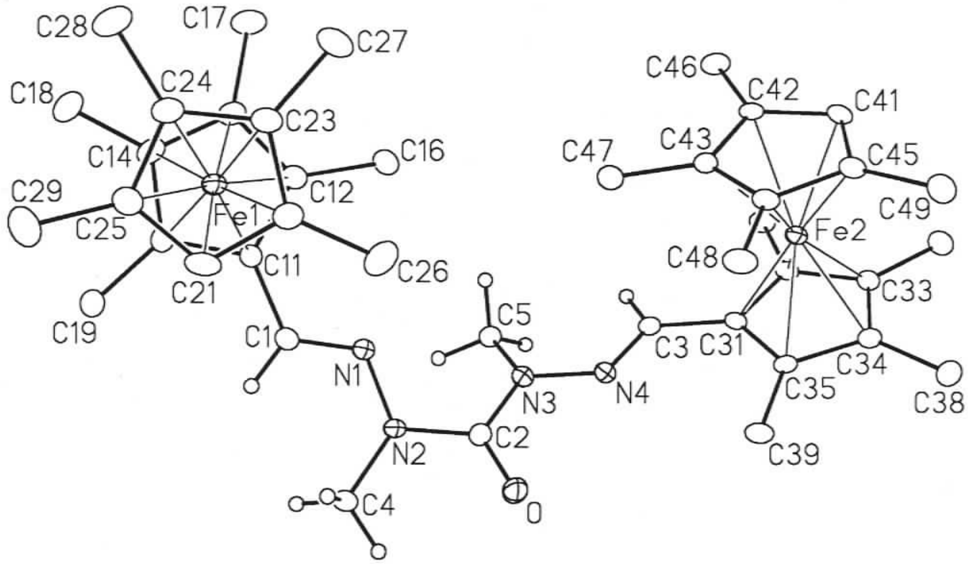

Figure 4.11 - ORTEP diagram of the molecular structure of **4.26** (Gaussian ellipsoids at the 20% probability level; the hydrogen atoms for all of the methyl groups are not shown.)

Table 4.2 - Selected bond distances and angles for the structure of tetrazane **4.26** (estimated standard deviations in parentheses)

Atoms	Distance (Å)	Atoms	Angle (deg.)
O-C(2)	1.212(4)	N(2)-N(1)-C(1)	119.0(3)
N(1)-N(2)	1.375(3)	N(1)-N(2)-C(2)	116.0(3)
N(1)-C(1)	1.269(4)	N(1)-N(2)-C(4)	122.0(3)
N(2)-C(2)	1.383(4)	C(2)-N(2)-C(4)	117.4(3)
N(2)-C(4)	1.458(4)	N(4)-N(3)-C(2)	112.7(3)
N(3)-N(4)	1.367(3)	N(4)-N(3)-C(5)	121.4(2)
N(3)-C(2)	1.391(4)	C(2)-N(3)-C(5)	125.0(3)
N(3)-C(5)	1.458(4)	N(3)-N(4)-C(3)	119.7(3)
N(4)-C(3)	1.280(4)	N(1)-C(1)-C(11)	120.9(3)
C(1)-C(11)	1.461(4)	O-C(2)-N(2)	121.2(3)
C(3)-C(31)	1.453(4)	O-C(2)-N(3)	123.1(3)
		N(2)-C(2)-N(3)	115.7(3)
		N(4)-C(3)-C(31)	119.2(3)

The disproportionation reaction leading to the bis-imine **4.26** led to another strategy to isolate the octamethylferrocenyl tetrazane cation **4.25** (Scheme 4.8). The octamethylformylferrocenium cation **4.27** was isolated by oxidizing **4.13** with ferrocenium hexafluorophosphate. The formylferrocenyl cation was anticipated to undergo condensation with carbonic acid *bis*(1-methylhydrazide), **2.54**, where the tetrazane formed would be stabilized in solution by the more electron deficient iron centre. However, **4.25** was not the observed product; instead, the aldehyde starting material was recovered quantitatively. Although the fate of **2.54** is unknown, but the net result is that **2.54** reduces the cation back to the starting material.

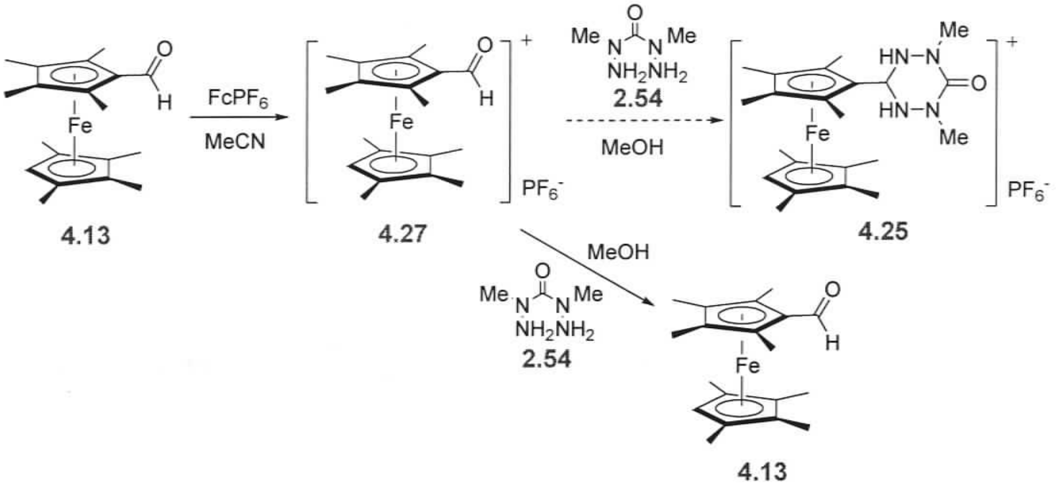

Scheme 4.8 - Attempted preparation of octamethylferrocenyl tetrazane cation

4.3 Synthesis and characterization of ferrocenyl verdazyl radicals

4.3.1 Synthesis

All ferrocenyl tetrazane oxidations were performed in DCM and the two oxidants used with the greatest degree of success were Fetizon's reagent[164] (Ag_2CO_3 on Celite) and *para*-benzoquinone (pBQ). All of the ferrocenyl tetrazanes were successfully oxidized following the procedure outlined in Scheme 4.9.

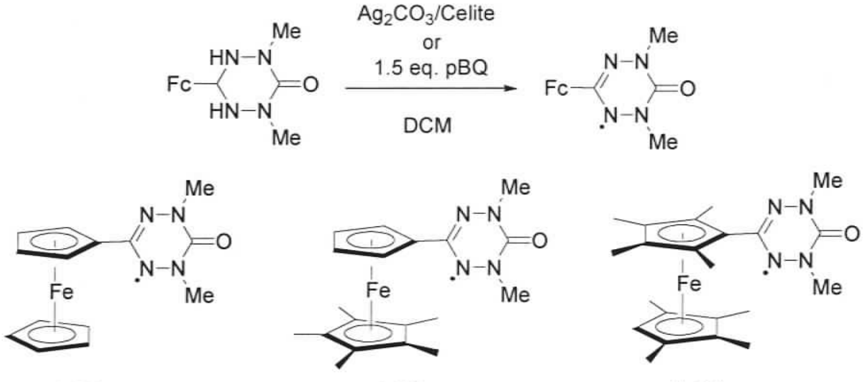

4.28 4.29 4.30

Scheme 4.9 - Oxidation of ferrocenyl tetrazanes to their corresponding verdazyls (**4.28-4.30**)

Small scale reactions were performed using Fetizon's reagent, but large scale preparations utilized pBQ as an oxidant resulting in moderate to good yields of **4.28** and **4.29** after column chromatography. The isolated yield of the octamethyl verdazyl derivative was lower because of tetrazane solution equilibria. In the case of **4.28** the product was recrystallized from a saturated toluene solution at -30 °C, resulting in deep green crystals sufficient for x-ray crystallography. Unfortunately, x-ray structures of the methylated radicals were not obtained.

Ferrocenyl verdazyls in general are much more stable than the N-heterocyclic verdazyls discussed previously. This observation was quantified by a simple UV-Vis experiment; periodically a millimolar solution (sealed and stored at ~0 °C) of **4.28** in DCM was analyzed to find that there was no appreciable decomposition over a 40 day trial period.

4.3.2 Structure of ferrocenyl verdazyls

An ORTEP drawing of **4.28** is shown in Figure 4.12 and a listing of selected bond lengths and angles is summarized in Table 4.3.

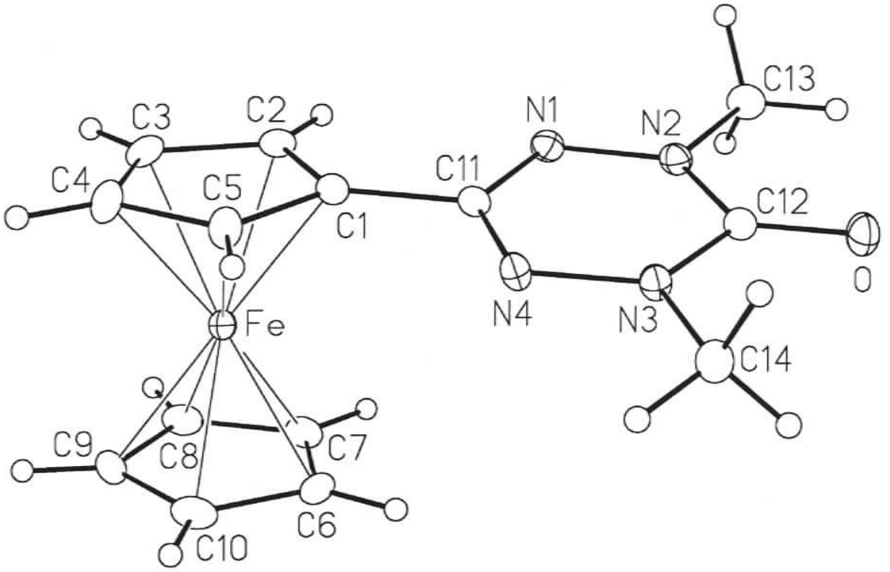

Figure 4.12 - ORTEP diagram of the molecular structure of **4.28** (Gaussian ellipsoids at the 20% probability level.)

Table 4.3 - Selected bond distances and angles for the structure of verdazyl **4.28** (estimated standard deviations in parentheses)

Atoms	Distance (Å)	Atoms	Angle (deg.)
O-C(12)	1.219(2)	O-C(12)-N(2)	123.54(17)
N(1)-N(2)	1.365(2)	N(2)-N(1)-C(11)	114.55(15)
N(1)-C(11)	1.334(2)	N(1)-N(2)-C(12)	124.96(15)
N(2)-C(12)	1.373(2)	N(1)-N(2)-C(13)	115.08(15)
N(2)-C(13)	1.457(2)	C(12)-N(2)-C(13)	119.96(16)
C(1)-C(11)	1.470(2)		

The verdazyl bond lengths and bond distances listed in Table 4.3 are typical for 6-oxo-verdazyls. Although there are two slightly different ferrocenyl verdazyls within the crystallographic unit cell, the verdazyl bond lengths and angles are virtually the same in both molecules. The ORTEP in Figure 4.12 depicts the ferrocenyl verdazyl in which the cyclopentadienyl (Cp) rings are eclipsed. The dihedral angle between the verdazyl plane and the adjacent Cp ring (C(5)-C(1)-C(11)-N(4)) is 12.6°. The ferrocene bond angles and distances are typical of most ferrocenyl species.

Further inspection of the extended solid state structure (Figure 4.13) demonstrates that packing consists of 'yin-yang' pairs of ferrocenyl radicals that stack like bricks in the *ab* plane. The two molecules in the 'dimeric' unit do not perfectly superimpose, but are instead slightly slipped along the c axis. These stacks alternate with orthogonal planes of slipped stacks throughout the extended structure. There is no interpenetration between the layers, and the molecules within the slipped stacks are nested at normal van der Waals π - stacking distances.

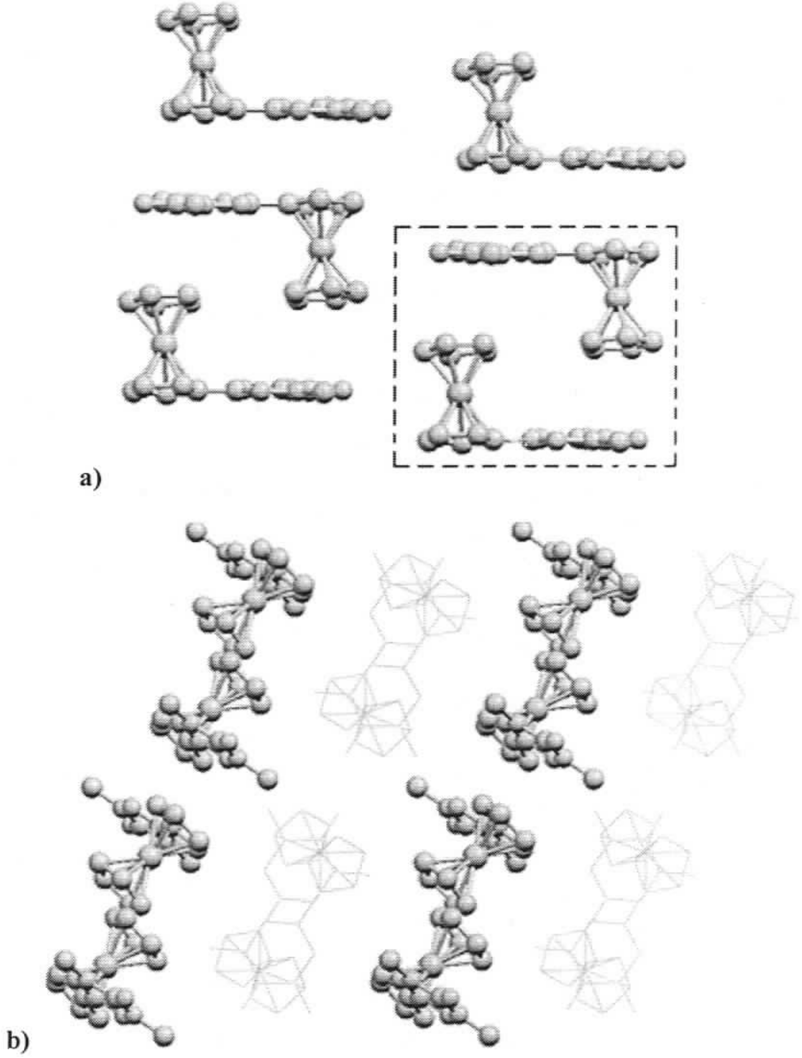

Figure 4.13 - Molecular solid state structure of **4.28** demonstrating a) the yin-yang pairs are stacked layers in the *ab* plane and b) staggered alternating orthogonal layers; ball and sticks show one layer and wire frame depicts alternate layer

4.3.3 Synthesis of verdazyl and tetrazine model compounds

4.3.3.1 Reactivity of ferrocenyl verdazyls

Like most radicals, verdazyls can be trapped with reactive radicals. A desirable model compound for electrochemical study would be a direct diamagnetic analogue of the ferrocenyl verdazyl. Therefore a ferrocenyl verdazyl was alkylated using the *para*-nitrobenzyl radical (Scheme 4.10). Radical **4.28** was trapped using an organocobaloxime **4.31**,[308]which under photolytic conditions produces a nitrobenzyl radical. This radical then reacts with the verdazyl resulting in a diamagnetic tetrazine **4.32**. The tetrazine **4.34** was characterized using FT-IR, high resolution EI-MS, elemental analysis and UV-Vis.

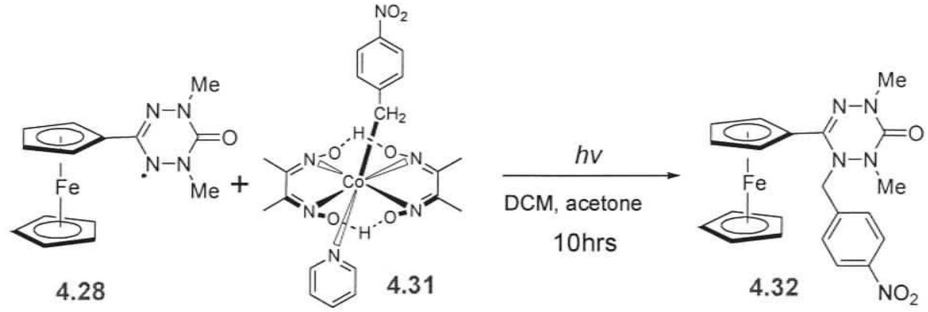

Scheme 4.10 - Trapping molecule **4.28** using a benzyl radical

Tetrazine **4.32** is one of several model compounds prepared in order to compare the electronic properties of the ferrocenyl verdazyls to other C3 substituted verdazyls. A series of verdazyl compounds were prepared as outlined in Scheme 4.11. Starting with commercially available aldehydes **4.33, 4.34**, and **4.35** and using conventional techniques, *p*-methoxyphenyl (**4.36**), *p-N,N*-dimethylaminophenyl (**4.37**), and *p*-tolyl (**4.38**) tetrazanes were prepared. Using pBQ as an oxidant, the respective verdazyls **4.39, 4.40,** and **4.41** were prepared using previously established techniques. Finally, the *p*-methoxyphenyl verdazyl was trapped using **4.31** to produce the corresponding tetrazine, **4.42**.

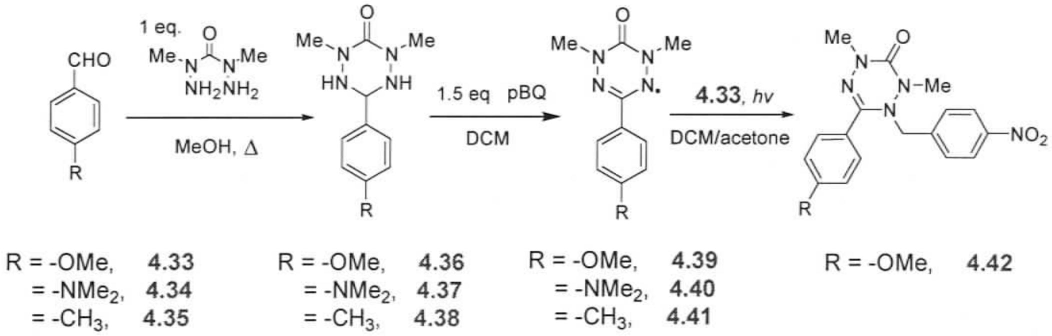

Scheme 4.11 - Synthesis of electron rich C3-substituted model verdazyl and tetrazine compounds.

4.4 Electronic and magnetic properties of ferrocenyl verdazyls

4.4.1 Electronic Spectra

The UV-Visible spectra of ferrocenyl verdazyl **4.28** and tetrazane **4.21** are presented in Figure 4.14. The UV-Vis spectrum of **4.21** shows a weak *d-d* transition belonging to the ferrocene moiety at 441 nm. The tetrazane absorption is qualitatively the same as ferrocene and the precursor aldehyde **4.11**. There is no contribution to the visible portion of the spectrum due to tetrazane as it does not possess an active chromophore in the visible region of the spectrum.

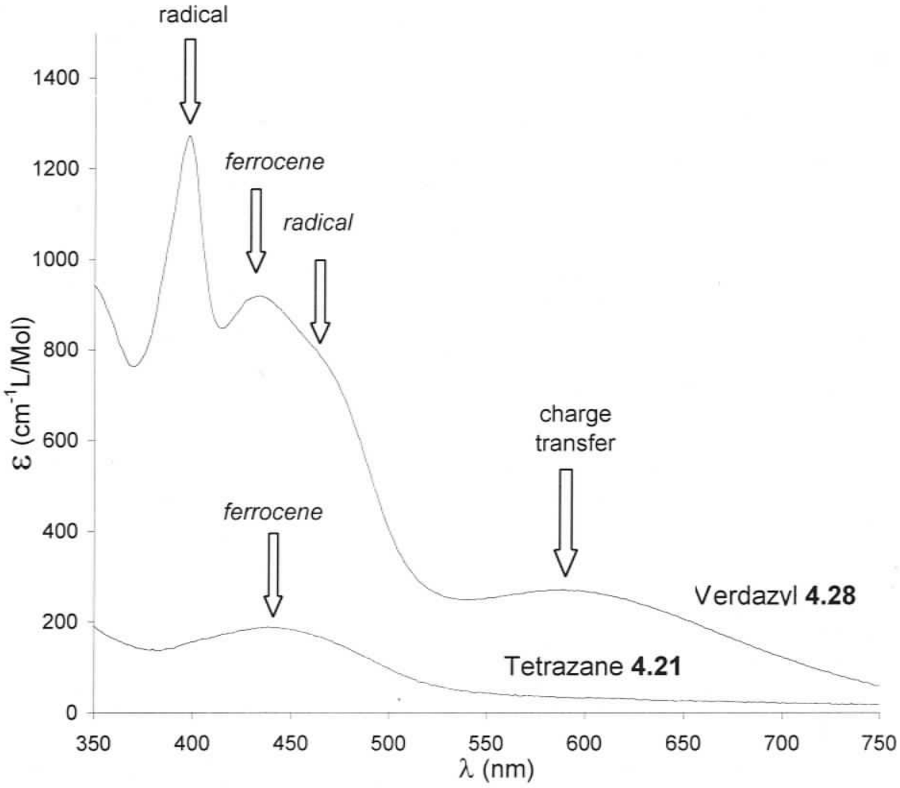

Figure 4.14 - UV-Vis spectra of **4.28** and **4.21** in DCM

The UV-Vis spectrum of the ferrocenyl radical **4.28** displays the consequence of adding an auxochrome to an existing ferrocene chromophore. The verdazyl component of **4.28** has two typical transitions at 398 nm and a lower energy shoulder around 470 nm. There is one other notable feature, namely the presence of a weak charge transfer (CT) transition at 589 nm, which is responsible for this radical's deep green colour. The CT transition is thought to arise from metal-to-radical charge transfer similar to what was reported by Veciana *et al.*[279] The concentration dependence of this CT band does not deviate from Beers law confirming that the transition is intramolecular in nature.

This CT transition may represent the promotion of an electron from the ferrocene HOMO to the verdazyl SOMO (Figure 4.15) resulting in an excited state that could correspond to the zwitterionic form, Fc$^+$/Vd$^-$. Usually extinction coefficients for charge transfer processes are large (ε ~1000-50000 L mol^{-1}cm^{-1}) because of their 'allowed' nature. This observed weak transition (ε =272 L mol^{-1}cm^{-1}) suggests that the probability of this transition is significantly lower than other CT processes. UV-Vis data in the solid state also shows evidence of a weak CT transition (see Figure 5.6).

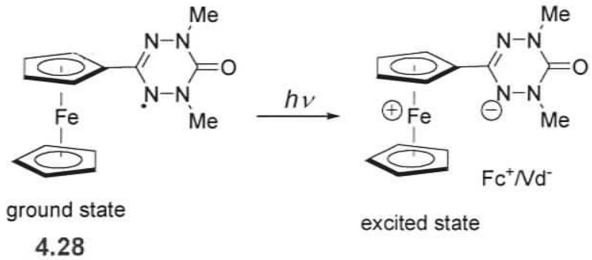

4.28

Figure 4.15 - Proposed excited state to explain CT transition

Generally speaking the methylated ferrocenyl verdazyls and tetrazanes have similar UV-Vis absorption profiles. The absorption maxima and extinction coefficients are presented in Table 4.4. Although the radical absorption energies and extinction coefficients are fairly constant within the set, the charge transfer bands shift bathochromically with increased methylation. These shifts are consistent with the intramolecular metal to radical charge transfer. As the degree of methylation increases so to does the energy of the ferrocene HOMO. As the energy of the HOMO increases the HOMO$_{Fc}$ – SOMO$_{Vd}$ energy gap decreases and this is consistent with the observed bathochromic shifts.

Table 4.4 – UV-Vis absorption maxima (nm) of ferrocenyl verdazyls in DCM. Molar extinction coefficients (ε) in italics ($M^{-1}cm^{-1}$)

Compound	verdazyl transition	ferrocene transiton	charge transfer
Ferrocene		441 (*1.0 x 10*^{2})	
4.21		441 (*1.9 x 10*^{2})	
4.28	398 (*1.3 x 10*^{3})	434 (*9.2 x 10*^{2})	589 (*2.7 x 10*^{2})
4.22		446 (*3.1 x 10*^{2})	
4.29	402 (*1.4 x 10*^{3})	442 (*1.2 x 10*^{3})	689 (*2.6 x 10*^{2})
4.23		458 (*3.5 x 10*^{2})	
4.30	399 (*1.3 x 10*^{3})	456 (*1.3 x 10*^{3})	771 (*2.8 x 10*^{2})

The fact that increased methylation perturbs the relative energy separation between the verdazyl π-SOMO and ferrocene HOMO is an indication that methylation is a good strategy for electronically tuning metal-radical interactions.

4.4.2 Electrochemistry

Ferrocene is one of the most heavily studied molecules electrochemically and it is known that the potential at which ferrocene is oxidized is very sensitive to the substitution effects on the Cp ring. Therefore the electrochemical properties of the ferrocenyl verdazyls, precursors, and model compounds were investigated using cyclic voltammetry (CV). The focus of this electrochemical study was to elucidate the mutual perturbation of combining two electrophores within the same molecule. The redox potentials of these compounds are assembled in Table 4.5.

Table 4.5 - Electrochemical Redox potentials vs Fc/Fc+ of ferrocenyl and model compounds

Ferrocenes	Aldehydes	Tetrazanes	Verdazyls	Tetrazines
			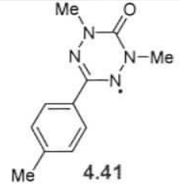 4.41 $E^{\circ}_{\mathrm{Vd/Vd+}}$ = 263mV	
			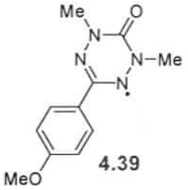 4.39 $E^{\circ}_{\mathrm{Vd/Vd+}}$ = 254mV	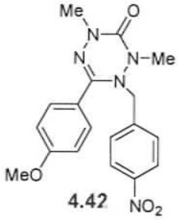 4.42 $E^{\circ}_{\mathrm{T/T+}}$ = 598mV
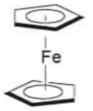 Ferrocene $E^{\circ}_{\mathrm{Fc/Fc+}}$ = 0mV	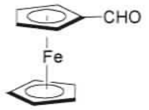 4.11 $E^{\circ}_{\mathrm{Fc/Fc+}}$ = 295mV	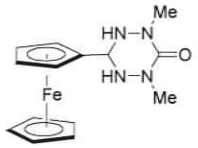 4.21 $E^{\circ}_{\mathrm{Fc/Fc+}}$ = 90mV	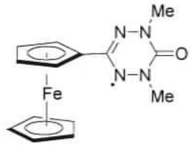 4.28 $E^{\circ}_{\mathrm{Fc/Fc+}}$ = 98mV $E^{\circ}_{\mathrm{Vd/Vd+}}$ = 339mV	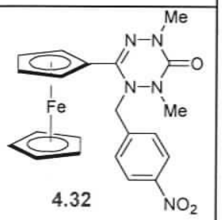 4.32 $E^{\circ}_{\mathrm{Fc/Fc+}}$ = 160mV $E^{\circ}_{\mathrm{T/T+}}$ = 667mV
	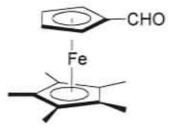 4.12 $E^{\circ}_{\mathrm{Fc/Fc+}}$ = 35mV	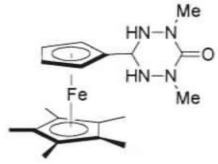 4.22 $E^{\circ}_{\mathrm{Fc/Fc+}}$ = -194mV	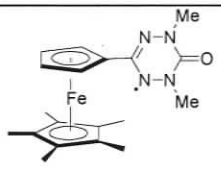 4.29 $E^{\circ}_{\mathrm{Fc/Fc+}}$ = -161mV $E^{\circ}_{\mathrm{Vd/Vd+}}$ = 405mV	
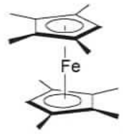 4.16 $E^{\circ}_{\mathrm{Fc/Fc+}}$ = -433mV	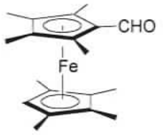 4.13 $E^{\circ}_{\mathrm{Fc/Fc+}}$ = -112mV	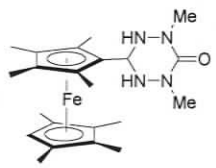 4.23 $E^{\circ}_{\mathrm{Fc/Fc+}}$ = -330mV	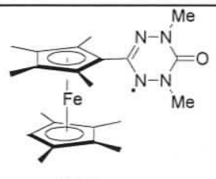 4.30 $E^{\circ}_{\mathrm{Fc/Fc+}}$ = -346mV $E^{\circ}_{\mathrm{Vd/Vd+}}$ = 310mV	

Aldehydes are strong electron withdrawing groups that result in the ferrocenyl aldehyde being harder to oxidize than unsubstituted ferrocene. Conversely, increasing the degree of methylation of the ferrocenyl unit increases the electron density of the metal centre resulting in lower oxidation potentials.[309] This is consistent with the redox potentials listed in Table 4.5. For example octamethylferrocene has a lower oxidation potential than ferrocene, but the ferrocene aldehyde has a higher oxidation potential than the parent ferrocene. Corresponding tetrazanes are also electron withdrawing, but the effect is diminished relative to the aldehyde

When investigating the interactions between two electrophores in a single molecule, it is important to consider the influence they exhibit on each other. Ferrocenyl verdazyls have two reversible oxidation potentials; one owing the ferrocene moiety and the other to the verdazyl radical. In all cases, the verdazyl oxidation has been assigned as the higher oxidative potential after investigating tetrazine model compounds. Based on the organic tetrazine **4.42** and ferrocenyl tetrazine **4.32**, the oxidation potential of the ferrocenyl unit in the latter has been assigned as +160 mV. This then suggests that in compound **4.28** the ferrocenyl unit has the lower oxidation potential (+98 mV).

Despite the ferrocene unit being an electron donating group, the verdazyl oxidation potential of **4.28-4.30** is significantly higher than the organic verdazyl derivatives (**4.39** and **4.41**). This can be rationalized when considering that the ferrocene unit is oxidized to the ferrocenium cation prior to the oxidation of the verdazyl. Therefore under electrochemical study only ferrocenium, an electron withdrawing group, is present when analyzing the verdazyl. This explains why the organic radicals (**4.39** and **4.41**) have lower oxidation potentials than the verdazyls possessing ferrocene moieties.

The oxidation potential of the verdazyl electrophore is also sensitive to the location and degree of methylation. **4.29** and **4.30** show significant deviation from the non-methylated ferrocenyl verdazyl. In **4.30** methylation of the Cp ring adjacent to the verdazyl lowers the oxidation potential of the verdazyl relative to the non-methylated verdazyl **4.28**. Conversely in the case of **4.29** where methylation is located on the other Cp ring, the radical oxidation potential is shifted to a higher oxidation potential than the non-methylated verdazyl **4.29**. This latter result is inconsistent with this methylation theory and is difficult to explain; a pentamethylferrocenium unit would be expected to be more electron-donating than the non-methylated ferrocenium, yet this is not supported by the electrochemical data.

Similar observations can be made when considering the effect methylation has on the ferrocenyl electrophore. In the case of **4.28** the ferrocene moiety has a similar oxidation potential as observed in the tetrazane precursor (**4.21**), despite significant electronic and geometric changes in going from the tetrazane to verdazyl. However, in the methylated derivatives **4.29** and **4.30** these relative differences become more significant. In **4.30** the electron donating methyl groups are attached directly to the Cp ring adjacent to the verdazyl. This negates the electron withdrawing effect of the verdazyl ring. Conversely, in the case of **4.29** where the degree of methylation is located on the other Cp ring, the radical has very strong electron withdrawing effect on the ferrocenyl moiety making it harder to oxidize. Ferrocene-based oxidation potentials within the groups are consistent with the degree of methylation.

4.4.3 EPR spectroscopy of ferrocenyl monoverdazyl radicals

The experimental and simulated EPR spectra of **4.29** are presented in Figure 4.16 as a representative example of the ferrocenyl verdazyls. All samples were recorded in DCM, and EPR experimental spectra were compared with simulated spectra in order to elucidate the hyperfine coupling constants (hfc) (*a*) and electron *g*-factors presented in Table 4.6. In all cases the spectra were found to have the same hyperfine coupling (hfc) constants. The unpaired electron couples to four nearly equivalent nitrogen atoms of the verdazyl ring, and to the six protons of the methyl substituents on N1 and N5.[112]

(a)

(b)

Figure 4.16 - EPR spectrum of **4.28** at 298 K in CH_2Cl_2 (a). The total spectral width is 80 G. Simulated EPR spectrum of **4.28** (b). Units are in Gauss (x-axis) and intensity (y-axis).

Table 4.6 - EPR parameters of ferrocenyl verdazyl mono-radicals.

Compound	$a_{N2,4}$ (G)	$a_{N1,5}$ (G)	$a_{(CH_3)}$ (G)	g-factor
4.29	6.5	5.3	5.3	2.0039
4.30	6.5	5.3	5.3	2.0042
4.31	6.5	5.3	5.3	2.0039

Simulations of the experimental data did not require contributions from the iron atom or the Cp hydrogens. This is consistent with the *N*-heterocyclic verdazyl derivatives discussed earlier and it indicates that the spin remains primarily on the verdazyl ring. This observation is in agreement with other 6-oxoverdazyl radicals in which hfc to C3 substituents is less than the spectral resolution (< 1 G).[165]

4.4.4 Mössbauer spectroscopy

Mössbauer spectroscopy can provide information about the oxidation state, geometry and relative energy levels of Fe. By analyzing an iron containing sample at different temperatures Mössbauer spectroscopy can help to determine if there more than one thermally accessible states such as those seen in valence tautomerism phenomenon. Experimental Mössbauer spectral data for **4.28** is presented in Figure 4.17.

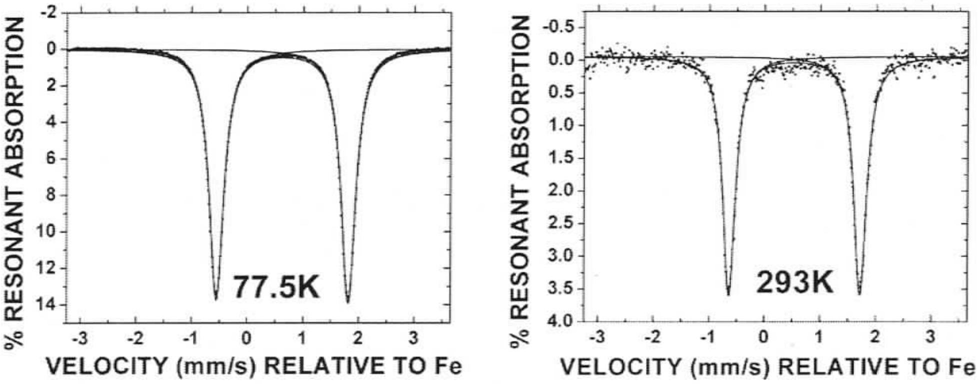

Figure 4.17 - Variable temperature Mössbauer spectroscopy of **4.28** - ferrocenyl verdazyl

At low temperature (77.5 K) the spectrum is indicative of a ferrocene (Fe^{2+}) with no observed ferrocenium (Fe^{3+}). As the temperature is increased (293 K), the signal representing Fe^{2+} remains the only iron species present. Similar results were observed for **4.31**. This data indicates that there is no valence tautomerism as observed by Veciana and co-workers.[279] Although this demonstrates the absence of ferrocene/ferrocenium-based valence tautomers it does not rule out the possibility of charge transfer leading to a zwitterionic exited state.

4.4.5 Magnetic properties of 4.28

4.4.5.1 Solid State Variable temperature Magnetic susceptibility

Solution magnetic susceptibilities using the Evans method and solid state variable temperature magnetic susceptibility data were obtained for the structurally characterized ferrocenyl verdazyl, **4.28**. Inability to isolate structures of the methylated derivatives will limit the discussion to only the non-methylated species **4.28**. The plot of χ vs T for **4.28** is presented in Figure 4.18.

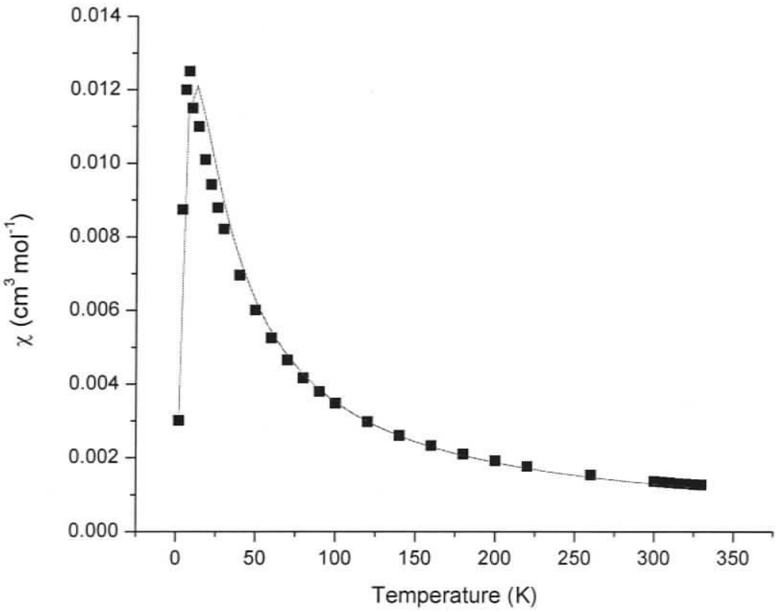

Figure 4.18 -Temperature dependence of χ for ferrocenyl verdazyl **4.28**. Points are experimental data, and the line is the modeled fit.

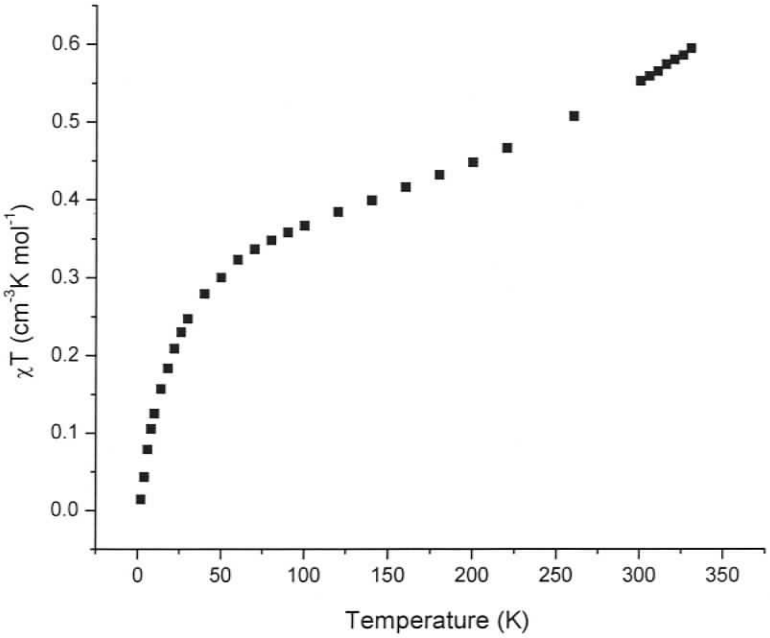

Figure 4.19 - χT vs T plots for ferrocenyl verdazyl **4.28**

The plot of χ vs T shows a maximum at 6.4K. This low temperature maximum is suggests the presence of low dimensional (1D or 2D) antiferromagnetic behaviour. A plot of χT vs T (Figure 4.19) shows that as the temperature is lowered the χT product decreases and this is another indication of antiferromagnetic behaviour. As the temperature exceeds 6.4 K this curve resembles that of a paramagnet obeying the Curie-Weiss law.

The structural data (Figure 4.13) indicated the presence of yin-yang pairs of ferrocenyl radicals in slipped stacks along the c axis; it is conceivable that these slipped stacks could provide a mechanism for 1D exchange. This packing arrangement suggests that these interactions between radicals are one-dimensional and 'alternating' in nature.

In the solid state there are two significant interactions; a radical-radical interaction within the dimeric ying-yang unit and another interaction between the dimeric units. With the radical-radical distances between the dimeric units being smaller than the distances between the radicals within the dimeric unit, it is expected that the shorter distance will have the largest interaction The alternating 1D antiferromagnetic chain model (Figure

4.20) also accommodates two types of interactions; J which is the largest exchange, and α is the alternation parameter that is restricted, $0 < \alpha < 1$. Thus the product αJ is some fraction of the parent J value. For this system and the remainder of the discussion the J will be relabeled to J_{inter}, and product of $\alpha J = J_{intra}$; a naming system complementary to the yin-yang pairs in the solid state.

$$\cdots\cdots \mathrm{A} \overset{\alpha J}{\text{———}} \mathrm{A'} \overset{J}{\text{———}} \mathrm{A} \overset{\alpha J}{\text{———}} \mathrm{A'} \overset{J}{\text{———}} \mathrm{A} \overset{\alpha J}{\text{———}} \mathrm{A'} \cdots\cdots$$

Figure 4.20 - 1D alternating antiferromagnetic chain model

The plot of χ vs T was modeled (solid line in Figure 4.18) using the alternating 1D antiferromagnetic chain model[3] as a means of elucidating the magnetic exchange (J_{inter}, J_{intra}) coupling constants. The alternating 1D antiferromagnetic chain model equation is a solution to the Eigen value problem with the spin Hamiltonian of the form, $H = -J\Sigma\ [S_A \cdot S_{A'} + \alpha\, S_{A'} \cdot S_A]$ and is presented in equation 4.1;

$$\chi = \frac{\mathrm{N}g^2\beta^2}{\mathrm{k}T} \frac{A + B\mathrm{x} + C\mathrm{x}^2}{1 + D\mathrm{x} + E\mathrm{x}^2 + F\mathrm{x}^3} + \mathrm{C_{TIPS}} \qquad \text{with } \mathrm{x} = |\mathrm{J}|/\mathrm{kT} \tag{4.1}$$

where $0.4 < \alpha < 1.0$ *and;*

$A = 0.25$
$B = -0.0684750 + 0.13194\alpha$
$C = 0.0042563 - 0.031670\alpha + 0.12278\alpha^2 - 0.29943\alpha^3 + 0.21814\alpha^4$
$D = 0.035255 + 0.65210\alpha$
$E = -0.00089418 - 0.10209\alpha + 0.87155\alpha^2 - 0.188472\alpha^3$
$F = 0.045230 - 0.0081910\alpha + 0.83234\alpha^2 - 2.6181\alpha^3 + 1.92813\alpha^4$
C_{TIPS} – temperature independant paramagnetic susceptibility constant

The experimental data was fitted using the "best" fit parameters as follows: $J_{inter} = -13.4\ \mathrm{cm}^{-1}$, $J_{intra} = -11.4\ \mathrm{cm}^{-1}$, $g = 2.0037$, and $\mathrm{C_{TIPS}} = 0.00007$ with $\mathrm{R} = 0.09$ (where $R = [\Sigma(\chi_{obs} - \chi_{calc})^2/\Sigma(\chi_{obs})^2]^{1/2}$) .

The high temperature limit (300 K) of μ_{eff} resembles an S=1/2 radical system, but after repeated measurements an average $\mu_{eff} = 1.95$ was found. This is higher than the expected theoretical value of $\mu_{eff} = 1.73$ for an S=1/2 radical system. This value is arguably significant, and is similar to the results seen by Veciana and co-workers[279] in the study of triphenylmethyl ferrocenyl radicals. They attributed a high μ_{eff} value to significant orbital contributions from remnant $[\mathrm{Fe^{III}Cp_2}]^+$. From previous discussions, the Mössbauer data does not support the notion of valence tautomerism as seen by Veciana,[279] so it is difficult to rationalize this unusually high μ_{eff} value in terms of $[\mathrm{Fe^{III}Cp_2}]^+$. This discrepancy in the data suggested that further magnetic susceptibility measurements were needed; therefore solution magnetic susceptibility measurements were performed in order to investigate the differences between the solid state and solution.

4.4.5.2 Solution susceptibilities: The Evans method

Solution magnetic susceptibilities can be elucidated using the Evans Method.[310] The Evans method of determining paramagnetic susceptibility uses nuclear magnetic resonance as its probing technique. The essence of the Evans method is that in the ^{1}H-NMR, a chemical shift is perturbed from its original frequency by adding a known amount of paramagnetic compound. The shift between the original solvent frequency and the perturbated paramagnetic solution signal is directly proportional to the magnetic moment at a given temperature. The original Evans equation representing this relationship is given as;[311]

$$\chi_g = \frac{3\Delta f}{2\pi f m} + \chi_o + \frac{\chi_o(d_o - d_s)}{m} \tag{4.2}$$

where: χ_g is mass susceptibility of the solute (cm^3/g); Δf is the observed frequency shift from the reference resonance (Hz); f is the spectrometer frequency (Hz); χ_o is the mass susceptibility of the solvent (cm^3/g); m is the mass of the substance per cm^3 of solution; d_o is the density of solvent (g/cm^3); and d_s is the density of solution (g/cm^3). The final two off-setting terms (based on solution density and solvent susceptibility), which are somewhat onerous to determine, can be safely removed from equation 4.2 for molecules with small molecular weights[312] (<500g/mol) studied at a single temperature.[313] These approximations in combination with the conversion to SI units[314, 315] leads to a molar susceptibility given in equation 4.3.

$$\chi_M = \frac{6}{10^3} \cdot \frac{1}{c} \cdot \frac{\delta v}{v_o} \tag{4.3}$$

χ_M is molar susceptibility of the analyte (m^3/mol); $\delta\nu$ is the observed frequency shift from the reference resonance (Hz); ν_o is the spectrometer frequency (Hz); c is the concentration of the paramagnetic solution (mol/dm^3). Converting molar susceptibility to effective magnetic dipole (μ_{eff}) leads to the more commonly used equation 4.4.[316, 317]

$$\mu_{eff} = \left(\frac{1}{10^3} \cdot \frac{18k}{N_o \mu_o (\mu_B)^2} \cdot \frac{T(\Delta\nu)}{c(\nu_o)} \right) \tag{4.4}$$

k is Boltzmann's constant; N_o is Avogadro's number; μ_o is the vacuum permeability; and μ_B is the Bohr magneton. It should be noted that this equation ignores the diamagnetic correction factor to the molar susceptibility. In the case of the ferrocenyl radicals this diamagnetic correction factor is small ($\chi_{dc} = 1.4 \times 10^{-4}$ m^3/mol which alters the $\mu_{eff} \sim 2\%$), and this is well within the ~10% uncertainty that is inherent in these type of measurements. High uncertainties in this method are caused from using small quantities of deuterated solvents. All further solution susceptibility data is uncorrected.

Trends that arise from the solution susceptibility measurements are reported in Table 4.7. Purely organic verdazyls (S=1/2) are well characterized using the Evans method regardless of the solvent used in the analysis. Good correlations between the theoretical value and experimental data using the Evans method are usually within 5%.[318] The second observation is that solution measurements and solid state measurements can be vastly different, as in the case of ferrocenium hexafluorophosphate ($[Fc]^+PF_6^-$). While the $Fc^+PF_6^-$ solid state susceptibilities are consistent with previously observed findings,[285] we do not know of any comparable solution magnetic studies involving $[Fc]^+PF_6^-$.

Table 4.7 - The Evans method data comparing and contrasting effective dipole moments

Compound	Method	Solvent	Average μ_{eff}	expected μ_{eff}	% diff.
4.39	Solution	$CDCl_3$	1.79	1.73	3.3%
4.41	Solution	DMSO	1.73	1.73	0.0%
4.28	Solution	$CDCl_3$	2.39	1.73	38%
$[Fc]^+PF_6^-$	Solution	DMSO	3.63	1.73	110%
$[Fc]^+PF_6^-$	Solid		2.54	1.73	47%

Keeping in mind the suggestion by Veciana *et al,*.[279] that the high μ_{eff} value could be caused by significant orbital contributions from remnant $[Fe^{III}Cp_2]^+$, it is intriguing to observe that in solution, μ_{eff} for **4.29** is well outside the level of uncertainty for an S=1/2 radical system and that the average value for **4.29** is high and qualitatively consistent with the solid state measurement discussed earlier. This then leads to the conclusion that the ferrocene component must be somehow contributing to the overall susceptibility at room temperature and the hypothesis that enhanced communication may be observed in solution because of its dynamic behaviour.

4.5 Summary

A series of electron-rich ferrocenyl tetrazanes and verdazyls were prepared and fully characterized. Several synthetic challenges were overcome in the design of methylated ferrocenyl tetrazanes, notably; octamethylferrocene tetrazane demonstrated that in solution a new equilibrium is established between the linear imine and tetrazane.

Ferrocenyl radicals were not designed to study the direct metal-radical interactions, but their structural connectivity makes them amenable for studying indirect electronic interactions. Ferrocene methylation strategies were effective at perturbing the relative energy separation between the verdazyl π-SOMO and ferrocene HOMO as confirmed by electronic absorption and electrochemical investigations. Electronic absorption studies concluded that the methylation of the ferrocenyl unit results in various forms of electronic communication between the verdazyl and ferrocene electrophores. Although Mössbauer spectroscopy ruled out the possibility of valence tautomerism the presence of a charge-transfer band suggests there is a low lying excited state where a metal to radical CT occurs.

Electrochemical investigations of the ferrocenyl verdazyls suggest that electronic influence of the ferrocene and verdazyl electrophores on each other is quite sensitive to the degree and location of methylation. In each case the ferrocene has been assigned as a lowest potential oxidation. Specificity of the electron donating methyl groups on the ferrocenyl moiety results in the ability to adjust oxidation potentials of the verdazyl and ferrocenyl moieties.

A structural determination of the non-methylated ferrocenyl verdazyl allowed for the investigation of the magnetic properties. However, inability to isolate crystals of the methylated derivatives prevented such a study. The crystal structure of **4.28** showed that the ferrocenyl verdazyls are stacked in yin-yang pairs. The magnetic data was modeled to a 1D alternating antiferromagnetic chain model, which suggested weak antiferromagnetic interactions within the ying yang pair (J_{intra} = -11.4 cm^{-1}), and between the ying yang pairs in the planar stack (J_{inter} = -13.4 cm^{-1}).

4.6 Experimental section

4.6.1 General synthetic procedures

Unless stated otherwise, all general synthetic procedures employed are similar to those presented in section 2.7.1.

4.6.2 Magnetic measurements

Details of the magnetic measurements have been previously reported in section 2.7.2.

4.6.3 Mössbauer measurements

All Mössbauer data presented was obtained by Professor William Reiff at the Northeastern University (Boston, MA.). In general, the Mössbauer spectra were determined using a conventional constant acceleration spectrometer operated in multi-channel scaling mode. The gamma ray source consisted of 60 mCi of ^{57}Co in a rhodium metal matrix that was maintained at ambient temperature. The spectrometer was calibrated using a 6-micron thick natural abundance iron foil. Isomer shifts are reported relative to the centre of the magnetic hyperfine pattern. The latter foil (at ambient temperature) is taken as zero velocity. The line widths of the inner-most pair of transitions of the latter Zeeman pattern were reproducibly determined to be 0.214 mm/s. Sample temperature variation was achieved using a standard exchange gas liquid helium cryostat (Cryo Industries of America, Inc.) with temperature measurement and control based on silicon diode thermometry in conjunction with a 10 micro ampère excitation source (Lakeshore Cryotronics, Inc). Spectra were fit and plotted using the program ORIGIN (Version 7.0) (Originlab Corporation, One Roundhouse Plaza, Northampton, MA 01060).

The thermometry of the Mössbauer spectroscopy instrumentation (Si diodes) was further calibrated via detailed study of the magnetic ordering of a polycrystalline sample of pure, anhydrous ferrous fluoride (Strem Chemical, 99.9%) whose purity was further verified via Mössbauer spectroscopy. FeF_2 has been shown by previous zero field techniques (heat capacity and Mössbauer spectroscopy) as well as classical susceptibility study to order antiferromagnetically at T_N =78.20 K ±0.20 K. Our values for T_N for FeF_2 via Mössbauer spectroscopy and AC susceptometry are within 0.5 K of the latter.

4.6.4 Synthesis

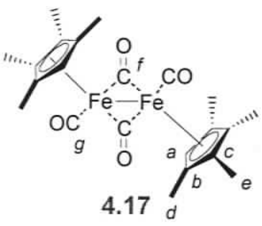

4.17

Tetramethylcyclopentadienyl-iron-*bis*-carbonyl dimer (4.17) – Although this a previously published compound the synthetic details and characterization are limited.[306] This procedure was done without knowledge of existing routes and is a modification of existing routes for pentamethylcyclopentadienyl iron carbonyls[304, 305]. In a 100 mL side arm RBF excess iron pentacarbonyl (15 mL, 114 mmol) and tetramethylcyclopentadiene (6 mL, 57 mmol) was solubilized in 40 mL of octane. The reaction was then heated to reflux for 3 days under argon. As the reaction began to reflux, the reaction mixture began to turn dark purple. Within 4 hours of refluxing there was a small amount of precipitate formed. The product was filtered in air and washed with octane (2 × 10 mL); the filtrate and washings were discarded. The product was then separated from an iron-based impurity by dissolving the product in DCM and filtering. The iron-based impurity is readily oxidized in air, and care should be taken to ensure that it does not ignite organic solvents. The DCM filtrate was then concentrated and the product crystallized at 0 °C overnight to yield **4.17** (55.3%, 7.35 g, 15.8 mmol). ^1H NMR (DMSO): δ 3.80 (s, 2H, H_a), 1.74 (br s, 24H, H_h) ppm. ^{13}C NMR ($CDCl_3$): δ 109.9(C_a), 99.9(C_d), 99.3(C_h), 87.4(C_f), 10.6(C_g), 9.1(C_d) ppm. FT-IR (KBr): 2905 (w), 1940 (s), 1897 (m), 1751 (s), 1724 (m), 1500 (w), 1465 (w), 1425 (w), 1383 (m), 1320 (w), 1263 (w), 1030 (m), 861 (m), 642 (s), 620 (s), 613 (s), 599 (w), 574 (w), 549 (m) cm^{-1}. Anal. Calculated for $C_{22}H_{26}Fe_2O_4$: C, 56.69; H, 5.62. Found: C, 57.22; H, 5.88. $\lambda_{max}(CH_2Cl_2)(\varepsilon(M^{-1}cm^{-1})$: 358 nm ($8.3 \times 10^3$), 530 nm ($1.1 \times 10^3$). MS (EI): *m/z* 466 {$M^+$, 20%}, 352 {100%}. HR-MS: 466.0521 +/- 0.0005 (466.0530 for M^+ $C_{22}H_{26}Fe_2O_4$). Mp 170-173 °C.

Tetramethylcyclopentadienyl-acetonitrile-*bis*-carbonyl iron(II) hexafluorophosphate (4.18) – This procedure is a modification of existing routes for pentamethylcyclopentadienyl iron carbonyls[304, 305]. In a 250 mL RBF 4.17 (1.5 g, 3.2 mmol) was combined with ferrocenium hexafluorophosphate (2.13 g, 6.44 mmol) and 100 mL of dry DCM/MeCN (2:1). The reaction was then allowed to stir at RT overnight in the dark. The solvent was evaporated and the crude product was suspended and triturated with ether to remove the ferrocene. The crude green-yellow solid was filtered and dried in air. The product was then recrystallized from acetone/ether mixture to yield a bright yellow solid **4.18** (96.4%, 2.6 g, 6.2 mmol). ^{1}H NMR (CH_3CN): δ 4.90 (s, 1H, H_a), 2.30 (s, 3H, H_h), 1.85 (s, 6H, H_d), 1.79 (s, 6H, H_e) ppm. ^{13}C NMR (CH_3CN): δ 211.5 (C_f), 102.9 (C_c or C_b), 102.5 (C_c or C_b), 81.4 (C_a), 11.4 (C_d), 9.7 (C_e), 5.1 (C_h) ppm. FT-IR (KBr): 3231 (w), 3099 (w), 3067 (w), 3011 (w), 2947 (w), 2928 (w), 2872 (w), 2055 (s), 2004 (s), 1699 (m), 1568 (w), 1500 (w), 1472 (w), 1431 (w), 1391 (w), 1357 (w), 1319 (w), 1090 (w), 1033 (w), 835 (s), 780 (w), 591 (m), 582 (m), 558 (m), 528 (m) cm^{-1}. Anal. Calculated for $C_{13}H_{16}F_6FeNO_2P$: C, 37.26; H, 3.85; N, 3.34. Found: C, 36.85; H, 3.78; N, 3.16. λ_{max}(MeCN)(ε($M^{-1}cm^{-1}$): 550 nm (1.6×10^2); 429 nm (7.1×10^2); 353 nm (4.2×10^2). MS (EI): *m/z* 274 {M^+, 100%}, 246 {$[M-CO]^+$, 25%}. HR-MS: 274.0531 +/- 0.0003 (274.0530 for M^+ $C_{13}H_{16}FeNO_2$). Mp 139-141 °C - decomposes.

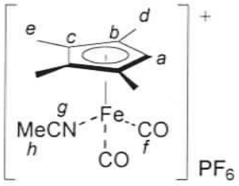

4.18

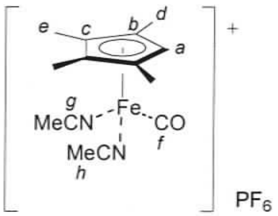

4.19

Tetramethylcyclopentadienyl-*bis*-acetonitrile-monocarbonyl-iron(II) hexafluorophosphate (4.19) – This procedure is a modification of existing routes for pentamethylcyclopentadienyl iron carbonyls[304, 305]. In a 200 mL quartz photolysis tube **4.18** (0.8 g, 1.9 mmol) was solubilized in 100 mL dry acetonitrile and irradiated in a full spectrum light box while being continuously sparged using argon. The irradiation was performed for 14 hours (overnight), and then the product was filtered to remove a small amount of sediment (decomposed starting material) and the solvent removed *in vacuo*. The brown crude solid was then recrystallized using acetonitrile/ether at 0 °C to yield **4.19** as a purple/brown microcrystalline solid (74.1%, 0.63 g, 1.4 mmol). The solid reacts quickly in air, and the solid slowly decomposes under argon. ^{1}H NMR (CH_3CN): δ 4.28 (s, 1H, H_a), 2.57 (s, 6H, H_h), 1.74 (s, 6H, H_d) 1.65 (s, 6H, H_e) ppm. FT-

IR (DCM): 2988 (w), 2950 (w), 2359 (w), 2347 (w), 2104 (w), 1976 (s), 1630 (br w), 1496 (w), 1454 (w), 1389 (w), 1062 (w), 1038 (w), 840 (s), 558 (m), 535 (w), 509 (w), cm^{-1}.

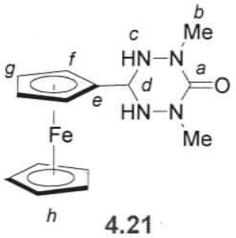

4.21

1,5-Dimethyl-3-{ferrocenyl}-1,2,4,5-tetrazane-6-oxide (4.21) - To a gently refluxing solution of **2.52** (0.83 g, 7.0 mmol) in methanol (10 mL) was added dropwise (over 3 hours) a solution of **4.11** (1.5 g, 7.0 mmol) in methanol (175 mL). The ferrocene monoaldehyde was prepared using an existing method.[293] After the addition was complete the reaction was gently heated to reflux overnight (10 hours). The reaction mixture (deep red/orange) was then cooled and the solvent removed under reduced pressure. The resulting solid was then precipitated from ethyl acetate using diethyl ether. The solid was filtered in air and washed with diethyl ether to yield a golden coloured tetrazane **4.21** (1.4 g, 63.6%). ^1H NMR (DMSO): δ 5.22 (d, 2H, J=10Hz, H_c), 4.60 (t, 1H, J=10Hz, H_d), 4.25 (s, 2H, H_f), 4.23 (s, 5H, H_h), 4.15 (s, 2H, H_g), 2.96 (s, 6H, H_b) ppm. ^{13}C NMR (DMSO): δ 154.6(C_a), 83.3(C_d), 68.6(C_h), 67.3(C_f), 66.5(C_g), 66.1(C_d), 37.5(C_b) ppm. FT-IR (KBr): 3436 (w, br), 3234 (w), 3087 (w), 2916 (w, br), 1636 (s), 1492 (m), 1449 (m), 1429 (m), 1391 (m), 1320 (w), 1129 (m), 1105 (m), 1060 (w), 1033 (w), 1020 (w), 1005 (w), 949 (m), 879 (m), 854 (m), 814 (m), 726 (w), 712 (w), 663 (w), 590 (w), 522 (w), 492 (m), 483 (m) cm^{-1}. Anal. Calculated for $C_{14}H_{18}FeN_4O$: C, 53.52; H, 5.77; N, 17.83. Found: C, 53.30; H, 5.61; N, 17.94. $\lambda_{max}(CH_2Cl_2)(\varepsilon(M^{-1}cm^{-1})$: 438 nm ($1.9 \times 10^2$). MS (EI): *m/z* 314 {$M^+$, 100%}. HR-MS: 314.0829 +/- 0.0003 (314.0830 for M^+ $C_{14}H_{18}FeN_4O$). Mp 127-129 °C.

1,5-Dimethyl-3-{1',2',3',4',5'-pentamethylferrocenyl}-1,2,4,5-tetrazane-6-oxide

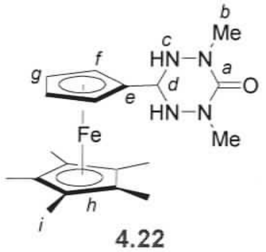

4.22

(4.22) - To a gently refluxing solution of **2.52** (0.29 g, 2.46 mmol) in methanol (10 mL) was added dropwise (over 3 hours) a solution of **4.12** (0.7 g, 2.5 mmol) in methanol (175 mL). The pentamethylferrocene aldehyde **4.12** was prepared using an existing method[295]. After the addition was complete the reaction was gently heated to reflux overnight (10 hours). The reaction mixture (orange/red) was then cooled and the solvent removed under reduced pressure . The resulting residue was then purified using column chromatography (N. Alumina/EtOAc:DCM (1:1) ; $R_f = 0.4$) to yield pure tetrazane (0.74 g, 78.2%). The solid was recrystallized using EtOAc, and ether to facilitate precipitation. ^{1}H NMR (DMSO): δ 5.24 (d, 2H, *J*=10Hz, H_c), 4.55 (t, 1H, *J*=10Hz, H_d), 3.73 (m, 2H, H_f), 3.63 (m, 2H, H_g), 2.93 (s, 6H, H_b), 1.84 (s, 15H, H_i) ppm. ^{13}C NMR (DMSO): δ 154.6 (C_a), 82.0 (C_e), 79.6 (C_h), 71.5 (C_f), 69.2 (C_g), 66.0 (C_d), 37.6 (C_b), 10.8 (C_i) ppm. FT-IR (KBr): 3257 (m), 2965 (m), 2944 (m), 2905 (m), 1609 (s), 1494 (w), 1478 (w), 1429 (m), 1379 (m), 1238 (w), 1118 (w), 1035 (w), 1020 (w), 958 (m), 859 (m), 809 (m), 732 (w), 567 (w), 538 (w), 482 (w) cm^{-1}. Anal. Calculated for $C_{19}H_{28}FeN_4O$: C, 59.38; H, 7.34; N, 14.58. Found: C, 56.71; H, 7.22; N, 14.30. $\lambda_{max}(CH_2Cl_2)(\varepsilon(M^{-1}cm^{-1})$: 446 nm ($3.1 \times 10^2$). MS (EI): *m/z* 384 {$M^+$, 100%}, 282 {$[M-C_3H_8N_3O]^+$, 20%}. HP-MS: 384.1617 +/- 0.0002 (384.1613 for M^+ $C_{19}H_{28}FeN_4O$). Mp 122-125 °C – yellow to red at 118 °C. Note: elemental is off in the carbon by ~3%. However the ^{13}C exceeds required *J. Org. Chem.* proof of purity.

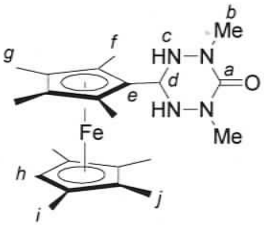

4.23

1,5-Dimethyl-3-{1,1',2,2',3,3',4,4'-octamethylferrocenyl}-1,2,4,5-tetrazane-6-oxide (4.23) - To a gently refluxing solution of **2.52** (0.51 g, 4.3 mmol) in methanol (10 mL) was added dropwise (over 3 hours) a solution of **4.13** (1.4 g, 4.3 mmol) in methanol (175 mL). The octamethylferrocene aldehyde was prepared using an existing methods[299, 302]. After the addition was complete the reaction was gently heated to reflux overnight (10 hours). The reaction mixture (orange) was then cooled, and the solvent removed under reduced pressure. The resulting residue was then purified using column chromatography (SiO_2/EtOAc - streaks; $R_f = 0.48$) to yield the crude tetrazane **4.23** (1.46 g, 79.3%). The solid was purified by recrystallization from a saturated toluene solution at -30 °C. ^{1}H NMR (DMSO): δ 5.18 (d, 2H, *J*=11.5Hz, H_c), 4.55 (t, 1H, *J*=11.5Hz, H_d), 3.35 (s, 1H, H_h), 2.97 (s, 6H, H_b), 1.79 (s, 6H, H_f), 1.71 (s, 6H, H_g), 1.67 (s, 6H, H_i), 1.64 (s, 4H, H_j) ppm. ^{13}C NMR (DMSO): δ 155.1 (C_a), 79.7 (C_e), 79.5 ($C_{i,j}$), 79.4 ($C_{i,j}$), 77.8 (C_f), 76.3 (C_g), 70.7 (C_h), 68.7 (C_d), 37.3 (C_b), 10.9, 10.2, 9.4, 9.0 ($C_{f,g,i,j}$) ppm. FT-IR (KBr): 3234 (m), 2965 (m), 2905 (m), 1635 (s), 1615 (s), 1493 (m), 1429 (m), 1383 (m), 1323 (w), 1261 (w), 1114 (w), 1082 (w), 1030 (m), 961 (m), 889 (m), 822 (w), 733 (w), 676 (w), 545 (w), 642 (w) cm^{-1}. Anal. Calculated for $C_{22}H_{34}FeN_4O$: C, 61.97; H, 8.04; N, 13.14. Found: C, 62.47; H, 8.20; N, 13.37. $\lambda_{max}(CH_2Cl_2)(\varepsilon(M^{-1}cm^{-1})$: 459 nm ($3.5 \times 10^2$). MS (EI): *m/z* 426 {M$^+$, 100%}, 323 {[M-$C_3H_8N_3O]^+$, 20%}. HR-MS: 426.2084 +/- 0.0004 (426.2082 for M$^+$ $C_{22}H_{34}FeN_4O$). Mp 118-122 °C.

***Bis*(*N'*-(1,2',2,3',3,4',4,5'-octamethylferrocenylmethylene)-*N*-methyl)-carbohydrazide (4.26)** – To a solution of **4.23** (0.30 g, 0.70 mmol) in acetonitrile (sparged 40 mL) was added ferrocenium hexafluorophosphate (0.233 g, 0.7 mmol) and the reaction was stirred at RT overnight. The solvent was then removed, and the crude solid triturated with ether, to remove the ferrocene byproduct. The green solid was then subjected to silica column chromatography using acetone as the eluent. The green band was collected and the solvent removed to yield a deep green solid, **4.26** (0.090 g, 25.0%). X-ray quality crystals were grown by vapor diffusion of Et_2O into a saturated acetone solution of **4.26**. FT-IR (KBr): 2966 (w), 2924 (w), 1686 (w), 1588 (w), 1475 (w), 1423 (w), 1387 (w), 1324 (w), 1229 (w), 1203 (w), 1172 (w), 1083 (w), 1027 (w), 840 (w), 751 (w), 605 (w), 557 (w) cm^{-1}. Anal. Calculated for $C_{41}H_{58}F_{12}Fe_2N_4OP_2$: C, 48.06; H, 5.71; N, 5.47. Found: C, 49.51; H, 6.05; N, 5.35. $\lambda_{max}(CH_3CN)(\varepsilon(M^{-1}cm^{-1})$: 277 nm ($2.0 \times 10^4$), 318 nm ($1.5 \times 10^4$), 686 nm ($4.7 \times 10^2$), 773 nm ($5.0 \times 10^2$). MS (LSIMS): *m/z* 879 {[M-$PF_6]^+$, 50%}, 734 {[MH-$(PF_6)_2]^+$, 90%} . HR-MS: 879.2951 +/- 0.0010 (879.2951 for [M-$PF_6]^+$ $C_{41}H_{58}F_6Fe_2N_4OP$). Mp 134-137 °C decomposes.

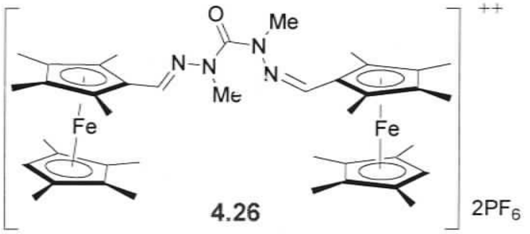

4.26

5-Formyl-1,1',2,2',3,3',4,4'-octamethyl-ferrocenium hexafluorophosphate (4.27) – To a solution of **4.13** (0.50 g, 1.53 mmol) in acetonitrile was added ferrocenium hexafluorophosphate (0.507 g, 1.53 mmol) and the reaction was stirred at RT overnight. The solvent was then removed and the crude solid triturated with ether to remove the ferrocene byproduct. The product was recrystallized from

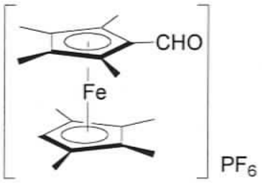

4.27

acetone/ether to yield **4.27** as a green solid (92.8%, 0.67 g, 1.4 mmol). FT-IR (KBr): 3124 (w), 2970 (w), 2925 (w), 1688 (m), 1454 (w), 1419 (w), 1406 (w), 1387 (w), 1169 (w), 1111 (w), 1074 (w), 1028 (w), 837 (s), 740 (w), 683 (w), 670 (w), 557 (m), 524 (w), cm^{-1}. Anal. Calculated for $C_{19}H_{26}F_6FeOP$: C, 48.43; H, 5.56. Found: C, 48.13; H, 5.05. $\lambda_{max}(CH_3CN)(\varepsilon(M^{-1}cm^{-1})$: 283 nm ($1.1 \times 10^4$), 630 nm ($2.3 \times 10^2$), 762 nm ($3.0 \times 10^2$). MS (LSIMS): *m/z* 326 {M^+, 100%}. HR-MS: 326.1334 +/- 0.0004 (326.1333 for M^+ $C_{19}H_{26}FeO$). Mp 188 °C decomposes.

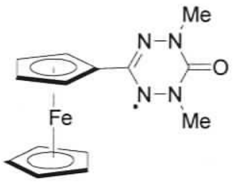

4.28

1,5-Dimethyl-3-{ferrocenyl}-6-oxoverdazyl (4.28) – **4.21** (300 mg, 0.95 mmol) was solubilized in DCM (40 mL) and stirred with *p*-benzoquinone (155 mg, 1.43 mmol) at RT for (16 hours) at which time the solvent was removed under reduced pressure. The solid was then purified by flash-column chromatography using basic alumina/DCM. The desired green band ($R_f = 0.45$) of the verdazyl, **4.28**, was collected and concentrated to dryness to yield pure product (235 mg, 79.1%). FT-IR (KBr): 3436 (w, br), 3078 (w), 2926 (w), 2854 (w), 1677 (s), 1510 (m), 1393 (m), 1294 (m), 1258 (m), 1199 (w), 1104 (w), 1042 (w), 1027 (w), 1003 (w), 956 (w), 884 (w), 832 (w), 818 (m), 716 (m), 697 (m), 667 (w), 627 (w), 600 (w), 546 (w), 535 (m), 502 (m), 484 (m) cm^{-1}. Anal. Calculated for $C_{14}H_{15}FeN_4O$: C, 54.04; H, 4.86; N, 18.01. Found: C, 53.70; H, 4.72; N, 17.86. $\lambda_{max}(CH_2Cl_2)(\varepsilon(M^{-1}cm^{-1})$: 398 nm ($1.3 \times 10^3$), 435 nm ($9.2 \times 10^2$), 592 nm ($2.7 \times 10^2$). MS (EI): *m/z* 121 {$FeCp^+$, 70%}, 211 {$(M-C_3H_6N_3O)^+$, 100%}, 311 {$M^+$, 70%}. HR-MS: 311.0600 +/- 0.0006 (311.0595 for M^+ $C_{14}H_{15}FeN_4O$). Mp 136-138 °C.-decomposes to red solid.

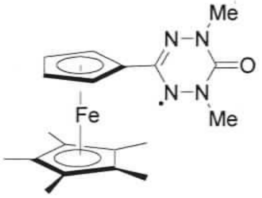

4.29

1,5-Dimethyl-3-{1',2',3',4',5'-pentamethylferrocenyl}-6-oxoverdazyl (4.29) – **4.22** (250 mg, 0.65 mmol) was solubilized in DCM (50 mL) and stirred with a slight excess of *p*-benzoquinone (freshly recrystallized, 110 mg, 1.0 mmol) for 24 hours at RT. After 24 h the solvent was removed under reduced pressure. The solid was then purified by column chromatography using N. alumina/DCM to remove pBQ and then Et_2O to remove the product; $R_f = 0.6$ in DCM and 0.75 in Et_2O. The organic fractions were collected and the solvent was removed to yield microcrystalline pure product, **4.29** (160 mg, 64.5%). FT-IR (KBr): 2948 (w), 2910 (m), 2857 (w), 1688 (s), 1680 (s), 1509 (m), 1476 (w), 1452 (w), 1424 (w), 1379 (m), 1292 (w), 1252 (m), 1039 (w), 1017 (w), 951 (w), 879 (w), 811 (w), 720 (w), 698 (w), 534 (m), 488 (m) cm^{-1}. Anal. Calculated for $C_{19}H_{25}FeN_4O$: C, 59.85; H, 6.61; N, 14.69. Found: C, 59.87; H, 6.78; N, 14.59. $\lambda_{max}(CH_2Cl_2)(\varepsilon(M^{-1}cm^{-1})$: 402 nm ($1.4 \times 10^3$), 442 nm ($1.2 \times 10^3$), 689 nm ($2.6 \times 10^2$). MS (EI): *m/z* 381 {$M^+$, 100%}, 281 {$[M-C_3H_6N_3O]^+$, 30%}, 256 {$[M-C_4H_6N_4O]^+$, 40%}. HR-MS: 381.1385 +/- 0.0005 (381.1378 for M^+ $C_{19}H_{25}FeN_4O$). Mp 125-127 °C decomposes.

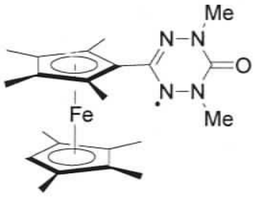

4.30

1,5-Dimethyl-3-{1,1',2,2',3,3',4,4'-octamethylferrocenyl}-6-oxoverdazyl (4.30) – **4.23** (300 mg, 0.70 mmol) was solubilized in DCM (40 mL) and stirred with excess *p*-benzoquinone (0.150 mg, 1.4 mmol) for (12 hours). Afer 12 h the solvent was removed under reduced pressure. The solid was then purified by flash-column chromatography using neutral alumina/DCM; $R_f = 0.70$. The organic fractions were collected and the solvent was removed to yield microcrystalline pure product**, 4.30** (87 mg, 29.2%). FT-IR (KBr): 2943 (w), 2904 (m), 2853 (w), 1694 (s), 1475 (w), 1455 (w), 1379 (w), 1272 (w), 1247 (w), 1030 (w), 1005 (w), 1171 (w), 816 (w), 714 (w), 692 (w), 542 (w), 469 (w) cm^{-1}. Anal. Calculated for $C_{22}H_{31}FeN_4O$: C, 62.41; H, 7.38; N, 13.19. Found: C, 62.27; H, 7.45; N, 12.89. $\lambda_{max}(CH_2Cl_2)(\varepsilon(M^{-1}cm^{-1})$: 399 nm ($1.4 \times 10^3$), 453 nm ($1.3 \times 10^3$), 771 nm ($2.8 \times 10^2$). MS (EI): *m/z* 423 {$M^+$, 100%}, 323 {$[M-C_3H_6N_3O]^+$, 30%}. HR-MS: 423.1847 +/- 0.0010 (423.1847 for M^+ $C_{22}H_{31}FeN_4O$). Mp 110-113 °C.

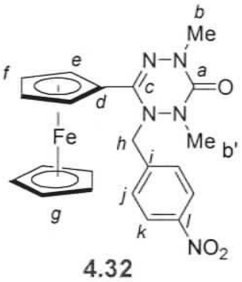

4.32

2,4-Dimethyl-6-ferrocenyl-1-(4-nitro-phenyl)-1,4-dihydro-2H-[1,2,4,5]tetrazin-3-one, (4.32) In a 100 mL RBF equipped with a small magnetic stir bar, 4-nitrobenzylcobaloxime pyridine complex[308] (**4.31**) (184 mg, 0.35 mmol) and **4.28** (110 mg, 0.35 mmol) were combined and dissolved in DCM (15 mL). To this was added 15 mL of acetone and the reaction was then placed in a full spectrum light box and stirred overnight (~14 h) at ambient conditions. An air condenser was added to avoid excessive solvent loss. Upon completion of the reaction, the solvent was removed via reduced pressure and the residue was then chromatographed using N. Alumina/EtOAc [R_f = 0.66 – Orange band] to yield the tetrazine product (0.08 g, 47%). Although pure by column chromatography the compound slowly decomposes, perhaps photolytically, and this may have led to large discrepancies in elemental data. ^{1}H NMR ($CDCl_3$): δ 8.24 (d, 2H, *J*=8.0Hz, H_k), 7.52 (d, 2H, *J*=8.0Hz, H_l), 4.72 (s, 2H, H_h), 4.42 (s, 2H, H_e), 4.25 (s, 2H, H_f), 4.20 (s, 5H, H_g), 3.06 (s, 3H, H_b), 2.95 (s, 3H, $H_{b'}$) ppm. ^{13}C NMR ($CDCl_3$): δ 149.5 (C_a), 147.8 (C_l), 142.5 (C_i), 130.6 (C_k), 123.6 (C_j), 109.6 (C_c), 74.8 (C_d), 70.4 (C_e), 69.8 (C_g), 67.5 (C_f), 55.6 (C_h), 36.5 ($C_{b'}$), 36.4 (C_b) ppm. FT-IR (KBr): 3095 (w), 2974 (w), 2927 (w), 2872 (w), 1663 (s), 1602 (m), 1520 (s), 1477 (m), 1427 (m), 1380 (m), 1364 (s), 1298 (w), 1271 (w), 1230 (w), 1203 (w), 1179 (w), 1130 (w), 1106 (m), 1041 (m), 1002 (w), 980 (w), 891 (w), 854 (w), 834 (w), 820 (w), 788 (w), 743 (w), 723 (m), 709 (w), 696 (w), 646 (w), 631 (w), 604 (w), 564 (w), 523 (w), 500 (m), 482 (m) cm^{-1}. Anal. Calculated for $C_{21}H_{21}FeN_5O_3$: C, 56.39; H, 4.73; N, 15.66. Found: C, 54.67; H, 4.59; N, 14.49. $\lambda_{max}(CH_2Cl_2)(\varepsilon(M^{-1}cm^{-1})$: 246 nm ($1.6 \times 10^4$), 449 nm ($5.6 \times 10^2$). MS (EI): *m/z* 447 {$M^+$, 10%}, 311 {$[M-C_6H_6NO_2]^+$, 100%}, 211 {$[M-C_9H_{12}N_4O_4]^+$, 35%}. HR-MS: 447.1003 +/- 0.0001 (447.0994 for M^+ $C_{21}H_{21}FeN_5O_3$). Mp 85-87 °C (decomposes).

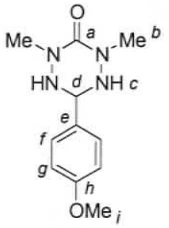

4.36

6-(4-Methoxy-phenyl)-2,4-dimethyl-[1,2,4,5]tetrazinan-3-one[91] (4.36) - To a gently refluxing solution of **2.52** (0.87 g, 7.34 mmol) in methanol (10 mL) was added dropwise (over 3 hours) a solution of *p*-methoxybenzaldehyde (**4.33**, 1.0 g, 7.34 mmol) in methanol (200 mL). After the addition was complete the reaction was gently heated to reflux overnight (10 hours). The reaction mixture (yellow) was cooled and the solvent removed under reduced pressure. The resulting solid was then purified via repeated trituration using EtOAc to yield pure tetrazane, **4.36** (1.51 g, 87.0%). ^{1}H NMR (DMSO): δ 7.44 (d, 2H, *J*=8.6Hz, H_f), 6.93 (d, 2H, *J*=8.6Hz, H_g), 5.63 (d, 2H, *J*=8Hz, H_c), 4.84 (t, 1H, *J*=8Hz, H_d), 3.75 (s, 3H, H_l), 2.95 (s, 6H, H_b) ppm. ^{13}C NMR (DMSO): δ

158.9 (C_h), 154.5 (C_a), 128.6 (C_e), 128.2 (C_f), 113.6 (C_g), 68.3 (C_d), 55.0 (C_l), 37.7 (C_b) ppm. FT-IR (KBr): 3248 (m), 2965 (w), 2920 (w), 2872 (w), 2841 (w), 1596 (s), 1499 (m), 1457 (m), 1440 (m), 1405 (m), 1392 (m), 1343 (w), 1324 (w), 1300 (m), 1244 (m), 1172 (m), 1123 (w), 1109 (w), 1094 (w), 1030 (m), 977 (m), 936 (w), 900 (w), 871 (w), 831 (m), 817 (m), 808 (m), 737 (m), 727 (m), 685 (w), 636 (w), 592 (m), 561 (m), 528 (w), 514 (w) cm^{-1}. Anal. Calculated for $C_{11}H_{16}N_4O_2$: C, 55.92; H, 6.83; N, 23.71. Found: C, 57.09; H, 6.49; N, 23.71. $\lambda_{max}(CH_2Cl_2)(\varepsilon(M^{-1}cm^{-1})$: 230 nm (1.8 × 10^4), 282 nm (5.6 × 10^3), 293 nm (4.6 × 10^3). MS (EI): *m/z* 236 {M^+, 55%}, 134 {$[M\text{-}C_3H_8N_3O]^+$, 100%}. HR-MS: 236.1278 +/- 0.0003 (236.1273 for M^+ $C_{11}H_{16}N_4O_2$). Mp 139-142 °C.

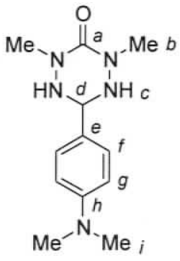

4.37

6-(4-Dimethylamino-phenyl)-2,4-dimethyl-[1,2,4,5]tetrazinan-3-one (4.37) - To a gently refluxing solution of **2.52** (0.8 g, 6.7 mmol) in methanol (10 mL) was added dropwise (over 3 hours) a solution of the *p-N,N*-dimethylaminobenzaldehyde (**4.34**, 1.0 g, 6.7 mmol) in methanol (200 mL). After the addition was complete the reaction was gently heated to reflux overnight (10 hours). The reaction mixture (yellow) was cooled and the solvent removed under reduced pressure. The resulting solid was purified via repeated trituration using EtOAc to yield pure tetrazane, **4.37** (1.24 g, 74.0%). ^{1}H NMR (DMSO): δ 7.31 (d, 2H, *J*=8.5Hz, H_f), 6.90 (d, 2H, *J*=8.5Hz, H_g), 5.53 (d, 2H, *J*=8.5Hz, H_c), 4.76 (t, 1H, *J*=8.5Hz, H_d), 2.94 (s, 6H, H_b), 2.88 (s, 6H, H_l) ppm. ^{13}C NMR (DMSO): δ 154.5 (C_a), 150.1 (C_h), 127.6 (C_f), 123.8 (C_e), 111.9 (C_g), 68.6 (C_d), 39.5 (C_l), 37.7 (C_b) ppm. FT-IR (KBr): 3256 (m), 3234 (m), 2970 (m), 2916 (m), 2879 (m), 2799 (m), 1599 (s), 1564 (m), 1525 (m), 1504 (m), 1438 (m), 1402 (m), 1389 (m), 1353 (m), 1342 (m), 1232 (m), 1181 (m), 1164 (m), 1129 (m), 1117 (m), 1095 (m), 1063 (m), 977 (m), 948 (m), 898 (w), 870 (m), 815 (m), 804 (m), 786 (m), 735 (m), 720 (m), 686 (m), 640 (w), 582 (m), 564 (m), 524 (m), 516 (m) cm^{-1}. Anal. Calculated for $C_{12}H_{19}N_5O$: C, 57.81; H, 7.68; N, 28.09. Found: C, 58.43; H, 7.26; N, 28.36. $\lambda_{max}(CH_2Cl_2)(\varepsilon(M^{-1}cm^{-1})$: 266 nm (2.0 × 10^4), 314 nm (8.5 × 10^3). MS (EI): *m/z* 249 {M^+, 75%}, 176 {$[M\text{-}C_2H_5N_2O]^+$, 35%} , 147 {$[M\text{-}C_3H_8N_3O]^+$, 100%}. HR-MS: 249.1594 +/- 0.0005 (249.3124 for M^+ $C_{12}H_{19}N_5O$). Mp 128-131°C.

1,5-Dimethyl-3-{*p*-tolyl}-1,2,4,5-tetrazane-6-oxide (4.38) - To a gently refluxing solution of **2.52** (2.004 g, 16.96 mmol) in methanol (10 mL) was added dropwise (over 3 hours) a solution of *p*-tolyl aldehyde (**4.35**, 1.95 mL, 16.49 mmol) in methanol (200 mL). After the addition was complete the reaction was gently heated to reflux overnight. The reaction mixture (clear, very light yellow) was cooled and the solvent removed under reduced pressure. The resulting solid was purified by trituration using hot ethyl acetate. The solid was filtered in air and washed with ethyl acetate to yield the pure tetrazane **4.38** (3.579 g, 98.5%). ^{1}H NMR (DMSO): δ 7.40 (d, 2H, *J*=8.0 Hz, H_f), 7.17 (d, 2H, *J*=8.0 Hz, H_g), 5.64 (d, 2H, *J*=8.0 Hz, H_c), 4.85 (t, 1H, 8.0 Hz, H_d), 2.94 (s, 6H, H_b), 2.29 (s, 3H, H_l) ppm. ^{13}C NMR (DMSO): δ 154.5 (C_a), 137.0 (C_e), 133.7 (C_f), 128.7 (C_g), 126.9 (C_h), 68.5 (C_d), 37.9 (C_b), 20.7 (C_h) ppm FT-IR (KBr): 3428 (w, br), 3256 (s), 3231 (s), 2921 (m, br), 1595 (s), 1503 (s), 1438 (s), 1391 (s), 1344 (m), 1234 (m), 1178 (m), 1130 (m), 1108 (m), 1065 (w), 1044 (w), 1019 (w), 980 (s), 944 (w), 871 (m), 812 (s), 736 (s), 722 (w), 686 (w), 582 (m), 562 (w), 523 (w), 490 (w) cm^{-1}. Anal. Calculated for $C_{11}H_{16}N_4O$: C, 59.98; H, 7.32; N, 25.44. Found: C, 60.11; H, 7.08; N, 25.36. $\lambda_{max}(CH_2Cl_2)(\varepsilon(M^{-1}cm^{-1})$: 290 nm (2.1 × 10^3). MS (EI): *m/z* 220 {M$^+$, 100%}. HR-MS: 220.1328 +/- 0.0004 (220.1324 for M$^+$ $C_{11}H_{16}N_4O$). Mp 155-160 °C.

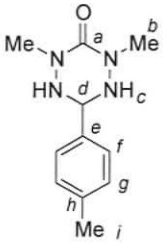

4.38

1,5-Dimethyl-3-(p-methoxybenzene)-6-oxoverdazyl[91] (4.39) – **4.36** (250 mg, 1.06 mmol) was solubilized in DCM (50 mL) and stirred with *p*-benzoquinone (0.172 mg, 1.59 mmol) for 12 hours at ambient temperature. After 12 h the solvent was removed under reduced pressure. The bright red solid was purified by flash-column chromatography using neutral alumina/DCM; $R_f = 0.58$. The organic fractions were collected and the solvent was removed to yield microcrystalline red product **4.39** (180 mg, 73%). FT-IR (KBr): 2967 (w), 2940 (m), 2834 (w), 1681 (s), 1608 (m), 1518 (m), 1469 (w), 1435 (w), 1414 (m), 1399 (m), 1340 (w), 1311 (m), 1300 (m), 1246 (s), 1172 (m), 1142 (w), 1110 (w), 1033 (m), 1021 (m), 1007 (w), 843 (m), 817 (w), 807 (w), 714 (m), 657 (m), 637 (w), 534 (m) cm^{-1}. Anal. Calculated for $C_{11}H_{13}N_4O_2$: C, 56.64; H, 5.62; N, 24.02. Found: C, 56.27; H, 5.68; N, 24.02. $\lambda_{max}(CH_2Cl_2)(\varepsilon(M^{-1}cm^{-1})$: 419 nm (9.3 × 10^2), 518

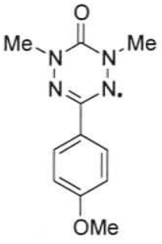

4.39

nm (4.3 × 10^2). MS (EI): *m/z* 233 {M^+, 100%}, 205 {$[M\text{-}CO]^+$, 55%}, 133 {$[M\text{-}C_3H_6N_3O]^+$, 30%}. HR-MS: 233.1044 +/- 0.0002 (233.1039 for M^+ $C_{11}H_{13}N_4O_2$). Mp 84-87 (desolvated), 139-141 °C (melted).

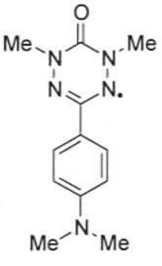
4.40

1,5-Dimethyl-3-(p-N,N-dimethylanaline)-6-oxoverdazyl (4.40) – 4.37 (250 mg, 1.0 mmol) was solubilized in DCM (50 mL) and stirred with *p*-benzoquinone (0.163 mg, 1.5 mmol) for 12 hours. At which time the solvent was removed under reduced pressure. The purple solid was purified by flash-column chromatography using neutral alumina/DCM; R_f = 0.53. The organic fractions were collected and the solvent was removed to yield an oily product. (162 mg, 66%). FT-IR (KBr): 2925 (w), 2810 (w), 1669 (s), 1611 (s), 1530 (m), 1414 (m), 1358 (m), 1318 (w), 1299 (w), 1248 (w), 1193 (w), 1142 (w), 1069 (w), 1024 (w), 948 (m), 819 (m), 713 (m), 657 (m), 537 (m) cm^{-1}. Anal. Calculated for $C_{12}H_{16}N_5O$: C, 58.52; H, 6.55; N, 28.44. Found: C, 58.41; H, 6.50; N, 28.38. $\lambda_{max}(CH_2Cl_2)(\varepsilon(M^{-1}cm^{-1})$: 432 nm (4.2 × 10^2), 569 nm (2.9 × 10^2). MS (EI): *m/z* 247 {MH^+, 100%}, 147 {$[M\text{-}C_3H_6N_3O]^+$, 75%}. HR-MS: 246.1356 +/- 0.0002 (246.1355 for M^+ $C_{12}H_{16}N_5O$).

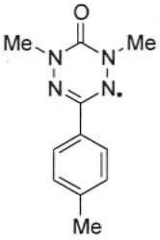
4.41

1,5-Dimethyl-3-{p-tolyl}-6-oxoverdazyl (4.41) – 4.38 (0.1998 g, 0.91 mmol) was dissolved in DMF (15 mL). A solution of $K_3Fe(CN)_6$ (0.9072 g, 2.76 mmol) in aq. Na_2CO_3 (8 mL, 0.5 M) was added to the tetrazane solution in large aliquots. Water was added to the reaction mixture until a red precipitate formed. The red reaction mixture was left to stir for ~ 20 min, and stirred at 0 °C for and additional 20 min. The red precipitate was isolated by vacuum filtration and washed with cold distilled water. **4.41** was obtained in a yield of 69.6% (0.137 g). FT-IR (KBr): 3437 (w, br), 2925 (w), 1684 (s), 1516 (w), 1453 (w), 1401 (m), 1296 (w), 1248 (w), 1176 (w), 1111 (w), 1015 (w), 843 (w), 823 (w), 714 (w), 658 (w), 533 (m) cm^{-1}. Anal. Calculated for $C_{11}H_{13}N_4O$: C, 60.81; H, 6.03; N, 25.79. Found: C, 52.14; H, 5.84; N, 24.27 . $\lambda_{max}(CH_2Cl_2)(\varepsilon(M^{-1}cm^{-1})$: 415 nm (1.3 × 10^3); 494 nm (4.8 × 10^2). MS (EI): *m/z* 217 {M^+, 100%}. HR-MS: 217.1092 +/- 0.0004 (217.1089 for M^+ $C_{11}H_{13}N_4O$). Mp 95-99 °C.

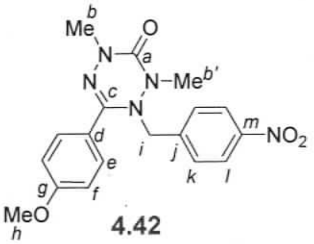

4.42

6-(4-Methoxy-phenyl)-2,4-dimethyl-1-(4-nitro-benzyl)-1,4-dihydro-2H-[1,2,4,5]tetrazin-3-one (4.42) - In a 100 mL RBF equipped with a small magnetic stir bar, 4-nitrobenzylcobaloxime pyridine complex^{308} (**4.31**, 254 mg, 0.5mmol), and **4.39** (110 mg, 0.5 mmol) were combined and dissolved in DCM (15 mL). To this was added 15 mL of acetone and the reaction was then placed in a full spectrum light box and stirred overnight (~14 h) at ambient conditions. An air condenser was added to avoid excessive solvent loss. Upon completion of the reaction, the solvent was removed under reduced pressure and the residue was then chromatographed using silica/EtOAc (Rf = 0.58 – yellow band). The product was recrystallized using petroleum ether to yield pure product **4.42** (0.11 g, 63%). ^{1}H NMR ($CDCl_3$): δ 8.18 (d, 2H, *J*=9Hz), 7.78 (d, 2H, *J*=9Hz), 7.41 (d, 2H, *J*=9Hz), 6.95 (d, 2H, *J*=9Hz), 4.13 (s, 2H), 3.86 (s, 3H), 3.02 (s, 3H), 2.97 (s, 3H) ppm. ^{13}C NMR ($CDCl_3$): δ 162.0 (C_g), 156.6 (C_d), 148.1 (C_a), 147.4 (C_m), 142.4 (C_j), 130.8 (C_l), 129.0 (C_e), 123.8 (C_k), 122.7 (C_c), 114.6 (C_f), 55.7 (C_i), 54.9 (C_h), 36.6 ($C_{b'}$), 36.1 (C_b) ppm. FT-IR (KBr): 3077 (w), 2937 (w), 2839 (w), 1675 (s), 1607 (m), 1515 (s), 1458 (m), 1425 (w), 1379 (m), 1346 (s), 1304 (w), 1254 (m), 1205 (w), 1169 (m), 1109 (w), 1030 (m), 977 (w), 838 (m), 808 (w), 764 (w), 713 (w), 684 (w), 639 (w), 596 (w), 541 (m), 497 (w) cm^{-1}. Anal. Calculated for $C_{18}H_{19}N_5O_4$: C, 58.53; H, 5.18; N, 18.96. Found: C, 58.06; H, 5.02; N, 18.84. $\lambda_{max}(CH_2Cl_2)(\varepsilon(M^{-1}cm^{-1})$: 267 nm (2.1 × 10^4). MS (EI): *m/z* 369 {M^+, 10%}, 233 {$[M\text{-}C_7H_6NO_2]^+$, 100%}, 205 {$[M\text{-}C_8H_6NO_3]^+$, 40%}, 100%}. HR-MS: 368.1353 +/- 0.0003 (369.1437 for M^+ $C_{18}H_{19}N_5O_4$). Mp 110-114 °C.

Chapter 5: Ferrocenyl Verdazyl Diradical

5.1.1 Objectives

Conceptually, the simplest magnetic model system is a molecule possessing two unpaired electrons. These two spins are aligned either ferromagnetically or antiferromagnetically and the alignment is dictated by either through-bond, or through-space magnetic interactions. In the preparation of diradicals this diamagnetic spacer is often referred to as a magnetic coupling unit.[20]

From the discussion in chapter 4, it would be safe to conclude that ferrocenyl *bis*-verdazyls are potentially interesting electronically because of the influence that the ferrocene and verdazyl electrophore exhibit on each other. However, ferrocenyl diradicals are also interesting magnetically because their structure makes them amenable to investigate the ferrocene scaffold as a through-space and/or through-bond magnetic coupling unit between the two verdazyl π-spins.

A significant number of studies have investigated the interactions between π-conjugated diradicals,[319] but far less is known about non-π-conjugated spacers. Although these molecules will not serve as ligands and are unlikely to form bulk magnetic materials, ferrocene represents another interesting scaffold that will allow us to investigate how two verdazyl radicals communicate electronically and magnetically.

5.1.2 Previously studied ferrocene diradicals

Unlike the ferrocenyl mono-radicals, the ferrocenyl diradicals have been less studied. There are only two known ferrocene-bridged diradicals (*bis*-nitronyl nitroxide radical **5.1** and the *bis*-triphenylmethyl radicals **5.2**) and both were synthesized and characterized by Veciana and coworkers.[276, 278]

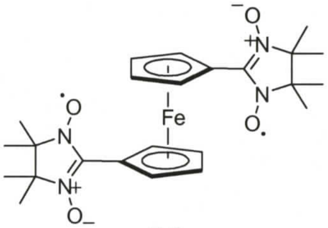
5.1

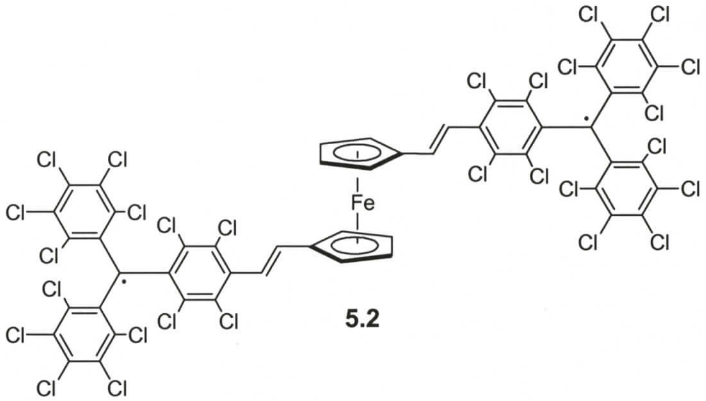
5.2

These diradicals were created in order to evaluate the effectiveness of metallocenes as spin couplers; a pursuit to test if a direct through-space interaction mimicking a super-exchange interaction between the π-spins of the two radicals and the metal orbitals of the metallocene unit was possible.

5.1.2.1 Structure and Magnetism

Conformationally, **5.1** exists in two different phases in the solid state. The α-phase[276] crystallizes in a *cisoid* geometry where the ferrocene unit has an eclipsed conformation, and the radicals are staggered by 72°. Sterics between the methyl groups of the two nitronyl-nitroxide radicals prevent the radicals from being fully eclipsed. The β-phase[320] crystallizes in a *transoid* geometry where the ferrocene unit is staggered and the molecule has a 2-fold rotation axis with the radicals separated by 180°. The α-phase of diradical **5.1** has dihedral angles (between Cp and imidazoline ring planes) of 7° and 24°, while both rings in the β-phase have the same dihedral angle of 13.4°. Both phases have intermolecular ordering with weak complementary C-H···O-N hydrogen bonds between neighboring radicals.

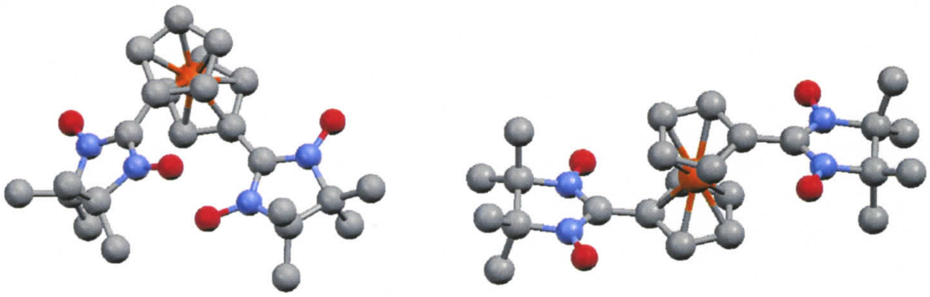

Figure 5.1 - α-phase (left) and β-phase (right) of **5.1**

The structural conformations lead to interesting manifestations in the solid state magnetic susceptibility. While both phases have the same weak intermolecular antiferromagnetic coupling (J_{inter} = -1.7 cm^{-1}), primarily due to the intermolecular hydrogen bonding, the α-phase and β-phase have different intramolecular magnetic exchange coupling constants. The *cisoid* α-phase has an exchange coupling of J_{intra} = -1.7 cm^{-1} and the *transoid* β-phase has an exchange coupling of $J_{intra'}$ = -3.9 cm^{-1}. This is a rather unusual result since the β-phase does not have any direct through-space interaction between radicals. This implies that the magnetic exchange must take place exclusively through-bond, and can be explained using the spin polarization effect.[276] In spin polarization if there are large dihedral angles between radicals and linker, the magnitude of the magnetic exchange significantly dimishes.[321]

Variable temperature solution EPR investigations[276] of **5.1** suggested that the ground state of the diradical is a singlet, and after fitting to the Bleaney-Bowers equation the magnetic exchange constant was determined to be J_{intra} = -20 cm^{-1}. This result is significantly higher than the solid state measurement, but the molecular conformations would be altered in frozen solutions. The room temperature isotropic solution EPR spectrum of **5.1** consisted of an overlap of two types of spectra. The contributions to the superimposed spectra are two fold: one is a broad intense single line assigned to the diradical molecules having a large spin-spin dipolar interactions. The second is a hyperfine coupling pattern that is less than 1% of the total signal intensity, which was attributed to monoradical impurity. With such sensitivity to conformation the authors were unable to effectively assess the metallocene unit as a magnetic coupler.

In the design of **5.2** it was originally thought that by introducing an alkene spacer between the ferrocene-bridge and triphenylmethyl radical, this particular topology would allow for a resonance contribution that would transfer spin density onto the ferrocene moiety. Having a non-negligible spin density on the ferrocene should make the metallocene a more effective magnetic coupling unit,[278] while the use of a larger bulkier radical was expected to eliminate intramolecular contacts and through-space coupling interactions. Unfortunately, no crystal structure of the ferrocenyl *bis*-triphenylmethyl radical exists. However, variable temperature solution EPR data was able to estimate the singlet-triplet gap for **5.2** to be J_{intra} = +7cm^{-1} by fitting to the Bleaney-Bowers equation.[322] Molecular modeling[322] suggests that the optimized structure has the *transoid* geometry between radicals. By comparing this weak ferromagnetic exchange interaction result to **5.1** the authors concluded that electron density from the triphenylmethyl radical is effectively being transmitted through the ferrocene spacer.

5.1.2.2 Electronic communication between radicals

Further investigation into the electronic properties of diradicals **5.1** and **5.2** demonstrate the electronic communication between radicals. The CV of diradical **5.1** consists of two reversible waves, which include oxidation of the ferrocenyl moiety (0.20 V vs. Fc/Fc$^+$) followed by oxidation of one of the radical substituents (0.40 V vs Fc/Fc$^+$). Both oxidations are one-electron processes. A third oxidation wave belonging to the second radical was an irreversible process, probably due to the instability of the resulting tri-cationic species. Like the monoradical, diradical **5.2** showed a high degree of electrochemical stability in solution with two reversible waves; one owing to the oxidation of the ferrocenyl moiety (0.67 V vs. Ag/AgCl) and the concurrent 2-electron reduction of the radical units (-0.18 V vs Ag/AgCl). The simultaneous reduction potential of the biradical derivative suggests that the spins do not communicate.

There are two other references to ferrocenyl diradicals, but their discussion is limited. Ferrocene diradical **5.1** was successfully employed in the creation of chiral coordination polymers via ligation to manganese(II) bis(hexafluoroacetylacetonate).[323] Furthermore, a *tert*-butyl nitroxide ferrocenyl diradical **5.3** was also studied, but it was not isolated as it rapidly decomposes in solution yielding a diamagnetic product.

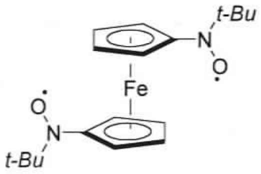

5.3

5.2 Synthesis and structure of a ferrocenyl *bis*verdazyl

Verdazyls are planar ring systems that do not exhibit the same steric bulk as nitronyl nitroxides. Therefore it may be possible to investigate through space interactions and coupling of the radicals via the ferrocene scaffold. The ferrocene bisverdazyl **5.6** was prepared using previously discussed (chapter 4) methodologies for ferrocenyl verdazyl formation.

5.2.1 Aldehyde synthesis

The ferrocene dialdehyde was formed from ferrocene via a low temperature lithiation, using *N,N,N'N'* tetramethylethylenediamine (TMEDA) as an ancillary ligand to help stabilize the intermediate dilithiated species. Using DMF as the electrophile results in the ferrocenedicarboxaldehyde derivative[324] shown in Scheme 5.1.

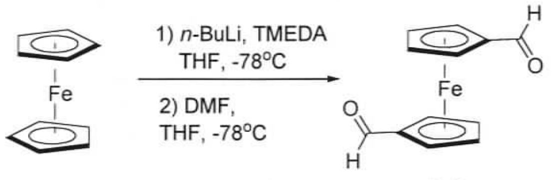

5.4

Scheme 5.1 - Synthesis of 1,1'-ferrocene-dicarbaldehyde, **5.4**

5.2.2 Tetrazane synthesis

The dialdehyde species **5.4** was then condensed (Scheme 5.2) with 2 equivalents of carbonic acid bis(1-methylhydrazide), **2.52**, with special attention given to the rate of aldehyde addition because dialdehydes readily undergo oligomerization (section 2.3.3).

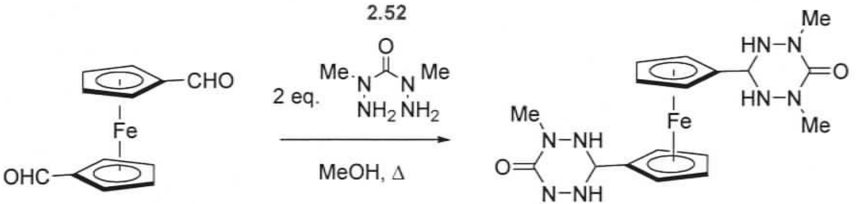

5.4 **5.5**

Scheme 5.2 - Preparation of *bis*-tetrazane **5.5**

Like the other ferrocenyl tetrazanes compound **5.5** was synthesized in good yield and with no observable bis-imine formation. There is a small amount of observed polyimine oligomer formed, that is easily removed because of it low solubility.

5.2.3 Ferrocene *bis*-verdazyl synthesis

The *bis*verdazyl **5.6** was prepared by oxidizing tetrazane **5.5** using pBQ as an oxidant (Scheme 5.3). The bisverdazyl was purified using column chromatography and isolated in moderate yield. The poor yields are primarily due to the insolubility of the *bis*verdazyl. **5.6** is only partially soluble in DCM and although the column chromatography was performed using EtOAc attempts to resolublize the product in EtOAc were unsuccessful. Purple x-ray quality crystals of **5.6** were grown from a saturated DCM solution via slow evaporation.

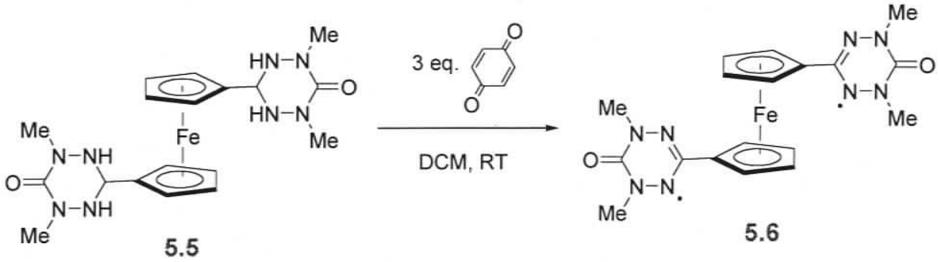

Scheme 5.3 - Synthesis of diradical **5.6**

5.2.4 Crystal structure of 5.6

The molecular structure of the diradical **5.6** is shown in Figure 5.2 and 5.3. The two verdazyl rings are nearly perfectly eclipsed with respect to one another, and the internal features of each radical are the same (within experimental error) as those of the monoverdazyl radical, as seen in Table 5.1.

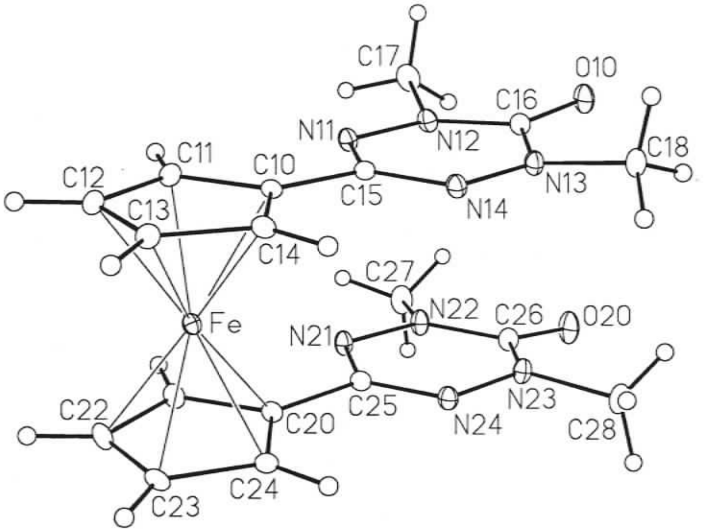

Figure 5.2 - ORTEP diagram of the molecular structure of **5.6** (Gaussian ellipsoids at the 20% probability level.)

Table 5.1 - Selected bond distances and angles for the structure of bisverdazyl **5.6** (estimated standard deviations in parentheses)

Atoms	Distance (Å)	Atoms	Angle (deg.)
O(10)-C(16)	1.220(3)	O(10)-C(16)-N(12)	122.7(2)
N(11)-N(12)	1.367(3)	N(12)-N(11)-C(15)	114.70(19)
N(11)-C(15)	1.331(3)	N(11)-N(12)-C(16)	124.36(19)
N(12)-C(16)	1.374(3)	N(11)-N(12)-C(17)	114.81(19)
N(12)-C(17)	1.458(3)	N(11)-C(15)-N(14)	127.6(2)
C(10)-C(15)	1.470(3)	N(11)-C(15)-C(10)	115.4(2)
		N(12)-C(16)-N(13)	114.17(19)

The face to face distance between the radicals is only 3.15 Å, which is much closer than non-associated π systems (van der Waals contact ~3.4 Å). Furthermore, the two radical planes seem to be attracted to one another. Strain can be observed in the ferrocene unit as canting of the Cp rings (tilt angle ~1.5°), and the bowing out of the N-methyl groups (average separation of 3.57 Å) and the carbonyl groups (oxygen-oxygen distance of 3.65 Å). The verdazyl contact distances are listed in Table 5.2. Despite this observed strain and repulsion there are only minimal deviations from local planar geometry, with the verdazyl ring and all of the atoms considered to be sp^2 hybridized. **5.6** is an example of an intramolecular π–dimer, and is the first demonstration of π-association between two verdazyl radicals.

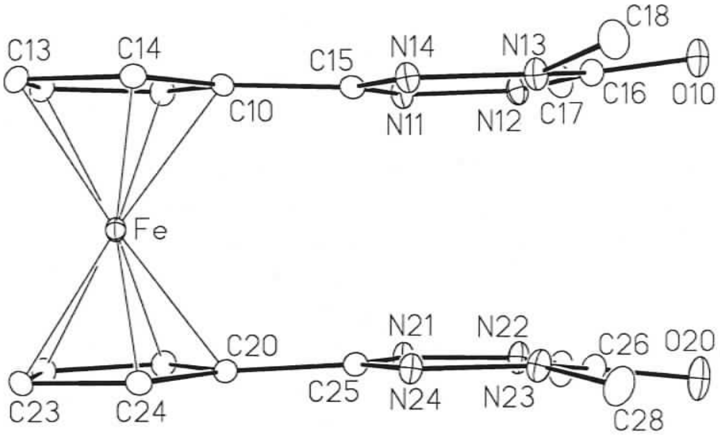

Figure 5.3 - ORTEP diagram of the molecular structure of **5.6** (Gaussian ellipsoids at the 20% probability level.)

Table 5.2 - Selected inter-annular contact distances in bisverdazyl **5.6**

Atoms	Distance (Å)
C(10)-C(20)	3.249
C(15)-C(25)	3.144
N(14)-N(24)	3.149
N(11)-N(21)	3.119
N(12)-N(22)	3.136
N(13)-N(23)	3.196
C(16)-C(26)	3.365
C(17)-C(27)	3.493
C(18)-C(28)	3.642
O(10)-O(20)	3.645

A packing diagram of **5.6** is depicted in Figure 5.4. Packing involves slipped stacks of the diradical layers in the *ab* plane, with neighboring layers oriented in the opposite direction. The distance between each molecule in the slipped stack is 3.34 Å which is close to the normal graphitic separation of 3.41 Å, and the radicals within a *bis*verdazyl unit have an average distance of 3.15 Å. This is consistent with other π-plane distances within π-dimers that is smaller than the van der Waals interaction (2.9-3.4) [325]

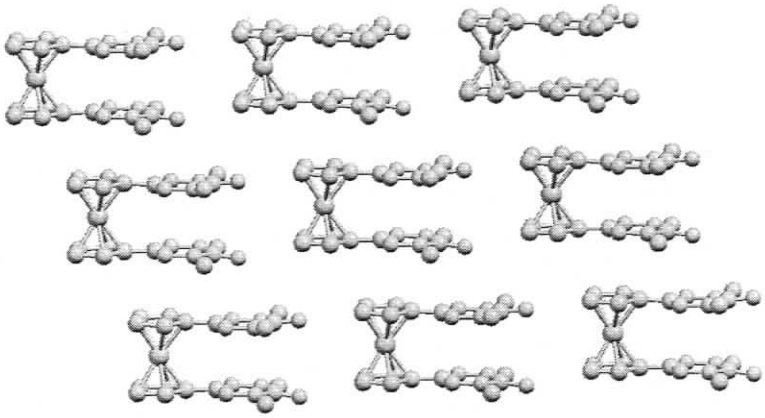

Figure 5.4 - Extended molecular structure of **5.6** - ab plane. Hydrogen atoms omitted for clarity

5.3 Electronic properties of ferrocenyl *bis*verdazyl

5.3.1 Electronic absorption spectroscopy: UV-Vis

The features observed in the solution UV-Visible spectra of **5.6** are similar to those of the monoverdazyl **4.28**. Figure 5.5 shows the characteristic verdazyl absorption with a molar extinction coefficient approximately double that of **4.28**. Tentatively the charge transfer transition has been assigned as the extremely broad tail that extends from 500 nm to nearly 800 nm, but it has no obvious maximum.

The solid state electronic spectrum of **5.6** is remarkably different to those of **4.28** and **5.6** in solution (Figure 5.6). It is possible to see the presence of the verdazyl absorptions in the monoverdazyl (400-450 nm), but not in the diradical. Also, **5.6** appears to have a rather broad absorption centreed near 530 nm, which is not present in the solution spectrum of **5.6** or the solid state spectrum of **4.28**. This data suggests that the electronic nature of the verdazyl diradical is different in solution and the solid state and that the π-dimer may not be present in solution. Further, this suggests that the presence of a π-dimer in the solid state dramatically perturbs the electronic structure of the verdazyl diradical.

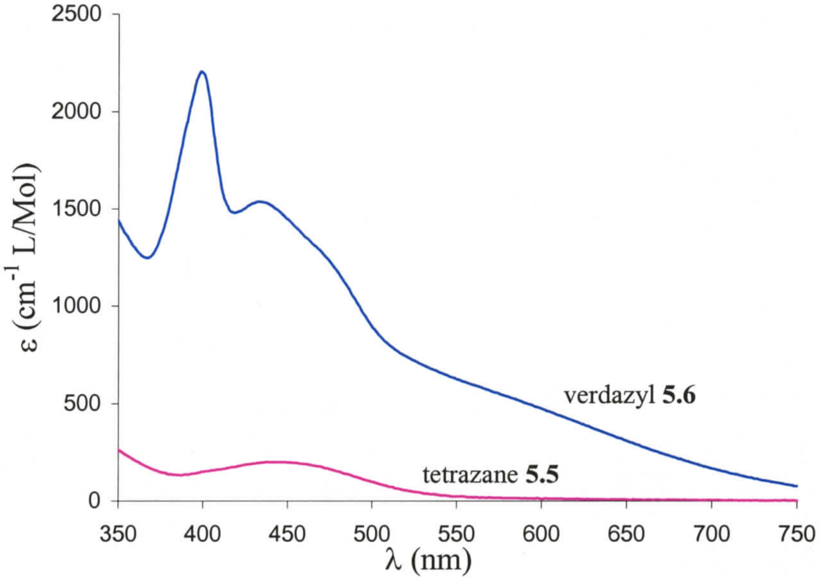

Figure 5.5 - UV-Vis spectrum of *bis*verdazyl **5.6** and precursor *bis*-tetrazane **5.5** in DCM

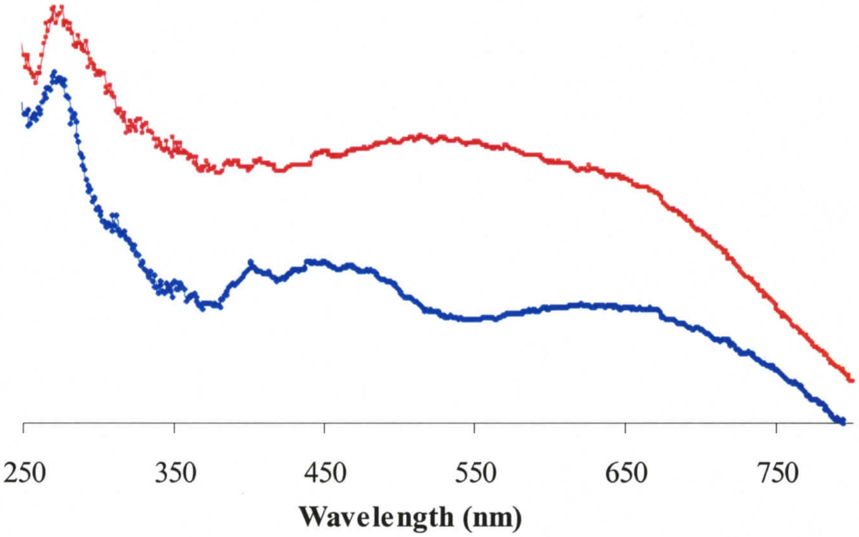

Figure 5.6 – Solid state electronic spectrum (reflectance mode) of *bis*verdazyl **5.6** (red) and monoverdazyl **4.28** (blue) in barium sulfate matrix

5.3.2 Electrochemistry : Cyclic voltammetry

The CV of **5.6** is presented in Figure 5.7. There are three reversible waves, but the lowest potential oxidation actually represents two separate one-electron processes and appears as the superposition of these two potentials. The two waves were resolved by Osteryoung square wave voltammetry[326] as depicted in Figure 5.8 and these two peaks are approximately 90mV apart.

The ferrocene peak potential is indicative of the electron withdrawing nature of the substituents attached. There are three possible assignments for the observed oxidation potentials. In the case of the monoverdazyl **4.28** the lower oxidation potential was assigned to the Fc/Fc$^+$ redox couple. This oxidation, which preceded the verdazyls, made the verdazyl component much harder to oxidize. Consider the possibility where the ferrocene is oxidized first followed by the radicals (Fc-Vd-Vd). The first oxidation potential appears at +190 mV. Although it is conceivable that two electron withdrawing verdazyl groups may only shift the ferrocene potential 92 mV compared to **4.28**, it is inconsistent to suggest that the second oxidation potential, belonging to a verdazyl radical, would be 60 mV lower for the more electron deficient **5.6** than monoverdazyl **4.28**. Based on this reasoning it is unlikely that the ferrocene is oxidized first.

Another possibility is that the first oxidation potential is assigned to a verdazyl, and the second oxidation potential is assigned to ferrocene (Vd-Fc-Vd). Upon oxidizing the first verdazyl, it is inconsistent to suggest that the second verdazyl oxidation is nearly 300 mV higher. Although the generation of a verdazyl cation would make the molecule electron deficient, it would not likely perturb the electronics of the second verdazyl to this extent. Therefore it is unlikely that the verdazyls are separated by a large potential difference.

The third, and most likely assignment of these observed oxidation potentials is that the ferrocene is oxidized last (Vd-Vd-Fc). It is conceivable that the ferrocene-based oxidation potential could be shifted to significantly higher potentials when compared to **4.28**, as the previously generated verdazyl cations would serve as strong electron withdrawing groups. Furthermore, having the verdazyl oxidations 90mV apart is consistent with only modest electronic modifications to the molecule after the first oxidation. Further confirmation of this assignment can be made from the Osteryoung square wave analysis which is very sensitive to reversible current. Typically the most reversible analytes show up as more intense or sharper peaks.[326] Based on other verdazyl studies, the ferrocene moiety is expected to be more reversible than the verdazyl, and as such the largest/sharpest peak is the one at +480mV. This is further evidence suggesting that the ferrocene redox couple is the highest of the three oxidation potentials observed for **5.6**. All of these assignments have been summarized in Table 5.3.

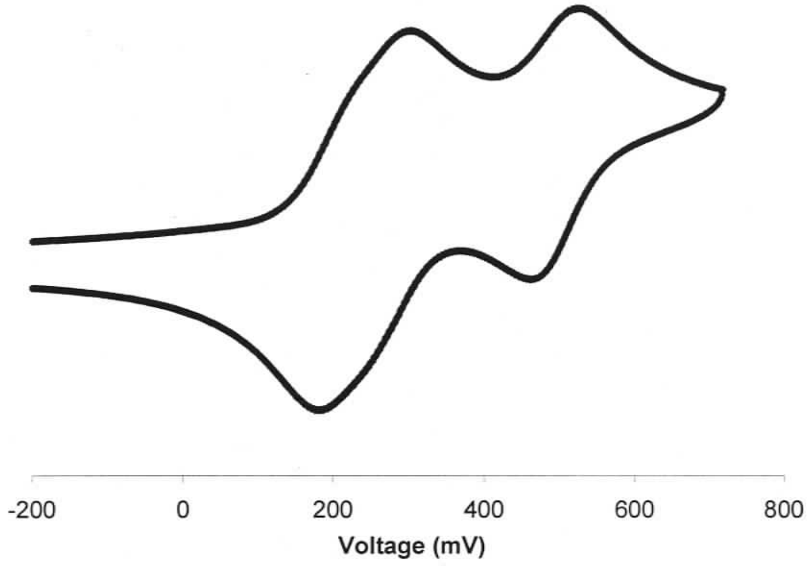

Figure 5.7 - Cyclic Voltammogram of **5.6** versus Fc/Fc$^+$ (y-axis (not shown) is current in μA)

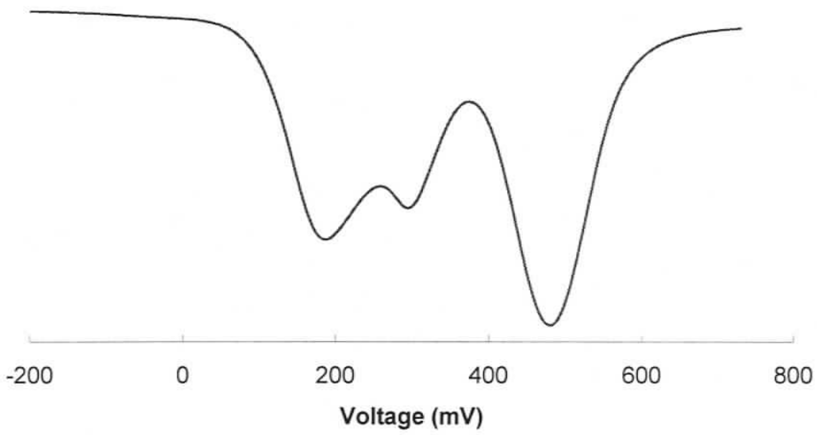

Figure 5.8 - Osteryoung Square Wave Voltammogram of **5.6** versus Fc/Fc$^+$ (y-axis (not shown) is current difference in μA)

Table 5.3 - Electrochemical redox potentials of ferrocene verdazyls and bisverdazyls vs Fc/Fc+

	Oxidation potentials (mV) vs. Fc/Fc$^+$		
Compound	**Fc/Fc$^+$**	**^{1}Vd$^\cdot$/ ^{1}Vd$^+$**	**^{2}Vd$^\cdot$/ ^{2}Vd$^+$**
4.11	295	—	—
4.28	98	339	—
5.4	560	—	—
5.6	480	190	280

The difference in oxidation potentials between chemically equivalent verdazyl substituents suggests that there is a degree of electronic communication between the substituents through the ferrocene scaffold.

5.3.3 EPR of 5.6

The EPR of **5.6** is qualitatively similar to what was observed by Veciana and co-workers[276] for the ferrocene-based nitronyl nitroxide diradical. The EPR room temperature solution spectrum consists of two superimposed signals (see Figure 5.9); a broad featureless peak superimposed on a multiplet that looks like a typical verdazyl monoradical hyperfine coupling pattern. The broad featureless peak is observable at the spectral width of 1000G and has been assigned to the diradical having a large spin-spin dipolar interaction that is not completely averaged out by molecular tumbling. The hyperfine coupling that is seen within this broad peak has been assigned to adventitious mono-radicals. The hyperfine coupling is less than 1% of the total signal intensity and it is reasonable to ascribe this hyperfine pattern to a small fraction of monoverdazyl-based impurity in the sample that may result from trace amounts of a monoradical species.

Variable temperature EPR studies were attempted, but due to the poor solubility of **5.6** in all solvents the product precipitated as the temperature was decreased. As the diradical precipitated the sample became EPR silent, this is consistent with the solid state π-dimer structure discussed earlier.

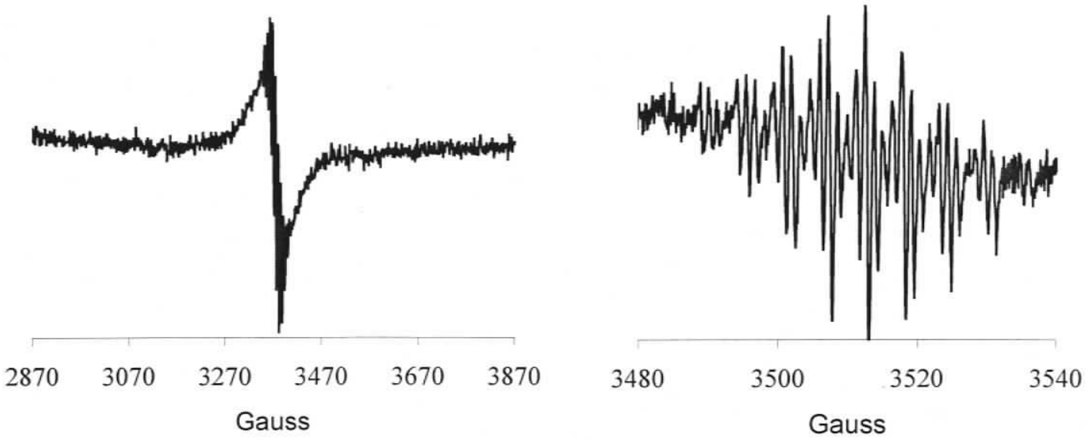

Figure 5.9 - Room temperature solution EPR of **5.6** in DCM. Left - 1000G width. Right - 80G width.

5.3.4 Mössbauer Spectroscopy

The Mössbauer spectrum of **5.6** is consistent with what was observed for the monoradical, **4.28**. The only oxidation state of iron present is Fe^{2+} and this suggests that there is no valence tautomerism exhibited by **5.6** between 77 K and room temperature.

5.4 Magnetic properties of ferrocenyl *bis*verdazyl 5.6

5.4.1 Solid state magnetic susceptibility

The solid state magnetic susceptibility data for **5.6** is presented in Figure 5.10. **5.6** appears to be diamagnetic with a very small amount of paramagnetic impurity. At 300K **5.6** is diamagnetic and the presence of a paramagnetic impurity is only noticeable as the temperature approaches 2 K. The paramagnetic impurity could result from small amounts of monoverdazyl, or from small amounts of structural defects involving *transoid*-diradicals. The observed diamagnetic behaviour suggests strong antiferromagnetic exchange and a lower limit of J_{intra} of at least -2000 cm^{-1}.

5.1 and **5.2** do not π-stack and therefore can only magnetically communicate through-bond and the through-bond contributions to the magnetic coupling is very small ($|J_{intra}|$<10 cm^{-1}). Veciana's systems and the intramolecular contacts observed in the solid state of **5.6** suggest that the diamagnetism of **5.6** results from intramolecular through-space interactions.

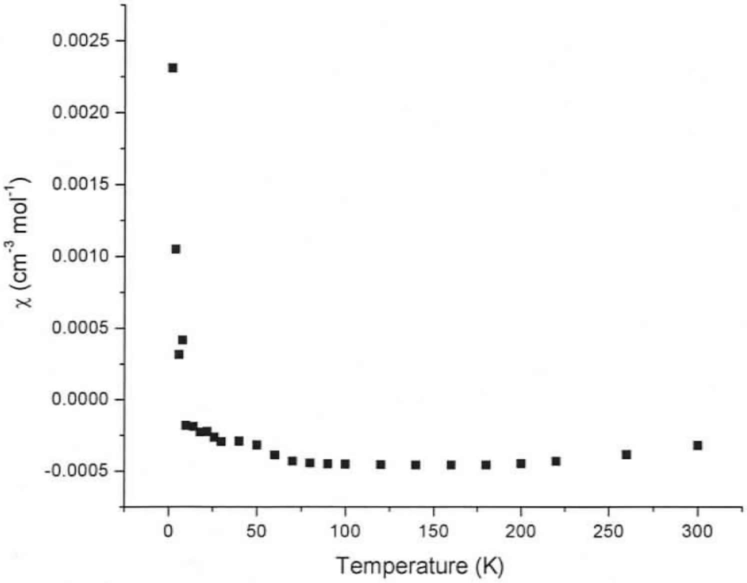

Figure 5.10 - Temperature dependence of χ (▪) for **5.6**.

The diamagnetism of π-dimers can be understood when considering that dimer formation results from the orbital interaction between two degenerate SOMOs, resulting in a singlet electronic structure (Figure 5.11). The newly generated molecular orbitals have extensive delocalization throughout the dimer, which typically results in the π-dimer possessing a new electronic structure that is not observed in the monomeric system.

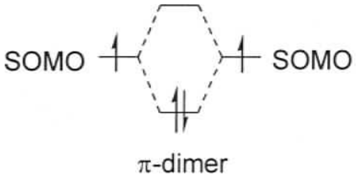

Figure 5.11 - Qualitative orbital interactions in π-dimers

π-dimers are commonplace in several radical families. Phenalenyl,[327, 328] TCNE radical anions,[329] sulfur-nitrogen radicals,[330] and oligothiophene-based cyclophanes[331] have all demonstrated formation of π-dimers in the solid state; however, this is the first π-dimer observed between two verdazyl radicals.

Although there are several examples of tethered diradicals that π-dimerize, this is the first to make use of a ferrocene tether. In fact with the exception of ferrocenophanes[332,333] there are few examples of association (e.g. π-stacking) between substituents in 1,1'-disubstituted ferrocenes. The structure of ferrocene has an optimal distance between the Cp rings for π-stacking arrangements, but conformational flexibility usually leads to staggered or transoid conformations. To our knowledge the only class of 1,1'-disubstituted ferrocenes that exhibit non-covalent attractive interactions (e.g. π-stacking, dipole-dipole) are the pentafluorophenyl disubstituted ferrocenes, where the pentafluorophenyl substituents of these ferrocenes π-stack ($\pi-\pi$ distance ~3.6 Å) due to C-F dipole-dipole interactions.[334]

In the case of diradical **5.6** the through space overlap of the π SOMOs provides the attractive interaction that causes the Cp units and substituents to perfectly eclipse. This attractive interaction arises from orbital overlap; therefore there is a degree of bonding between the verdazyls of the dimer. However, this is not a covalent interaction at the same level as a normal bond. Verdazyls do not typically π-dimerize and the interaction is only obvious in the solid state. Therefore it can be safely assumed that the energy of this association is reasonably weak.

5.4.2 Solution susceptibility: The Evans method

In chapter 4, the Evans method was discussed as a reliable means of investigating solution magnetic susceptibility. From equation 4.4, μ_{eff} can be readily obtained from ^{1}H-NMR data. Within the 10% experimental error, the Evans method data suggests that the ferrocenyl bisverdazyl does not exist as a π-dimer in solution (Table 5.4). If the solution product were diamagnetic the μ_{eff} would be zero, but the experimental μ_{eff} modestly exceeds the expected value for a two-spin system. Although this method is not able to assess the details of through bond coupling, it is clearly not a strongly antiferromagnetically coupled diradical in solution. This result is consistent with solution electronic data from EPR and UV-Vis that suggests **5.6** appears to be a weakly coupled diradical in solution.

Table 5.4 - Evans method solution magnetic susceptibilities

Compound	Solvent	Average μ_{eff}	expected μ_{eff}
4.28	$CDCl_3$	2.39	1.73
5.6	DCM	3.17	2.45 - 2.83

5.5 Summary

Herein the synthesis and characterization of the first ever verdazyl radical π-dimer has been reported. In the solid state the two radicals of the dimer are strongly antiferromagnetically coupled, with a lower limit to intramolecular antiferromagnetic exchange of $J_{intra} \approx -2000$ cm^{-1}. The ferrocene tether plays a structurally important role. This intramolecular dimerization is the only example of a conformationally flexible ferrocene unit in which the substituents π–π distances are less than normal graphitic separation. It may also be possible that there is a synergistic effect leading to radical dimerization, where the ferrocene is more than a scaffold and it mediates radical-radical through-bond interactions.

Solutions studies suggest that this verdazyl dimer does not exist in solution. The Evans method and UV-Vis data indicate that **5.6** exhibits the properties of a diradical possessing two weakly coupled spins. EPR also shows the presence of a dipolar paramagnetic species, which is consistent with two weakly coupled spins. Furthermore, electrochemical analysis in solution suggests significant electronic communication between the two chemically equivalent radicals. All oxidations are fully reversible, but the radicals have two different oxidation potentials, which suggests there is strong through-bond electronic coupling mediated by the ferrocene scaffold.

5.6 Experimental section

5.6.1 General synthetic procedures

Unless stated otherwise, all general synthetic procedures employed are similar to those presented in section 2.7.1.

5.6.2 Magnetic measurements

Details of the magnetic measurements have been previously reported in section 2.7.2.

5.6.3 Mössbauer measurements

Details of the Mössbauer measurements have been previously reported in section 4.6.3

5.6.4 Synthesis

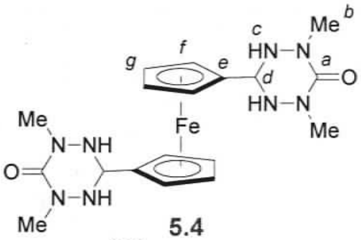

5.4

***Bis*-(1,5-dimethyl-1,2,4,5-tetrazane-6-oxide-3-)-1,1'-ferrocene (5.6)** - To a gently refluxing solution of **2.52** (1.46 g, 12.4 mmol) in methanol (10 mL) was added dropwise (over 3 hours) a solution of **5.5** (1.5 g, 6.2 mmol) in methanol (175 mL). **5.5** was prepared using an existing method[335]. After the addition was complete the reaction was gently heated to reflux overnight (10 hours). The reaction mixture (deep red/orange) was then cooled, filtered, and the solvent removed under reduced pressure. The resulting solid was then triturated using ethyl acetate. The solid was recrystallized from MeOH and EtOAc to yield pure tetrazane, **5.6** (1.5 g, 55%). ^{1}H NMR (DMSO): δ 5.36 (d, 4H, J=10Hz, H_c), 4.68 (t, 1H, J=10Hz, H_d), 4.30 (s, 4H, H_f), 4.22 (s, 4H, H_g), 2.95 (s, 12H, H_b) ppm. ^{13}C NMR (DMSO): δ 154.7 (C_a), 83.7 (C_e), 68.2 (C_d), 67.7 (C_f), 65.9 (C_g), 37.6 (C_b) ppm. FT-IR (KBr): 3436 (w, br), 3235 (m), 3222 (w), 3091 (w), 2928 (w, br), 2869 (w), 1634 (s), 1618 (s) 1491 (m), 1432 (m), 1385 (m), 1335 (w), 1154 (w), 1155 (w), 961 (w), 894 (w), 831 (w), 731 (w), 670 (w), 590 (w), 530 (w), 491 (w), 464 (w) cm^{-1}. Anal. Calculated for

$C_{14}H_{18}FeN_4O$: C, 48.88; H, 5.93; N, 25.33. Found: C, 49.23; H, 5.83; N, 25.09. $\lambda_{max}(CH_2Cl_2)(\varepsilon(M^{-1}cm^{-1})$: 438 nm (2.0 × 10^2). MS (EI): *m/z* 442 {M^+, 30%}. HR-MS: 442.1525 +/- 0.0005 (442.1528 for M^+ $C_{18}H_{26}FeN_8O_2$). Mp 205-208 °C.

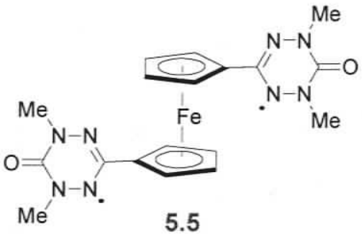

5.5

Bis(1,5-dimethyl-6-oxoverdazyl-3-)-1,1'-ferrocene (5.7)- **5.6** (294 mg, 0.66 mmol) was solubilized in DCM (40 mL) and stirred with *p*-benzoquinone (216 mg, 2.0 mmol) for 10 hours, after which time the solvent was removed under reduced pressure. The solid was then purified by flash-column chromatography using neutral alumina/EtOAc eluting first with DCM to remove the pBQ. The desired maroon band (R_f = 0.65 in EtOAc, R_f = 0.12 in DCM) of the verdazyl was collected using copious amounts of EtOAc (due to limited solubility), where the solvent was then removed to yield microcrystalline pure product. (160 mg, 55.2%). FT-IR (KBr): 3436 (w, br), 3100 (w), 3086 (w), 2938 (w), 1689 (s), 1667 (m), 1514 (w), 1465 (w), 1394 (w), 1353 (w), 1290 (w), 1261 (w), 1202 (w), 1171 (w), 1048 (w), 1026 (w), 957 (w), 886 (w), 837 (w), 830 (w), 803 (w), 716 (w), 701 (w), 627 (w), 603 (w), 552 (w), 538 (w), 509 (m) cm^{-1}. Anal. Calculated for $C_{18}H_{20}FeN_8O$: C, 49.56; H, 4.62; N, 25.69. Found: C, 49.39; H, 4.66; N, 25.32. $\lambda_{max}(CH_2Cl_2)(\varepsilon(M^{-1}cm^{-1})$: 399 nm (2.2 × 10^3), 433 nm (1.5 × 10^3). MS (EI): *m/z* 436 {M^+, 100%}. HR-MS: 436.1072 +/- 0.0002 (436.1059 for M^+ $C_{18}H_{20}FeN_8O_2$). Mp 246-248 °C (decomp. 205 °C – salmon coloured).

Chapter 6: General Summary, Conclusions and Future work

6.1 General conclusions

There have been several different approaches taken to realize molecular based magnetic materials, but the coordination chemistry of stable free radicals is perhaps the most attractive. Currently major classes of radical ligands are the nitroxides, semiquinones, and polynitrile radical anions. However, previous studies combined with this body of work have reinforced the notion that verdazyl radicals are another radical family that show enormous potential as building blocks towards molecular magnetism.

Despite the coordination chemistry challenges faced in this work, several new synthetic strategies towards more exotic verdazyl radicals have been investigated. Furthermore, an introductory study into the electroactive nature of verdazyls has also been initiated. From these studies, it has been demonstrated that through modification of the C3 substituent of the verdazyl ring it is possible to examine the electronic influences that these substituents have on the properties of the verdazyl radical. Although verdazyl-verdazyl radical electronic interactions have been investigated previously, this is the first detailed examination of indirect metal-verdazyl interactions. It is the study of these interactions that will lead undoubtedly to a better understanding of verdazyl stability and utility essential to materials design.

6.2 *N*-Heterocyclic verdazyl ligands

With the completion of a series of octahedral M(hfac)(**2.15**) complexes, which now include Mn, Fe, Co, and Ni, there exists a more detailed understanding of how verdazyls magnetically interact with octahedral metal ions. The metal-verdazyl exchange can be explained using molecular orbital symmetry and orbital orthogonality arguments. Octahedral Mn(II) and Fe(II) complexes showed antiferromagnetic coupling between radical and metal, while octahedral Co(II) and Ni(II) complexes demonstrated ferromagnetic coupling between the metal and radical. This is in contrast to the magnetic exchange coupling found in coordination complexes with other families of free radicals, particularly nitroxide radicals, in which small structural changes to the radical ligands result in dramatically different magnetic coupling.

To further understand the nature of metal-verdazyl coordination chemistry a series of potentially anionic verdazyls were prepared with imidazole and pyrrole substituents Pyrrole substituted verdazyls are not particularly stable due to the reactivity of the pyrrole substituent. Imidazole substituted verdazyls seem to be fairly robust and were found to coordinate to diamagnetic tetrahedral Cu(I) metal ions. As of yet, the imidazole has not been shown to bind to octahedral metal centres, although current work in the Hicks group does suggest that the imidazole radical can also bind to metals with square planar geometries. Although these particular ligands were designed with the capacity to assemble into anionic coordination polymers due to a limited understanding of the molecular magnetism, these studies have yet to be undertaken, but will undoubtedly be the focus of further investigation.

A series of oligopyridine verdazyl diradicals have shown that increasing the distance of the oligopyridine spacer between the verdazyls helps to stabilize the diradical species. However, these oligopyridine based diradicals are not generally stable to coordination as complete degradation of the verdazyl ring occurs.

6.2.1 Future work

While the pyrrole verdazyls and oligopyridine diradicals do appear to be effective ligands, there are still several variants that need to be explored. Of these experiments, Cu(II) metal centres have yet to be effectively used in coordination complexes. Although octahedral copper (II) complexes are known to distort tetragonally, based on orbital orthogonality relationships a copper(II)-verdazyl exchange is expected to be ferromagnetic.

Another potentially useful endeavor is to investigate new radical substituents that are potentially less electron withdrawing, but still able to chelate and/or bridge metal ions. One particular ligand, **6.1**, is topologically equivalent to a pyrimidine-substituted verdazyl.

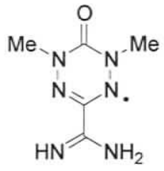

6.1

6.3 Discrete metallosupramolecular structures

The objective of chapter 3 was to synthesize a series of polypyridyl verdazyl ligands that possess the topology necessary to form 2 × 2 metallosupramolecular grids. Diradical **3.8** possesses the desired topology to form 2 × 2 grids and was successfully prepared using a 10-step synthesis. Unfortunately it was not effective at coordinating to metal ions. IR and UV-Vis experiments suggest that **3.8** may decompose before metal-radical assemblies can form.

A series of experiments were undertaken to prepare a new class of N1, N5-symmetrically substituted verdazyl radicals. Despite the synthetic challenges these are attractive targets in grid design because a verdazyl radical bridging metal ions would likely result in strong ferromagnetic interactions between each of the grid metal ions. Unfortunately attempts to form novel verdazyls failed, owing generally to the nucleophilic nature of the pyridyl ring.

6.3.1 Future work

If the nucleophilicity of the pyridine is responsible for the premature ring closure observed in chapter 3, then a simple way of protecting this group is by chelating it to a metal ion. One potential sequence could involve lithium as the chelating ion (Scheme 6.1). By deprotonating the hydrazine, a more nucleophilic nitrogen is generated and the other lone pairs (hydrazine and pyridine) are protected via chelation.

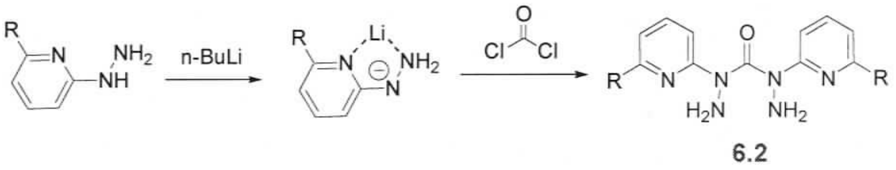

Scheme 6.1 - Proposed synthetic scheme to N1,N5-pyridyl-substituted verdazyls

Although oligopyridines would be the first choice for ligand design because of their rigid nature, hydrazone ligands also show potential for grid synthesis. Although **6.3** and **6.4** would be challenging synthetic targets, they do possess the topology needed to form 2 × 2 grids.

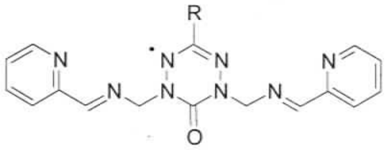

6.3

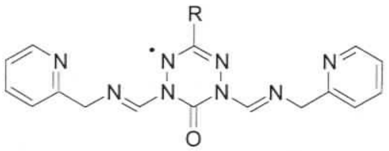

6.4

6.4 Metallocene-based verdazyls

Metal-verdazyl indirect interactions have been explored in a series of ferrocenyl verdazyls. Not surprisingly, the ferrocene monoverdazyls magnetic interactions in the solid state were not particularly strong, as the only mechanism for exchange is through-space.

The ferrocenyl bis-verdazyl showed some rather interesting magnetic behaviour. In the solid state the radical is a π-dimer with strong antiferromagnetic exchange that appears to be essentially diamagnetic. However, in solutio, the freely rotating diradicals exhibit the properties of weakly coupled diradicals.

By substituting the verdazyl with a second electroactive group it was also possible to explore the electronic properties of ferrocenyl verdazyls. Electrochemical investigations showed that the verdazyl could be oxidized reversibly; this was not observed for oligopyridine substituted verdazyls. This effect of adding an electron donor to the verdazyl ring seemed to stabilize the verdazyl and verdazyl diradical systems. Even in solution the ferrocene radicals did not appear to appreciably decompose under ambient conditions.

Valence tautomerism of ferrocenyl verdazyls was investigated using Mössbauer spectroscopy, but was not observed in this system. However, in solution the presence of low energy charge transfer bands suggest that methylation of the ferrocenyl moiety can tune the relative energies between the ground and excited states. Electrochemically methylation was observed to have similar effects on both the ferrocene and verdazyl electrophores.

6.4.1 Future work

A notable feature of the ferrocenyl verdazyl series in chapter 4 is that the potential window between the verdazyl and ferrocene oxidations ($|E_{Fc}-E_{Vd}|$) increases as a function of increased methylation. As a result of increased methylation it should be easier to selectively chemically oxidize the ferrocene moiety to a ferrocenium cation. Ferrocenium verdazyls should have distinctly different properties, and allow for further investigation into the intramolecular electronic and magnetic communication between metallocene and radical.

While ferrocenyl verdazyls do not exhibit reversible reductive behaviour, they do appear to be much more suitable to the oxidative mode. Therefore with this in mind, perhaps other metallocene based compounds could be investigated for their valence tautomeric phenomena. One example that may exhibit valence tautomerism is **6.5**, where the oxidation state of the iron in the ferrocenyl unit is Fe^{2+}.

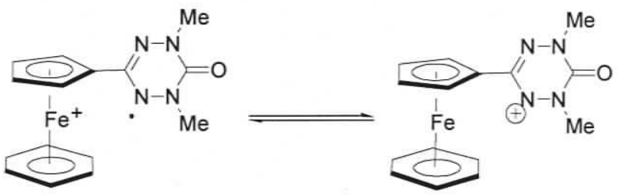

6.5

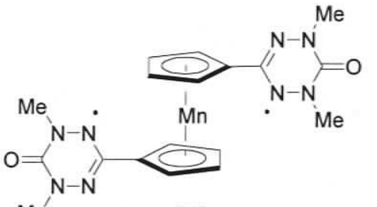

6.6

Another interesting feature of **6.6** is that the metallocenes has a paramagnetic metal ion. Therefore the magnetic interactions between the radical and metal may be potentially explored. Furthermore, the presence of a paramagnetic metal centre may also result in strongly coupled radicals.

6.5 Other possibilities for verdazyls

Current research in the Hicks laboratory is focused on the preparation of new radicals in which the N1 and N5 positions are substituted (**6.7,** R1 = alkyl or aromatic).

This will most likely be achieved by using a variety of alkyl and aromatic hydrazines. These new verdazyls will undoubtedly have more varied stabilities and electronic properties owing, to electronics and sterics of the different substituents.

From an electronic interest, bridging verdazyls may be able to strongly couple electronic transitions between mixed valent metal species. An example of this is **6.8** where a verdazyl bridge links mixed valent ruthenium ions. This Creutz-Taube type of system may exhibit enhanced charge transfer between the metal ions, due to the paramagnetic nature of the bridge.

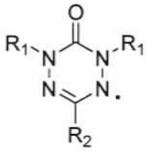

6.7

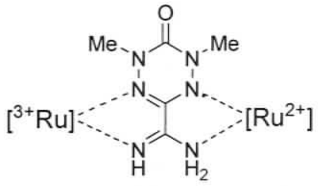

6.8

Owing to the success of the verdazyl in coordination chemistry and the recently developed understanding of the electroactive nature of this radical family, it is likely that more exotic applications may be explored in the realm of metal-verdazyl assemblies. These new metal-verdazyl radical assemblies may exhibit both unique magnetic and electronic properties.

Bibliography

1. Coronado, E.; Delhaes, P.; Gatteschi, D.; Miller, J. S., *Molecular Magnetism : From Molecular Assemblies to the Devices*. Kluwer Academic: Dordrecht, **1995**.

2. Itoh, K.; Kinoshita, M., *Molecular Magnetism: New Magnetic Materials*. Kodansha: Tokyo, **2000**.

3. Kahn, O., *Molecular Magnetism*. Wiley-VCH: New York, **1993**; p 1-380.

4. Lahti, P. M., *Magnetic Properties of Organic Materials*. Marcel Dekker Inc.: New York, **1999**.

5 Miller, J. S.; Epstein, A. J., *Angew. Chem.-Int. Edit.* **1994**, 33, 385-415.

6. Pilawa, B., *Ann. Phys.-Berlin* **1999**, 8, 191-254.

7. Coronado, E.; Gimenez-Lopez, M. C.; Levchenko, G.; Romero, F. M.; Garcia-Baonza, V.; Milner, A.; Paz-Pasternak, M., *J. Am. Chem. Soc.* **2005**, 127, 4580-4581.

8. Hendrickson, D. N.; Pierpont, C. G. In *Spin Crossover In Transition Metal Compounds* **2004**; Vol. 234, p 63-95.

9. Kou, H. Z.; Zhou, B. C.; Liao, D. Z.; Wang, R. J.; Li, Y. D., *Inorg. Chem.* **2002**, 41, 6887-6891.

10. Smith, J. A.; Galan-Mascaros, J. R.; Clerac, R.; Sun, J. S.; Xiang, O. Y.; Dunbar, K. R., *Polyhedron* **2001**, 20, 1727-1734.

11. Ohba, M.; Okawa, H., *Coord. Chem. Rev.* **2000**, 198, 313-328.

12. Verdaguer, M.; Bleuzen, A.; Marvaud, V.; Vaissermann, J.; Seuleiman, M.; Desplanches, C.; Scuiller, A.; Train, C.; Garde, R.; Gelly, G.; Lomenech, C.; Rosenman, I.; Veillet, P.; Cartier, C.; Villain, F., *Coord. Chem. Rev.* **1999**, 192, 1023-1047.

13. Sato, O.; Einaga, Y.; Fujishima, A.; Hashimoto, K., *Inorg. Chem.* **1999**, 38, 4405-4412.

14. Entley, W. R.; Girolami, G. S., *Science* **1995**, 268, 397-400.

15. Ferlay, S.; Mallah, T.; Ouahes, R.; Veillet, P.; Verdaguer, M., *Nature* **1995**, 378, 701-703.

16. Verdaguer, M., *Science* **1996**, 272, 698-699.

17. Sato, O.; Iyoda, T.; Fujishima, A.; Hashimoto, K., *Science* **1996**, 272, 704-705.

18. Mallah, T.; Thiebaut, S.; Verdaguer, M.; Veillet, P., *Science* **1993**, 262, 1554-1557.

19. Sato, O., *Acc. Chem. Res.* **2003**, 36, 692-700.

20. Rajca, A., *Chem. Rev.* **1994**, 94, 871-893.

21. Caneschi, A.; Gatteschi, D.; Sessoli, R.; Rey, P., *Acc. Chem. Res.* **1989**, 22, 392-398.

22. Ward, M. D.; McCleverty, J. A., *J. Chem. Soc.-Dalton Trans.* **2002**, 275-288.

23. Evangelio, E.; Ruiz-Molina, D., *Eur. J. Inorg. Chem.* **2005**, 2957-2971.

24. Wasielewski, M. R., *Chem. Rev.* **1992**, 92, 435-461.

25. Tom, G. M.; Creutz, C.; Taube, H., *J. Am. Chem. Soc.* **1974**, 96, 7827-7829.

26. Creutz, C.; Taube, H., *J. Am. Chem. Soc.* **1973**, 95, 1086-1094.

27. Creutz, C.; Taube, H., *J. Am. Chem. Soc.* **1969**, 91, 3988-3989.

28. Ford, P.; Rudd, D. F. P.; Gaunder, R.; Taube, H., *J. Am. Chem. Soc.* **1968**, 90, 1187-1194.

29. Launay, J. P., *Chem. Soc. Rev.* **2001**, 30, 386-397.

30. Juris, A.; Balzani, V.; Barigelletti, F.; Campagna, S.; Belser, P.; Vonzelewsky, A., *Coord. Chem. Rev.* **1988**, 84, 85-277.

31. Ray, K.; Bill, E.; Weyhermuller, T.; Wieghardt, K., *J. Am. Chem. Soc.* **2005**, 127, 5641-5654.

32. Chun, H.; Verani, C. N.; Chaudhuri, P.; Bothe, E.; Bill, E.; Weyhermuller, T.; Wieghardt, K., *Inorg. Chem.* **2001**, 40, 4157-4166.

33. Chun, H.; Weyhermuller, T.; Bill, E.; Wieghardt, K., *Angew. Chem.-Int. Edit.* **2001**, 40, 2489-2492.

34. Chaudhuri, P.; Verani, C. N.; Bill, E.; Bothe, E.; Weyhermuller, T.; Wieghardt, K., *J. Am. Chem. Soc.* **2001**, 123, 2213-2223.

35. Ziessel, R.; Hissler, M.; El-Ghayoury, A.; Harriman, A., *Coord. Chem. Rev.* **1998**, 180, 1251-1298.

36. Gomberg, M., *J. Am. Chem. Soc.* **1900**, 22, 757-771.

37. Kaim, W.; Moscherosch, M., *Coord. Chem. Rev.* **1994**, 129, 157-193.

38. Miller, J. S.; Epstein, A. J.; Reiff, W. M., *Science* **1988**, 240, 40-47.

39. Miller, J. S.; Epstein, A. J.; Reiff, W. M., *Acc. Chem. Res.* **1988**, 21, 114-120.

40. Miller, J. S.; Epstein, A. J.; Reiff, W. M., *Chem. Rev.* **1988**, 88, 201-220.

41. Miller, J. S.; Calabrese, J. C.; Rommelmann, H.; Chittipeddi, S. R.; Zhang, J. H.; Reiff, W. M.; Epstein, A. J., *J. Am. Chem. Soc.* **1987**, 109, 769-781.

42. Kollmar, C.; Kahn, O., *Acc. Chem. Res.* **1993**, 26, 259-265.

43. Kollmar, C.; Couty, M.; Kahn, O., *J. Am. Chem. Soc.* **1991**, 113, 7994-8005.

44. Manriquez, J. M.; Yee, G. T.; McLean, R. S.; Epstein, A. J.; Miller, J. S., *Science* **1991**, 252, 1415-1417.

45. Miller, J. S.; Epstein, A. J., *Chem. Commun.* **1998**, 1319-1325.

46. Zhao, H.; Heintz, R. A.; Ouyang, X.; Dunbar, K. R.; Campana, C. F.; Rogers, R. D., *Chem. Mat.* **1999**, 11, 736-746.

47. Zhao, H. H.; Heintz, R. A.; Dunbar, K. R.; Rogers, R. D., *J. Am. Chem. Soc.* **1996**, 118, 12844-12845.

48. Rittenberg, D. K.; Baars-Hibbe, L.; Bohm, A.; Miller, J. S., *J. Mater. Chem.* **2000**, 10, 241-244.

49. Sugiura, K.; Arif, A. M.; Rittenberg, D. K.; Schweizer, J.; Ohrstrom, L.; Epstein, A. J.; Miller, J. S., *Chem.-Eur. J.* **1997**, 3, 138-142.

50. Sugiura, K.; Mikami, S.; Johnson, M. T.; Miller, J. S.; Iwasaki, K.; Umishita, K.; Hino, S.; Sakata, Y., *Chem. Lett.* **1999**, 925-926.

51. Kaim, W., *Coord. Chem. Rev.* **1987**, 76, 187-235.

52. Richardson, P. F.; Kreilick, R. W., *J. Am. Chem. Soc.* **1977**, 99, 8183-8187.

53. Luneau, D.; Risoan, G.; Rey, P.; Grand, A.; Caneschi, A.; Gatteschi, D.; Laugier, J., *Inorg. Chem.* **1993**, 32, 5616-5622.

54. Caneschi, A.; Gatteschi, D.; Grand, A.; Laugier, J.; Pardi, L.; Rey, P., *Inorg. Chem.* **1988**, 27, 1031-1035.

55. Luneau, D.; Rey, P., *Coord. Chem. Rev.* **2005**, 249, 2591-2611.

56. Fegy, K.; Sanz, N.; Luneau, D.; Belorizky, E.; Rey, P., *Inorg. Chem.* **1998**, 37, 4518-4523.

57. Lescop, C.; Luneau, D.; Rey, P.; Bussiere, G.; Reber, C., *Inorg. Chem.* **2002**, 41, 5566-5574.

58. Lescop, C.; Belorizky, E.; Luneau, D.; Rey, P., *Inorg. Chem.* **2002**, 41, 3375-3384.

59. Lescop, C.; Luneau, D.; Belorizky, E.; Fries, P.; Guillot, M.; Rey, P., *Inorg. Chem.* **1999**, 38, 5472-5473.

60. Fegy, K.; Luneau, D.; Belorizky, E.; Novac, M.; Tholence, J. L.; Paulsen, C.; Ohm, T.; Rey, P., *Inorg. Chem.* **1998**, 37, 4524-4532.

61. Fegy, K.; Luneau, D.; Ohm, T.; Paulsen, C.; Rey, P., *Angew. Chem.-Int. Edit.* **1998**, 37, 1270-1273.

62. Inoue, K.; Iwahori, F.; Markosyan, A. S.; Iwamura, H., *Coord. Chem. Rev.* **2000**, 198, 219-229.

63. Iwamura, H.; Inoue, K.; Hayamizu, T., *Pure Appl. Chem.* **1996**, 68, 243-252.

64. Inoue, K.; Hayamizu, T.; Iwamura, H.; Hashizume, D.; Ohashi, Y., *J. Am. Chem. Soc.* **1996**, 118, 1803-1804.

65. Caneschi, A.; Ferraro, F.; Gatteschi, D.; Rey, P.; Sessoli, R., *Inorg. Chem.* **1990**, 29, 1756-1760.

66. Caneschi, A.; Ferraro, F.; Gatteschi, D.; Rey, P.; Sessoli, R., *Inorg. Chem.* **1990**, 29, 4217-4223.

67. Stroh, C.; Turek, P.; Rabu, P.; Ziessel, R., *Inorg. Chem.* **2001**, 40, 5334-5342.

68. Min, K. S.; Weyhermuller, T.; Bothe, E.; Wieghardt, K., *Inorg. Chem.* **2004**, 43, 2922-2931.

69. Ross, S.; Weyhermuller, T.; Bill, E.; Bothe, E.; Florke, U.; Wieghardt, K.; Chaudhuri, P., *Eur. J. Inorg. Chem.* **2004**, 984-997.

70. Herebian, D.; Bothe, E.; Neese, F.; Weyhermuller, T.; Wieghardt, K., *J. Am. Chem. Soc.* **2003**, 125, 9116-9128.

71. Ghosh, P.; Begum, A.; Herebian, D.; Bothe, E.; Hildenbrand, K.; Weyhermuller, T.; Wieghardt, K., *Angew. Chem.-Int. Edit.* **2003**, 42, 563-567.

72. Chun, H. P.; Chaudhuri, P.; Weyhermuller, T.; Wieghardt, K., *Inorg. Chem.* **2002**, 41, 790-795.

73. Herebian, D.; Bothe, E.; Bill, E.; Weyhermuller, T.; Wieghardt, K., *J. Am. Chem. Soc.* **2001**, 123, 10012-10023.

74. Pierpont, C. G., *Coord. Chem. Rev.* **2001**, 219, 415-433.

75. Pierpont, C. G., *Coord. Chem. Rev.* **2001**, 216, 99-125.

76. Kahn, O.; Prins, R.; Reedijk, J.; Thompson, J. S., *Inorg. Chem.* **1987**, 26, 3557-3561.

77. Benelli, C.; Dei, A.; Gatteschi, D.; Pardi, L., *Inorg. Chem.* **1988**, 27, 2831-2836.

78. Caneschi, A.; Dei, A.; Mussari, C. P.; Shultz, D. A.; Sorace, L.; Vostrikova, K. E., *Inorg. Chem.* **2002**, 41, 1086-1092.

79. Caneschi, A.; Dei, A.; Lee, H.; Shultz, D. A.; Sorace, L., *Inorg. Chem.* **2001**, 40, 408-411.

80. Shultz, D. A.; Fico, R. M.; Bodnar, S. H.; Kumar, R. K.; Vostrikova, K. E.; Kampf, J. W.; Boyle, P. D., *J. Am. Chem. Soc.* **2003**, 125, 11761-11771.

81. Hicks, R. G., *Aust. J. Chem.* **2001**, 54, 597-600.

82. Koivisto, B. D.; Hicks, R. G., *Coord. Chem. Rev.* **2005**, 249, 2612-2630.

83. Brook, D. J. R.; Lynch, V.; Conklin, B.; Fox, M. A., *J. Am. Chem. Soc.* **1997**, 119, 5155-5162.

84. Kaim, W., *Coord. Chem. Rev.* **2002**, 230, 127-139.

85. Polumbrik, O. M., *Russian Chem. Rev.* **1978**, 47, 767-785.

86. Neugebauer, F. A., *Angew. Chem.-Int. Edit.* **1973**, 12, 455-464.

87. Lemaire, M. T., *Pure Appl. Chem.* **2004**, 76, 277-293.

88. Kuhn, R.; Trischmann, H., *Angew. Chem.-Int. Edit.* **1963**, 2, 155.

89. Nesterenko, A. M.; Polumbrik, O. M.; Markovskii, L. N., *J. Struct. Chem.* **1981**, 22, 481-485.

90. Neugebauer, F. A.; Fischer, H., *Angew. Chem.-Int. Edit.* **1980**, 19, 724-725.

91. Neugebauer, F. A.; Fischer, H.; Siegel, R., *Chem. Ber.-Recl.* **1988**, 121, 815-822.

92. Buryak, N. I.; Polumbrik, O. M.; Yasnikov, A. A., *Ukr. Khim. Zh.* **1985**, 51, 1111-1112.

93. Barclay, T. M.; Hicks, R. G.; Ichimura, A. S.; Patenaude, G. W., *Can. J. Chem.* **2002**, 80, 1501-1506.

94. Hicks, R. G.; Hooper, R., *Inorg. Chem.* **1999**, 38, 284-286.

95. Hicks, R. G.; Ohrstrom, L.; Patenaude, G. W., *Inorg. Chem.* **2001**, 40, 1865-1870.

96. Kornuta, P. P.; Bobkov, V. N.; Polumbrik, O. M.; Markovskii, L. N., *Zh. Obshch. Khim.* **1978**, 48, 697-698.

97. Nesterenko, A. M.; Polumbrik, O. M.; Markovskii, L. N., *J. Struct. Chem.* **1984**, 25, 209-214.

98. Hicks, R. G.; Koivisto, B. D.; Lemaire, M. T., *Org. Lett.* **2004**, 6, 1887-1890.

99. Neugebauer, F. A.; Bernhardt, R.; Fischer, H., *Chem. Ber.-Recl.* **1977**, 110, 2254-2275.

100. Neugebauer, F. A.; Fischer, H., *J. Chem. Soc.-Perkin Trans. 2* **1981**, 896-900.

101. Neugebauer, F. A.; Fischer, H.; Meier, P., *Chem. Ber.-Recl.* **1980**, 113, 2049-2051.

102. Fico, R. M.; Hay, M. F.; Reese, S.; Hammond, S.; Lambert, E.; Fox, M. A., *J. Org. Chem.* **1999**, 64, 9386-9392.

103. Elwahy, A. H. M.; Abbas, A. A.; Ibrahim, Y. A., *J. Chem. Res.* **1998**, 184-185A.

104. Brook, D. J. R.; Fox, H. H.; Lynch, V.; Fox, M. A., *J. Phys. Chem.* **1996**, 100, 2066-2071.

105. Lang, A.; Naarmann, H.; Rosler, G.; Gotschy, B.; Winter, H.; Dormann, E., *Mol. Phys.* **1993**, 79, 1051-1062.

106. Kothe, G.; Neugebauer, F. A.; Zimmermamm, H., *Angew. Chem.-Int. Edit.* **1972**, 11, 830-832.

107. Neugebauer, F. A.; Fischer, H.; Bernhardt, R., *Chem. Ber.-Recl.* **1976**, 109, 2389-2394.

108. Kurusu, Y.; Yoshida, H.; Okawara, M., *Tetrahedron Lett.* **1967**, 3595-3597.

109. Kamachi, M.; Enomoto, H.; Shibasaka, M.; Mori, W.; Kishita, M., *Polym. J.* **1986**, 18, 439-441.

110. Miura, Y.; Makita, N.; Kinoshit.M, *J. Macromol. Sci.-Chem.* **1973**, A 7, 1007-1012.

111. Neugebauer, F. A.; Trischmann, H., *J. Polymer. Sci. B.-Polym. Lett.* **1968**, 6, 255-256.

112. Neugebauer, F. A.; Fischer, H.; Krieger, C., *J. Chem. Soc.-Perkin Trans. 2* **1993**, 535-544.

113. Williams, D. E., *Acta Crystallogr. Sect. B.* **1973**, B 29, 96-102.

114. Polumbrik, O. M.; Nesterenko, A. M.; Markovskii, L. N., *J. Struct. Chem.* **1979**, 20, 487-490.

115. Fischer, P. H. H., *Tetrahedron* **1967**, 23, 1939-1952.

116. Degtyarev, L. S.; Stetsenko, A. A.; Gorlov, Y. I., *Chem. Phys. Lett.* **1980**, 69, 323-326.

117. Podenko, L. S.; Chirkov, A. K.; Shchipanov, V. P., *Zh. Strukt. Khimii* **1980**, 21, 559-564.

118. Podenko, L. S.; Chirkov, A. K.; Petroshen, V. E.; Shchipanov, V. P., *J. Struct. Chem.* **1981**, 22, 667-670.

119. Degtyarev, L. S.; Gorlov, Y. I., *J. Struct. Chem.* **1975**, 16, 715-718.

120. Neugebauer, F., A., *Mon. Chem.* **1967**, 98, 231-244.

121. Dalal, N. S.; Smirnov, A. I.; Smirnova, T. I.; Belford, R. L.; Katritzky, A. R.; Belyakov, S. A., *J. Phys. Chem. B* **1997**, 101, 11249-11253.

122. Mukai, K.; Yamamoto, T.; Kohno, M.; Azuma, N.; Ishizu, K., *Bull. Chem. Soc. Jpn.* **1974**, 47, 1797-1798.

123. Mukai, K.; Shikata, H.; Azuma, N.; Kuwata, K., *J. Magn. Reson.* **1979**, 35, 133-137.

124. Glazer, R. L.; Poindexter, E. H., *J. Chem. Phys.* **1971**, 55, 4548-4553.

125. Neugebauer, F. A., *Tetrahedron* **1970**, 26, 4853-4857.

126. Neugebauer, F. A.; Brunner, H., *Tetrahedron* **1974**, 30, 2841-2850.

127. Neugebauer, F. A.; Trischmann, H.; Taigel, G., *Mon. Chem.* **1967**, 98, 713-&.

128. Brunner, H.; Hausser, K. H.; Neugebauer, F. A., *Tetrahedron* **1971**, 27, 3611-&.

129. Neugebauer, F. A.; Brunner, H.; Hausser, K. H., *Tetrahedron* **1971**, 27, 3623-&.

130. Nakatsuji, S.; Kitamura, A.; Takai, A.; Nishikawa, K.; Morimoto, Y.; Yasuoka, N.; Kawamura, H.; Anzai, H., *Z. Naturforsch. B.* **1998**, 53, 495-502.

131. Barr, C. L.; Chase, P. A.; Hicks, R. G.; Lemaire, M. T.; Stevens, C. L., *J. Org. Chem.* **1999**, 64, 8893-8897.

132. Degtyarev, L. S., *Teor. Eksp. Khimiya* **1987**, 23, 86-91.

133. Polumbrik, O. M.; Vasilkevich, N. G.; Kalinin, V. N., *Ukr. Khim. Zh.* **1976**, 42, 724-726.

134. Jaworski, J. S., *J. Electroanal. Chem.* **1991**, 300, 167-174.

135. Jaworski, J. S.; Krawczyk, I., *Mon. Chem.* **1992**, 123, 43-50.

136. Samarskaya, T. G.; Ganyuk, L. N.; Ogenko, V. M., *Mendeleev Commun.* **1994**, 19-20.

137. Chung, G.; Lee, D., *Chem. Phys. Lett.* **2001**, 350, 339-344.

138. Barone, V.; Bencini, A.; Ciofini, I.; Daul, C., *J. Phys. Chem. A* **1999**, 103, 4275-4282.

139. Lahti, P. M.; Esat, B.; Liao, Y.; Serwinski, P.; Lan, J.; Walton, R., *Polyhedron* **2001**, 20, 1647-1652.

140. Teki, Y.; Nakatsuji, M.; Miura, Y., *Int. J. Mod. Phys. B* **2001**, 15, 4029-4031.

141. Teki, Y.; Nakatsuji, M.; Miura, Y., *Mol. Phys.* **2002**, 100, 1385-1394.

142. Teki, Y.; Kimura, M.; Narimatsu, S.; Ohara, K.; Mukai, K., *Bull. Chem. Soc. Jpn.* **2004**, 77, 95-99.

143. Brook, D. J. R.; Fornell, S.; Noll, B.; Yee, G. T.; Koch, T. H., *J. Chem. Soc.-Dalton Trans.* **2000**, 2019-2022.

144. Brook, D. J. R.; Fornell, S.; Stevens, J. E.; Noll, B.; Koch, T. H.; Eisfeld, W., *Inorg. Chem.* **2000**, 39, 562-567.

145. Barclay, T. M.; Hicks, R. G.; Lemaire, M. T.; Thompson, L. K., *Inorg. Chem.* **2001**, 40, 6521-6524.

146. Brook, D. J. R.; Abeyta, V., *J. Chem. Soc.-Dalton Trans.* **2002**, 4219-4223.

147. Wu, J. Z.; Bouwman, E.; Reedijk, J.; Mills, A. M.; Spek, A. L., *Inorg. Chim. Acta* **2003**, 351, 326-330.

148. Hicks, R. G.; Lemaire, M. T.; Thompson, L. K.; Barclay, T. M., *J. Am. Chem. Soc.* **2000**, 122, 8077-8078.

149. Lemaire, M. T. Synthesis and Coordination Chemistry of Chelating Verdazyl Radicals. Doctoral Thesis, University of Victoria, Victoria, BC, Canada, **2002**.

150. Barclay, T. M.; Hicks, R. G.; Lemaire, M. T.; Thompson, L. K., *Chem. Commun.* **2000**, 2141-2142.

151. Barclay, T. M.; Hicks, R. G.; Lemaire, M. T.; Thompson, L. K., *Inorg. Chem.* **2003**, 42, 2261-2267.

152. Cai, D. W.; Hughes, D. L.; Verhoeven, T. R., *Tetrahedron Lett.* **1996**, 37, 2537-2540.

153. Gilman, H.; Spatz, S. M., *J. Org. Chem.* **1951**, 16, 1485.

154. Parks, J. E.; Wagner, B. E.; Holm, R. H., *Inorg. Chem.* **1971**, 10, 2472-2478.

155. Parks, J. E.; Wagner, B. E.; Holm, R. H., *J. Organometallic Chem.* **1973**, 56, 53-66.

156. Peterson, M. A.; Mitchell, J. R., *J. Org. Chem.* **1997**, 62, 8237-8239.

157. Mukkala, V.-M.; Sund, C.; Kwiatkowski, M.; Pasanen, P.; Hogberg, M.; Kankare, J.; Takalo, H., *Helv. Chim. Acta* **1992**, 75, 1621-1632.

158. Negishi, E. I., *Acc. Chem. Res.* **1982**, 15, 340-348.

159. Fang, Y. Q.; Hanan, G. S., *Synlett* **2003**, 852-854.

160. Fang, Y. G.; Polson, M. I. J.; Hanan, G. S., *Inorg. Chem.* **2003**, 42, 5-7.

161. Loren, J. C.; Siegel, J. S., *Angew. Chem.-Int. Edit.* **2001**, 40, 754-757.

162. El-ghayoury, A.; Ziessel, R., *Tetrahedron Lett.* **1998**, 39, 4473-4476.

163. El-Ghayouy, A.; Harriman, A.; De Cian, A.; Fischer, J.; Ziessel, R., *J. Am. Chem. Soc.* **1998**, 120, 9973-9974.

164. Balogh, V.; Golfier, M.; Fetizon, M., *J. Org. Chem.* **1971**, 36, 1339-1341.

165. Neugebauer, F. A.; Brunner, H.; Hausser, K. H., *Tetrahedron* **1971**, 27, 3623-3628.

166. Stroh, C.; Ziessel, R., *Tetrahedron Lett.* **1999**, 40, 4543-4546.

167. Hicks, R. G.; Lemaire, M. T.; Ohrstrom, L.; Richardson, J. F.; Thompson, L. K.; Xu, Z. Q., *J. Am. Chem. Soc.* **2001**, 123, 7154-7159.

168. El-ghayoury, A.; Ziessel, R., *J. Org. Chem.* **2000**, 65, 7757-7763.

169. Morgan, G.; Burstall, F. H., *J. Chem. Soc.* **1937**, 1649-1655.

170. Karkalic, R.; Bugarcic, Z. D., *Mon. Chem.* **2000**, 131, 819-824.

171. Breuning, E.; Ziener, U.; Lehn, J. M.; Wegelius, E.; Rissanen, K., *Eur. J. Inorg. Chem.* **2001**, 1515-1521.

172. Baxter, P. N. W.; Lehn, J. M.; Baum, G.; Fenske, D., *Chem.-Eur. J.* **1999**, 5, 102-112.

173. Brunet, P.; Simard, M.; Wuest, J. D., *J. Am. Chem. Soc.* **1997**, 119, 2737-2738.

174. Leininger, S.; Olenyuk, B.; Stang, P. J., *Chem. Rev.* **2000**, 100, 853-907.

175. Bassani, D. M.; Lehn, J. M.; Fromm, K.; Fenske, D., *Angew. Chem.-Int. Edit.* **1998**, 37, 2364-2367.

176. Lehn, J.-M., *Supramolecular Chemistry - Concepts and Perspectives*. VHC: Weinheim, **1995**.

177. Manna, J.; Kuehl, C. J.; Whiteford, J. A.; Stang, P. J.; Muddiman, D. C.; Hofstadler, S. A.; Smith, R. D., *J. Am. Chem. Soc.* **1997**, 119, 11611-11619.

178. Muller, C.; Whiteford, J. A.; Stang, P. J., *J. Am. Chem. Soc.* **1998**, 120, 9827-9837.

179. Fan, J.; Whiteford, J. A.; Olenyuk, B.; Levin, M. D.; Stang, P. J.; Fleischer, E. B., *J. Am. Chem. Soc.* **1999**, 121, 2741-2752.

180. Kuehl, C. J.; Huang, S. D.; Stang, P. J., *J. Am. Chem. Soc.* **2001**, 123, 9634-9641.

181. Leininger, S.; Schmitz, M.; Stang, P. J., *Org. Lett.* **1999**, 1, 1921-1923.

182. Schweiger, M.; Seidel, S. R.; Arif, A. M.; Stang, P. J., *Angew. Chem.-Int. Edit.* **2001**, 40, 3467-+.

183. Schweiger, M.; Seidel, S. R.; Arif, A. M.; Stang, P. J., *Inorg. Chem.* **2002**, 41, 2556-2559.

184. Kaim, W.; Schwederski, B.; Dogan, A.; Fiedler, J.; Kuehl, C. J.; Stang, P. J., *Inorg. Chem.* **2002**, 41, 4025-4028.

185. Campbell, K.; Kuehl, C. J.; Ferguson, M. J.; Stang, P. J.; Tykwinski, R. R., *J. Am. Chem. Soc.* **2002**, 124, 7266-7267.

186. Barbour, L. J.; Orr, G. W.; Atwood, J. L., *Nature* **1998**, 393, 671-673.

187. Olenyuk, B.; Whiteford, J. A.; Fechtenkotter, A.; Stang, P. J., *Nature* **1999**, 398, 796-799.

188. Levin, M. D.; Stang, P. J., *J. Am. Chem. Soc.* **2000**, 122, 7428-7429.

189. Radhakrishnan, U.; Schweiger, M.; Stang, P. J., *Org. Lett.* **2001**, 3, 3141-3143.

190. Fujita, M.; Yu, S. Y.; Kusukawa, T.; Funaki, H.; Ogura, K.; Yamaguchi, K., *Angew. Chem.-Int. Edit.* **1998**, 37, 2082-2085.

191. Chand, D. K.; Biradha, K.; Fujita, M., *Chem. Commun.* **2001**, 1652-1653.

192. Yamanoi, Y.; Sakamoto, Y.; Kusukawa, T.; Fujita, M.; Sakamoto, S.; Yamaguchi, K., *J. Am. Chem. Soc.* **2001**, 123, 980-981.

193. Garcia, A. M.; Bassani, D. M.; Lehn, J. M.; Baum, G.; Fenske, D., *Chem.-Eur. J.* **1999**, 5, 1234-1238.

194. Fujita, M.; Sasaki, O.; Watanabe, K. Y.; Ogura, K.; Yamaguchi, K., *New J. Chem.* **1998**, 22, 189-191.

195. Rojo, J.; Romero-Salguero, F. J.; Lehn, J. M.; Baum, G.; Fenske, D., *Eur. J. Inorg. Chem.* **1999**, 1421-1428.

196. Rojo, J.; Lehn, J. M.; Baum, G.; Fenske, D.; Waldmann, O.; Muller, P., *Eur. J. Inorg. Chem.* **1999**, 517-522.

197. Garcia, A. M.; Romero-Salguero, F. J.; Bassani, D. M.; Lehn, J. M.; Baum, G.; Fenske, D., *Chem.-Eur. J.* **1999**, 5, 1803-1808.

198. Breuning, E.; Ruben, M.; Lehn, J. M.; Renz, F.; Garcia, Y.; Ksenofontov, V.; Gutlich, P.; Wegelius, E.; Rissanen, K., *Angew. Chem.-Int. Edit.* **2000**, 39, 2504-2507.

199. Ruben, M.; Breuning, E.; Gisselbrecht, J. P.; Lehn, J. M., *Angew. Chem.-Int. Edit.* **2000**, 39, 4139-4142.

200. Baxter, P. N. W.; Lehn, J. M.; Baum, G.; Fenske, D., *Chem.-Eur. J.* **2000**, 6, 4510-4517.

201. Marquis, A.; Kintzinger, J. P.; Graff, R.; Baxter, P. N. W.; Lehn, J. M., *Angew. Chem.-Int. Edit.* **2002**, 41, 2760-2764.

202. Breuning, E.; Hanan, G. S.; Romero-Salguero, F. J.; Garcia, A. M.; Baxter, P. N. W.; Lehn, J. M.; Wegelius, E.; Rissanen, K.; Nierengarten, H.; van Dorsselaer, A., *Chem.-Eur. J.* **2002**, 8, 3458-3466.

203. Fujita, M.; Fujita, N.; Ogura, K.; Yamaguchi, K., *Nature* **1999**, 400, 52-55.

204. Hori, A.; Kumazawa, K.; Kusukawa, T.; Chand, D. K.; Fujita, M.; Sakamoto, S.; Yamaguchi, K., *Chem.-Eur. J.* **2001**, 7, 4142-4149.

205. Linton, B.; Hamilton, A. D., *Chem. Rev.* **1997**, 97, 1669-1680.

206. Fujita, M., *Chem. Soc. Rev.* **1998**, 27, 417-425.

207. Youinou, M. T.; Rahmouni, N.; Fischer, J.; Osborn, J. A., *Angew. Chem.-Int. Edit.* **1992**, 31, 733-735.

208. Hanan, G. S.; Volkmer, D.; Schubert, U. S.; Lehn, J. M.; Baum, G.; Fenske, D., *Angew. Chem.-Int. Edit.* **1997**, 36, 1842-1844.

209. Siegel, J. S., Current Pursuits in Supramolecular Chemistry - **2002**.

210. Thompson, L. K.; Kelly, T. L.; Dawe, L. N.; Grove, H.; Lemaire, M. T.; Howard, J. A. K.; Spencer, E. C.; Matthews, C. J.; Onions, S. T.; Coles, S. J.; Horton, P. N.; Hursthouse, M. B.; Light, M. E., *Inorg. Chem.* **2004**, 43, 7605-7616.

211. Ruben, M.; Rojo, J.; Romero-Salguero, F. J.; Uppadine, L. H.; Lehn, J. M., *Angew. Chem.-Int. Edit.* **2004**, 43, 3644-3662.

212. Zhao, L.; Xu, Z. Q.; Grove, H.; Milway, V. A.; Dawe, L. N.; Abedin, T. S. M.; Thompson, L. K.; Kelly, T. L.; Harvey, R. G.; Miller, D. O.; Weeks, L.; Shapter, J. G.; Pope, K. J., *Inorg. Chem.* **2004**, 43, 3812-3824.

213. Milway, V. A.; Niel, V.; Abedin, T. S. M.; Xu, Z. Q.; Thompson, L. K.; Grove, H.; Miller, D. O.; Parsons, S. R., *Inorg. Chem.* **2004**, 43, 1874-1884.

214. Xu, Z. Q.; Thompson, L. K.; Milway, V. A.; Zhao, L.; Kelly, T.; Miller, D. O., *Inorg. Chem.* **2003**, 42, 2950-2959.

215. Thompson, L. K.; Zhao, L.; Xu, Z. Q.; Miller, D. O.; Reiff, W. M., *Inorg. Chem.* **2003**, 42, 128-139.

216. Thompson, L. K., *Coord. Chem. Rev.* **2002**, 233, 193-206.

217. Zhao, L.; Xu, Z. Q.; Thompson, L. K.; Miller, D. O., *Polyhedron* **2001**, 20, 1359-1364.

218. Grove, H.; Kelly, T. L.; Thompson, L. K.; Zhao, L. A.; Xu, Z. Q.; Abedin, T. S. M.; Miller, D. O.; Goeta, A. E.; Wilson, C.; Howard, J. A. K., *Inorg. Chem.* **2004**, 43, 4278-4288.

219. Milway, V. A.; Zhao, L.; Abedin, T. S. M.; Thompson, L. K.; Xu, Z. Q., *Polyhedron* **2003**, 22, 1271-1279.

220. Xu, Z. Q.; Thompson, L. K.; Miller, D. O., *J. Chem. Soc.-Dalton Trans.* **2002**, 2462-2466.

221. Xu, Z. Q.; Thompson, L. K.; Miller, D. O., *Polyhedron* **2002**, 21, 1715-1720.

222. Neubebauer, F. A., *Angew. Chem., Int. Ed. Engl.* **1973**, 12, 455-464.

223. Hanan, G. S.; Schubert, U. S.; Volkmer, D.; Riviere, E.; Lehn, J. M.; Kyritsakas, N.; Fischer, J., *Can. J. Chem.* **1997**, 75, 169-182.

224. Hanan, G. S.; Volkmer, D.; Schubert, U. S.; Lehn, J. M.; Baum, G.; Fenske, D., *Angew. Chem.-Int. Edit.* **1997**, 36, 1842-1844.

225. Barclay, T. M.; Hicks, R. G.; Lemaire, M. T.; Thompson, L. K., *Inorg. Chem.* **2001**, 40, 5581-5584.

226. Dodson, R. M.; Seyler, J. K., *J. Org. Chem.* **1951**, 16, 461-465.

227. Jones, P. D.; Glass, T. E., *Tetrahedron Lett.* **2001**, 42, 2265-2267.

228. Anctil, E. J. G.; Snieckus, V., *J. Organomet. Chem.* **2002**, 653, 150-160.

229. Green, M. T.; McCormick, T. A., *Inorg. Chem.* **1999**, 38, 3061-3065.

230. Kalinin, A. V.; Bower, J. F.; Riebel, P.; Snieckus, V., *J. Org. Chem.* **1999**, 64, 2986-2987.

231. Stefinovic, M.; Snieckus, V., *J. Org. Chem.* **1998**, 63, 2808-2809.

232. Kirchmeyer, S.; Mertens, A.; Arvanaghi, M.; Olah, G. A., *Synthesis* **1983**, 498-500.

233. Marvel, C. S.; Coleman Jr., L. E.; Scott, G. P., *J. Org. Chem.* **1955**, 20, 1785-1792.

234. Sadana, A. K.; Mirza, Y.; Aneja, K. R.; Prakash, O., *Eur. J. Med. Chem.* **2003**, 38, 533-536.

235. Lam, P. Y. S.; Vincent, G.; Clark, C. G.; Deudon, S.; Jadhav, P. K., *Tetrahedron Lett.* **2001**, 42, 3415-3418.

236. Kwong, F. Y.; Klapars, A.; Buchwald, S. L., *Org. Lett.* **2002**, 4, 581-584.

237. Yin, J. J.; Buchwald, S. L., *Org. Lett.* **2000**, 2, 1101-1104.

238. Klapars, A.; Antilla, J. C.; Huang, X. H.; Buchwald, S. L., *J. Am. Chem. Soc.* **2001**, 123, 7727-7729.

239. Klapars, A.; Huang, X. H.; Buchwald, S. L., *J. Am. Chem. Soc.* **2002**, 124, 7421-7428.

240. Shen, Q. L.; Shekhar, S.; Stambuli, J. P.; Hartwig, J. F., *Angew. Chem.-Int. Edit.* **2005**, 44, 1371-1375.

241. Kataoka, N.; Shelby, Q.; Stambuli, J. P.; Hartwig, J. F., *J. Org. Chem.* **2002**, 67, 5553-5566.

242. Wolter, M.; Klapars, A.; Buchwald, S. L., *Org. Lett.* **2001**, 3, 3803-3805.

243. Russavskaya, N. V.; Grabel'nykh, V. A.; Levanova, E. P.; Sukhomazova, E. N.; Deryagina, E. N., *Russ. J. Organ. Chem.* **2002**, 38, 1498-1500.

244. Kaszynski, P.; Young, V. G., *J. Am. Chem. Soc.* **2000**, 122, 2087-2095.

245. Hunter, D.; Neilson, D. G., *J. Chem. Soc.-Perkin Trans. 1* **1985**, 1081-1086.

246. Barrett, A. G. M.; Read, R. W.; Barton, D. H. R., *J. Chem. Soc.-Perkin Trans. 1* **1980**, 2184-2190.

247. Ko, S.; Na, Y.; Chang, S., *J. Am. Chem. Soc.* **2002**, 124, 750-751.

248. Blomquist, A. T.; Moriconi, E. J., *J. Org. Chem.* **1961**, 26, 3761-3769.

249. Erickson, J. G., *J. Am. Chem. Soc.* **1951**, 73, 1338-1339.

250. Schaefer, F. C.; Peters, G. A., *J. Org. Chem.* **1961**, 26, 412-418.

251. Shriner, R. L.; Neumann, F. W., *Chem. Rev.* **1944**, 35, 351-425.

252. Moran, D. B.; Morton, G. O.; Albright, J. D., *J. Heterocycl. Chem.* **1986**, 23, 1071-1077.

253. Wang, Q. R.; Jcchims, J. C.; Kohlbrandt, S.; Dahlenburg, L.; Altalib, M.; Hamed, A.; Ismail, A. E. H., *Synthesis* **1992**, 710-718.

254. Sullivan, B. P.; Calvert, J. M.; Meyer, T. J., *Inorg. Chem.* **1980**, 19, 1404-1407.

255. Long, N. J., *Metallocenes: An introduction to sandwich complexes*. Blackwell Science: Oxford, **1998**; p 1-285.

256. Adams, R. D., *J. Organomet. Chem.* **2001**, 637-639, 1.

257. Atkinson, R. C. J.; Gibson, V. C.; Long, N. J., *Chem. Soc. Rev.* **2004**, 33, 313-328.

258. Dai, L. X.; Tu, T.; You, S. L.; Deng, W. P.; Hou, X. L., *Acc. Chem. Res.* **2003**, 36, 659-667.

259. Bandoli, G.; Dolmella, A., *Coord. Chem. Rev.* **2000**, 209, 161-196.

260. van Staveren, D. R.; Metzler-Nolte, N., *Chem. Rev.* **2004**, 104, 5931-5985.

261. Cullen, W. R.; Woollins, J. D., *Coord. Chem. Rev.* **1981**, 39, 1-30.

262. Cowan, D. O.; Levanda, C.; Park, J.; Kaufman, F., *Acc. Chem. Res.* **1973**, 6, 1-7.

263. Floris, B.; Illuminati, G.; Jones, P. E.; Ortaggi, G., *Coord. Chem. Rev.* **1972**, 8, 39-43.

264. Togni, A.; Hayashi, T., *Ferrocenes: homogeneous catalysis, organic synthesis, materials science*. VCH: Weinheim, **1995**; p 1-540.

265. Nguyen, P.; Gomez-Elipe, P.; Manners, I., *Chem. Rev.* **1999**, 99, 1515-1548.

266. Rulkens, R.; Lough, A. J.; Manners, I., *J. Am. Chem. Soc.* **1994**, 116, 797-798.

267. Foucher, D. A.; Tang, B. Z.; Manners, I., *J. Am. Chem. Soc.* **1992**, 114, 6246-6248.

268. Barlow, S.; Ohare, D., *Chem. Rev.* **1997**, 97, 637-669.

269. Miller, J. S.; Krusic, P. J.; Dixon, D. A.; Reiff, W. M.; Zhang, J. H.; Anderson, E. C.; Epstein, A. J., *J. Am. Chem. Soc.* **1986**, 108, 4459-4466.

270. Gallucci, J. C.; Opromolla, G.; Paquette, L. A.; Pardi, L.; Schirch, P. F. T.; Sivik, M. R.; Zanello, P., *Inorg. Chem.* **1993**, 32, 2292-2297.

271. Reis, A. H.; Preston, L. D.; Williams, J. M.; Peterson, S. W.; Candela, G. A.; Swartzendruber, L. J.; Miller, J. S., *J. Am. Chem. Soc.* **1979**, 101, 2756-2758.

272. Miller, J. S.; Glatzhofer, D. T.; Vazquez, C.; McLean, R. S.; Calabrese, J. C.; Marshall, W. J.; Raebiger, J. W., *Inorg. Chem.* **2001**, 40, 2058-2064.

273. Elschenbroich, C.; Cais, M., *J. Organomet. Chem.* **1969**, 18, 135-143.

274. Nakamura, Y.; Koga, N.; Iwamura, H., *Chem. Lett.* **1991**, 69-72.

275. Okamura, T.; Takano, Y.; Yoshioka, Y.; Ueyama, N.; Nakamura, A.; Yamaguchi, K., *J. Organomet. Chem.* **1998**, 569, 177-187.

276. Jürgens, O.; Vidal-Gancedo, J.; Rovira, C.; Wurst, K.; Sporer, C.; Bildstein, B.; Schottenberger, H.; Jaitner, P.; Veciana, J., *Inorg. Chem.* **1998**, 37, 4547-4558.

277. Sporer, C.; Ruiz-Molina, D.; Wurst, K.; Kopacka, H.; Veciana, J.; Jaitner, P., *J. Organomet. Chem.* **2001**, 637, 507-513.

278. Elsner, O.; Ruiz-Molina, D.; Vidal-Gancedo, J.; Rovira, C.; Veciana, J., *Chem. Commun.* **1999**, 579-580.

279. Ratera, I.; Ruiz-Molina, D.; Renz, F.; Ensling, J.; Wurst, K.; Rovira, C.; Gutlich, P.; Veciana, J., *J. Am. Chem. Soc.* **2003**, 125, 1462-1463.

280. Xu, Z. F.; Xie, Y. M.; Feng, W. L.; Schaefer, H. F., *J. Phys. Chem. A* **2003**, 107, 2716-2729.

281. Hendrickson, D. N.; Sohn, Y. S.; Gray, H. B., *Inorg. Chem.* **1971**, 10, 1559-1563.

282. Levy, D. A.; Orgel, L. E., *Mol. Phys.* **1961**, 4, 93-94.

283. Scott, D. R.; Becker, R. S., *J. Phys. Chem.* **1965**, 69, 3207-3208.

284. Prins, R.; Van Voorst, J. D. W., *J. Chem. Phys.* **1968**, 49, 4665-4673.

285. Sohn, Y. S.; Hendrickson, D. N.; Gray, H. B., *J. Am. Chem. Soc.* **1970**, 92, 3233-3234.

286. Prins, R.; Reinders, F. J., *J. Am. Chem. Soc.* **1969**, 91, 4929-4931.

287. Ratera, I.; Ruiz-Molina, D.; Vidal-Gancedo, J.; Novoa, J. J.; Wurst, K.; Letard, J. F.; Rovira, C.; Veciana, J., *Chem.-Eur. J.* **2004**, 10, 603-616.

288. Togashi, K.; Imachi, R.; Tomioka, K.; Tsuboi, H.; Ishida, T.; Nogami, T.; Takeda, N.; Ishikawa, M., *Bull. Chem. Soc. Jpn.* **1996**, 69, 2821-2830.

289. Schmittel, M.; Langels, A., *J. Chem. Soc.-Perkin Trans. 2* **1998**, 565-571.

290. Chai, X. D.; Jiang, Y. S.; Yang, W. S.; Zhang, D.; Cao, Y. W.; Zhu, Z. J.; Li, T. J., *Chem. J. Chin. Univ.-Chin.* **1996**, 17, 1899-1903.

291. Mendiratta, A.; Barlow, S.; Day, M. W.; Marder, S. R., *Organometallics* **1999**, 18, 454-456.

292. Okamoto, K.; Araki, Y.; Ito, O.; Fukuzumi, S., *J. Am. Chem. Soc.* **2004**, 126, 56-57.

293. Sanders, R.; Mueller-Westerhoff, U. T., *J. Organomet. Chem.* **1996**, 512, 219-224.

294. Calabrese, J. C.; Cheng, L. T.; Green, J. C.; Marder, S. R.; Tam, W., *J. Am. Chem. Soc.* **1991**, 113, 7227-7232.

295. Bildstein, B.; Hradsky, A.; Kopacka, H.; Malleier, R.; Ongania, K. H., *J. Organomet. Chem.* **1997**, 540, 127-145.

296. Herzog, S.; Gustav, K.; Kruger, E.; Oberender, H.; Schuster, R., *Z. Chem.* **1963**, 3, 428-429.

297. Bunel, E. E.; Valle, L.; Manriquez, J. M., *Organometallics* **1985**, 4, 1680-1682.

298. Hart, W. P.; Macomber, D. W.; Rausch, M. D., *J. Am. Chem. Soc.* **1980**, 102, 1196-1198.

299. Schmitt, G.; Ozman, S., *Chem. Z.* **1976**, 100, 143-143.

300. Hobi, M.; Ruppert, O.; Gramlich, V.; Togni, A., *Organometallics* **1997**, 16, 1384-1391.

301. Minkin, V. I.; Dorofeenko, G. N., *Russ. Chem. Rev.* **1960**, 29, 599-633.

302. Zou, C. F.; Wrighton, M. S., *J. Am. Chem. Soc.* **1990**, 112, 7578-7584.

303. Cantrell, R. D.; Shevlin, P. B., *J. Am. Chem. Soc.* **1989**, 111, 2348-2349.

304. Herberich, G. E.; Gaffke, A.; Eckenrath, H. J., *Organometallics* **1998**, 17, 5931-5932.

305. Catheline, D.; Astruc, D., *Organometallics* **1984**, 3, 1094-1100.

306. McArdle, P.; Oneill, L.; Cunningham, D., *Organometallics* **1997**, 16, 1335-1338.

307. Pérez, S.; López, C.; Caubet, A.; Roig, A.; Molins, E., *J. Org. Chem.* **2005**, 70, 4857-4860.

308. Gupta, B. D.; Vijaikanth, V.; Singh, V., *Organometallics* **2004**, 23, 2069-2079.

309. Connelly, N. G.; Geiger, W. E., *Chem. Rev.* **1996**, 96, 877-910.

310. Evans, D. F., *J. Chem. Soc.* **1959**, 2003-2005.

311. Schubert, E. M., *J. Chem. Educ.* **1992**, 69, 62-62.

312. Piguet, C., *J. Chem. Educ.* **1997**, 74, 815-816.

313. Ostfeld, D.; Cohen, I. A., *J. Chem. Educ.* **1972**, 49, 829.

314. Pass, G.; Sutcliffe, H., *J. Chem. Educ.* **1971**, 48, 180-182.

315. Quickenden, T. I.; Marshall, R. C., *J. Chem. Educ.* **1972**, 49, 114-117.

316. Grant, D. H., *J. Chem. Educ.* **1995**, 72, 39-40.

317. Löliger, J.; Scheffol.R, *J. Chem. Educ.* **1972**, 49, 646-647.

318. Stickley, K. R.; Selby, T. D.; Blackstock, S. C., *J. Org. Chem.* **1997**, 62, 448-449.

319. Borden, W. T., *Diradicals*. John Wiley & Sons: New York, **1982**; p 1-343.

320. Sporer, C.; Heise, H.; Wurst, K.; Ruiz-Molina, D.; Kopacka, H.; Jaitner, P.; Kohler, F.; Novoa, J. J.; Veciana, J., *Chem.-Eur. J.* **2004**, 10, 1355-1365.

321. Shultz, D. A.; Boal, A. K.; Farmer, G. T., *J. Am. Chem. Soc.* **1997**, 119, 3846-3847.

322. Elsner, O.; Ruiz-Molina, D.; Ratera, I.; Vidal-Gancedo, J.; Rovira, C.; Veciana, J., *J. Organomet. Chem.* **2001**, 637, 251-257.

323. Sporer, C.; Wurst, K.; Amabilino, D. B.; Ruiz-Molina, D.; Kopacka, H.; Jaitner, P.; Veciana, J., *Chem. Commun.* **2002**, 2342-2343.

324. Mueller-Westerhoff, U. T.; Yang, Z.; Ingram, G., *J. Organomet. Chem.* **1993**, 463, 163-167.

325. Nishinaga, T.; Komatsu, K., *Org. Biomol. Chem.* **2005**, 3, 561-569.

326. Osteryoung, J. G.; Osteryoung, R. A., *Anal. Chem.* **1985**, 57, A101-A110.

327. Small, D.; Zaitsev, V.; Jung, Y. S.; Rosokha, S. V.; Head-Gordon, M.; Kochi, J. K., *J. Am. Chem. Soc.* **2004**, 126, 13850-13858.

328. Goto, K.; Kubo, T.; Yamamoto, K.; Nakasuji, K.; Sato, K.; Shiomi, D.; Takui, T.; Kubota, M.; Kobayashi, T.; Yakusi, K.; Ouyang, J. Y., *J. Am. Chem. Soc.* **1999**, 121, 1619-1620.

329. Lu, J. M.; Rosokha, S. V.; Kochi, J. K., *J. Am. Chem. Soc.* **2003**, 125, 12161-12171.

330. Cameron, T. S.; Lemaire, M. T.; Passmore, J.; Rawson, J. M.; Shuvaev, K. V.; Thompson, L. K., *Inorg. Chem.* **2005**, 44, 2576-2578.

331. Sakai, T.; Satou, T.; Kaikawa, T.; Takimiya, K.; Otsubo, T.; Aso, Y., *J. Am. Chem. Soc.* **2005**, 127, 8082-8089.

332. Csampai, A.; Abran, A.; Kudar, V.; Turos, G.; Wamhoff, H.; Sohar, P., *J. Organomet. Chem.* **2005**, 690, 802-810.

333. Heo, R. W.; Lee, T. R., *J. Organomet. Chem.* **1999**, 578, 31-42.

334. Blanchard, M. D.; Hughes, R. P.; Concolino, T. E.; Rheingold, A. L., *Chem. Mat.* **2000**, 12, 1604-1610.

335. Balavoine, G. G. A.; Doisneau, G.; Fillebeenkhan, T., *J. Organomet. Chem.* **1991**, 412, 381-382.

Appendix A: Crystallographic parameters

Table A-1 - Crystallographic parameters for **4.23**

A. Crystal Data

formula	$C_{22}H_{34}FeN_4O$
formula weight	426.38
crystal dimensions (mm)	0.34 × 0.22 × 0.12
crystal system	monoclinic
space group	$P2_1/c$ (No. 14)
unit cell parameters[a]	
a (Å)	8.5680 (5)
b (Å)	7.4218 (5)
c (Å)	33.759 (2)
β (deg)	94.9390 (10)
V (Å^3)	2138.8 (2)
Z	4
ρ_{calcd} (g cm^{-3})	1.324
μ (mm^{-1})	0.725

B. Data Collection and Refinement Conditions

diffractometer	Bruker PLATFORM/SMART 1000 CCD[b]
radiation (λ [Å])	graphite-monochromated Mo Kα (0.71073)
temperature (°C)	–80
scan type	ω scans (0.2°) (45 s exposures)
data collection 2θ limit (deg)	52.78
total data collected	14146 ($-9 \le h \le 10$, $-9 \le k \le 9$, $-42 \le l \le 42$)
independant reflections	4378 ($R_{\text{int}} = 0.0280$)
number of observed reflections (*NO*)	3933 [$F_o^2 \ge 2\sigma(F_o^2)$]
structure solution method	direct methods (*SIR97*[c])
refinement method	full-matrix least-squares on F^2
absorption correction method	multi-scan (*SADABS*)
range of transmission factors	0.9181–0.7907
data/restraints/parameters	4378 [$F_o^2 \ge -3\sigma(F_o^2)$] / 0 / 271
goodness-of-fit (S)[e]	1.080 [$F_o^2 \ge -3\sigma(F_o^2)$]
final R indices[f]	
R_1 [$F_o^2 \ge 2\sigma(F_o^2)$]	0.0335
wR_2 [$F_o^2 \ge -3\sigma(F_o^2)$]	0.0937
largest difference peak and hole	0.491 and –0.275 e Å^{-3}

Table A-2 - Crystallographic parameters for **4.26**

A. Crystal Data

formula	$C_{47}H_{70}F_{12}Fe_2N_4O_3P_2$
formula weight	1140.71
crystal dimensions (mm)	0.51 × 0.33 × 0.08
crystal system	triclinic
space group	$P\bar{1}$ (No. 2)
unit cell parameters[a]	
a (Å)	10.5710 (10)
b (Å)	11.8153 (12)
c (Å)	21.917 (2)
α (deg)	88.9592 (18)
β (deg)	88.5937 (19)
γ (deg)	80.6813 (18)
V (Å^3)	2700.2 (5)
Z	2
ρ_{calcd} (g cm^{-3})	1.403
μ (mm^{-1})	0.680

B. Data Collection and Refinement Conditions

diffractometer	Bruker PLATFORM/SMART 1000 CCD[b]
radiation (λ [Å])	graphite-monochromated Mo Kα (0.71073)
temperature (°C)	–80
scan type	ω scans (0.2°) (15 s exposures)
data collection 2θ limit (deg)	52.76
total data collected	20597 ($-13 \leq h \leq 13$, $-14 \leq k \leq 14$, $-27 \leq l \leq 27$)
independant reflections	10953 ($R_{int} = 0.0465$)
number of observed reflections (*NO*)	6447 [$F_o^2 \geq 2\sigma(F_o^2)$]
structure solution method	direct methods (*SHELXS–86*[c])
refinement method	full-matrix least-squares on F^2
absorption correction method	Gaussian integration (face-indexed)
range of transmission factors	0.9476–0.7231
data/restraints/parameters	10953 [$F_o^2 \geq -3\sigma(F_o^2)$] / 0 / 577
goodness-of-fit (S)[e]	0.936 [$F_o^2 \geq -3\sigma(F_o^2)$]
final R indices[f]	
R_1 [$F_o^2 \geq 2\sigma(F_o^2)$]	0.0535
wR_2 [$F_o^2 \geq -3\sigma(F_o^2)$]	0.1285
largest difference peak and hole	0.533 and –0.302 e Å^{-3}

Table A-3 - Crystallographic parameters for **4.28**

A. Crystal Data

formula	$C_{14}H_{15}FeN_4O$
formula weight	311.15
crystal dimensions (mm)	0.53 × 0.24 × 0.22
crystal system	triclinic
space group	$P\bar{1}$ (No. 2)
unit cell parameters^a	
a (Å)	10.6210 (8)
b (Å)	10.7705 (8)
c (Å)	13.4916 (10)
α (deg)	113.3892 (11)
β (deg)	108.9896 (11)
γ (deg)	92.2013 (12)
V (Å^3)	1314.23 (17)
Z	4
ρ_{calcd} (g cm^{-3})	1.573
μ (mm^{-1})	1.148

B. Data Collection and Refinement Conditions

diffractometer	Bruker PLATFORM/SMART 1000 CCD^b
radiation (λ [Å])	graphite-monochromated Mo Kα (0.71073)
temperature (°C)	–80
scan type	ω scans (0.3°) (25 s exposures)
data collection 2θ limit (deg)	52.82
total data collected	10488 ($-13 \leq h \leq 13$, $-13 \leq k \leq 13$, $-16 \leq l \leq 16$)
independant reflections	5379 ($R_{\text{int}} = 0.0180$)
number of observed reflections (NO)	4780 [$F_o^2 \geq 2\sigma(F_o^2)$]
structure solution method	direct methods (*SHELXS–86*^{c})
refinement method	full-matrix least-squares on F^2
absorption correction method	Gaussian integration (face-indexed)
range of transmission factors	0.7863–0.5814
data/restraints/parameters	5379 [$F_o^2 \geq -3\sigma(F_o^2)$] / 0 / 365
goodness-of-fit (S)^e	1.055 [$F_o^2 \geq -3\sigma(F_o^2)$]
final R indices^f	
R_1 [$F_o^2 \geq 2\sigma(F_o^2)$]	0.0287
wR_2 [$F_o^2 \geq -3\sigma(F_o^2)$]	0.0787
largest difference peak and hole	0.357 and –0.276 e Å^{-3}

Table A-4 - Crystallographic parameters for **5.7**

A. Crystal Data

formula	$C_{18}H_{20}FeN_8O_2$
formula weight	436.27
crystal dimensions (mm)	0.33 × 0.11 × 0.07
crystal system	triclinic
space group	$P\bar{1}$ (No. 2)
unit cell parameters[a]	
a (Å)	7.1485 (5)
b (Å)	10.4318 (7)
c (Å)	13.3666 (9)
α (deg)	70.5166 (12)
β (deg)	89.5578 (12)
γ (deg)	72.0020 (12)
V (Å^3)	888.65 (10)
Z	2
ρ_{calcd} (g cm^{-3})	1.630
μ (mm^{-1})	0.885

B. Data Collection and Refinement Conditions

diffractometer	Bruker PLATFORM/SMART 1000 CCD[b]
radiation (λ [Å])	graphite-monochromated Mo Kα (0.71073)
temperature (°C)	–80
scan type	ω scans (0.2°) (20 s exposures)
data collection 2θ limit (deg)	52.78
total data collected	6765 ($-8 \le h \le 8$, $-13 \le k \le 12$, $-16 \le l \le 16$)
independant reflections	3605 ($R_{\text{int}} = 0.0287$)
number of observed reflections (*NO*)	3089 [$F_o^2 \ge 2\sigma(F_o^2)$]
structure solution method	direct methods (*SHELXS–86*[c])
refinement method	full-matrix least-squares on F^2
absorption correction method	Gaussian integration (face-indexed)
range of transmission factors	0.9407–0.7589
data/restraints/parameters	3605 [$F_o^2 \ge -3\sigma(F_o^2)$] / 0 / 266
goodness-of-fit (S)[e]	1.063 [$F_o^2 \ge -3\sigma(F_o^2)$]
final R indices[f]	
R_1 [$F_o^2 \ge 2\sigma(F_o^2)$]	0.0372
wR_2 [$F_o^2 \ge -3\sigma(F_o^2)$]	0.0960
largest difference peak and hole	0.393 and –0.327 e Å^{-3}

Appendix B: Complete listings of bond lengths and angles

Table B-1 - Bond lengths [Å], angles [deg] and atomic coordinates for **4.23.**

Atom1	Atom2	Distance
Fe	C11	2.0452(17)
Fe	C12	2.0595(18)
Fe	C13	2.0581(17)
Fe	C14	2.0605(17)
Fe	C15	2.0588(17)
Fe	C21	2.0447(18)
Fe	C22	2.0535(18)
Fe	C23	2.0617(18)
Fe	C24	2.0607(18)
Fe	C25	2.0540(19)
O	C2	1.240(2)
N1	N2	1.427(2)
N1	C1	1.457(2)
N1	H1N	0.89(2)
N2	C2	1.353(3)
N2	C3	1.429(3)
N3	N4	1.426(2)
N3	C2	1.355(3)
N3	C4	1.442(3)
N4	C1	1.456(2)
N4	H4N	0.94(3)
C1	C11	1.513(2)
C11	C12	1.437(2)
C11	C15	1.435(2)
C12	C13	1.428(2)
C12	C16	1.502(3)
C13	C14	1.419(3)
C13	C17	1.501(2)
C14	C15	1.433(2)
C14	C18	1.499(3)
C15	C19	1.505(3)
C21	C22	1.421(3)
C21	C25	1.418(3)
C22	C23	1.428(3)

C22	C26	1.504(3)
C23	C24	1.421(3)
C23	C27	1.499(3)
C24	C25	1.425(3)
C24	C28	1.504(3)
C25	C29	1.502(3)

Atom1	Atom2	Atom3	Angle
C11	Fe	C12	41.00(7)
C11	Fe	C13	68.49(7)
C11	Fe	C14	68.60(7)
C11	Fe	C15	40.93(7)
C11	Fe	C21	109.06(7)
C11	Fe	C22	124.58(8)
C11	Fe	C23	160.44(8)
C11	Fe	C24	158.31(7)
C11	Fe	C25	123.16(7)
C12	Fe	C13	40.60(7)
C12	Fe	C14	68.35(7)
C12	Fe	C15	68.77(7)
C12	Fe	C21	123.39(7)
C12	Fe	C22	107.82(7)
C12	Fe	C23	123.12(7)
C12	Fe	C24	158.83(7)
C12	Fe	C25	159.25(7)
C13	Fe	C14	40.30(7)
C13	Fe	C15	68.27(7)
C13	Fe	C21	158.40(8)
C13	Fe	C22	121.84(8)
C13	Fe	C23	106.67(7)
C13	Fe	C24	122.45(7)
C13	Fe	C25	159.00(8)
C14	Fe	C15	40.71(7)
C14	Fe	C21	160.60(8)
C14	Fe	C22	156.67(8)
C14	Fe	C23	120.78(7)
C14	Fe	C24	106.67(7)
C14	Fe	C25	123.44(8)
C15	Fe	C21	124.90(8)
C15	Fe	C22	161.40(8)
C15	Fe	C23	156.70(8)
C15	Fe	C24	121.77(8)
C15	Fe	C25	108.00(8)

C21	Fe	C22	40.58(8)
C21	Fe	C23	68.05(8)
C21	Fe	C24	67.98(7)
C21	Fe	C25	40.49(8)
C22	Fe	C23	40.60(8)
C22	Fe	C24	68.13(7)
C22	Fe	C25	68.33(8)
C23	Fe	C24	40.32(8)
C23	Fe	C25	68.12(7)
C24	Fe	C25	40.53(7)
N2	N1	C1	108.71(16)
N2	N1	H1N	107.9(15)
C1	N1	H1N	107.4(15)
N1	N2	C2	122.84(18)
N1	N2	C3	114.50(19)
C2	N2	C3	122.6(2)
N4	N3	C2	122.68(17)
N4	N3	C4	114.80(19)
C2	N3	C4	122.0(2)
N3	N4	C1	109.08(16)
N3	N4	H4N	111.7(16)
C1	N4	H4N	106.0(16)
N1	C1	N4	110.92(16)
N1	C1	C11	112.01(15)
N4	C1	C11	111.61(15)
O	C2	N2	121.4(2)
O	C2	N3	120.9(2)
N2	C2	N3	117.74(17)
Fe	C11	C1	133.15(12)
Fe	C11	C12	70.04(10)
Fe	C11	C15	70.04(10)
C1	C11	C12	125.70(16)
C1	C11	C15	125.45(16)
C12	C11	C15	108.12(15)
Fe	C12	C11	68.97(10)
Fe	C12	C13	69.65(10)
Fe	C12	C16	130.28(13)
C11	C12	C13	107.36(15)
C11	C12	C16	129.12(16)
C13	C12	C16	123.35(16)
Fe	C13	C12	69.76(10)
Fe	C13	C14	69.94(10)
Fe	C13	C17	129.46(13)

C12	C13	C14	108.76(15)
C12	C13	C17	125.16(17)
C14	C13	C17	125.96(17)
Fe	C14	C13	69.76(10)
Fe	C14	C15	69.58(10)
Fe	C14	C18	129.74(14)
C13	C14	C15	108.21(15)
C13	C14	C18	126.29(17)
C15	C14	C18	125.35(17)
Fe	C15	C11	69.02(10)
Fe	C15	C14	69.71(10)
Fe	C15	C19	130.41(15)
C11	C15	C14	107.55(15)
C11	C15	C19	129.03(16)
C14	C15	C19	123.23(17)
Fe	C21	C22	70.05(11)
Fe	C21	C25	70.11(11)
C22	C21	C25	108.66(17)
Fe	C22	C21	69.38(11)
Fe	C22	C23	70.01(10)
Fe	C22	C26	129.32(15)
C21	C22	C23	107.53(17)
C21	C22	C26	126.1(2)
C23	C22	C26	126.2(2)
Fe	C23	C22	69.39(11)
Fe	C23	C24	69.80(10)
Fe	C23	C27	129.32(14)
C22	C23	C24	108.01(16)
C22	C23	C27	126.84(19)
C24	C23	C27	125.04(19)
Fe	C24	C23	69.88(11)
Fe	C24	C25	69.48(10)
Fe	C24	C28	129.51(14)
C23	C24	C25	108.17(16)
C23	C24	C28	125.12(18)
C25	C24	C28	126.58(18)
Fe	C25	C21	69.40(11)
Fe	C25	C24	69.99(10)
Fe	C25	C29	129.39(16)
C21	C25	C24	107.62(17)
C21	C25	C29	125.67(19)
C24	C25	C29	126.56(19)

Atomic Coordinates and Equivalent Isotropic Displacement Parameters

Atom	*x*	*y*	*z*	U_{eq}, Å^2
Fe	0.26043(3)	0.18050(3)	0.103570(7)	0.02048(10)*
O	0.5114(2)	0.6883(2)	0.26780(5)	0.0562(5)*
N1	0.5123(2)	0.4859(3)	0.17173(5)	0.0359(4)*
H1N	0.521(3)	0.367(3)	0.1759(7)	0.034(6)
N2	0.5622(2)	0.5753(3)	0.20806(5)	0.0424(4)*
N3	0.3126(2)	0.5608(3)	0.22943(5)	0.0440(5)*
N4	0.2536(2)	0.4725(3)	0.19370(5)	0.0375(4)*
H4N	0.263(3)	0.347(4)	0.1958(8)	0.046(7)
C1	0.3471(2)	0.5256(3)	0.16162(5)	0.0275(4)*
C2	0.4647(3)	0.6099(3)	0.23658(6)	0.0399(5)*
C3	0.7227(3)	0.6305(5)	0.21134(9)	0.0662(8)*
C4	0.1946(4)	0.6158(4)	0.25495(7)	0.0612(7)*
C11	0.2865(2)	0.4414(2)	0.12248(5)	0.0235(3)*
C12	0.3764(2)	0.4111(2)	0.08905(5)	0.0245(4)*
C13	0.2697(2)	0.3554(2)	0.05652(5)	0.0257(4)*
C14	0.1161(2)	0.3520(2)	0.06922(5)	0.0262(4)*
C15	0.1250(2)	0.4059(2)	0.11010(5)	0.0264(4)*
C16	0.5477(2)	0.4435(3)	0.08549(6)	0.0349(4)*
C17	0.3128(3)	0.3193(3)	0.01508(5)	0.0357(4)*
C18	-0.0320(2)	0.3125(3)	0.04377(6)	0.0381(5)*
C19	-0.0170(2)	0.4324(3)	0.13278(6)	0.0398(5)*
C21	0.3398(2)	0.0118(3)	0.14877(6)	0.0339(4)*
C22	0.4246(2)	-0.0185(3)	0.11501(6)	0.0340(4)*
C23	0.3146(2)	-0.0714(2)	0.08297(6)	0.0298(4)*
C24	0.1632(2)	-0.0729(2)	0.09716(6)	0.0284(4)*
C25	0.1787(2)	-0.0212(3)	0.13797(6)	0.0313(4)*
C26	0.5996(3)	-0.0099(4)	0.11408(10)	0.0594(7)*
C27	0.3505(3)	-0.1278(3)	0.04210(7)	0.0468(6)*
C28	0.0153(3)	-0.1319(3)	0.07351(7)	0.0438(5)*
C29	0.0506(3)	-0.0157(4)	0.16561(7)	0.0530(6)*

Table B-2 - Bond lengths [Å], angles [deg] and atomic coordinates for **4.26**.

Atom1	Atom2	Distance
Fe1	C11	2.074(3)
Fe1	C12	2.078(3)
Fe1	C13	2.100(3)
Fe1	C14	2.120(3)

Fe1	C15	2.089(3)
Fe1	C21	2.054(3)
Fe1	C22	2.092(3)
Fe1	C23	2.104(3)
Fe1	C24	2.090(3)
Fe1	C25	2.078(3)
Fe2	C31	2.095(3)
Fe2	C32	2.112(3)
Fe2	C33	2.100(3)
Fe2	C34	2.097(3)
Fe2	C35	2.097(3)
Fe2	C41	2.072(3)
Fe2	C42	2.110(3)
Fe2	C43	2.114(3)
Fe2	C44	2.097(3)
Fe2	C45	2.089(3)
O	C2	1.212(4)
N1	N2	1.375(3)
N1	C1	1.269(4)
N2	C2	1.383(4)
N2	C4	1.458(4)
N3	N4	1.367(3)
N3	C2	1.391(4)
N3	C5	1.458(4)
N4	C3	1.280(4)
C1	C11	1.461(4)
C3	C31	1.453(4)
C11	C12	1.444(4)
C11	C15	1.429(4)
C12	C13	1.429(5)
C12	C16	1.502(5)
C13	C14	1.414(5)
C13	C17	1.500(5)
C14	C15	1.431(5)
C14	C18	1.494(5)
C15	C19	1.500(5)
C21	C22	1.416(5)
C21	C25	1.411(5)
C22	C23	1.424(5)
C22	C26	1.498(5)
C23	C24	1.426(5)
C23	C27	1.511(5)
C24	C25	1.429(5)

C24	C28	1.500(5)
C25	C29	1.498(5)
C31	C32	1.442(4)
C31	C35	1.431(4)
C32	C33	1.428(4)
C32	C36	1.491(4)
C33	C34	1.424(4)
C33	C37	1.497(4)
C34	C35	1.430(4)
C34	C38	1.503(5)
C35	C39	1.496(4)
C41	C42	1.426(4)
C41	C45	1.417(4)
C42	C43	1.425(4)
C42	C46	1.503(4)
C43	C44	1.414(4)
C43	C47	1.496(4)
C44	C45	1.431(4)
C44	C48	1.509(4)
C45	C49	1.487(5)
P1	F1	1.594(2)
P1	F2	1.584(2)
P1	F3	1.585(2)
P1	F4	1.585(2)
P1	F5	1.582(3)
P1	F6	1.572(3)
P2	F7	1.575(2)
P2	F8	1.569(2)

P2	F9	1.576(3)
P2	F10	1.549(3)
P2	F11	1.540(3)
P2	F12	1.543(4)

Atom1	Atom2	Atom3	Angle
C11	Fe1	C12	40.69(12)
C11	Fe1	C13	67.09(13)
C11	Fe1	C14	66.88(13)
C11	Fe1	C15	40.16(12)
C11	Fe1	C21	110.84(14)
C11	Fe1	C22	112.81(13)
C11	Fe1	C23	141.95(14)
C11	Fe1	C24	176.84(13)
C11	Fe1	C25	136.76(13)
C12	Fe1	C13	39.98(13)
C12	Fe1	C14	66.96(14)
C12	Fe1	C15	67.85(13)
C12	Fe1	C21	136.64(14)
C12	Fe1	C22	110.58(14)
C12	Fe1	C23	113.46(14)
C12	Fe1	C24	142.47(14)
C12	Fe1	C25	176.40(14)
C13	Fe1	C14	39.14(13)
C13	Fe1	C15	66.66(14)
C13	Fe1	C21	176.50(15)
C13	Fe1	C22	137.64(14)
C13	Fe1	C23	113.08(14)
C13	Fe1	C24	115.32(13)
C13	Fe1	C25	143.47(14)
C14	Fe1	C15	39.74(13)
C14	Fe1	C21	143.29(15)
C14	Fe1	C22	176.77(14)
C14	Fe1	C23	138.75(14)
C14	Fe1	C24	113.50(14)
C14	Fe1	C25	115.19(14)
C15	Fe1	C21	113.79(14)
C15	Fe1	C22	141.96(13)
C15	Fe1	C23	177.81(14)
C15	Fe1	C24	138.17(14)
C15	Fe1	C25	111.73(14)
C21	Fe1	C22	39.94(13)

C21	Fe1	C23	66.60(13)
C21	Fe1	C24	66.85(14)
C21	Fe1	C25	39.94(14)
C22	Fe1	C23	39.67(13)
C22	Fe1	C24	67.00(14)
C22	Fe1	C25	67.38(14)
C23	Fe1	C24	39.76(14)
C23	Fe1	C25	67.07(14)
C24	Fe1	C25	40.09(13)
C31	Fe2	C32	40.09(12)
C31	Fe2	C33	66.80(12)
C31	Fe2	C34	66.74(12)
C31	Fe2	C35	39.92(12)
C31	Fe2	C41	155.66(13)
C31	Fe2	C42	121.56(13)
C31	Fe2	C43	110.02(12)
C31	Fe2	C44	127.04(12)
C31	Fe2	C45	163.27(12)
C32	Fe2	C33	39.65(12)
C32	Fe2	C34	66.74(12)
C32	Fe2	C35	67.24(12)
C32	Fe2	C41	121.33(12)
C32	Fe2	C42	109.05(12)
C32	Fe2	C43	127.15(13)
C32	Fe2	C44	163.28(13)
C32	Fe2	C45	155.14(13)
C33	Fe2	C34	39.65(12)
C33	Fe2	C35	66.95(12)
C33	Fe2	C41	109.35(12)
C33	Fe2	C42	126.63(12)
C33	Fe2	C43	163.05(13)
C33	Fe2	C44	156.00(14)
C33	Fe2	C45	121.35(13)
C34	Fe2	C35	39.85(12)
C34	Fe2	C41	126.78(13)
C34	Fe2	C42	162.98(12)
C34	Fe2	C43	156.20(12)
C34	Fe2	C44	122.30(13)
C34	Fe2	C45	109.23(13)
C35	Fe2	C41	163.05(13)
C35	Fe2	C42	155.68(13)
C35	Fe2	C43	122.20(12)
C35	Fe2	C44	109.70(12)

C35	Fe2	C45	126.58(13)
C41	Fe2	C42	39.85(12)
C41	Fe2	C43	66.18(12)
C41	Fe2	C44	66.46(12)
C41	Fe2	C45	39.80(12)
C42	Fe2	C43	39.42(11)
C42	Fe2	C44	66.48(12)
C42	Fe2	C45	67.15(12)
C43	Fe2	C44	39.25(12)
C43	Fe2	C45	66.62(13)
C44	Fe2	C45	39.97(13)
N2	N1	C1	119.0(3)
N1	N2	C2	116.0(3)
N1	N2	C4	122.0(3)
C2	N2	C4	117.4(3)
N4	N3	C2	112.7(3)
N4	N3	C5	121.4(2)
C2	N3	C5	125.0(3)
N3	N4	C3	119.7(3)
N1	C1	C11	120.9(3)
O	C2	N2	121.2(3)
O	C2	N3	123.1(3)
N2	C2	N3	115.7(3)
N4	C3	C31	119.2(3)
Fe1	C11	C1	122.5(2)
Fe1	C11	C12	69.82(18)
Fe1	C11	C15	70.48(19)
C1	C11	C12	127.8(3)
C1	C11	C15	124.0(3)
C12	C11	C15	108.1(3)
Fe1	C12	C11	69.49(18)
Fe1	C12	C13	70.84(19)
Fe1	C12	C16	127.3(3)
C11	C12	C13	106.8(3)
C11	C12	C16	128.1(3)
C13	C12	C16	124.9(3)
Fe1	C13	C12	69.18(18)
Fe1	C13	C14	71.18(19)
Fe1	C13	C17	127.3(3)
C12	C13	C14	109.2(3)
C12	C13	C17	125.5(3)
C14	C13	C17	125.3(3)
Fe1	C14	C13	69.7(2)

Fe1	C14	C15	68.97(18)
Fe1	C14	C18	128.3(3)
C13	C14	C15	108.1(3)
C13	C14	C18	126.2(3)
C15	C14	C18	125.7(3)
Fe1	C15	C11	69.35(19)
Fe1	C15	C14	71.3(2)
Fe1	C15	C19	127.2(2)
C11	C15	C14	107.8(3)
C11	C15	C19	126.7(3)
C14	C15	C19	125.5(3)
Fe1	C21	C22	71.49(19)
Fe1	C21	C25	70.96(19)
C22	C21	C25	109.8(3)
Fe1	C22	C21	68.57(19)
Fe1	C22	C23	70.62(19)
Fe1	C22	C26	125.8(3)
C21	C22	C23	107.0(3)
C21	C22	C26	125.9(3)
C23	C22	C26	127.1(3)
Fe1	C23	C22	69.71(19)
Fe1	C23	C24	69.6(2)
Fe1	C23	C27	126.4(3)
C22	C23	C24	108.2(3)
C22	C23	C27	126.2(3)
C24	C23	C27	125.6(3)
Fe1	C24	C23	70.7(2)
Fe1	C24	C25	69.51(19)
Fe1	C24	C28	127.6(3)
C23	C24	C25	108.1(3)
C23	C24	C28	126.8(3)
C25	C24	C28	125.1(4)
Fe1	C25	C21	69.10(19)
Fe1	C25	C24	70.40(19)
Fe1	C25	C29	127.2(3)
C21	C25	C24	107.0(3)
C21	C25	C29	125.3(3)
C24	C25	C29	127.7(4)
Fe2	C31	C3	124.8(2)
Fe2	C31	C32	70.59(17)
Fe2	C31	C35	70.12(18)
C3	C31	C32	123.6(3)
C3	C31	C35	128.0(3)

C32	C31	C35	108.4(3)
Fe2	C32	C31	69.33(17)
Fe2	C32	C33	69.73(18)
Fe2	C32	C36	127.1(2)
C31	C32	C33	107.1(3)
C31	C32	C36	126.5(3)
C33	C32	C36	126.3(3)
Fe2	C33	C32	70.62(18)
Fe2	C33	C34	70.06(18)
Fe2	C33	C37	128.0(2)
C32	C33	C34	108.5(3)
C32	C33	C37	125.8(3)
C34	C33	C37	125.6(3)
Fe2	C34	C33	70.29(18)
Fe2	C34	C35	70.08(18)
Fe2	C34	C38	128.6(2)
C33	C34	C35	108.5(3)
C33	C34	C38	125.8(3)
C35	C34	C38	125.6(3)
Fe2	C35	C31	69.95(17)
Fe2	C35	C34	70.06(18)
Fe2	C35	C39	128.8(2)
C31	C35	C34	107.4(3)
C31	C35	C39	128.3(3)
C34	C35	C39	124.2(3)
Fe2	C41	C42	71.51(17)
Fe2	C41	C45	70.75(18)
C42	C41	C45	109.6(3)
Fe2	C42	C41	68.64(17)
Fe2	C42	C43	70.43(17)
Fe2	C42	C46	127.0(2)
C41	C42	C43	106.6(3)
C41	C42	C46	126.5(3)
C43	C42	C46	126.8(3)
Fe2	C43	C42	70.15(17)
Fe2	C43	C44	69.72(18)
Fe2	C43	C47	126.6(2)
C42	C43	C44	108.6(3)
C42	C43	C47	125.8(3)
C44	C43	C47	125.5(3)
Fe2	C44	C43	71.03(18)
Fe2	C44	C45	69.73(18)
Fe2	C44	C48	127.5(2)

C43	C44	C45	108.4(3)
C43	C44	C48	124.1(3)
C45	C44	C48	127.4(3)
Fe2	C45	C41	69.45(18)
Fe2	C45	C44	70.30(18)
Fe2	C45	C49	125.7(2)
C41	C45	C44	106.7(3)
C41	C45	C49	126.3(3)
C44	C45	C49	127.0(3)
F1	P1	F2	179.19(14)
F1	P1	F3	89.92(13)
F1	P1	F4	90.44(13)
F1	P1	F5	89.59(15)
F1	P1	F6	90.35(16)
F2	P1	F3	90.78(14)
F2	P1	F4	88.84(14)
F2	P1	F5	90.02(16)
F2	P1	F6	90.03(17)
F3	P1	F4	178.26(18)
F3	P1	F5	89.87(16)
F3	P1	F6	90.45(18)
F4	P1	F5	88.43(15)
F4	P1	F6	91.24(18)
F5	P1	F6	179.7(2)
F7	P2	F8	178.97(19)
F7	P2	F9	89.72(13)
F7	P2	F10	89.26(14)
F7	P2	F11	90.46(19)
F7	P2	F12	89.2(2)
F8	P2	F9	90.02(14)
F8	P2	F10	91.01(15)
F8	P2	F11	90.5(2)
F8	P2	F12	89.8(2)
F9	P2	F10	178.72(18)
F9	P2	F11	87.9(2)
F9	P2	F12	90.1(2)
F10	P2	F11	91.4(2)
F10	P2	F12	90.6(3)
F11	P2	F12	178.0(3)

Atomic Coordinates and Equivalent Isotropic Displacement Parameters

(a) atoms of $[\{(\eta^5\text{–}C_5HMe_4)Fe(\eta^5\text{–}C_5Me_4CHNNMe)\}_2CO]^{2+}$

Atom	*x*	*y*	*z*	U_{eq}, Å^2
Fe1	0.08173(4)	0.73277(4)	0.13981(2)	0.03285(14)*
Fe2	0.21354(4)	0.76988(4)	0.55307(2)	0.02863(13)*
O	0.2255(2)	0.3737(2)	0.38246(11)	0.0508(7)*
N1	0.2866(3)	0.5240(2)	0.25517(12)	0.0342(6)*
N2	0.2894(3)	0.4231(2)	0.28778(12)	0.0385(7)*
N3	0.3560(3)	0.5104(2)	0.37414(12)	0.0342(6)*
N4	0.3243(3)	0.5361(2)	0.43372(12)	0.0325(6)*
C1	0.2598(3)	0.5263(3)	0.19896(15)	0.0347(8)*
C2	0.2854(3)	0.4323(3)	0.35065(15)	0.0361(8)*
C3	0.3858(3)	0.6028(2)	0.46229(14)	0.0305(7)*
C4	0.2463(4)	0.3233(3)	0.26215(17)	0.0546(11)*
C5	0.4676(3)	0.5469(3)	0.34408(15)	0.0361(8)*
C11	0.2538(3)	0.6320(3)	0.16277(15)	0.0349(8)*
C12	0.2494(3)	0.7472(3)	0.18453(16)	0.0394(8)*
C13	0.2384(3)	0.8215(3)	0.13208(17)	0.0411(9)*
C14	0.2354(3)	0.7553(3)	0.07920(16)	0.0420(9)*
C15	0.2433(3)	0.6377(3)	0.09785(15)	0.0363(8)*
C16	0.2612(4)	0.7852(3)	0.24891(16)	0.0526(10)*
C17	0.2349(4)	0.9489(3)	0.1327(2)	0.0607(12)*
C18	0.2289(4)	0.7994(4)	0.01484(17)	0.0607(11)*
C19	0.2468(4)	0.5384(3)	0.05581(16)	0.0491(10)*
C21	-0.0683(3)	0.6436(3)	0.15278(18)	0.0451(9)*
C22	-0.0666(3)	0.7174(3)	0.20282(17)	0.0410(9)*
C23	-0.0829(3)	0.8315(3)	0.17882(17)	0.0418(9)*
C24	-0.0944(3)	0.8265(3)	0.11428(17)	0.0419(9)*
C25	-0.0863(3)	0.7088(3)	0.09820(17)	0.0423(9)*
C26	-0.0504(4)	0.6808(4)	0.26833(17)	0.0625(12)*
C27	-0.0874(4)	0.9397(3)	0.2151(2)	0.0646(12)*
C28	-0.1174(4)	0.9262(3)	0.0704(2)	0.0649(12)*
C29	-0.0990(4)	0.6612(4)	0.03616(19)	0.0678(13)*
C31	0.3504(3)	0.6307(2)	0.52536(14)	0.0307(7)*
C32	0.4113(3)	0.7071(3)	0.56103(15)	0.0322(8)*
C33	0.3496(3)	0.7140(3)	0.61989(15)	0.0355(8)*
C34	0.2534(3)	0.6425(3)	0.62092(15)	0.0355(8)*
C35	0.2530(3)	0.5907(3)	0.56250(15)	0.0331(8)*
C36	0.5202(3)	0.7658(3)	0.54090(16)	0.0394(8)*
C37	0.3856(4)	0.7796(3)	0.67286(16)	0.0474(9)*
C38	0.1720(4)	0.6189(3)	0.67542(16)	0.0498(10)*
C39	0.1704(3)	0.5041(3)	0.54723(17)	0.0433(9)*
C41	0.1405(3)	0.9415(3)	0.56615(15)	0.0329(8)*
C42	0.1904(3)	0.9282(2)	0.50521(15)	0.0304(7)*
C43	0.1201(3)	0.8520(3)	0.47618(14)	0.0316(7)*

C44	0.0292(3)	0.8193(3)	0.51860(15)	0.0332(8)*
C45	0.0408(3)	0.8755(3)	0.57499(16)	0.0355(8)*
C46	0.2945(3)	0.9860(3)	0.47682(17)	0.0440(9)*
C47	0.1380(3)	0.8137(3)	0.41139(15)	0.0429(9)*
C48	-0.0667(3)	0.7427(3)	0.50371(18)	0.0474(9)*
C49	-0.0371(3)	0.8678(3)	0.63188(16)	0.0471(9)*

(b) hexafluorophosphate ion atoms

Atom	*x*	*y*	*z*	U_{eq}, Å^2
P1	0.97364(11)	0.27655(8)	0.14435(5)	0.0514(3)*
F1	0.9067(3)	0.36347(19)	0.09391(11)	0.0765(7)*
F2	1.0407(3)	0.19162(19)	0.19499(11)	0.0828(8)*
F3	1.0035(3)	0.1796(2)	0.09457(12)	0.0902(9)*
F4	0.9482(3)	0.37405(19)	0.19395(10)	0.0838(8)*
F5	1.1063(3)	0.3168(2)	0.12819(11)	0.0841(8)*
F6	0.8416(3)	0.2372(3)	0.16064(16)	0.1198(12)*
P2	0.60160(10)	0.85590(9)	0.34609(5)	0.0503(3)*
F7	0.5753(2)	0.9561(2)	0.39347(12)	0.0821(8)*
F8	0.6262(3)	0.7574(3)	0.29808(13)	0.1029(11)*
F9	0.4647(2)	0.8247(2)	0.36126(14)	0.0929(9)*
F10	0.7364(3)	0.8872(3)	0.33270(18)	0.1547(19)*
F11	0.6542(4)	0.7710(3)	0.39704(16)	0.1346(13)*
F12	0.5440(5)	0.9405(3)	0.29575(16)	0.174(2)*

Table B-3 - Bond lengths [Å], angles [deg] and atomic coordinates for **4.28**.

Atom1	Atom2	Distance
Fe	C1	2.0420(18)
Fe	C2	2.0553(19)
Fe	C3	2.0440(19)
Fe	C4	2.040(2)
Fe	C5	2.0366(19)
Fe	C6	2.032(2)
Fe	C7	2.044(2)
Fe	C8	2.044(2)
Fe	C9	2.0400(19)
Fe	C10	2.032(2)
O	C12	1.219(2)
N1	N2	1.365(2)
N1	C11	1.334(2)

N2	C12	1.373(2)
N2	C13	1.457(2)
N3	N4	1.369(2)
N3	C12	1.374(2)
N3	C14	1.450(2)
N4	C11	1.332(2)
C1	C2	1.427(3)
C1	C5	1.430(3)
C1	C11	1.470(2)
C2	C3	1.424(3)
C3	C4	1.414(3)
C4	C5	1.424(3)
C6	C7	1.400(4)
C6	C10	1.408(3)
C7	C8	1.405(3)
C8	C9	1.407(3)
C9	C10	1.412(3)
Fe	C1	2.0401(17)
Fe	C2	2.0471(17)
Fe	C3	2.0488(18)
Fe	C4	2.0429(18)
Fe	C5	2.0369(17)
Fe	C6	2.0413(19)
Fe	C7	2.0432(19)
Fe	C8	2.0428(18)
Fe	C9	2.0465(18)
Fe	C10	2.0478(19)
O	C12	1.218(2)
N1	N2	1.369(2)
N1	C11	1.331(2)
N2	C12	1.374(3)
N2	C13	1.457(2)
N3	N4	1.367(2)
N3	C12	1.370(3)
N3	C14	1.453(3)
N4	C11	1.334(2)
C1	C2	1.426(2)
C1	C5	1.432(2)
C1	C11	1.466(2)
C2	C3	1.424(3)
C3	C4	1.420(3)
C4	C5	1.423(3)
C6	C7	1.414(3)

C6	C10	1.421(3)
C7	C8	1.421(3)
C8	C9	1.418(3)
C9	C10	1.416(3)

Atom1	Atom2	Atom3	Angle
C1	Fe	C2	40.76(7)
C1	Fe	C3	68.49(8)
C1	Fe	C4	68.75(8)
C1	Fe	C5	41.04(8)
C1	Fe	C6	109.80(8)
C1	Fe	C7	118.77(8)
C1	Fe	C8	150.99(8)
C1	Fe	C9	168.00(9)
C1	Fe	C10	130.19(9)
C2	Fe	C3	40.64(8)
C2	Fe	C4	68.47(9)
C2	Fe	C5	68.77(8)
C2	Fe	C6	132.71(9)
C2	Fe	C7	111.46(8)
C2	Fe	C8	118.41(8)
C2	Fe	C9	149.05(8)
C2	Fe	C10	170.15(9)
C3	Fe	C4	40.50(9)
C3	Fe	C5	68.54(8)
C3	Fe	C6	171.38(10)
C3	Fe	C7	132.52(10)
C3	Fe	C8	109.41(9)
C3	Fe	C9	115.47(9)
C3	Fe	C10	146.99(10)
C4	Fe	C5	40.90(8)
C4	Fe	C6	147.63(11)
C4	Fe	C7	169.18(9)
C4	Fe	C8	129.59(9)
C4	Fe	C9	106.38(9)
C4	Fe	C10	114.16(10)
C5	Fe	C6	116.15(10)
C5	Fe	C7	149.84(9)
C5	Fe	C8	167.35(9)
C5	Fe	C9	128.29(9)
C5	Fe	C10	106.57(9)
C6	Fe	C7	40.17(10)

C6	Fe	C8	67.69(10)
C6	Fe	C9	68.03(9)
C6	Fe	C10	40.55(10)
C1	Fe	C2	40.83(7)
C1	Fe	C3	68.59(7)
C1	Fe	C4	68.80(7)
C1	Fe	C5	41.13(7)
C1	Fe	C6	107.92(7)
C1	Fe	C7	123.96(8)
C1	Fe	C8	160.46(8)
C1	Fe	C9	157.59(8)
C1	Fe	C10	122.14(7)
C2	Fe	C3	40.70(7)
C2	Fe	C4	68.61(7)
C2	Fe	C5	68.91(7)
C2	Fe	C6	123.25(8)
C2	Fe	C7	108.43(8)
C2	Fe	C8	124.01(8)
C2	Fe	C9	159.79(8)
C2	Fe	C10	158.70(8)
C3	Fe	C4	40.62(7)
C3	Fe	C5	68.62(7)
C3	Fe	C6	159.13(8)
C3	Fe	C7	123.12(8)
C3	Fe	C8	107.82(8)
C3	Fe	C9	123.04(8)
C3	Fe	C10	158.80(8)
C4	Fe	C5	40.83(7)
C4	Fe	C6	159.14(8)
C4	Fe	C7	158.28(8)
C4	Fe	C8	121.83(8)
C4	Fe	C9	106.58(7)
C4	Fe	C10	122.32(8)
C5	Fe	C6	123.18(8)
C5	Fe	C7	160.03(8)
C5	Fe	C8	157.22(8)
C5	Fe	C9	121.11(7)
C5	Fe	C10	106.47(7)
C6	Fe	C7	40.52(9)
C6	Fe	C8	68.18(8)
C6	Fe	C9	68.17(8)
C6	Fe	C10	40.68(8)
C7	Fe	C8	40.22(9)

C7	Fe	C9	67.79(9)
C7	Fe	C10	67.88(10)
C8	Fe	C9	40.29(9)
C8	Fe	C10	67.93(9)
C9	Fe	C10	40.59(9)
N2	N1	C11	114.55(15)
N1	N2	C12	124.96(15)
N1	N2	C13	115.08(15)
C12	N2	C13	119.96(16)
N4	N3	C12	124.77(15)
N4	N3	C14	115.55(14)
C12	N3	C14	119.57(15)
N3	N4	C11	114.58(14)
Fe	C1	C2	70.12(10)
Fe	C1	C5	69.28(11)
Fe	C1	C11	124.95(13)
C2	C1	C5	107.99(16)
C2	C1	C11	125.92(17)
C5	C1	C11	126.06(17)
Fe	C2	C1	69.12(10)
Fe	C2	C3	69.26(11)
C1	C2	C3	107.54(18)
Fe	C3	C2	70.11(11)
Fe	C3	C4	69.62(12)
C2	C3	C4	108.61(17)
Fe	C4	C3	69.89(11)
Fe	C4	C5	69.41(11)
C3	C4	C5	108.12(18)
Fe	C5	C1	69.69(10)
Fe	C5	C4	69.70(11)
C1	C5	C4	107.73(18)
Fe	C6	C7	70.36(12)
Fe	C6	C10	69.70(13)
C7	C6	C10	108.3(2)
Fe	C7	C6	69.47(13)
Fe	C7	C8	69.92(12)
C6	C7	C8	108.07(19)
Fe	C8	C7	69.87(12)
C7	Fe	C8	40.69(8)
C7	Fe	C9	68.36(8)
C7	Fe	C10	68.42(8)
C8	Fe	C9	40.58(8)
C8	Fe	C10	68.26(8)

C9	Fe	C10	40.48(8)
N2	N1	C11	114.68(15)
N1	N2	C12	124.67(15)
N1	N2	C13	115.73(16)
C12	N2	C13	119.51(16)
N4	N3	C12	125.00(16)
N4	N3	C14	114.32(16)
C12	N3	C14	120.62(17)
N3	N4	C11	114.51(15)
Fe	C1	C2	69.85(10)
Fe	C1	C5	69.32(9)
Fe	C1	C11	125.63(12)
C2	C1	C5	107.91(15)
C2	C1	C11	127.13(15)
C5	C1	C11	124.96(16)
Fe	C2	C1	69.32(10)
Fe	C2	C3	69.71(10)
C1	C2	C3	107.87(15)
Fe	C3	C2	69.58(10)
Fe	C3	C4	69.46(10)
C2	C3	C4	108.24(16)
Fe	C4	C3	69.91(10)
Fe	C4	C5	69.36(10)
C3	C4	C5	108.19(15)
Fe	C5	C1	69.55(10)
Fe	C5	C4	69.81(10)
C1	C5	C4	107.78(15)
Fe	C6	C7	69.81(11)
Fe	C6	C10	69.91(11)
C7	C6	C10	108.41(17)
Fe	C7	C6	69.67(11)
Fe	C7	C8	69.64(11)
C6	C7	C8	107.70(18)
Fe	C8	C7	69.67(11)
Fe	C8	C9	69.69(12)
C7	C8	C9	108.2(2)
Fe	C9	C8	70.02(11)
Fe	C9	C10	69.38(12)
C8	C9	C10	107.76(19)
Fe	C10	C6	69.75(12)
Fe	C10	C9	70.03(12)
C6	C10	C9	107.7(2)
N1	C11	N4	127.26(17)

N1	C11	C1	116.25(16)
N4	C11	C1	116.49(15)
O	C12	N2	123.54(17)
O	C12	N3	122.59(17)
N2	C12	N3	113.87(16)
Fe	C8	C9	69.85(11)
C7	C8	C9	108.08(18)
Fe	C9	C8	69.57(10)
Fe	C9	C10	69.81(10)
C8	C9	C10	108.14(17)
Fe	C10	C6	69.41(11)
Fe	C10	C9	69.71(11)
C6	C10	C9	107.66(18)
N1	C11	N4	127.16(16)
N1	C11	C1	117.16(15)
N4	C11	C1	115.68(15)
O	C12	N2	123.09(19)
O	C12	N3	122.99(19)
N2	C12	N3	113.91(16)

Atomic Coordinates and Equivalent Isotropic Displacement Parameters

(a) atoms of 1,5-dimethyl-3-ferrocenyl-6-oxoverdazyl, molecule A

Atom	*x*	*y*	*z*	U_{eq}, Å^2
Fe	0.21266(3)	0.23993(2)	0.50059(2)	0.02586(8)*
O	0.33864(15)	-0.32133(14)	0.59945(13)	0.0387(3)*
N1	0.26388(15)	-0.14114(16)	0.42371(13)	0.0289(3)*
N2	0.26730(15)	-0.24377(15)	0.45919(13)	0.0286(3)*
N3	0.40266(15)	-0.09450(15)	0.64733(13)	0.0283(3)*
N4	0.40494(16)	0.01383(15)	0.61865(13)	0.0290(3)*
C1	0.33242(18)	0.09573(19)	0.47291(16)	0.0278(4)*
C2	0.24716(19)	0.0909(2)	0.36450(16)	0.0321(4)*
C3	0.2755(2)	0.2236(2)	0.36866(19)	0.0389(5)*
C4	0.3776(2)	0.3094(2)	0.4776(2)	0.0411(5)*
C5	0.41345(19)	0.2313(2)	0.54301(19)	0.0341(4)*
C6	0.1288(3)	0.2304(2)	0.6136(2)	0.0514(6)*
C7	0.0276(2)	0.1854(2)	0.5030(2)	0.0455(5)*
C8	0.0261(2)	0.2937(2)	0.46971(19)	0.0400(5)*
C9	0.1265(2)	0.4065(2)	0.56025(19)	0.0394(5)*
C10	0.1905(3)	0.3671(2)	0.64978(18)	0.0472(5)*
C11	0.33386(17)	-0.01777(18)	0.50747(15)	0.0256(4)*
C12	0.33642(18)	-0.22741(18)	0.57044(16)	0.0280(4)*
C13	0.1915(2)	-0.3790(2)	0.36848(18)	0.0397(5)*

C14	0.4842(2)	-0.0639(2)	0.76672(16)	0.0347(4)*

(b) atoms of 1,5-dimethyl-3-ferrocenyl-6-oxoverdazyl, molecule B

Atom	*x*	*y*	*z*	U_{eq}, Å^2
Fe	-0.22916(2)	0.30711(2)	0.01816(2)	0.02269(8)*
O	0.38316(15)	0.19677(17)	-0.02457(15)	0.0497(4)*
N1	0.16258(14)	0.29597(15)	0.12953(13)	0.0270(3)*
N2	0.27654(15)	0.28808(16)	0.10255(14)	0.0298(3)*
N3	0.15516(16)	0.12728(17)	-0.08507(14)	0.0317(3)*
N4	0.03731(15)	0.12720(16)	-0.06456(14)	0.0305(3)*
C1	-0.07422(17)	0.21235(17)	0.06843(15)	0.0240(3)*
C2	-0.09532(18)	0.30895(18)	0.16769(15)	0.0270(4)*
C3	-0.23123(19)	0.26973(19)	0.15520(16)	0.0295(4)*
C4	-0.29429(18)	0.14967(19)	0.04869(16)	0.0282(4)*
C5	-0.19795(17)	0.11360(18)	-0.00554(15)	0.0257(4)*
C6	-0.1780(2)	0.4054(2)	-0.06917(18)	0.0355(4)*
C7	-0.2018(2)	0.5010(2)	0.02775(19)	0.0362(4)*
C8	-0.3374(2)	0.4588(2)	0.01360(18)	0.0348(4)*
C9	-0.39660(19)	0.3374(2)	-0.09204(17)	0.0318(4)*
C10	-0.2982(2)	0.3039(2)	-0.14349(17)	0.0329(4)*
C11	0.05001(17)	0.21259(17)	0.04324(15)	0.0241(3)*
C12	0.27945(19)	0.2036(2)	-0.00403(18)	0.0327(4)*
C13	0.39981(19)	0.3830(2)	0.19376(19)	0.0380(5)*
C14	0.1413(2)	0.0325(2)	-0.20198(18)	0.0430(5)*

Table B-4 - Bond lengths [Å], angles [deg] and atomic coordinates for **5.7**.

Atom1	Atom2	Distance
Fe	C10	2.034(2)
Fe	C11	2.041(2)
Fe	C12	2.056(2)
Fe	C13	2.050(2)
Fe	C14	2.044(2)
Fe	C20	2.039(2)
Fe	C21	2.045(2)
Fe	C22	2.056(2)
Fe	C23	2.052(2)
Fe	C24	2.040(2)
O10	C16	1.220(3)
O20	C26	1.210(3)
N11	N12	1.367(3)
N11	C15	1.331(3)
N12	C16	1.374(3)
N12	C17	1.458(3)
N13	N14	1.375(3)
N13	C16	1.377(3)
N13	C18	1.455(3)
N14	C15	1.335(3)
N21	N22	1.369(3)
N21	C25	1.329(3)
N22	C26	1.372(3)
N22	C27	1.458(3)
N23	N24	1.375(3)
N23	C26	1.380(3)
N23	C28	1.455(3)
N24	C25	1.328(3)
C10	C11	1.425(3)
C10	C14	1.429(3)
C10	C15	1.470(3)
C11	C12	1.423(3)
C12	C13	1.416(3)
C13	C14	1.429(3)
C20	C21	1.430(3)
C20	C24	1.424(3)
C20	C25	1.474(3)
C21	C22	1.426(3)

C22	C23	1.420(4)
C23	C24	1.425(3)

Atom1	Atom2	Atom3	Angle
C10	Fe	C11	40.95(9)
C10	Fe	C12	68.63(9)
C10	Fe	C13	68.68(9)
C10	Fe	C14	41.04(9)
C10	Fe	C20	105.83(9)
C10	Fe	C21	121.41(9)
C10	Fe	C22	158.24(10)
C10	Fe	C23	158.95(10)
C10	Fe	C24	121.81(9)
C11	Fe	C12	40.65(9)
C11	Fe	C13	68.32(10)
C11	Fe	C14	68.85(9)
C11	Fe	C20	120.70(9)
C11	Fe	C21	105.62(10)
C11	Fe	C22	122.45(10)
C11	Fe	C23	159.53(10)
C11	Fe	C24	157.31(9)
C12	Fe	C13	40.34(10)
C12	Fe	C14	68.53(10)
C12	Fe	C20	157.07(10)
C12	Fe	C21	121.52(10)
C12	Fe	C22	107.91(10)
C12	Fe	C23	124.49(9)
C12	Fe	C24	160.89(9)
C13	Fe	C14	40.86(9)
C13	Fe	C20	160.33(10)
C13	Fe	C21	158.09(10)
C13	Fe	C22	123.49(9)
C13	Fe	C23	109.51(9)
C13	Fe	C24	124.77(10)
C14	Fe	C20	122.76(9)
C14	Fe	C21	158.62(9)
C14	Fe	C22	159.55(9)
C14	Fe	C23	123.77(10)
C14	Fe	C24	107.84(10)
C20	Fe	C21	40.98(9)
C20	Fe	C22	68.54(9)
C20	Fe	C23	68.45(9)
C20	Fe	C24	40.85(9)

C21	Fe	C22	40.68(9)
C21	Fe	C23	68.40(10)
C21	Fe	C24	68.87(10)
C22	Fe	C23	40.45(10)
C22	Fe	C24	68.54(10)
C23	Fe	C24	40.75(9)
N12	N11	C15	114.70(19)
N11	N12	C16	124.36(19)
N11	N12	C17	114.81(19)
C16	N12	C17	119.48(19)
N14	N13	C16	124.37(19)
N14	N13	C18	115.03(19)
C16	N13	C18	119.12(19)
N13	N14	C15	114.18(19)
N22	N21	C25	114.43(19)
N21	N22	C26	124.5(2)
N21	N22	C27	115.30(19)
C26	N22	C27	119.1(2)
N24	N23	C26	124.2(2)
N24	N23	C28	115.59(19)
C26	N23	C28	119.1(2)
N23	N24	C25	114.15(19)
Fe	C10	C11	69.79(13)
Fe	C10	C14	69.87(12)
Fe	C10	C15	125.36(16)
C11	C10	C14	107.99(19)
C11	C10	C15	125.0(2)
C14	C10	C15	127.0(2)
Fe	C11	C10	69.26(13)
Fe	C11	C12	70.25(13)
C10	C11	C12	108.1(2)
Fe	C12	C11	69.10(13)
Fe	C12	C13	69.60(13)
C11	C12	C13	108.0(2)
Fe	C13	C12	70.06(13)
Fe	C13	C14	69.35(13)
C12	C13	C14	108.5(2)
Fe	C14	C10	69.09(12)
Fe	C14	C13	69.79(13)
C10	C14	C13	107.4(2)
N11	C15	N14	127.6(2)
N11	C15	C10	115.4(2)
N14	C15	C10	117.0(2)

O10	C16	N12	122.7(2)
O10	C16	N13	123.1(2)
N12	C16	N13	114.17(19)
Fe	C20	C21	69.74(13)
Fe	C20	C24	69.60(13)
Fe	C20	C25	124.73(16)
C21	C20	C24	108.1(2)
C21	C20	C25	125.2(2)
C24	C20	C25	126.6(2)
Fe	C21	C20	69.28(13)
Fe	C21	C22	70.05(14)
C20	C21	C22	107.7(2)
Fe	C22	C21	69.27(13)
Fe	C22	C23	69.62(13)
C21	C22	C23	108.0(2)
Fe	C23	C22	69.93(13)
Fe	C23	C24	69.20(13)
C22	C23	C24	108.3(2)
Fe	C24	C20	69.54(13)
Fe	C24	C23	70.05(13)
C20	C24	C23	107.8(2)
N21	C25	N24	128.1(2)
N21	C25	C20	115.2(2)
N24	C25	C20	116.7(2)
O20	C26	N22	123.0(2)
O20	C26	N23	122.9(2)
N22	C26	N23	114.1(2)

Atomic Coordinates and Equivalent Isotropic Displacement Parameters

Atom	x	y	z	U_{eq}, Å^2
Fe	-0.01411(4)	0.47834(3)	0.29867(3)	0.01633(11)*
O10	0.8069(3)	0.01011(18)	0.19277(14)	0.0306(4)*
O20	0.3952(3)	-0.11186(19)	0.15560(15)	0.0363(5)*
N11	0.4357(3)	0.3401(2)	0.16233(16)	0.0219(4)*
N12	0.5661(3)	0.2289(2)	0.13952(15)	0.0217(4)*
N13	0.6296(3)	0.0849(2)	0.31754(16)	0.0222(4)*
N14	0.5009(3)	0.1914(2)	0.34689(16)	0.0213(4)*
N21	0.0796(3)	0.2349(2)	0.13062(16)	0.0236(4)*
N22	0.2046(3)	0.1226(2)	0.10665(16)	0.0239(5)*
N23	0.2763(3)	-0.0205(2)	0.28470(16)	0.0227(4)*
N24	0.1496(3)	0.0862(2)	0.31477(16)	0.0216(4)*
C10	0.2825(3)	0.4342(2)	0.29202(18)	0.0178(5)*
C11	0.1786(3)	0.5725(3)	0.21635(19)	0.0222(5)*

C12	0.0662(3)	0.6589(3)	0.27280(19)	0.0229(5)*
C13	0.0993(3)	0.5746(3)	0.38277(19)	0.0220(5)*
C14	0.2337(3)	0.4351(3)	0.39576(18)	0.0193(5)*
C15	0.4139(3)	0.3132(2)	0.26556(18)	0.0181(5)*
C16	0.6781(3)	0.1014(3)	0.21509(19)	0.0217(5)*
C17	0.6143(4)	0.2651(3)	0.0295(2)	0.0305(6)*
C18	0.7506(4)	-0.0392(3)	0.4056(2)	0.0293(6)*
C20	-0.0833(3)	0.3233(3)	0.26082(19)	0.0200(5)*
C21	-0.1896(3)	0.4625(3)	0.1862(2)	0.0232(5)*
C22	-0.3085(3)	0.5441(3)	0.2443(2)	0.0255(5)*
C23	-0.2751(3)	0.4562(3)	0.3538(2)	0.0233(5)*
C24	-0.1354(3)	0.3199(3)	0.3645(2)	0.0212(5)*
C25	0.0599(3)	0.2067(2)	0.23400(18)	0.0195(5)*
C26	0.2984(4)	-0.0113(3)	0.18014(19)	0.0235(5)*
C27	0.2032(4)	0.1425(3)	-0.0066(2)	0.0326(6)*
C28	0.3596(4)	-0.1592(3)	0.3695(2)	0.0292(6)*